Università degli Studi di Pavia
Dipartimento di Scienze della Terra e dell'Ambiente

SCUOLA DI ALTA FORMAZIONE DOTTORALE
MACRO-AREA SCIENZE E TECNOLOGIE

DOTTORATO DI RICERCA IN SCIENZE DELLA TERRA E
DELL'AMBIENTE

Roberta Occhipinti

Valorization of secondary raw materials through alkali activation: study of binders based on sulfate-bearing clay and Pietra Serena sewage sludge

Anno Accademico 2016-2017
Ciclo XXX

Coordinatore
Prof. Roberto Sacchi

Tutor
Prof. Serena Chiara Tarantino
Co-tutor
Dott. ssa Ana Fernández-Jiménez

TABLE OF CONTENTS

List of Figures

List of Tables

List of Abbreviations

Minerals

Alb = albite

Alu = alunite

An = anorthite

Cal = calcite

Dol = dolomite

Fds = feldspars

Kln = kaolinite

Mu = muscovite

Per = periclase

Qtz = quartz

Reaction phases

A = zeo-A

E = ettringite

G = gibbsite

L = lime

T = thenardite

U = U-phase

W = wattevillite

β = YUG- type zeolites

γ, * = CAN-type zeolites

σ = SOD-type zeolites

Cements nomenclature

A = Al_2O_3

AAMs = Alkali Activated Materials

C = CaO

β-C_2S = dicalciumsilicate

C_3S = tricalcium silicate

C_3A=ticalcium aluminate

$C_2(A, F))$=ferrite solid solution

C-A-S-H = Calcium-Aluminum-Silicate-Hydrate

C-S-H = Calcium – Silicate - Hydrate

$F = Fe_2O_3$

$H = H_2O$

$M = MgO$

N-A-S-H = Sodium Aluminum - Silicate-Hydrate

OPC = Ordinary Portland Cement

$S = SiO_2$

$\hat{S} = SO_4$

Other abbreviations related to the techniques employed in the present work.

ASTM = American Society for Testing and Materials

BSE = Back Scattered Electron

DTA = Differential Thermal Analysis

EDS = Energy Dispersive X-ray Spectrometry

FTIR = Fourier Transform Infrared Spectroscopy

ICP-AES = Inductive Coupled Plasma-Atomic Emission Spectroscopy

MAS-NMR = Magic-Angle Spinning-Nuclear Magnetic Resonance

SEM = Scanning Electronic Microscopy

TG = Thermogravimetric analysis

UNI = Ente Nazionale Italiano di Unificazione

XRF = X-Ray Fluorescence spectroscopy

XRPD = X-ray Powder Diffraction

INTRODUCTION AND OBJECTIVES

Alkali activation is the chemical process through which precursors sufficiently rich in reactive silica and alumina and with amorphous or vitreous structures interact with a strongly alkaline medium to give rise, under mild processing conditions, to materials with good binding and cementing properties. Nowadays, Alkali Activated Materials (AAMs) have emerged as alternative to traditional construction materials, such as mortars or Ordinary Portland Cement (OPC), with the aim to become primary components in the development of environmentally sustainable building products, in the context of the growing interest of the scientific community for the themes of sustainability and CO_2 footprint reduction. The OPC industry is in fact one of the major contributors to the overall emission of greenhouse gases. Furthermore, the increasing production of different urban, agriculture, industrial and mining wastes, and its respective storage, independently of their classification (which in Europe is ruled by the Council Directive 1999/31/EC, with limit values specified by the Council Decision 64 2003/33/EC), is another major environmental concern. Therefore, maximizing the re-use and recycling of these residues (as for example, blast furnace slag, fly ash, mining and mineral wastes, ceramic and demolition wastes) is certainly a way for minimizing the environmental impact associated with their treatment and disposal. The use of high-volume wastes in the production of blended or novel cements (including alkali activated cements) is a well-known pathway, by which these wastes can be reused.

Studies and efforts are needed in order to increase the volume of these residues and to introduce new types of resources and industrial by-products in the production chain. The alkaline activation technique constitutes a very promising way to transform recycle materials into resources. It requires two main components, namely the solid precursor, rich in alumina and silica, and the activator, a basic solution of an alkaline or alkaline earth metal. Valorization of a wide variety of mining, metallurgical, societal and agricultural wastes can be achieved through the use of these materials as precursors or activators for alkali-activated binders. Considering that transportation of material at all stages leading up to the production of the binder is of key importance, the cost and emissions metrics (especially for waste products) can be highly affected by the distance and mode of transport (O'Brien et al., 2009; Weil et al., 2009).

The present work is aimed at evaluating Italian feedstock in alkali activation. In particular, two local raw materials have been selected: sulfate-bearing clay and sewage sludge of Pietra Serena, an ornamental sandstone rock.

The issues related to these materials are different: for the first material, the occurrence of alunite, $KAl_3(SO_4)_2(OH)_6$, which is present in kaolin deposits deriving from trachyte, rhyolite, and similar potassium-rich volcanic rocks, normally hinders its use in the ceramic industry due to the release of SO_3 at high temperature. However, alunite can be considered a valuable source of potassium and aluminum in alkali activation. In a previous study (Gasparini et al., 2015), the possibility of using this kaolinitic clay containing alunite to prepare AAMs has been assessed by activating the clay at temperature below desulfation (<700°C, Kristof et al., 2010). Results are promising, as evidenced by high thermal stability and high compressive strength (ca. 80 MPa) of the AAMs obtained from this material, opening the way for utilizing sulfate-bearing kaolin. However, the presence of thenardite, Na_2SO_4, deriving from the dissolution of alunite, was observed in the final products.

The issue associated to the Pietra Serena sandstone sewage sludge, common to all stone processing, is its suitable disposal which needs precise requirements; while the coarser fractions of quarrying wastes can be reused in construction industries, (Akbulut et al., 2007, Felekoglu et al., 2007) the finest fraction often contains heavy metals, organic matters, and high content of water, and could represent a long-term risk of environmental pollution or problems of uneconomical energy-consuming drying process (Yang et al., 2013). To this purpose, the reuse, rather than disposal, would be the ideal solution.

The versatility of the alkali activation process, which allows to employ different materials as precursors, has led to assess the synergic use of more than one type of raw materials. Such study will allow to start building the bases of designing materials that may achieve a balance of commercial and technical goals, and increase resource efficiency.

Aim of this work is therefore the valorization of "secondary raw materials" for designing cements and binders, through alkaline activation process. In particular, the use of kaolitic clay containing sulfate in the alkali activation process has been evaluated. Sulfate can in fact act as promoter of zeolite crystallization, as proposed by Criado et al. (2010), or can be hosted by the metakaolin-based AAM gel. In addition, the reactivity of Pietra Serena sewage sludge and its behavior in the alkali activation process when mixed to the sulfate-bearing clay have been investigated.

The local structure and properties of the products have been investigated in order to strengthen the basis upon which alternative materials can be developed.

With this premise, the present Ph.D. thesis has been designed in three parts:

- In the **first section**, a detailed characterization of all raw materials used for the AAMs syntheses has been carried out. Different techniques have been used in order to study chemical and mineralogical features before and after thermal treatments. An evaluation of amorphous, vitreous and crystalline phases present in the materials has been assessed in order to establish the synthesis parameters.

- In the **second section**, the feasibility of using sulfate-bearing clay for alkali activation has been assessed using sodium silicate as activator. In particular, the effects of the presence of SO_4^{2-} on the microstructure and chemical composition of the resulting AAMs and, in particular, on the N-A-S-H gel have been evaluated; non-soluble sulfate-bearing phases have been identified; finally, the possibility of sulfate uptake by the gel itself assessed.

- In the **third section**, the synergic use of sandstone sewage sludge in binary mixtures with sulfate-bearing clay has been studied. Sodium hydroxide solution has been used as activator. The resulting cements are called *hybrid alkaline cements*, in which binders of two different compositions form C-(A)-S-H and N-A-S-H. The former, well known, is characteristic of Portland cement hydration, while the second is characteristic of the alkaline activation of aluminosilicate, such as fly ash or metakaolin. As in Portland cement manufacture, in which a small amount of gypsum is added to the clinker to control the initial hydration reactions and prevent flash setting, in the studied system, alunite, a sulfate-bearing mineral, is present. At the high pH of the slurry, this mineral dissolves to release SO_4^{2-} and Al^{3+}, which, in turn, react with $Ca(OH)_2$ to form sulfo-aluminate compounds, which could improve the mechanical properties (Katsioti et al., 2009) of the resulting binder. Compositional and microstructural characterizations of the synthesised samples were performed to explain the different mechanisms involved in the alkaline process.

1 STATE OF THE ART

1.1 Alkali activated materials and geopolymers

Alkali Activated Materials (AAMs) are defined as amorphous materials obtained by the reaction between an alkaline solution (e.g., sodium hydroxide and sodium silicate) and an aluminosilicate source. The alkali sources essentially include any soluble substance, which can supply alkali metal cations, raise the pH of the reaction mixture, and accelerate the dissolution of the solid precursor. The aluminosilicate sources can be made from a great number of natural aluminosilicate minerals and industrial by-products, including pozzolans, fly ash, and granulated blast furnace slag, mine tailing, waste glass, etc. The final products, generated after a suitable curing process, give rise to mechanically strong and chemically durable materials. Nowadays, AAMs are receiving noteworthy attention because they can provide comparable performance to traditional cementitious binders in a variety of applications, such as high-tech ceramics, thermal insulating foams, protective coatings, fire-proof building materials, refractory adhesive, and hybrid inorganic-organic composites for toxic waste immobilization (Balaguru, 1998; Gordon et al., 2005; Duxon et al., 2007; Buchwald et al., 2009; Zhang et al., 2010). In the last twenty years, a wide variety of alkaline activated binders, mainly conceived for the construction industry, have been developed with the aim of a technological, environmental and economic earning (Van Deventer et al., 2012).

"AAMs" is the most widespread term for defining these materials (Provis & Bernal, 2014; Provis & Van Deventer, 2014). However, the technology of alkali activation is dated back to a first patent awarded to Kühl in 1908 (Kühl, 1908), the research conducted by Purdon in the 1930s-1940s (Purdon, 1940), and the extensive program of research, development and commercial-scale production grown from the work of Glukhovsky from the 1950s onwards (Glukhovsky, 1959). Davidovits, in the 1970s, introduced the name "geopolymers", developing and patenting materials obtained from the alkali-activation of metakaolin. Nowadays, this term is largely known and used also for marketing purposes, highlighting the similarities between these synthetic materials and the three-dimensional silico-aluminate structures of natural tectosilicate minerals, like feldspathoids and zeolites (Davidovits, 1988; 1991). Nevertheless, there is a surplus of names referring to alkali activated aluminosilicate materials, like mineral polymers (Wastiels et al., 1994), inorganic polymers (Barbosa et al., 2000), soil-cements (Krivenko, 1997; Krivenko & Kovalchuk, 2007), hydroceramic (Siemer,

2002), low temperature aluminosilicate glass (Rahier et al., 1997), zeocements (Krivenko et al., 2007) and zeoceramics (Fernández-Jiménez et al., 2008a).

Based on the nature of their cementitious components (M_2O, CaO-SiO_2-Al_2O_3 system, where M = Na or K), alkaline materials may be grouped by calcium content and classified as high-calcium and low-calcium cements. In the first model, calcium- and silicon-rich materials, such as blast furnace slags (SiO_2 + CaO > 70%), are activated under quite moderate alkaline conditions (Bakharev et al., 2000; Fernández-Jiménez, 2000; Shi et al., 2006). In this case, the main reaction product is a C-A-S-H (calcium silicate hydrate) gel, similar to the gel obtained during Portland cement hydration, which takes Al in its structure. In the second system, the materials activated comprise primarily aluminum and silicon, such as metakaolin or type F fly ash (from coal-fired steam power plants). In this case, more severe working conditions are required to trigger the reactions (highly alkaline media and curing temperatures of 60-200°C). The main reaction product formed in this case is a three-dimensional N-A-S-H (or alkaline aluminosilicate hydrate) gel that has been considered as the amorphous equivalent of synthetic zeolites and have more or less the same chemical composition (Palomo et al., 1999a; Provis et al., 2005; Duxson et al., 2007).

Recently, a new model based on a combination of the preceding two has been assessed. The reaction products are binders known as *blended* or *hybrid alkaline cements*, in which CaO, SiO_2 and Al_2O_3 content is >20% (Alonso & Palomo, 2001; Yip et al., 2005; Palomo et al., 2007; García-Lodeiro et al., 2013a; 2013b), and include a mix of cementitious gels, such as C-A-S-H (which takes sodium into its composition) and N(C)-A-S-H (high calcium content N-A-S-H gels) gels (Garcia-Lodeiro et al., 2010).

In Figure 1.1, a simplified representation of the chemistry of concrete-forming systems, based mainly on the system CaO-Al_2O_3-M_2O-H_2O (where M is the alkali cation) is reported. It shows the classification and position of the AAMs with respect to OPC and sulfo-aluminate cementing systems. Geopolymers are shown as a subset of AAMs, with the highest Al and lowest Ca concentrations, to enable the formation of a network structure rather than the chains characteristic of calcium silicate hydrates. Low-calcium fly ashes and calcined clays are the most prevalent precursors used in geopolymer synthesis.
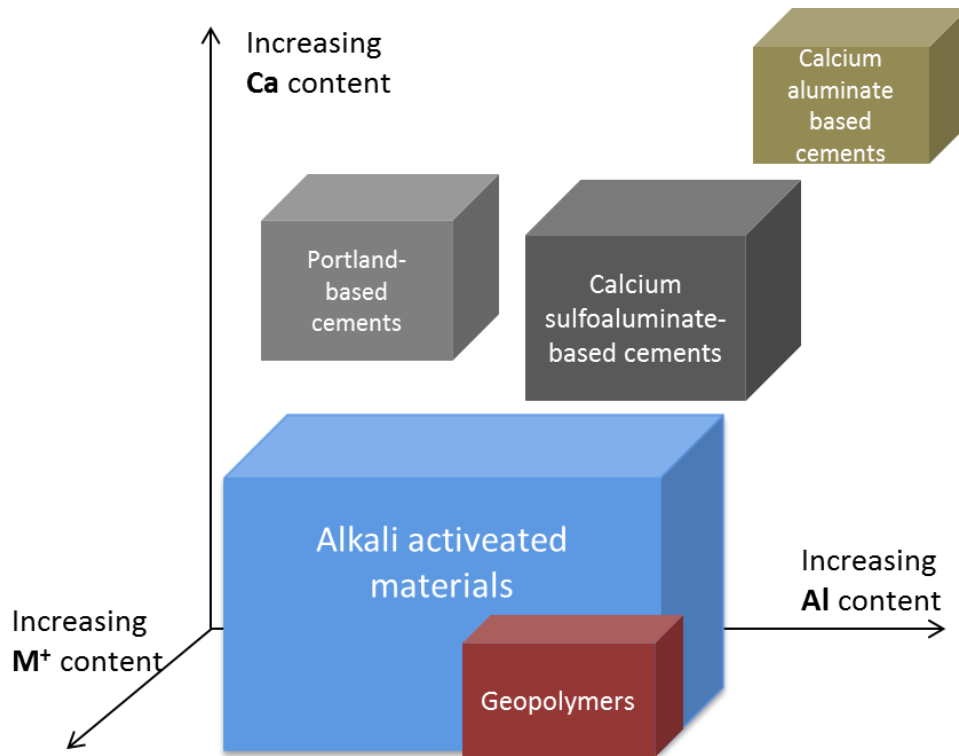
FIGURE 1.1. Classification of AAMs and comparison with OPC and calcium sulfo-aluminate binder chemistry. Grey indicates approximate alkali content; blue corresponds to higher concentrations of alkali (indicated as M^+ on the axis) (readapted from Fig. 1.2 in Provis & van Deventer, 2014).

1.2 Synthesis procedure and reaction process

Alkali activation process can be achieved by mixing the alkaline solution to a finely milled aluminosilicate precursor. Chemical composition, grain size distribution and solid/liquid ratio are parameters that control the workability of the mixture (Palomo & Glasser, 1992; Duxson et al., 2005a; Duxson et al., 2006a). The maturation phase, commonly called curing, can be carried out at temperature between 20°C and about 100°C in controlled humidity conditions (99% R.H.), for different lengths of time. At the end of the curing, specimens are generally stored at room temperature until their use (Fernández-Jiménez & Palomo, 2005a; Duxson et al., 2006b; Zuhua et al., 2009).

The reaction process can be theoretically described by using the model proposed for the formation of some zeolites. Aluminum and silicon dissolved in the medium react to form a three-dimensional poly-hydroxy-silicoaluminate complex (Weng et al., 2005; Fernández-Jiménez et al., 2006). Al and Si, in the solid product, are tetrahedrally coordinated, while the alkalis, that balance the electric charge generated by the substitution of Al^{3+} for Si^{4+}, are

located in the voids of this framework. The resulting product is an alkaline aluminosilicate hydrate $Na_2O \cdot Al_2O_3 \cdot 2SiO_2 \cdot nH_2O$-type gel (N-A-S-H gel), with a three-dimensional structure that, on an atomic to nanometric scale, and resembles zeolitic structures (Provis et al., 2005; Shi et al., 2011).

It is worth highlighting that the alkali-activation of aluminosilicates differs from the chemical process involved in traditional cement hydration, where the main reaction product is a calcium silicate gel, $CaO \cdot SiO_2 \cdot nH_2O$ gel type (C-S-H) (Shi et al., 2011).

Glukhovsky (1959) first proposed an explanation of the mechanism, which governs the formation of the three-dimensional structure of aluminosilicate alkaline gel. The model describes a number of destruction–condensation transformations that take place in the starting solid. The initial units, with an unstable structure, give rise to a series of coagulated structures that at the end condense to generate the hydrated products. In the last years, this model described by Glukhovsky has been improved by the work of different researchers (Duxson et al., 2006a; Shi et al., 2011), who proposed schematic models of N-A-S-H gel reaction process. Figure 1.2 (Shi et al., 2011) outlines the processes occurring in the transformation of a solid aluminosilicate source into a synthetic alkali aluminosilicate.
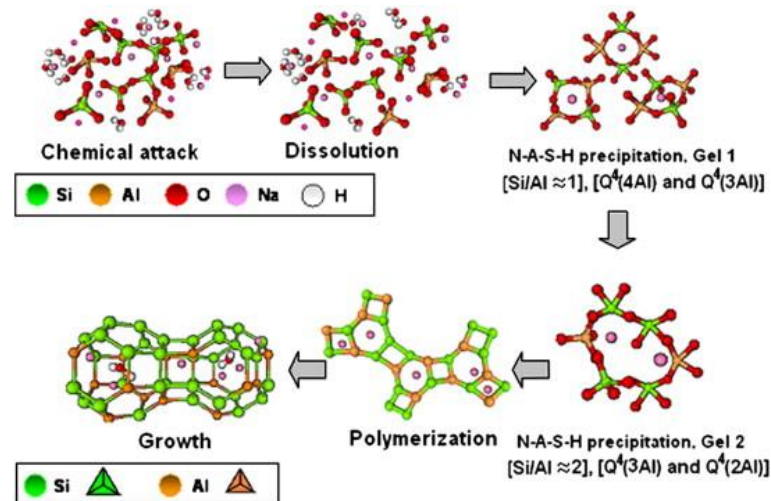
FIGURE 1.2. Descriptive model for alkali activation of aluminosilicates (from Shi et al., 2011).

At first, disaggregation process entails the break of the M-O (M indicates the alkaline cation), Si-O-Si and Al-O-Si bonds in the starting material. The strongly basic environment associated to water consumption and the formation of complex unstable products promotes this process. The dissolution rate increases linearly with pH of the solution, and it is favored by reducing the dimension of the alkaline cation used in the activation solution. At high pH, the fast

dissolution rate gives rise to the formation of a supersaturated aluminosilicate solution, which, by condensation, leads first to the formation of oligomers and then of large networks gel. This process releases the water that was consumed during dissolution, forming a bi-phasic system, which is composed by the aluminosilicate binder and the water. The first intermediate reaction product (denominated Gel 1) contains high aluminum amount due to the higher concentration of Al^{3+} ions in the alkaline medium during the early period of the process. Such higher concentration, in turn, can be attributed to the faster dissolution of aluminum than silicon, because Al-O bonds are weaker and hence more easily severed than Si-O bonds (Provis et al., 2005; Fernández-Jiménez et al., 2006). As the reaction progresses, more Si-O groups of the initial solid source are dissolved, favoring the evolution of the initial Gel 1 into a new Si-rich gel (Gel 2). After gelation, the gel structure continues to rearrange and reorganize, increasing oligomers connectivity and developing a three-dimensional aluminosilicate network. These processes of structural reorganization generate the microstructure and pores distribution of the material, which are fundamental in determining many physical properties (Duxson et al., 2005b).

1.3 Precursors

Two main compounds, an alkaline activator and an aluminosilicate precursor are the starting materials required in the synthesis of AAMs, as described in previous paragraphs. Among the natural raw materials, largely widespread are clay minerals, such as kaolinite, illite and smectite, which need to be activated to improve their reactivity under alkaline conditions. The clay activation generally consists in the thermal treatments in a temperature range between 500°C and 800°C (Buchwald et al., 2009; Elimbi et al., 2011; Gasparini et al., 2013), but a mechanochemically prolonged milling was also successfully used (Makó et al., 2001; Temuujin et al., 2009; Rescic et al., 2011). The result is the loss of structural hydroxyl ions of the clay minerals and the consequently breakdown or partial breakdown of their layered structure, which is responsible of the material reactivity under alkaline conditions. Among the calcined clays, metakaolin represents the most studied precursor, due to its high reactivity and the good properties in terms of resistance and durability of the final products (Palomo et al., 1999b; Duxson et al., 2006a; Siddique & Klaus, 2009; Rashad, 2013). The structure of metakaolin is that of a highly disrupted phyllosilicate structure containing silicon and aluminum only. Although most commercial metakaolin contains levels of impurities, the

effect of these impurities is generally limited by their low dissolution to affect the formation mechanism. In general, the knowledge gained by investigation of metakaolin-based alkali activated materials may be applied to all metakaolin supplies in the world (Duxson et al., 2006a). Among the industrial by-products, largely used are the blast furnace slags (BFS) from iron-making processes and the fly ashes from coal combustion power plant. In recent years, there has been significant growth in the use of different urban, industrial and mining wastes as precursors for production of alkali-activated materials. These materials can be further combined with secondary raw materials to maximize the conversion of wastes into novel resources (Ruiz-Santaquiteria et al., 2013; Horpibulsuk et al., 2015). However, alkali activation can be applied to any material with a sufficiently high content of reactive Al_2O_3 and SiO_2 species.

1.4 Chemistry and structure of hardened alkali activated materials

Aluminosilicate sources and activation solutions are responsible of the good mechanical, physical and chemical properties of AAMs. Based on the nature of starting components, AAMs show extremely diverse chemistry and structure, so much to be grouped under two main categories as mentioned before: low-calcium and high-calcium AAMs. Scheme of primary reaction products either an alkali aluminosilicate N-A-S-H type gel or a calcium aluminosilicate hydrate C-A-S-H type, proposed by Provis and Bernal (2014) is reported in Figure 1.3. The image shows a N-A-S-H gel structure formed by silicon and aluminum tetrahedra distributed at random, forming a three-dimensional skeleton in which cavities are suitable to accommodate alkaline cations, to compensate for the deficit generated by electronegative charge presence of aluminum in tetrahedral coordination (Palomo et al., 2004; Fernández-Jiménez et al., 2003; Provis & Van Deventer, 2009). This type of gel can be also considered as a zeolite precursor (Davidovits, 1991; Provis et al., 2005). Indeed zeolites can be revealed as secondary products of the reaction. AAMs formed by alkali activation of metakaolin and fly ashes (type F according to ASTM classification) belong to this first group. Furthermore, water is not a major structural component as it is in C-A-S-H (Allen et al., 2007). In calcium-rich AAMs, C-A-S-H gels include layers of tetrahedrally coordinated silicate chains with a *dreierketten* structure, in which each chain contains (3*n*-1) tetrahedra for an integer value of *n*. The same structural units are observed in OPC systems. The interlayer region contains Ca^{2+} cations, alkalis and water of hydration that is structurally incorporated

into the gel structure. Some alkali cations also balance the negative charge generated when Al^{3+} replaces Si^{4+} in the tetrahedral chain sites (Fernández-Jiménez et al., 2003; Myers et al., 2013). The second group is mainly represented by vitreous blast furnace slag (BFS). In fact, activation of BFS takes place through a process of polymerization and crystallization of a main C-S-H (calcium silicate hydrate) gel, similar to that obtained in hydration Portland cement that incorporates a significant percentage of aluminum (Puertas et al., 2011).
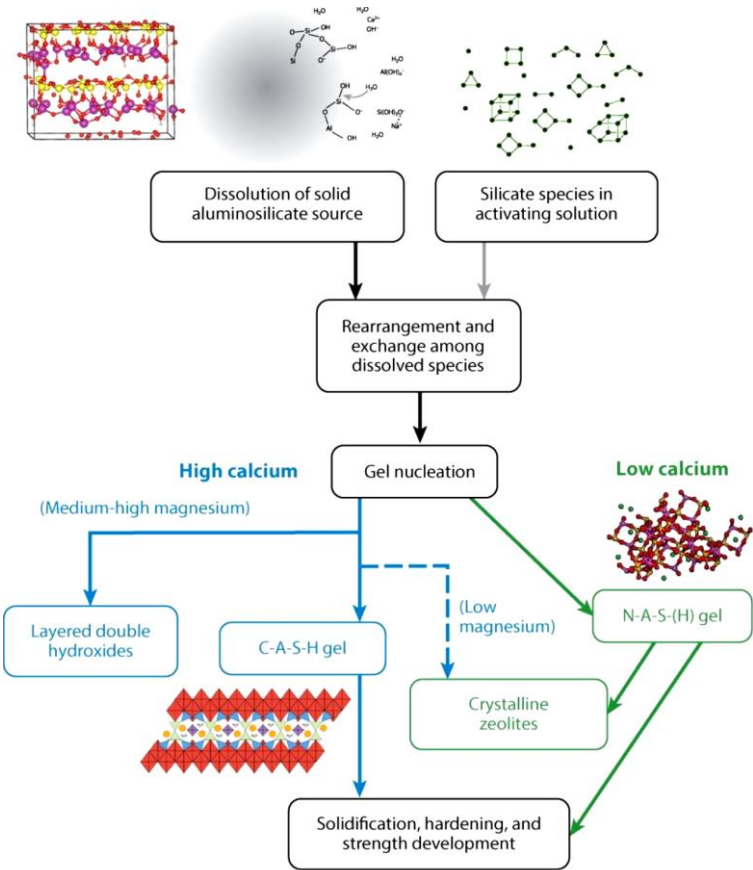
FIGURE 1.3. Processes and reaction products of alkaline activation of a solid aluminosilicate precursor. High-calcium systems react according to the left-hand (blue) pathway; low-calcium systems react according to the right-hand (green) pathway (from Provis & Bernal, 2014).

1.5 Environmental perspectives and technical applications

Nowadays, AAMs are viewed as potential materials to reduce the environmental footprint associated to cement production and they are considered a viable alternative to OPC in large-scale construction applications. Cement production is an important industrial activity in terms of its volumes and impact to greenhouse gas emissions. Worldwide production of cement

contributes at least 5 to 7% of CO_2 emissions (IEA, 2008; Allwood et al., 2010; Friedlingstein et al., 2010; UNSTATS, 2010). The original comparisons between OPC and AAMs that have been drawn in the literature have been largely based on the production step of cement and alkaline activated materials (Davidovits, 1993). These studies claimed AAMs greenhouse emissions up to 5-6 times lower than cement avoiding the high direct emissions of CO_2 as for cement production and reducing some process energy (Davidovits, 2002). A number of studies (e.g. Flower & Sanjayan, 2007; O'Brien et al., 2009) have examined the greenhouse emissions of concrete and cement, and the impact of fly ash content on the total emissions. However, the impacts associated with the production, processing and transportation of feedstock are likely to contribute significantly to the life cycle emissions of the concrete. Some researchers have recently used this approach in examining the life cycle impacts of OPC and AAMs (e.g., Huntzinger & Eatmon, 2009; Habert et al, 2011; Chen et al., 2010; McLellan et al., 2011; Turner & Collins, 2013; Habert & Ouellet-Plamondon, 2016). The variation in financial and environmental costs of AAMs and geopolymers depends on the source of the materials and energy, and the mode and distance of transportation (McLellan et al., 2011). Moreover, there is also a variability of the impact depending on the source of energy and the technology to produce the reagents. The common result of all studies is that sodium silicate solution is the greatest contributor to the CO_2 emissions, representing nearly half of the total emissions, while the clinker represents two-thirds of the impact for standard concrete (Turner & Collins, 2013). Another important issue influencing the environmental assessment of alkali activation technology is related to the availability of raw materials. One of the limitations that constrains or inhibits the worldwide introduction of alkaline cements is the local unavailability and non-uniformity of the raw materials whose chemical and physical properties of alkaline materials are strictly dependent, and which requires control of the quality and origin of the precursors used. In recent years, there has been significant growth in the use of different urban, industrial and mining wastes as precursors for production of alkali-activated materials. However, the existing high demand for blast furnace slag and fly ash in blends with Portland cement represents one of the main barriers to the further deployment of alkali-activated cements on a large industrial scale (Bernal et al., 2016). Moreover, in the near future, the development of alternative energy sources could drive to the decay of fly ash production, as well as blast furnace slag are related to exploitation of iron ores. This means that most of the "traditional" precursors are limited resources and they are likely to be substituted by the "non-conventional" resources. In order to assess the potential usefulness of

these new/alternative precursors, new relationships among them need to be established, and alternative routes to prepare "blended" system explored. The use of secondary raw materials or industrial self-generated wastes in each country could open the way to the development of alkali activation technology reducing the dependence of Portland cement.

From a technical point of view, AAMs achieve good mechanical performances already after one day of curing, developing strengths comparable to OPC after 28 days of hardening (Hawa et al., 2013). Furthermore, they reach similar or greater durability than that offered by traditional cements.

Alkali-activated binders have been shown to be highly resistant to the effects of acidic solutions (Shi et al., 2006; Fernández-Jiménez & Palomo, 2009). They are resistant to attack by sulfates (Palomo et al., 1999a; Bakharev, 2005a; Fernandez-Jimenez et al., 2007); to acid attack by chloride, like sea water (Bakharev, 2005b; Zhang et al., 2012); to freeze-thaw (Škvára et al., 2005; Brooks et al. 2010; Sun & Wu, 2013), maintaining up to 70% of their mechanical strength after 150 cycles (Škvára et al., 2005). Several studies have demonstrated that AAMs preserve good properties at high temperatures, they have ceramic-like properties that make them resistant upon heating at high temperatures, due to formation of several crystalline aluminosilicate phases with potentially high melting points (>1100°C). They are considered valid candidates for passive fire protection applications under intermediate exposure temperatures (<900°C), fire resistant composite materials such as fiber-reinforced composites (Barbosa & MacKenzie, 2003; Kong et al., 2007; Fernández-Jiménez et al., 2010; Davidovits, 2011; Hung et al., 2011; Rickard et al., 2013).

Other studies have been conducted to evaluate the development of alkali-activated mixtures from industrial by-products as sustainable lime/cement replacements for chemical soil stabilization (Al-Tabbaa, 2003; Ahnberg, 2007; Hughes & Glendinning, 2010; Hughes et al., 2011). The laboratory research and small-scale on-site experiments have shown that alkali-activated metakaolin can be applied as an inorganic coating for the protection of existing marine concrete structures (Balaguru et al., 2008; Hu et al., 2008; Fernández-Jiménez & Palomo, 2009; Bhutta et al., 2013; Aydın & Baradan, 2014).

AAMs can be used as immobilizers of toxic and/or hazardous waste, diminishing the severe environmental impacts, which can be associated with their chemistry and toxicity. Several studies have been conducted in the inertization of solid and liquid wastes. The matrices used in these studies include kaolin, metakaolin and cement added with coal fly ash and/or blast furnace slag (Palomo & Palacios, 2003; Phair et al., 2004; Fernández-Jiménez et al., 2005;

12

Hanzlìcekw & Steinerovà-Vondràkova, 2006; Shi & Fernandez-Jimenez, 2006; Xu et al., 2006; Hanzlìcekw et al., 2006; Álvarez-Ayuso et al., 2008; Zhang et al., 2008; Lancellotti et al., 2013). It is known that AAMs behave similarly to zeolites, which are known for their ability to absorb toxic ions (Davidovits, 1988). Therefore, the metals are believed to be microencapsulated as hydroxide or monomeric/small chain silicate species within the Al- and Si-rich amorphous phase of the AAMs (Van Jaarsveld & van Deventer, 1999a). The heavy metals present in the waste mass seem to affect the chemical and physical characteristics of the final product, while the concentration of the alkali activator influences the immobilization behavior of a geopolymeric system (Xu et al., 2006).

Any material used in such applications need to be well understood in terms of nanostructure and durability. Although the scientific and technical advances have provided a very good foundation for the initial deployment of this technology, a correct mix and processing design have been required in order to optimize their performance and/or reduce the costs.

1.6 Low purity clays and secondary raw materials

The research for low cost or easily available materials for production of alkali-activated cements has led to the assessment of a series of "non-commercial" raw materials, as low purity clays or waste raw materials. Low purity clays, include those called *normal clay* such as montmorillonites, illites and smectites, among the others. However, they tend to be more variable in composition and mineralogy than commercial kaolinites, and the parameters of the thermal activation process must be particularly controlled in order to reach high reactivity (Snellings et al., 2016).

Secondary raw materials include industrial waste materials, such as fly ash, blast furnace slag, waste glass, ceramic waste, mine tailings. For example, mine tailing, are generally inert form chemical and environmental point of view. They involve materials that must be removed to gain access to the mineral resource, such as topsoil, overburden and waste rock, as well as tailings remaining after minerals have been largely extracted from the ore. In current practice, mine tailing are transported in slurry form and deposited in storage impoundments. Storage of these materials in such impoundments leads to occupation of large areas of land, costly construction and maintenance, and potential environmental and ecological risks. In fact, management of tailings is an intrinsically risky activity, often involving residual processing chemicals and elevated levels of metals. Some studies have been carried out about the sludge

reutilization as a precursor in AAMs: as building bricks (Ahmari & Zhang, 2012), lightweight aggregates (Tay et al., 1997), additives in mortar or concrete (Valls & Vàzquez, 2001; Yagüe et al., 2005), materials for conservation, restoration and/or rehabilitation of historic monuments, sculptures, decorative and architectural interventions, or simply as materials for building coatings (Castro-Gomes et al., 2012); as new construction materials in stabilized/solidified admixtures of cement–bentonite or cement–jarosite/alunite and as new construction materials and cementitious materials (Cheilas et al., 2007; Katsioti et al., 2008). Although many researchers have shown potential applications of sewage sludge utilized as building and construction materials, further investigations should be carried out in terms of long-term performance.

Blending of non-commercial raw materials or specific wastes in defined combinations, often involving better-understood materials, can offer a lower-risk and potentially highly attractive pathway toward the utilization of a broader range of wastes. In this way, the quality control and metals leachability issues, which are often associated with many of these materials, are reduced through dilution. However, these precursors tend to be more variable in composition and mineralogy than commercial ones, and the parameters of the thermal activation process must be precisely controlled in order to reach high reactivity of the precursors. It is clear from the above discussion that the challenge of producing consistent AAMs from "non-commercial" raw materials requires *a priori* characterization of the precursors each time. The amount of impurities in the raw materials and the form in which they are present both play significant roles in the determining the reaction pathway and the physical properties of the final product. Tailoring compositional and synthesis parameters for a certain system is important in order to define a mix design which allow the exploitation of using several different sources but also focus out on suitable stream of the resource is therefore necessary to draw on reserves of different sources to meet future binder requirements. As example, waste from extractive operations (i.e. waste from extraction and processing of mineral resources) is one of the largest waste streams in the EU. The availability of new and cheap products with good properties, based on self-generated wastes could allow to lower the dependence on Portland cement in the developing countries (Pacheco-Torgal et al., 2014) and to minimize the environmental impacts associated with waste treatment and disposal in developed countries. Although, most of the mixtures now being used at production scale are based on a limited selection of precursors (coal fly ash, blast furnace slag, and calcined clays), a performance-based approach to standardization does certainly offers a possibility for the

14

utilization and valorization of a wide range of silicate and aluminosilicate raw materials as precursors for the production of alkali-activated materials. Standardization and large-scale commercial use of alkali-activation technology is taking place rapidly. In the future, most precursors will probably not belong to the 'conventional' category, due to the high availability and appropriate characteristics of 'new' precursors. Alternative routes must be assessing for optimizing their properties and reactivity, and different options for preparing 'blended' precursors may be explored.

1.7 Alkali activated materials and sulfates

So far, the effect of some anions only on geopolymer properties have been studied (e.g. Lee and van Deventer, 2002; Criado et al., 2010; Desbats-Le Chequer, 2011; Komnitsas et al., 2013). These studies have focused on the effect of anions on fly ash, metakaolin and ferronickel slag-based geopolymers. These researches have shown that anions that can commonly be found in aqueous waste streams, such as nitrates and sulfates, modify the properties of geopolymers. Frizon et al. (2011) have studied the impact caused by the introduction of monovalent and divalent anions, such as sulfate and nitrate, in alkali activated metakaolin systems on the setting time and mechanical properties of the binders. Their immobilization appears to be related to the progress of the geopolymerization reaction. Moreover, depending on the alkali ions used in the activation solution, the anionic species considered may also enhance the precipitation of some zeolites. It has been seen that the compressive strength of geopolymers is negatively affected by the presence of NO_3^- or SO_4^{2-} ions in the starting mixture. Both anions consume most of the available alkali activator moles, hinder geopolymerization reactions and thus the quantity of the gel produced is limited and scarcely connected (Komnitsas et al., 2013).

Kumar et al. (1996) and Laha and Kumar (2002) claimed that the presence of certain oxyanions could act as promoter of crystallization of definite zeolites and they studied the effect of these promoters on the synthesis of mesoporous materials. These authors observed that nitrates, sulfates and phosphates were the compounds that shortened crystallization time most effectively.

Criado et al. (2013) have stated that the presence of sulfate (in the form of Na_2SO_4) in the alkaline activation of fly ash accelerates the conversion of N-A-S-H gel into zeolites, driving the zeolites crystallization. Moreover, they state that the sodium sulfate presence does not

accelerate the fly ash dissolution and consequently lower degrees of reaction and lower mechanical strength have been recorded.

Therefore, sulfate is believed to be a retarding agent in the N-A-S-H gel formation, obstructing the condensation of the aluminosilcates species. No new compounds have been formed by the sulfate and its uptake by the reaction products has not been observed. Sulfates are less commonly applied as activators, not many works have been published on their use in alkaline activation (Fernández-Jiménez, 2000; Shi et al., 2006). Studies on slag activation with a saturated Na_2SO_4 solution have demonstrated that the activation takes place at a relatively low pH (~7), although the process is slow. Similarly to when gypsum is the activator, a sufficient source of hydroxyl ions is needed to accelerate activation. Activation with a combination of gypsum and NaOH yields Na_2SO_4 (Shi et al., 2006).

Recently, studies on the immobilization of sulfate bearing radioactive wastes in blast furnace slag (BFS) based binders have been conducted. Some authors (e.g., Wu et al. 1991, Milestone et al., 2006) have suggested that alkaline activated slag might be a better option for stabilization/solidification (S/S) of low/intermediate level waste than Portland cement due to its low permeability, low reaction heat, and high resistance to aggressive chemical attack. Bai et al. (2006) have demonstrated that the activation of slag using near-neutral salts such as Na_2CO_3 and Na_2SO_4 has been considered as a potential alternative for the immobilization of nuclear wastes including reactive metals. Asano et al. (2008) reported a possible S/S process for sulfate-rich aqueous low level waste using $Ba(OH)_2$ and blast furnace slag (BFS) via a two-step process in which a cement-like solid can be formed. Mombasher et al. (2014) have demonstrated that the immobilization of soluble sulfate-bearing aqueous wastes is effectively achievable in $Ba(OH)_2$-BFS composites via either a one- or two-step process, promoting the simultaneous formation of $BaSO_4$ and the activation of the BFS, favoring the formation of a stable cement-like composite.

1.8 Alkali activated materials and zeolites

Alkaline activation can be viewed as a similar process to that of zeolites formation, as both processes involve the dissolution of solid reactants, hydrolysis of the dissolved species and condensation of the gel phase (Xu & Van Deventer., 2000; Fernandez-Jimenez & Palomo, 2005). Many studies have concluded that AAMs phases can be viewed as an analogue of zeolite (Davidovits, 1982; Krivenko, 1994) and thermodynamically, as metastable with respect to zeolites (Kriven at al., 2004). The conversion of amorphous aluminosilicate gels into zeolites involves two steps: (1) formation of an aluminosilicate gel and (2) crystal nucleation and growth (Akolekar et al., 1997). Palomo and Fernández-Jiménez (2004) proposed this model to describe the alkaline activation process of fly ash and metakaolin based on zeolite synthesis (Palomo et al., 2004). Generally, in the alkaline activation of silica- and alumina rich materials such as fly ash and metakaolin, beside the main reaction product (amorphous alkaline aluminosilicate hydrate, $Mn\text{-}(SiO_2)\text{-}(AlO_2)n.wH_2O$), secondary reaction products are zeolites such as hydroxysodalite, zeolite P, Na-chabazite, zeolite Y and faujasite (Palomo et al., 1999; Fernández-Jiménez et al., 2003, 2006; Duxson et al., 2007a). The specific type of zeolite obtained depends on the NaOH concentration, solid/liquid ratio (Alkan et al., 2005) and Na_2O/SiO_2 ratio (Miao et al., 2009), in addition to the presence or absence of small amounts of other minerals in the starting raw materials (Laha & Kumar, 1996; Cahndrasekhar & Pramada, 2001; Desbats-Le Chequer et al., 2011). The degree of crystallization in AAMs systems is related to the formulation and condition of the synthesis as well as several factors controls the chemistry and nature of final products, such as temperature and pressure, which are generally a prerequisite for zeolites formation. Temperature and water content are usually higher in zeolite synthesis systems than in alkali activation, but also particularly Si/Al ratio and reaction time are variables that can condition zeolites formation (Provis et al., 2005). Nevertheless, some zeolites types can be synthesized at lower temperatures, or even under ambient conditions (Atkins et al., 1995; Valtchev & Bozhilov, 2004).

Silica-rich fly ashes, activated by NaOH, are reported to result in zeolite Na-P1 and/or hydroxysodalite phases (Inada et al., 2005). Exposition with deionized water, seawater, Na_2SO_4 solutions, of amorphous or semi-crystalline AAMs have been shown to crystallize into a zeolite material belonging to the faujasite family (Palomo et al., 1999).

The main synthesis products obtained after activation of kaolinite in NaOH solutions included zeolite LTA (LTA), sodalite (SOD), cancrinite (CAN), faujasite (FAU), zeolite Na-P1 (GIS), JBW-type zeolite (JBW), analcime (ANA), whereas the activation of kaolinite in KOH solutions produced chabazite (CHA), zeolite Barrer-KF, phillipsite (PHI) and K-feldspar (Dudzik and Kowalak, 1974; Rocha et al., 1991; Akolekar et al., 1997; Gualtieri et al., 1997; Chorover et al., 2003; Liu et al., 2003; Zhao et al., 2004; Lin et al., 2004; Ríos et al., 2007).

In general, zeolite molecular sieves are crystalline porous aluminosilicate minerals whose unique pore and channel systems in the molecular size range are the basis of their important contribution in catalysis, separation and ion exchange (Davis & Lobo, 1992; Meier, 1996). These aluminosilicates are characterized by a three-dimensional framework, which contain cages and channels in their negatively charged frameworks because of the substitution of Si_4^+ ions by Al_3^+ ions. Both the β- and ε- cages, which compose their framework, need positively charged species to neutralize them so cations can enter these porous materials to balance the charge of their structural frameworks (Ríos et al., 2008). Due to their porous properties, they are used in various applications such as petrochemical cracking, ion-exchange and separation and removal of gases and solvents. The main environmental applications of zeolites are particularly concern in wastewater treatment. Many industrial processing and wastewater streams, such as waters from leaching, mining, rinsing, etc., contain rare and/or toxic heavy metals mixed with other pollutants, frequently organic substances and ammonium (Šiška, 2005).

In hydrated CaO-Al_2O_3-SiO_2 systems (Portland and pozzolanic cements), for example, the formation of zeolitic phases from corresponding gel phases has been shown to have significantly altered the immobilization potential of these cements towards various waste metals (De Silva & Glasser 1993; Atkins & Glasser 1995). Wang et al. (2006) have demonstrated that conversion of coal fly ash into low-grade zeolites brings not only economic benefits but also environmental benefits, in terms of reducing the landfill and the potential geological risks (Wang et al., 2006).

Sodalite and cancrinite minerals are an interesting group in that they may be synthesized with their open frameworks filled either with water (zeolitic variety) or by salts such as NaC1, Na_2SO_4, Na_2CO_3 and $CaSO_4$ (felspathoid variety). Various intermediate situations with both water and salts presence can be achieved in hydrothermal systems (Barrer, 1984). The salts occupy some or all of the same intracrystalline channels and cavities as water molecules, and they can support and stabilize these frameworks causing the formation of specific zeolites and

determing which of the frameworks of sodalite or cancrinite would form (Barrer, 1970; Barrer 1976). Both SOD and CAN have common chemical formula $Na_6[Al_6Si_6O_{24}]\cdot 2NaX\cdot 6H_2O$, where X can be OH^-, Cl^-, NO_3^-, ½ CO_3^{2-}, or ½ SO_4^{2-}. Cancrinite-group (CAN) compounds cannot be grouped along with the materials showing good zeolitic properties, such as high cation exchange capacity or molecular sieving (Fechtelkord et al., 2003) On the contrary, being extra-framework ions diffusion limited by the presence of fairly strong bonds, CAN can be considered as ion sequestrating materials. The main advantages of synthetic zeolites when compared with naturally-occurring zeolites are that they can be engineered with a wide variety of chemical properties and pore sizes and that they have greater thermal stability. The identification of zeolitic nanocrystals within the AAMs binder is potentially a highly significant data, as it provides a link between the chemical composition and engineering properties of geopolymeric materials.

1.9 Portland cement: a concise overview

Cements and concretes are the most widely used building materials. More important today are the hydraulic cements. Starting from the beginning of the 19th century, the Ordinary Portland Cement (OPC) has become the most used binder in the construction industry. Currently, in the field of inorganic waste management, cement-based processes are widely used for immobilization and encapsulation as well as for stabilization (Sharp et al., 2003).

OPC is obtained by heating a mixture of limestone and clay, or other materials of similar bulk composition, to a temperature at which partial fusion occurs (1300-1500°C). The product, which is called clinker, is ground and mixed with a few percent of gypsum ($CaSO_4\cdot 2H_2O$) or anhydrite ($CaSO_4$) (Jawed et al., 1983) in order to control the initial reaction and prevent flash setting. Portland cement clinker contains four major phases: tricalcium silicate (C_3S), β-dicalcium silicate (β-C_2S), tricalcium aluminate (C_3A), and ferrite solid solution ($C_2(A,F)$) (Taylor, 1986). The hydration of the Portland cement is associated to a sequence of reactions between the phases of clinker, calcium sulfate and water, which lead first to the setting and subsequently to the hardening of the material (Jawed et al., 1983). When the cement is in contact with water, an exchange of species takes place between the solid and the liquid phases, resulting in a rapid increase in the concentration of aluminates, sulfates and alkalis in the liquid phase. During this phase of hydration, a large amount of heat is released and

crystals of ettringite ($6CaO \cdot Al_2O_3 \cdot 3CaSO_4 \cdot 32H_2O$) are formed. Ca^{2+} and Si^{4+} ions from C_3S pass into the solution.

The main reaction product of Portland cement is a very poorly crystalline calcium silicate hydrate known as C-S-H. It is produced by hydration of C_3S and β-C_2S and is often designated as a gel when there are other phases admixed on a sub-micrometer scale. This compound gives long term mechanical strength since the hydration is a slow process. From a structural point of view, C-S-H gel consists of silica tetrahedra linked to each other forming linear chains with similarities to the 1.4-nm tobermorite [$Ca_5Si_6O_{16}(OH)_2 \cdot 8H_2O$ or $C_5S_6H_9$] and/or jennite [$Ca_9H_2Si_6O_{18}(OH)_8 \cdot 6H_2O$ or C_9S_6H] (Taylor, 1986).

With regard to the high-energy consumption, it is necessary to emphasize that during the manufacture of the Portland cement, in the stage of clinker preparation, it is necessary to reach very high temperatures for the formation of each one of its phases.

1.10 Calcium sulfo-aluminate cements

Calcium sulfo-aluminate (CŜA) cements have essentially been developed in China in the 1970s. Designed by the China Building Materials Academy (CBMA), they were intended to the manufacturing of self-stress concrete pipes due to their swelling properties. These cements were produced by adding gypsum to CŜA clinkers, which consist mainly of $C_4A_3\hat{S}$ (ye'elimite), belite and ferrite. The temperatures for the production of CŜA clinkers range from 1200 to 1300°C, i.e., about 200°C lower than needed to manufacture Portland cement clinkers.

The amount of limestone required to produce CŜA cements is considerably smaller than that needed for Portland cement (i.e. 50%, 56%, 59% and 80% of the unit mass needed to form C_3S, C_2S, C_3A and C_4AF, respectively) (Gartner, 2004). It combines economy of cost and low emission of CO_2 with rapid strength gain and compatibility with other construction materials. Hydration provides an internal pore solution where the pH is considerably lower than that of OPC, in which the higher alkalinity can sometimes cause the formation of expansive reaction corrosion products. For this reason, CŜA would allow wastes containing these metals to be encapsulated with lower reactivity than OPC and these cements are currently considered alternative to OPC in waste encapsulation because providing different hydration chemistry. The hydration products are mainly ettringite $3CaO \cdot Al_2O_3 \cdot 3CaSO_4 \cdot 32H_2O$, and alumina gel, $Al_2O_3 \cdot nH_2O$, but monosulfate, $3CaO \cdot Al_2O_3 \cdot CaSO_4 \cdot 12H_2O$, can co-exist depending on the

level of sulfate addition. Ettringite can incorporate a number of ions into its crystal structure, making it an ideal candidate for waste immobilization (Zhou et al., 2006). Limestone, bauxite and gypsum are the main raw materials involved in the manufacture of $C\hat{S}A$ cements. Actually, these cements are not able to substitute entirely the OPC as "cement for the future" (Shi et al., 2011), due to the issues related to the formation of sulfuric acid, with the by-product being Portland cement clinker, which could be considerably worse than that of the normal cement manufacturing process. Moreover, good deposits of calcium sulfate are less abundant than good deposits of limestone. Therefore, it is difficult to try to obtain two useful products at the same time, relative economic variabilities in the raw materials supply and in the market for both products for long periods. For this reason, replacing some of these natural materials with industrial waste and by-products is a challenge of greatest social and technical importance.

References

Ahmari, S., Zhang, L., 2012. Production of eco-friendly bricks from copper mine tailings through geopolymerization. Construction and Building Materials, 29, 323-331.

Åhnberg, H., 2007. On yield stresses and the influence of curing stresses on stress paths and strength measured in triaxial testing of stabilized soils. Canadian Geotechnical Journal, 44(1), 54-66.

Akbulut, H., Gürer, C., 2007. Use of aggregates produced from marble quarry waste in asphalt pavements, Building and Environment 42(5) 1921-1930.

Akolekar, D., Chaffee, A., & Howe, R. F., 1997. The transformation of kaolin to low-silica X zeolite. Zeolites, 19(5-6), 359-365.

Alkan, M., Hopa, Ç., Yilmaz, Z., & Güler, H., 2005. The effect of alkali concentration and solid/liquid ratio on the hydrothermal synthesis of zeolite NaA from natural kaolinite. Microporous and Mesoporous Materials, 86(1), 176-184.

Allen, A.J., Thomas, J.J., Jennings, H.M., 2007. Composition and density of nanoscale calcium-silicate-hydrate in cement. Nature Materials, 6, 311-316.

Allwood, J.M., Cullen, J.M., Milford, R.L., 2010. Options for Achieving a 50% cut in industrial carbon emissions by 2050. Environmental Science & Technology, 44 (6), 1888-1894.

Alonso, S., & Palomo, A., 2001. Alkaline activation of metakaolin and calcium hydroxide mixtures: influence of temperature, activator concentration and solids ratio. Materials Letters, 47(1), 55-62.

Al-Tabbaa, A., 2003. Soil mixing in the UK 1991-2000: state of practice report. Ground Improvement, 7, 117-126.

Álvarez-Ayuso, E., Querol, X., Plana, F., Alastuey, A., Moreno, N., Izquierdo, M., Font, O., Moreno, T., Diez, S., Vázquez, E., & Barra M., 2008. Environmental, physical and structural characterization of geopolymer matrixes synthesized from coal combustion fly ashes. Journal of Hazard Mater, 154(1-3), 175-183.

Asano, T., Kawasaki, T., Higuchi, N., & Horikawa, Y., 2008. Feasibility study of solidification for low-level liquid waste generated by sulfuric acid elution treatment of spent ion exchange resin. Journal of Power and Energy Systems, 2(1), 206-214.

Atkins, M., Glasser, F.P., Jack, J.J., 1995. Zeolite P in cements: its potential for immobilizing toxic and radioactive waste species. Waste Management, 15, 127-135.

Aydın, S., & Baradan, B., 2014. Effect of activator type and content on properties of alkali-activated slag mortars. Composites Part B: Engineering, 57, 166-172.

Bai, Y., Milestone, N. B., & Yang, C., 2006. Sodium sulphate activated GGBS/PFA and its potential as a nuclear waste immobilisation matrix. MRS Online Proceedings Library Archive, 932.

Bakharev, T., Sanjayan, J. G., & Cheng, Y. B., 2000. Effect of admixtures on properties of alkali-activated slag concrete. Cement and Concrete Research, 30(9), 1367-1374.

Bakharev, T., 2005a. Durability of geopolymer materials in sodium and magnesium sulfate solutions. Cement and Concrete Research, 35, 1233-1246.

Bakharev, T., 2005b. Resistance of geopolymer materials to acid attack. Cement and Concrete Research, 35, 658-670.

Balaguru, P., & Kurtz, S., 1998. Use of inorganic polymer-fiber composites for repair and rehabilitation of infrastructures. Repair and Rehabilitation of Reinforced Concrete Structures: The State of the Art, 155-168.

Balaguru, P., Nazier, M., & Arafa, M.D., 2008. Field implementation of geopolymer coatings. Project report of Center for Advanced Infrastructure and Transportation (CAIT) (No. FHWA-NJ-2002-11). Civil and Environmental Engineering. Piscataway, NJ: Rutgers State University.

Barbosa, V.F., MacKenzie, K.J., Thaumaturgo, C., 2000. Synthesis and characterization of materials based on inorganic polymers of alumina and silica: Sodium polysialate polymers. International Journal of Inorganic Materials, 2, 309-317.

Barbosa, V.F., MacKenzie, K.J., 2003. Synthesis and thermal behaviour of potassium sialate geopolymers. Materials Letters, 57, 1477-1482.

Barrer, R.M., & Davies, J.A., 1970. Sorption in decationated zeolites. I. Gases in hydrogen-chabazite. Proceedings of the Royal Society of London. Series A, Mathematical and Physical Sciences, 289-308.

Barrer, R.M., & Townsend, R.P., 1976. Transition metal ion exchange in zeolites. Part 1-Thermodynamics of exchange of hydrated Mn^{2+}, Co^{2+}, Ni^{2+}, Cu^{2+} and Zn^{2+} ions in ammonium mordenite. Journal of the Chemical Society, Faraday Transactions 1: Physical Chemistry in Condensed Phases, 72, 661-673.

Barrer, R.M., & Townsend, R.P., 1984. Ion-exchange equilibria in zeolites and clay minerals. Different concentration scales and derived thermodynamic functions. Journal of the Chemical Society, Faraday Transactions 2: Molecular and Chemical Physics, 80(5), 629-640.

Bernal, S.A., Rodríguez, E.D., Kirchheim, A.P., Provis, J.L., 2016. Management and valorisation of wastes through use in producing alkali-activated cement materials. Journal of Chemical Technology and Biotechnology, 91(9), 2365-2388.

Bhutta, M.A.R., Maruya, T., & Tsuruta, K., 2013. Use of polymer-impregnated concrete permanent form in marine environment: 10-year outdoor exposure in Saudi Arabia. Construction and Building Materials, 43, 50-57.

Brooks, R., Bahadory, M., Tovia, F., & Rostami, H., 2010. Properties of alkali-activated fly ash: high performance to lightweight. International journal of sustainable engineering, 3(3), 211-218.

Buchwald, A., Hohmann, M., Posern, K., Brendler, E., 2009. The suitability of thermally activated illite/smectite clay as raw material for geopolymer binders. Applied Clay Science, 46, 300-304.

Castro-Gomes, J.P., Silva, A.P., Cano, R.P., Durán Suarez, J., Albuquerque, A., 2012. Potential for reuse of tungsten mining waste-rock in technical-artistic value added products. Journal of Cleaner Production, 25, 34-41.

Chandrasekhar, S., & Pramada, P. N., 2001. Sintering behavior of calcium exchanged low silica zeolites synthesized from kaolin. Ceramics International, 27(1), 105-114.

Cheilas, A., Katsioti, M., Georgiades, A., Malliou, O., Teas, C., Haniotakis, E., 2007. Impact of hardening conditions on to stabilized/solidified products of cement-sewage sludge-jarosite/alunite. Cement and Concrete Composites, 29(4), 263-269.

Chen, C., Habert, G., Bouzidi, Y., Jullien, A., 2010. Environmental impact of cement production: detail of the different processes and cement plant variability evaluation. Journal of Cleaner Production, 18 (5), 478-485.

Chorover, J., Choi, S., Amistadi, M. K., Karthikeyan, K. G., Crosson, G., & Mueller, K. T., 2003. Linking cesium and strontium uptake to kaolinite weathering in simulated tank waste leachate. Environmental Science & Technology, 37(10), 2200-2208.

Criado, M., Jiménez, A. F., & Palomo, A., 2010. Effect of sodium sulfate on the alkali activation of fly ash. Cement and Concrete Composites, 32(8), 589-594.

Criado, M., Martínez-Ramirez, S., Fajardo, S., Gómez, P. P., & Bastidas, J. M., 2013. Corrosion rate and corrosion product characterization using Raman spectroscopy for steel embedded in chloride polluted fly ash mortar. Materials and Corrosion, 64(5), 372-380.

Davidovits, J., 1982. U.S. Patent No. 4,349,386. Washington, DC: U.S. Patent and Trademark Office.

Davidovits, J., 1988. Geopolymer chemistry and properties. Geopolymer, 88(1), 25-48.

Davidovits, J., 1991. Geopolymers - Inorganic polymeric new materials. Journal of Thermal Analysis, 37, 1633-1656.

Davidovits, J., 1993. Geopolymer cements to minimise carbon-dioxide greenhouse-warming. Ceramic Transaction, 37, 165-182.

Davidovits, J., 2002. Years of successes and failures in geopolymer applications. Market trends and potential breakthroughs. In Geopolymer Conference, vol. 28, p.29. Geopolymer Institute, Saint-Quentin France, Melbourne, Australia.

Davidovits, J., 2011. Geopolymer Chemistry and Applications, Institut Géopolymère, 16-Rue Galilée, F-02100 Saint-Quentin, France.

Davis, M.E., & Lobo, R.F., 1992. Zeolite and molecular sieve synthesis. Chemistry of Materials, 4(4), 756-768.

De Silva, P.S., Glasser, F.P., 1993. Phase relations in metakaolin/calcium hydroxide/water system. Cement and Concrete Research, 23, 627-639.

Desbats-Le Chequer, C., & Frizon, F., 2011. Impact of sulfate and nitrate incorporation on potassium-and sodium-based geopolymers: geopolymerization and materials properties. Journal of materials science, 46(17), 5657-5664.

Dudzik, Z., & Kowalak, S., 1974. Preparation of zeolites of faujasite type from porcelain clay. Przemysl Chemiczny, 53(10), 616-618.

Duxson, P., Lukey, G.C., Separovic, F., Van Deventer, J.S.J., 2005a. Effect of alkali cations on aluminum incorporation in geopolymeric gels. Industrial and Engineering Chemistry Research, 44, 832-839.

Duxson, P., Provis, J.L., Lukey, G.C., Mallicoat, S.W., Kriven, W.M., van Deventer, J.S.J., 2005b. Understanding the relationship between geopolymer composition, microstructure and mechanical properties. Colloids and Surfaces A: Physicochemical and Engineering Aspects, 269, 47-58.

Duxson, P., Fernández-Jiménez, A., Provis, J.L., Lukey, G.C., Palomo, A., van Deventer, J.S.J., 2006a. Geopolymer technology: the current state of the art. Journal of Materials Science, 42, 2917-2933.

Duxson, P., Lukey, G.C., van Deventer, J.S., 2006b. Thermal evolution of metakaolin geopolymers: Part 1-Physical evolution. Journal of Non-Crystalline Solids, 352, 5541-5555.

Duxson, P., Provis, J.L., Lukey, G.C., van Deventer, J.S.J., 2007. The role of inorganic polymer technology in the development of 'green concrete'. Cement and Concrete Research, 37, 1590-1597.

Elimbi, A., Tchakoute, H., Njopwouo, D., 2011. Effects of calcination temperature of kaolinite clays on the properties of geopolymer cements. Construction and Building Materials, 25, 2805-2812.

Fechtelkord, M., Posnatzki, B., & Buhl, J. C., 2003. Characterization of basic cancrinite synthesized in a butanediol-water system. European journal of mineralogy, 15(3), 589-598.

Felekoglu, B., 2007. Utilisation of high volumes of limestone quarry wastes in concrete industry (self-compacting concrete case), Resources, Conservation and Recycling 51(4) 770-791.

Fernández-Jiménez A., 2000. Cementos de escorias activadas alcalinamante: influencia de las variables y modelización del proceso. Ph.D. Thesis, Universidad Autónoma de Madrid.

Fernández-Jiménez, A., Puertas, F., Sobrados, I., Sanz, J., 2003. Structure of calcium silicate hydrates formed in alkaline-activated slag: influence of the type of alkaline activator. Journal of the American Ceramic Society, 86, 1389-1394.

Fernandez-Jimenez, A., Palomo, A., 2005a. Composition and microstructure of alkali activated fly ash binder: effect of activator. Cement and Concrete Research, 35, 1984-1992.

Fernández-Jiménez, A., Palomo, A., 2005b. Mid-infrared spectroscopic studies of alkali-activated fly ash structure. Microporous and Mesoporous Materials, 86, 207-214.

Fernández-Jiménez, A., Palomo, A., Sobrados, I., Sanz, J., 2006. The role played by the reactive alumina content in the alkaline activation of fly ashes. Microporous and Mesoporous Materials, 91, 111-119.

Fernandez-Jimenez, A., García-Lodeiro, I., Palomo, A., 2007. Durability of alkali-activated fly ash cementitious materials. Journal of Materials Science, 42, 3055-3065.

Fernández-Jiménez, A., Monzó, M., Vicent, M., Barba, A., Palomo, A., 2008a. Alkaline activation of metakaolin-fly ash mixtures: obtain of Zeoceramics and Zeocements. Microporous and Mesoporous Materials, 108, 41-49.

Fernández-Jiménez, A., Palomo, A., Pastor, J.Y., Martin, A., 2008b. New Cementitious Materials Based on Alkali-Activated Fly Ash: Performance at High Temperatures. Journal of the American Ceramic Society, 91, 3308-3314.

Fernández-Jiménez, A., & Palomo, A., 2009. Chemical durability of geopolymers. Geopolymers: Structures, Processing, Properties and Industrial Applications, 167-190.

Fernández-Jiménez, A., Pastor, J.Y., Martín, A., Palomo, A., 2010. High-Temperature Resistance in Alkali-Activated Cement. Journal of the American Ceramic Society, 93, 3411-3417.

Flower, D., & Sanjayan, J., 2007. Greenhouse gas emissions due to concrete manufacture. The International Journal of Life Cycle Assessment, 12(5), 282-288.

Friedlingstein, P., Houghton, R.A., Marland, G., Hackler, J., Boden, T.A., Conway, T.J., 2010. Update on CO_2 emissions. Nature Geoscience, 3(12), 811-812.

García-Lodeiro, I., Fernández-Jiménez, A., Palomo, A., Macphee, D.E., 2010. Effect of calcium additions on N-A-S-H cementitious gels. Journal of the American Ceramic Society, 93(7), 1934-1940.

Garcia-Lodeiro, I., Fernández-Jiménez, A., & Palomo, A., 2013a. Variation in hybrid cements over time. Alkaline activation of fly ash–portland cement blends. Cement and Concrete Research, 52, 112-122.

Garcia-Lodeiro, I., Fernández-Jiménez, A., & Palomo, A., 2013b. Hydration kinetics in hybrid binders: Early reaction stages. Cement and Concrete Composites, 39, 82-92.

Gartner, E., 2004. Industrially interesting approaches to "low-CO_2" cements. Cement and Concrete Research, 34(9), 1489-1498.

Gasparini, E., Tarantino, S. C., Ghigna, P., Riccardi, M. P., Cedillo-González, E. I., Siligardi, C., Zema, M., 2013. Thermal dehydroxylation of kaolinite under isothermal conditions. Applied Clay Science, 80-81, 417-425.

Gasparini, E., Tarantino, S. C., Conti, M., Biesuz, R., Ghigna, P., Auricchio, F., & Zema, M., 2015. Geopolymers from low-T activated kaolin: Implications for the use of alunite-bearing raw materials. Applied Clay Science, 114, 530-539.

Glukhovsky, V. D., 1959. Soil silicates. Gostroiizdat Publish. Kiev, USSR.

Gordon, M., Bell, J.L., & Kriven, W.M., 2005. Comparison of naturally and synthetically-derived, potassium-based geopolymers. In Advances in Ceramic Matrix Composites X: Proceedings of the 106th Annual Meeting of The American Ceramic Society, Indianapolis, Indiana, USA 2004, Ceramic Transactions (vol. 165, p. 95). Wiley-American Ceramic Society.

Gualtieri, A., Norby, P., Artioli, G., & Hanson, J., 1997. Kinetics of formation of zeolite Na-A [LTA] from natural kaolinites. Physics and Chemistry of Minerals, 24(3), 191-199.

Habert, G., Roussel, N., 2009. Study of two concrete mix-design strategies to reach carbon mitigation objectives. Cement and Concrete Composites, 31(6), 397-402.

Habert, G., De Lacaillerie, J.D.E., Roussel, N., 2011. An environmental evaluation of geopolymer based concrete production: reviewing current research trends. Journal of Cleaner Production, 19, 1229-1238.

Habert, G., & Ouellet-Plamondon, C., 2016. Recent update on the environmental impact of geopolymers. RILEM Technical Letters, 1, 17-23.

Hanzlìcekw, T., & Steinerovà-Vondràkova, M., 2006. Immobilization of toxic metals in solidified systems of siloxo-sial networks. Journal of American Ceramic Socety, 89(3), 968-970.

Hawa, A., Tonnayopas, D., Prachasaree, W., Taneerananon, P., 2013. Development and performance evaluation of very high early strength geopolymer for rapid road repair. Advances. Materials Science and Engineering, 9.

Horpibulsuk, S., Suksiripattanapong, C., Samingthong, W., Rachan, R., Arulrajah, A., 2015. Durability against wetting-drying cycles of water treatment sludge-fly ash geopolymer and water treatment sludge-cement and silty clay-cement systems. Journal of Materials in Civil Engineering, 28(1), 04015078.

Hu, S., Wang, H., Zhang, G., & Ding, Q., 2008. Bonding and abrasion resistance of geopolymeric repair material made with steel slag. Cement and concrete composites, 30(3), 239-244.

Hughes, P.N., Glendinning, S., Manning, D.A.C., Noble, B.C., 2010. Production of 'green'concrete using red gypsum and waste. Engineering Sustainability, 163, 137-146.

Hughes, P. N., Glendinning, S., Manning, D. A. C. White, M. L., 2011. Use of red gypsum in soil mixing engineering applications. Geotechnical Engineering, 164, 223-234.

Hung, T.D., Louda, P., Kroisova, D., Bortnovsky, O., Xiem, N.T., 2011. New generation of geopolymer composite for fire-resistance, in Tesinova P., (ed.) Advances in Composite Materials - Analysis of Natural and Man-Made Materials, Rijeka: InTech, 73-94.

Huntzinger, D.N., Eatmon, T.D., 2009. A life-cycle assessment of Portland cement manufacturing: comparing the traditional process with alternative technologies. Journal of Cleaner Production, 17 (7), 668-675.

IEA, 2008. CO_2 Emissions from Fuel Combustion. International Energy Agency, Paris, France, p. 512.

Inada, M., Eguchi, Y., Enomote, N., Hojo, J., 2005. Synthesis of zeolite from coal fly ashes with different silica-alumina composition, Fuel, 84, 299-304.

Jawed, I., Skalny J., Young J. F., 1983. Structure and performance of cements. Hydration ofPortland cement. Ed. P. Barnes, 6, London, England.

Katsioti, M., Katsiotis, N., Rouni, G., Bakirtzis, D., Loizidou, M., 2008. The effect of bentonite/cement mortar for the stabilization/solidification of sewage sludge containing heavy metals. Cement and Concrete Composite, 30(10), 1013-1019.

Katsioti, M., Tsakiridis, P. E., Giannatos, P., Tsibouki, Z., & Marinos, J., 2009. Characterization of various cement grinding aids and their impact on grindability and cement performance.Construction and Building Materials, 23(5), 1954-1959.

Komnitsas, K., Zaharak, D., Bartzas, G., 2013. Effect of sulphate and nitrate anions on heavy metal immobilisation in ferronickel slag geopolymers. Applied Clay Science, 73, 103-109.

Kong, D.L., Sanjayan, J.G., Sagoe-Crentsil, K., 2007. Comparative performance of geopolymers made with metakaolin and fly ash after exposure to elevated temperatures. Cement and Concrete Research, 37, 1583-1589.

Kristóf, J., Frost, R.L., Palmer, S.J., Horváth, E., Jakab, E., 2010. Thermoanalytical studies of natural potassium, sodium and ammonium alunites. Journal of Thermal Analysis and Calorimetry, 100(3), 961-966.

Kriven, W.M., Gordon M., Bell J.L., 2004. Geopolymers: nanoparticulate, nanoporous ceramics made under ambient conditions. Microscopy and Microanalysis 2004, Proc. 62nd Annual Meeting of the Microscopy Society of America, 10, 404-405.

Krivenko, P. V., 1994. Alkaline cements. In Proceedings of the 1st International Conference on Alkaline Cements and Concretes, Kiev, Ukraine, 1994. 1, 11-129.

Krivenko, P. V., 1997. Alkaline cements: terminology, classification, aspects of durability, Proceedings of the 10th International Congress on the Chemistry of Cement, Gothenburg, Sweden, Amarkai and Congrex Göteborg, Gothenburg, Sweden, p. 6.

Krivenko, P. V., Kovalchuk, G., Palomo, A., Fernandez-Jiménez, A., 2007. Fly Ash based geocements: genesis of microstructure and properties at hydration-dehydration process. Brittle Matrix Composites, 8, 55-64.

Krivenko, P.V., Kovalchuk, G.Y., 2007. Directed synthesis of alkaline aluminosilicate minerals in a geocement matrix. Journal of Materials Science, 42, 2944-2952.

Kuehl, H., 1908. U.S. Patent No. 900,939. Washington, DC: U.S. Patent and Trademark Office.

Kumar, R., Bhaumik, A., Ahedi, R. K., & Ganapathy, S., 1996. Promoter-induced enhancement of the crystallization rate of zeolites and related molecular sieves. Nature, 381(6580), 298-300.

Laha, S. C., & Kumar, R., 2002. Promoter-induced synthesis of MCM-41 type mesoporous materials including Ti-and V-MCM-41 and their catalytic properties in oxidation reactions. Microporous and Mesoporous Materials, 53(1), 163-177.

Lancellotti, I., Ponzoni, C., Barbieri, L., Leonelli, C., 2013. Inertization of chromium liquid waste in inorganic polymers via alkali activation of metakaolin. Extended abstract. Environmental Engineering and Management Journal, 12(S11), 39-42.

Lee, W. K. W., & Van Deventer, J. S. J., 2002. The effects of inorganic salt contamination on the strength and durability of geopolymers. Colloids and Surfaces A: Physicochemical and Engineering Aspects, 211(2), 115-126.

Lin, D. C., Xu, X. W., Zuo, F., & Long, Y. C., 2004. Crystallization of JBW, CAN, SOD and ABW type zeolite from transformation of meta-kaolin. Microporous and Mesoporous Materials, 70(1), 63-70.

Liu, X., Yan, Z., Wang, H., & Luo, Y., 2003. In situ synthesis of NaY zeolite with coal-based kaolin. Journal of Natural Gas Chemistry, 12(1), 63-70.

Makó, É., Frost, R.L., Kristóf, J., Horváth, E., 2001. The effect of quartz content on themechanochemical activation of kaolinite. Journal of Colloid and Interface Science, 244, 359-364.

McLellan, B.C., Williams, R.P., Lay, J., van Riessen, A., Corder, G.D., 2011. Costs and carbonemissions for geopolymer pastes in comparison to ordinary Portland cement. Journal of Cleaner Production, 19(9-10), 1080-1090.

Meier, W. M., 1996. Olson; DH and Baercocher, Ch. Zeolites, 17, 1.

Miao, Q., Zhou, Z., Yang, J., Lu, J., Yan, S., Wang, J., 2009. Synthesis of NaA zeolite from kaolin source. Frontiers of Chemical Engineering in China, 3(1), 8-11.

Milestone, N.B., 2006. Reactions in cement encapsulated nuclear wastes. Need for toolbox of different cement types, Advanced in Applied Ceramics, 105(1), 13-20.

Mobasher, N., Bernal, S.A., Hussain, O.H., Apperley, D.C., Kinoshita, H., Provis, J.L., 2014. Characterisation of $Ba(OH)_2$-Na_2SO_4- blast furnace slag cement-like composites for the immobilisation of sulfate bearing nuclear wastes. Cement and Concrete Research, 66, 64-74.

Myers, R.J., Bernal, S.A., San Nicolas, R., Provis, J.L., 2013. Generalized structural description of calcium-sodium aluminosilicate hydrate gels: the cross-linked substituted tobermorite model. Langmuir, 29, 5294-5306.

O'Brien, K., Ménaché, J., O'Moore, L., 2009. Impact of fly ash content and fly ash transportation distance on embodied greenhouse gas emissions and water consumption in concrete. The International Journal of Life Cycle Assessment, 14(7), 621-629.

Pacheco-Torgal, F., Labrincha, J., Leonelli, C., Palomo, A., & Chindaprasit, P., (Eds.), 2014. Handbook of alkali-activated cements, mortars and concretes. Elsevier.

Pacheo-Torgal, F., Castro-Gomes, J., Jalili, S., 2010. Durability and environmental performance of alkali-activated tungsten mine waste mud mortars. Journal of Materials in Civil Engineering, 22(9), 897-904.

Palomo, A., & Glasser, F., 1992. Chemically-bonded cementitious materials based on metakaolin. British ceramic. Transactions and Journal, 91(4), 107-112.

Palomo, A., Blanco-Varela, M.T., Granizo, M.L., Puertas, F., Vazquez, T., Grutzeck, M.W., 1999a. Chemical stability of cementitious materials based on metakaolin. Cement and Concrete Research, 29, 997-1004.

Palomo, A., & Palacios, M., 2003. Alkali-activated cementitious materials: alternative matrices for the immobilisation of hazardous wastes: Part II. Stabilisation of chromium and lead. Cement and concrete research, 33(2), 289-295.

Palomo, A., Alonso, S., Fernández-Jiménez, A., Sobrados, I., and Sanz, J., 2004. Alkaline activation of fly ashes. A NMR study of the reaction products. Journal of the American Ceramic Society, 87(6), 1141-1145.

Palomo, A., Fernández-Jiménez, A., Kovalchuk, G., Ordoñez, L. M., & Naranjo, M. C., 2007. OPC-fly ash cementitious systems: study of gel binders produced during alkaline hydration. Journal of Materials Science, 42(9), 2958-2966.

Palomo, A., Grutzeck, M.W., Blanco, M.T., 1999b. Alkali-activated fly ashes: A cement for the future. Cement and Concrete Research, 29, 1323-1329.

Palomo, A., Krivenko, P., Garcia-Lodeiro, I., Kavalerova, E., Maltseva, O., Fernández-Jiménez, A., 2014. A review on alkaline activation: new analytical perspectives. Materiales de Construcción, 64(315), 022.

Phair, J. W., Van Deventer, J. S. J., & Smith, J. D., 2004. Effect of Al source and alkali activation on Pb and Cu immobilisation in fly-ash based "geopolymers". Applied Geochemistry, 19(3), 423-434.

Provis, J.L., Lukey, G.C., Van Deventer, J.S.J., 2005. Do geopolymers actually contain nanocrystalline zeolites? A re-examination of existing results, Chemistry of Materials, 17(12), 3075-3085.

Provis, J.L., & Van Deventer, J.S.J., (Eds.), 2009. Geopolymers: structures, processing, properties and industrial applications. Elsevier.

Provis, J.L., Bernal, S.A., 2014a. Geopolymers and related alkali-activated materials, Annual Review of Materials Research, 44, 299-327.

Provis, J.L., Van Deventer, J.S.J., 2014b. Alkali Activated Materials: State-of-the-art Report, Springer, RILEM TC 224-AAM. 24.

Puertas, F., Palacios, M., Manzano, H., Dolado, J.S., Rico, A., Rodríguez, J., 2011. A model for the C-A-S-H gel formed in alkali-activated slag cements. Journal of the European Ceramic Society, 31, 2043-2056.

Purdon, A.O., 1940. The action of alkalis on blast-furnace slag. Journal of the Society of Chemical Industry, 59(9), 191-202.

Rahier, H., Simons, W., Van Mele, B., Biesemans, M., 1997. Low-temperature synthesized aluminosilicate glasses: Part III Influence of the composition of the silicate solution on production, structure and properties. Journal of Materials Science, 32, 2237-2247.

Rashad, A.M., 2013. Alkali-activated metakaolin: A short guide for civil Engineer - An overview. Construction and Building Materials, 41, 751-765.

Rescic, S., Plescia, P., Cossari, P., Tempesta, E., Capitani, D., Proietti, N., Mecchi, A.M., 2011. Mechano-chemical activation: an ecological safety process in the production of materials to stone conservation. Procedia Engineering, 21, 1061-1071.

Rickard, W. D., Vickers, L., & Van Riessen, A., 2013. Performance of fibre reinforced, low density metakaolin geopolymers under simulated fire conditions. Applied Clay Science, 73, 71-77.

Rios, C.A., Williams, C.D., Fullen, M.A., 2009. Nucleation and growth history of zeolite LTA synthesized from kaolinite by two different methods. Applied Clay Science, 42(3), 446-454.

Rocha, J., Klinowski, J., & Adams, J. M., 1991. Synthesis of zeolite Na-A from metakaolinite revisited. Journal of the Chemical Society, Faraday Transactions, 87(18), 3091-3097.

Ruiz-Santaquiteria, C., Fernández-Jiménez, A., Skibsted, J., Palomo, A., 2013. Clay reactivity: Production of alkali activated cements. Applied Clay Science, 73, 11-16.

Sharp, J., Hill, J., Milestone N., Miller, E., 2003. Cementitious systems for encapsulation of intermediate level waste. In ASME (American Society of Mechanical Engineers) 2003, 9th International Conference on Radioactive Waste Management and Environmental Remediation, 1425-1433.

Shi, C., Fernandez-Jimenez, A., 2006. Stabilization/solidification of hazardous and radioactive wastes with alkali-activated cements. Journal of hazardous materials, 137, 1656-1663.

Shi, C., Jiménez, A.F., Palomo, A., 2011. New cements for the 21st century: The pursuit of an alternative to Portland cement. Cement and Concrete Research, 41, 750-763.

Siddique, R., & Klaus, J., 2009. Influence of metakaolin on the properties of mortar and concrete: A review. Applied Clay Science, 43(3), 392-400.

Siemer, D.D., 2002. Hydroceramics, a "new" cementitious waste form material for US defense-type reprocessing waste. Materials Research Innovations, 6(3), 96-104.

Šiška, J., 2005. Extraction of heavy metals and ammonium from waters by unsaturated fatty acids and their soaps, Hydrometallurgy 76, 155-172.

Škvára, F., Jílek, T., Kopecký, L., 2005. Geopolymer materials based on fly ash. Journal Ceramics Silikaty, 49, 195-204.

Snellings, R., Mertens, G., Elsen, J., 2012. Supplementary cementitious materials. Reviews in Mineralogy and Geochemistry, 74(1), 211-278.

Sun, P., & Wu, H. C., 2013. Chemical and freeze–thaw resistance of fly ash-based inorganic mortars. Fuel, 111, 740-745.

Tay, J., Show, K., 1997. Resource recovery of sludge as a building and construction material - a future trend in sludge management. Water Science and Technology, 36(11), 259-266.

Taylor, H. F. W., 1993. Nanostructure of C-S-H: Current status. Advanced Cement Based Materials, 1(1), 38-46.

Temuujin, J. V., Van Riessen, A., & Williams, R., 2009. Influence of calcium compounds on the mechanical properties of fly ash geopolymer pastes. Journal of hazardous materials, 167(1-3), 82-88.

Turner, L. K., & Collins, F. G., 2013. Carbon dioxide equivalent (CO_2-e) emissions: A comparison between geopolymer and OPC cement concrete. Construction and Building Materials, 43, 125-130.

Valls, S., & Vazquez, E., 2001. Accelerated carbonatation of sewage sludge–cement–sand mortars and its environmental impact. Cement and Concrete Research, 31(9), 1271-1276.

Valtchev, V. P., & Bozhilov, K. N., 2004. Transmission electron microscopy study of the formation of FAU-type zeolite at room temperature. The Journal of Physical Chemistry B, 108(40), 15587-15598.

Van Deventer, J. S., Provis, J. L., & Duxson, P., 2012. Technical and commercial progress in the adoption of geopolymer cement. Minerals Engineering, 29, 89-104.

Wang, S., & Wu, H., 2006. Environmental-benign utilisation of fly ash as low-cost adsorbents. Journal of hazardous materials, 136(3), 482-501.

Wastiels, J., Wu, X., Faignet, S., & Patfoort, G., 1994. Mineral polymer based on fly ash. J Resour Manage Technol, 22(3), 135-141.

Weil, M., Dombrowski, K., Buchwald, A., 2009. Life-cycle analysis of geopolymers. In: Provis, J. L., Van Deventer, J. S. J. (Eds.), Geopolymers: Structures, Processing, Properties and Industrial Applications. Woodhead Publishing Limited, Cambridge, England, pp. 194-210.

Weng, L., Sagoe-Crentsil, K., Brown, T., & Song, S., 2005. Effects of aluminates on the formation of geopolymers. Materials Science and Engineering: B, 117(2), 163-168.

Xu, H., & Van Deventer, J. S., 2002. Geopolymerisation of multiple minerals. Minerals engineering, 15(12), 1131-1139.

Xu, J. Z., Zhou, Y. L., Chang, Q., & Qu, H. Q., 2006. Study on the factors of affecting the immobilization of heavy metals in fly ash-based geopolymers. Materials letters, 60(6), 820-822.

Yagüe, A., Valls, S., Vázquez, E., & Albareda, F., 2005. Durability of concrete with addition of dry sludge from waste water treatment plants. Cement and concrete research, 35(6), 1064-1073.

Yang, K. H., Song, J. K., & Song, K. I., 2013. Assessment of CO_2 reduction of alkali-activated concrete. Journal of Cleaner Production, 39, 265-272.

Yip, C. K., Lukey, G. C., & Van Deventer, J. S. J., 2005. The coexistence of geopolymeric gel and calcium silicate hydrate at the early stage of alkaline activation. Cement and concrete research, 35(9), 1688-1697.

Zhang, Z., Yao, X., & Zhu, H., 2010. Potential application of geopolymers as protection coatings for marine concrete: II. Microstructure and anticorrosion mechanism. Applied clay science, 49(1-2), 7-12.

Zhang, Z., Yao, X., & Zhu, H., 2010. Potential application of geopolymers as protection coatings for marine concrete: II. Microstructure and anticorrosion mechanism. Applied clay science, 49(1-2), 7-12.

Zuhua, Z., Xiao, Y., Huajun, Z., & Yue, C., 2009. Role of water in the synthesis of calcined kaolin-based geopolymer. Applied Clay Science, 43(2), 218-223.

EXPERIMENTAL

2 STARTING MATERIALS

In the present work, different natural aluminosilicate raw materials have been used as precursors in the alkaline activation process:

- Sulfate-bearing clay (L02-K) from Piloni di Torniella mine (Italy);

- High grade kaolin (Sl-K) from Seiltz deposits (Germany);

- Sewage sludge of Pietra Serena sandstone (Italy);

- Alunite (B1) from Piloni di Torniella (Italy);

All these materials have been thermally treated in order to improve their reactivity prior to be employed as precursors in the AAMs preparation.

2.1 Sulfate-bearing (L02-K) clay

The sulfate-bearing clay (L02-K) used in this work derives from Piloni di Torniella quarry, located in Tuscany, Central Italy. This clay is found in kaolinitic deposits belonging to the Roccastrada district. They have been originated by alteration process of rhyolites and other calc-alkaline or high-potassium calcalkalin rocks due to post-magmatic hydrothermal phenomena (Mazzuoli, 1967; Bertolani & Loschi Ghittoni, 1989; Gorga et al., 1995; Peccerillo et al., 2003; Viti et al., 2007). Representative geochemical composition of Roccastrada rhyolites (data from Peccirillo & Donati, 2003) has been reported in the following table.

TABLE 2.1. Chemical composition of major and trace elements of Roccastrada rhyolite (from Peccirillo & Donati, 2003)

Major oxides (wt%)	SiO_2	Al_2O_3	CaO	Fe_2O_3	K_2O	MgO	MnO	Na_2O	P_2O_5	TiO_2	L.o.I	Tot.
	73.4	13.67	0.72	1.82	4.76	0.81	0.02	2.48	0.11	0.27	2.1	100.1
Trace elements (ppm)	Ba	Cr	Ni	Rb	Sr	V	Y	Zr	La	Ce		
	105	11	8	521	55	29	23	100	19	38		

Alunite, $KAl_3(SO_4)_2(OH)_6$, is present in these deposits and its formation has been related to the alteration of plagioclase and K-feldspars due to an high S concentration in the fluid during hydrothermal process of these riolites (Viti et al., 2007). In the past, Piloni di Torniella mine was a very productive mining site for the alum extraction from alunite deposits. Since 1800, with technological advances, extraction process of the alum became too expensive and the mine was finally closed in 1950. Nowadays, the Piloni di Torniella mine is still in activity for kaolin extraction. However, the clays are selectively exploited in order to enrich the kaolinitic fraction and lower the sulfur content. The presence of alunite in these clays normally hinders

their use in ceramic industry because it affects strongly the rheological behavior of ceramic slips, increasing drastically their viscosity. Furthermore, this mineral fosters the formation of efflorescence on both dried and fired wares, and causes the emissions of SO_3 compound during firing (Lombardi & Mattias, 1987; Ligas et al., 1997; Dondi et al., 2000). Sulfate-bearing clay from Piloni di Torniella mine was provided by Eurit s.r.l. (Italy). Chemical composition has been analyzed by X-ray fluorescence (XRF) using XRF-fusion method. Sulfate content was determined by using Combustion Infrared Detection method, and samples were analyzed by Eltra CS-2000 devices and the results are reported in Table 2.2. The analyses were carried out at Activation Laboratories Ldt. (Canada). Loss on Ignition (L.o.I.), determined by mass loss up to 1000°C is also reported in table.

TABLE 2.2. Chemical composition of L02 clay (XRF, wt% of oxides).

Oxides	SiO_2	Al_2O_3	Fe_2O_3	CaO	MgO	Na_2O	K_2O	TiO_2	Others[a]	L.o.I[b]	Sum	SO_4^{2-} [c]
L02-K	59.02	22.85	1.26	0.11	0.12	0.82	3.30	0.28	0.26	12.07	100.27	5.2

[a] Minor elements: Cr_2O_3; MnO; NiO; P_2O_5; V_2O_5.
[b] L.o.I: Loss on Ingnition at 1000°C
[c] SO_4^{2-} is calculated separately by Combustion Infrared Detection Method

Particles size distribution was carried out by Malvern Mastersizer S particle size analyzer equipped with a laser diffraction sensor
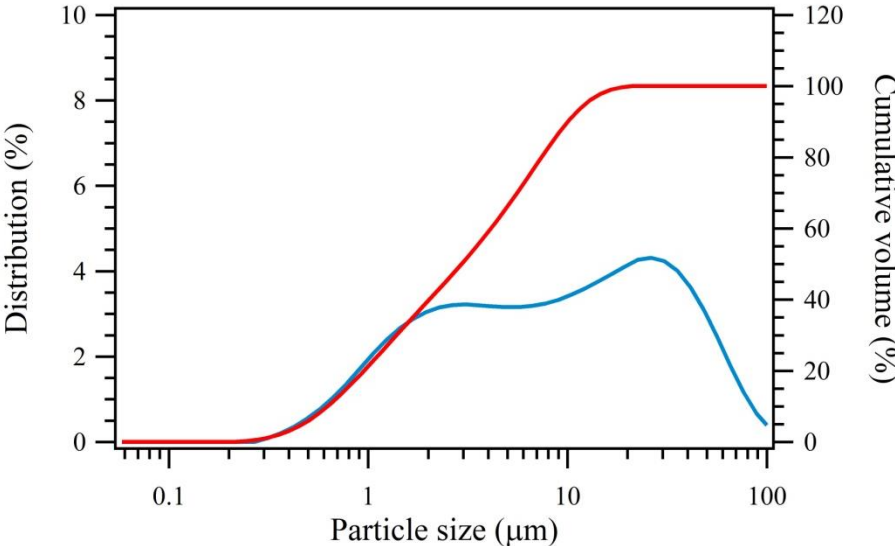
FIGURE 2.1. Particle size distribution of L02-K clay. Red curve = cumulative volume (%); Blue curve = volume distribution (%)

The measurement was conducted on a wet sample (using ethanol as solvent). The results reported in Figure 2.1 display two maxima indicating a bimodal distribution. It has been found that 50% of particles have size below 8.5 µm whereas 90% below 45 µm.

L02-K mineralogical composition has been characterized by XRPD as reported in Figure 2.2. As shown from the XRPD pattern (red line), the most intense reflections are related to quartz and feldspars. Defined peaks at 12.4°, 20.3° and 21.3° 2θ reveal the presence of kaolinite, while peaks at 15.5°, 18.0° and 30° 2θ are related to alunite.
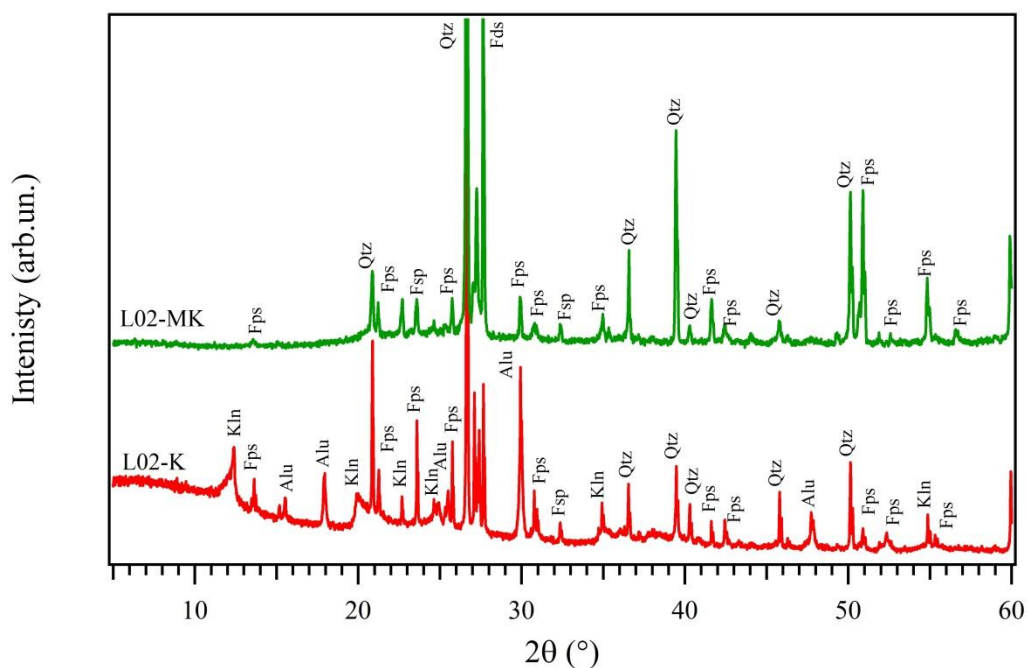
FIGURE 2.2. XRPD pattern of L02-K (red line) and respective thermal-treated L02-MK (green line); Alu = alunite; Fsp = Feldspars; Kln = kaolinite; Qtz = quartz.

The amount of each phase has been quantified by Rietveld refinement method, the refined pattern is plotted in Figure 2.3. Rietveld quantitative analysis was performed using α-Al$_2$O$_3$ as internal standard and the results were carried out by GSAS software. Results are reported in Table 2.3. The data obtained from Rietveld quantification are in good agreement with the calculation carried out by the XRF analysis and with those obtained from thermal analyses as reported in Table 2.3.
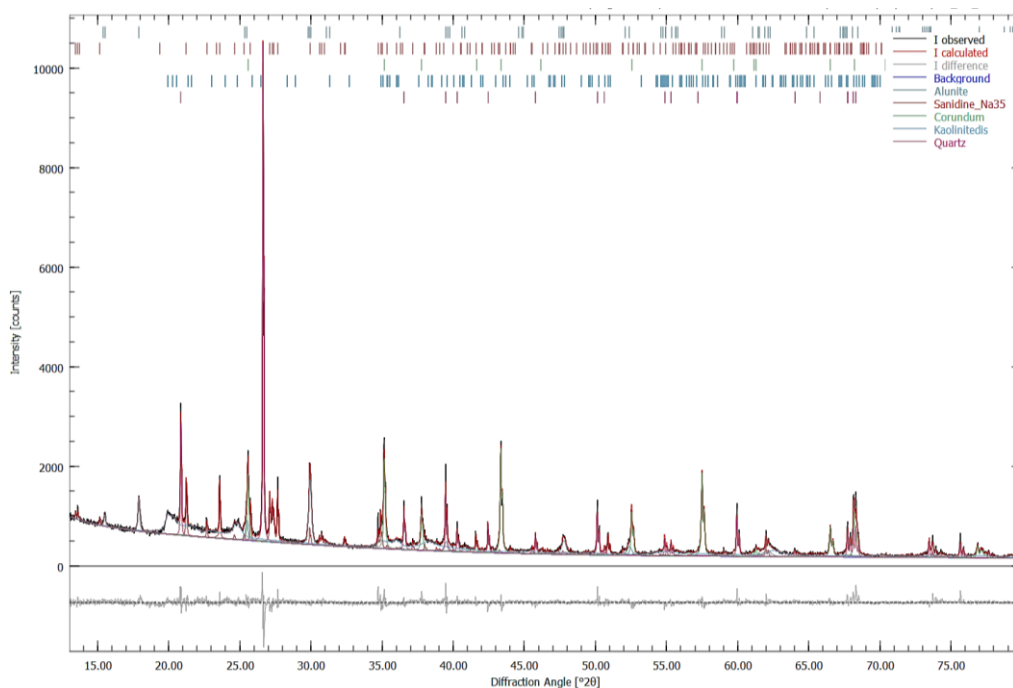
FIGURE 2.3. Rietveld plot of L02-K mixed with 20% of α-Al$_2$O$_3$ (Rwp = 6.88%; Rexp = 4.57% X^2 = 2.35%).

TABLE 2.3. Mineralogical analyses of L02-K clay evaluated by Rietveld method and data from weight loss analysis (TG) and XRF analysis.

Minerals	Calculated by Rietveld method (wt %)[a]	Calculated by Rietveld method (wt %)[b]	Calculated by weight loss (TG) (wt %)	Calculated from L.o.I. and measured SO$_4^{2-}$
Alunite	13.0 (2)	12.3 (2)	12.0	11.2
Kaolinite	47.6 (7)	44.9 (7)	45.0	45.7
Quartz	26.0 (3)	24.6 (3)		
Feldspars	19.0 (5)	18.2 (5)		
Total	105	100		

[a] With internal standard, [b] calculated without internal standard

Thermal analyses have been conducted up to 1000°C in order to understand the effect of the heat treatment on the kaolinite and alunite. Thermogravimetric (TG) and Differential Thermal Analysis (DTA) results are shown in Figure 2.4. DTA curve of L02-K shows a first endothermic peak around 500-550°C, with a corresponding weight loss in the TG curve of ca. 8 wt%. This endothermic event corresponds to the transformation of kaolinite into metakaolinite and to the dehydroxylation of alunite, which generates K-alum, KAl$_3$(SO$_4$)$_2$, and amorphous alumina (Kristof et al., 2010).
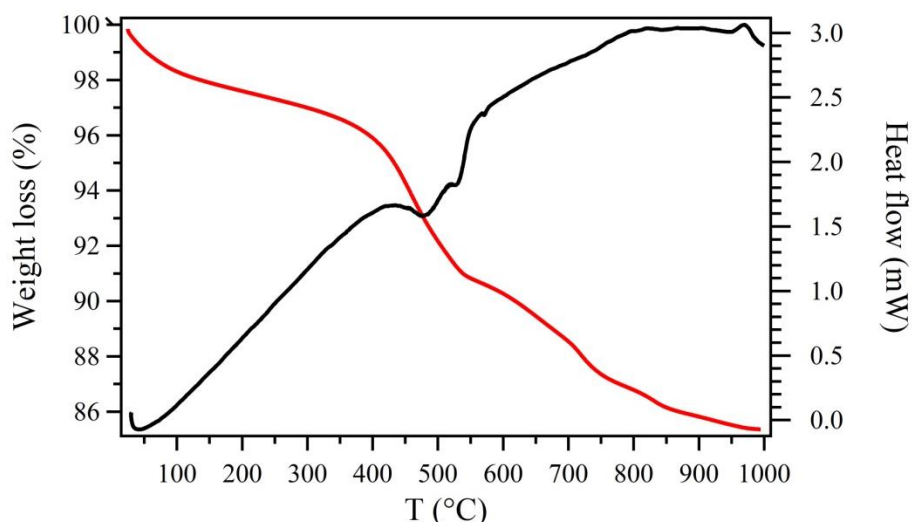
FIGURE 2.4. TG (red line) and DTA (black line) of L02-K clay.

In the range above 500°C and up to 700°C, other two small endothermic peaks (at 528°C and 570°C) are visible in the DTA curve. These are associated to a weight loss of ca. 5.5 wt% and are related to alunite desulfation (Gasparini et al., 2013; Osornio-Rubio et al., 2016). The desulfation is associated with the formation of amorphous Al_2O_3 and release of SO_3. L02-K has been thermally treated at 550°C for 3 hours in order to transform kaolinite into metakaolinite (labelled L02-MK) for the AAMs preparation. The XRD pattern of L02-MK (Figure 2.2, green line) shows that the peaks related to kaolinite and alunite have disappeared, meaning that all the kaolinite and alunite are transformed into metakaolinite and amorphous alumina and alum-K respectively. The only crystalline phases, which are obviously, not affected by thermal treatment, are quartz and feldspars.

FT-IR spectra of the L02-K and L02-MK are reported in Figure 2.5. The bands at 3690 cm^{-1} and at 3621 cm^{-1} represent the Al-OH and Al-OH-Al stretching vibration respectively (Bish, 1993; Petit et al., 1999; Zemenová et al., 2014). Another band at 3481 cm^{-1} represents the Al-OH alunite stretching vibration (Frost & Wain, 2008; Toumi & Tlili, 2008). These bands disappear after heat treatment due to the loss of hydroxyl groups (Chakraborty, 2003). One peak related to stretching vibration of SO_4^{2-} is observed as a shoulder of the main band near 1120 cm^{-1} in L02-K. From a visual point of view, a band in the sulfate stretching region seems to be retained after thermal treatment. The main feature of the IR spectra is an intense band centered at 1010 cm^{-1}, showing two maxima at 1006 cm^{-1} and 1024 cm^{-1}, as observed in spectra from kaolinite (Balan et al., 2001; Gasparini et al., 2013).

Peaks in this area correspond to Si-O stretching modes. According to literature (Frost & Wain, 2008; Toumi & Tlili, 2008), SO_4^{2-} symmetric stretching modes of alunite are in this wavenumber region as well. After thermal treatment, the main Si-O band is broad and show a single maximum centered at 1030 cm^{-1}. This shift towards higher frequency could be likely due to redistribution of the Si-O environment as result of dehydroxylation (Lambert et al., 1989). In the spectrum from L02-K there is a peak at 914 cm^{-1} corresponding to Al^{VI} deformation vibrations, this disappears in the L02-MK spectrum due to the dehydroxylation and the change in coordination of Al^{VI} to Al^{III,IV,V} (Frost et al., 1999). Both the spectra in Fig. 2.5 show a doublet near 770 cm^{-1} related to the presence of quartz, which is present before and after thermal treatment (Farmer, 1974; Gasparini et al., 2015).
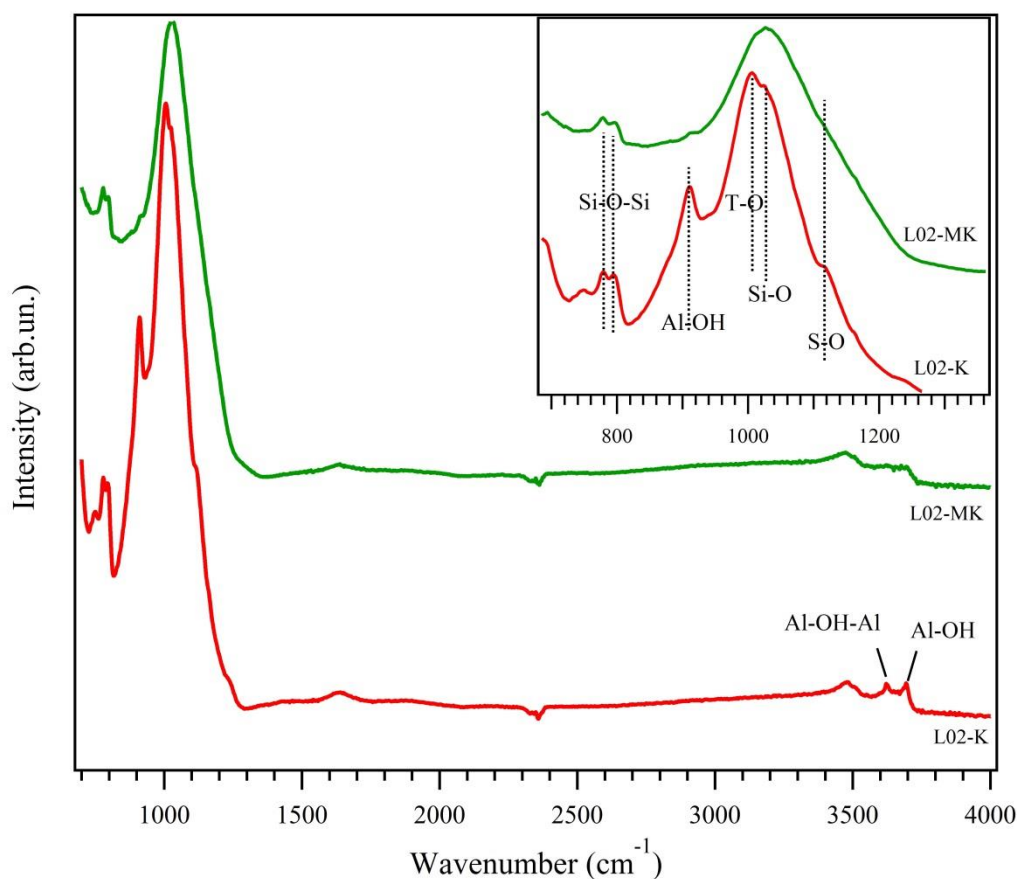
FIGURE 2.5 FT-IR spectra of the L02 clay before (L02-K) and after (L02-MK) thermal treatment.

In order to determine the potential reactivity of this sulfate bearing kaolin as aluminosilicate source in AAMs, a selective acid attack with (1% HF) has been conducted on L02-K and

L02-MK respectively. This approach is based on the study of Ruiz-Santaquiteria et al. (2013), who assessed the accuracy of the quantification of the potential reactivity of a series of natural aluminosilicates (white clays, red clay) with respect to acid and basic chemical attacks. They have demonstrated that the quantification of the material dissolved in the two media is comparable for all the analyzed aluminosilicates. Moreover, they also proposed an analytical procedure, which allows determining the silica and reactive alumina content. Such *reactive* SiO_2/Al_2O_3 ratio can be used to predict the properties of the alkaline cements obtained from a given aluminosilicate and therefore speedily and simply assess its aptness for use as a prime material in alkaline activation (Ruiz-Santaquiteria et al., 2013).

Powders of L02-K (1.008 g) and of L02-MK (1.006 g) have been attacked with 100 ml of HF (1% V/V) solution for 5 hours. Then the solid residue and the solution were separated by filtering. The solid residue was calcined at 1000°C. The percentage of soluble phase content was quantified by subtracting the final weight of the calcined residue from the initial mass of the aluminosilicate. The percentage of silica and alumina released during selective chemical attack was determined in the leachates by means of ICP-AES. The data for L02-K and L02-MK, are reported in Table 2.4 together with the calculations of the corresponding oxides (wt %).

TABLE 2.4. Solubility of Si and Al after HF attack for L02-K kaolin and L02-MK metakaolin

Samples	L02-K			L02-MK		
Soluble phase wt %	59.0			63.3		
SiO_2/Al_2O_3 reactive	1.32			1.0		
SiO_2/Al_2O_3 total (XRF)	2.2					
elements in the liquid	ppm	ppm corresponding oxides	Wt% corresponding oxides[a]	ppm	ppm corresponding oxides	Wt% corresponding oxides[a]
Si	105.04	224.73	22.29	110.29	235.95	22.24
Al	89.53	169.18	16.78	117.19	221.44	20.87
Fe	8.36	11.96	1.19	9.46	13.53	1.28
Ca	1.12	1.57	0.16	1.25	1.76	0.17
Mg	0.26	0.44	0.04	0.27	0.46	0.04
S	1.63	4.08	0.41	17.13	42.78	4.03

[a] Oxides percentage normalized at the initial weight of the analyzed samples

According to the findings given in the table, both materials have shown potentially reactive phase of 59 wt% for L02-K and of 63.3 wt% for L02-MK. Metakaolin display a higher reactivity towards alkaline activation process, as expected. The percentage of soluble phases

in the samples is above 50 wt%, therefore above the minimum required to ensure satisfactory results (Fernandez & Palomo, 2003; Ruiz-Santaquiteria et al., 2013). Table 2.4 gives also the reactive SiO_2/Al_2O_3 ratios compared to those calculated from XRF results. As expected, SiO_2/Al_2O_3 ratio found by XRF, differ significantly from the reactive SiO_2/Al_2O_3 ratios determined by using selective chemical attack, because not all the silica and the alumina from the original raw material are reactive. L02-K shows a SiO_2/Al_2O_3 of 1.3 while L02-MK of 1.0, meaning that more aluminum is dissolved after thermal treatment.
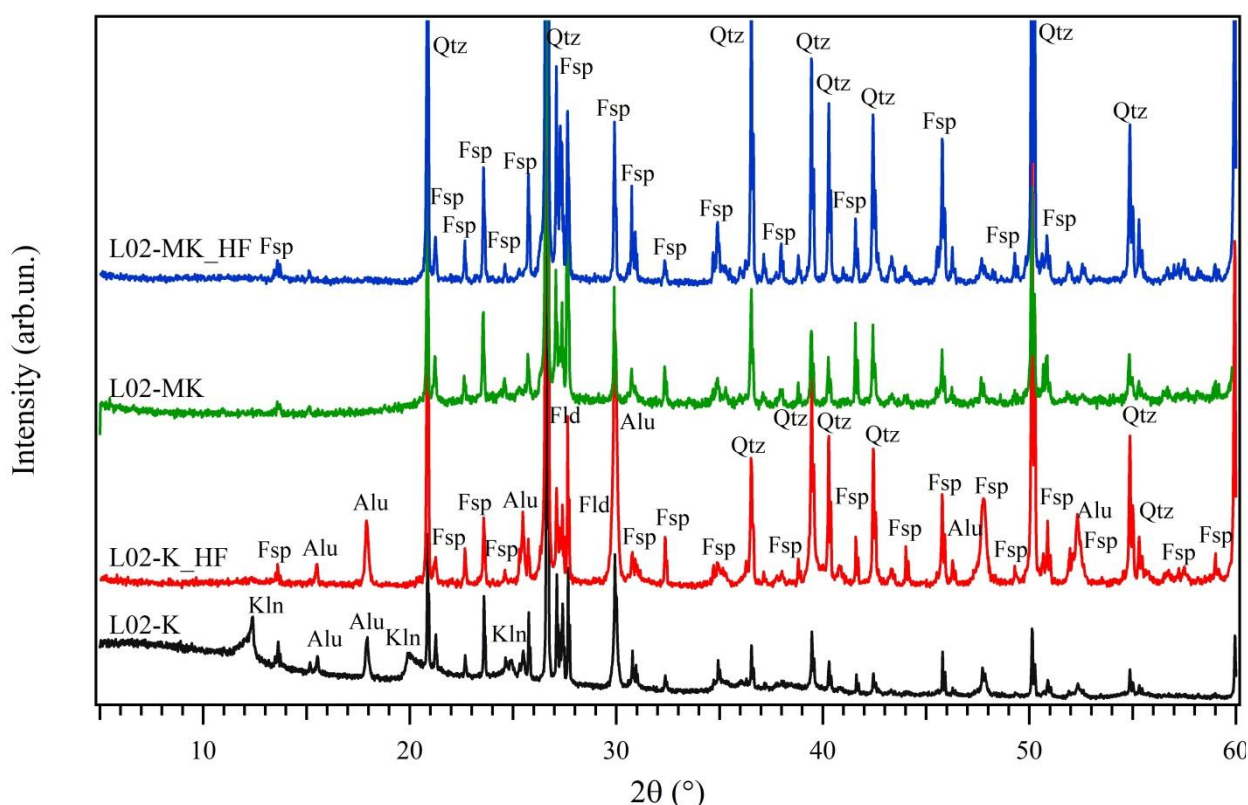
FIGURE 2.6 XRPD patterns of L02-K and L02-MK before (green and black line respectively) and after (red and blue line respectively) chemical HF attack.

Figure 2.6 shows the XRPD patterns of the residues of L02-K_HF and L02-MK_HF after selective chemical attack. For comparison, the L02-K and L02-MK patterns before acid treatment have been also reported in the graph. After HF attack, only quartz, feldspars have been detected in patterns of both clays. Alunite peaks are still evident in the pattern of L02-K_HF, while kaolinite peaks are not present, thus indicating its dissolution in the acid medium. The higher amount of Al in the leachead from L02-MK_HF might be explained by considering the alunite dissolution after thermal treatment.

41

2.2 High grade (Sl-K) kaolin

Industrial kaolin, labelled Sl-K, deriving from the Seilitz kaolin deposits (Germany) and provided by Sibelco Italia S.p.a, has been selected for the AAMs preparation. Its chemical composition determined by XRF and L.o.I are reported in Table 2.5.

TABLE 2.5. Chemical composition Sl-K kaolin (XRF, wt% oxides)

Oxides	SiO_2	Al_2O_3	Fe_2O_3	CaO	MgO	Na_2O	K_2O	TiO_2	SO_4	Others[b]	L.o.I[c]
Sl-K[a]	67.0	31.5	0.32	0.12	0.23	-	0.35	0.24	-	0.24	10.02

[a] Gasparini et al., 2013. [b] Minor elements: Cr_2O_3; MnO; NiO; P_2O_5; V_2O_5. [c] L.o.I: Loss on Ignition at 1000 °C.

Sl-K is considered high-grade kaolin as revealed also by the XRF analysis and by the XRD analysis, as shown in Figure 2.7 (red line). Sharp and intense peaks related to kaolinite are revealed together to those related to quartz. Its mineralogical composition results exclusively composed by 73 wt% of kaolinite and 27 wt% of quartz as determined by Gasparini et al. (2013), who studied also the dehydroxylation kinetics of this sample. In this study, Sl-K has been heated at 550°C for 3 hours in order to be comparable to L02-MK even if at this temperature the dehydroxylation of Sl-K is not complete (see also, Gasparini et al., 2013).
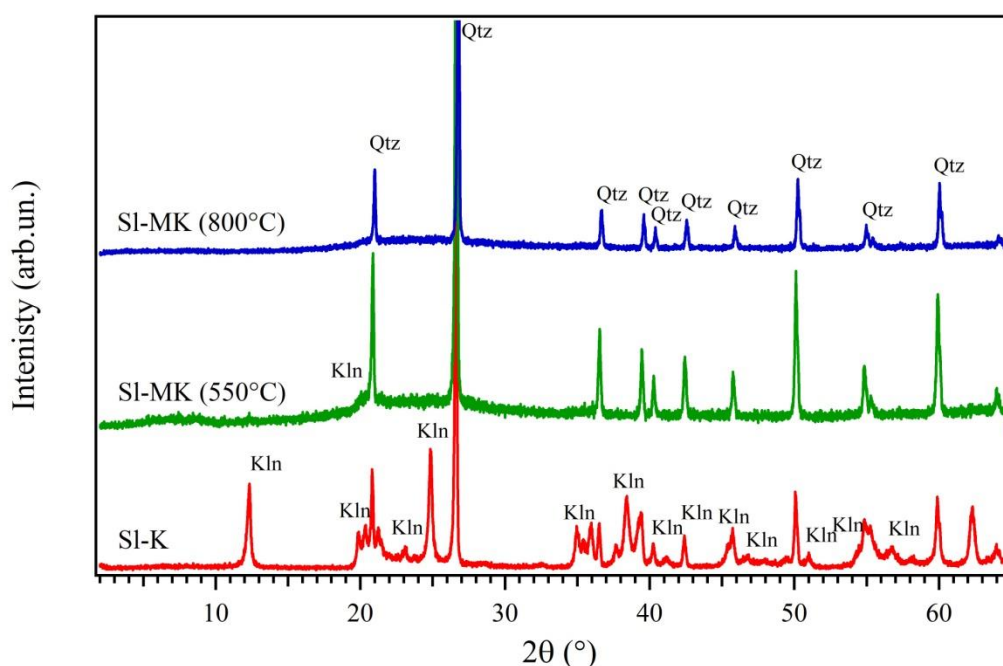
FIGURE 2.7. XRPD patterns of Sl-K and Sl-MK before and after thermal treatments (at temperature of 550°C, green line, and at 800°C, blue line).

From XRPD pattern after thermal treatment at 550°C (green line) is possible to observe that traces of kaolinite are still present. Sl-K has been also treated at 800°C for 2 hours (blue line)

in order to reach the full transformation of kaolinite into reactive metakaolinite, as deduced by the absence of peaks of kaolinite from the XRPD pattern. The only crystalline phase detected is quartz. However, studies by microscopy techniques on the kaolinite dehydroxylation via transmission electron have demonstrated that, after dehydroxylation, structure does not completely collapse along the c-axis and maintains a two-dimensional regularity (Gualtieri & Bellotto, 1998), and it has been found that metakaolinite consists of planar entities, which result from the combination of two successive dehydroxylated sheets (Bergaya et al., 1996).

Kaolinite dehydroxylation is related to many different factors such as Kaolinite structure (e.g., particle size, shape and morphology, density of defects) (Bellotto et al., 1995; Dion et al., 1998), associated minerals, heating rate (Castelein et al., 2001; Ptáček et al., 2010; 2011), sample treatment (Vizcayano et al., 2005), pressure and partial water vapor pressure (Dion et al., 1998). FT-IR spectra of the untreated Sl-K and Sl-MK samples after thermal treatments are reported in Figure 2.8.
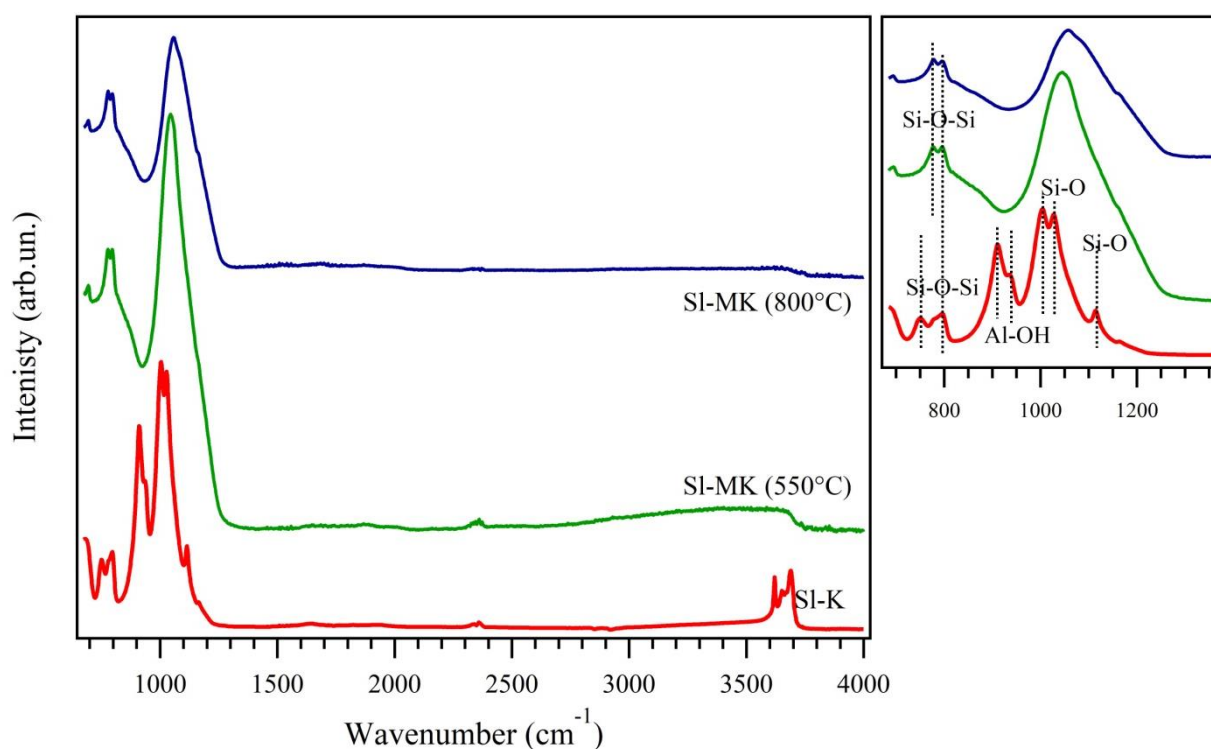
FIGURE 2.8. FT-IR spectra of Sl-K and Sl-MK before (red line) and after thermal treatment (at temperature of 550°C, green line, and at 800°C, blue line).

Intense well-resolved peaks at 3689, 3650 and 3689 cm^{-1} correspond to the stretching modes of the OH groups (Farmer, 1974; Balan et al.; 2001) as reported by the red line. The three

peaks observed at 1112 cm^{-1}, 1027 cm^{-1} and 1004 cm^{-1} correspond to Si-O stretching modes (Russel & Fraser, 1971; Frost et al, 2001). The bands observed at 935 cm^{-1} and 910 cm^{-1} are related to asymmetric deformation modes of Al-O-H group (Frost et al., 1999; Frost et al., 2001). Double peak at 750 cm^{-1} are indicative of quartz existence in the sample. Significant changes in width and intensity appears with heating. The peaks related to OH groups are reduced in intensity and collapse into one broad band in the spectrum from the sample heated at 550 °C, and disappear after heating at 800°C. The Si-O peaks in the range 1000-1200 cm^{-1} have become a unique broad band centered at 1050 cm^{-1} and peaks at 910-935 cm^{-1} are not present after both thermal treatments.

2.3 Pietra Serena sewage sludge

Pietra Serena sewage sludge (hereafter labelled sPS), has been provided by Pietra Serena Group S.r.l. of Firenzuola (Italy). Pietra Serena sandstone comes from a quarry in the Firenzuola district (Florence, Italy) and it can be classified as a feldspathic litharenite.

Chemical composition of sPS was determined by XRF after drying at 100º C for 24 hours in an oven and the data are reported in L.o.I., determined by mass loss up to 1000° C is also reported in table.

TABLE 2.6. Chemical composition of Pietra Serena sewage sludge (XRF, wt% oxides)

Oxides	SiO$_2$	Al$_2$O$_3$	Fe$_2$O$_3$	CaO	MgO	SO$_3$	Na$_2$O	K$_2$O	TiO$_2$	Other	L.o.I.[a]	Sum
sPS	43.50	8.28	2.44	19.53	4.19	0.18	1.46	1.74	0.42	0.25	18	99.99

[a]L.o.I.: Loss on Ignition at 1000 C for 1 hour.

The mineralogical composition provided by Pietra Serena Group s.r.l. company on the basis of UNI-EN 12407:2007 "Natural Stone Test Methods- Petrographic Examination", indicated a dominant silicoclastic component, constituted by quartz, feldspars (K-feldspar and plagioclase), phyllosilicates (biotite, chlorite and muscovite), accessories minerals and a carbonatic component (clasts and cement), the XRPD pattern is reported in Figure 2.10. In this study, the sludge have been thermally treated at 800° C for 2 hours (sPS_800) in order to obtain the decomposition of carbonates. Results from TG-DTA analyses, performed by using a TA instruments Q600 are reported in Figure 2.9.

A total weight loss of 17 % was detected together with three main endothermic changes. A first weight loss at 0.5 % in the range 26-200° C is ascribed to the loss of adsorbed or weakly bonded water; a second weight loss of 1.1% corresponding to the DTA peak centered at 520°

C is attributed to the dehydroxylation of chlorite group minerals. The DTA peak at 573° C corresponds to the α-β quartz polymorphic transition. The broad endothermic peak at 755° C in the DTA curve is due to carbonates decomposition (dolomite and calcite). The corresponding weight loss in TGA is of 15.4%. Decomposition of carbonates may occur in different steps depending on the experimental atmosphere, sample grinding, grain size and other factors (McIntosh et al., 1990; Caceres & Attiogbe, 1997).

The weight percentage of calcium and magnesium carbonates contained in sPS has been determined by considering XRF and TG results. Assuming that all the MgO content, as measured by XRF, forms dolomite, the sludge result constituted by ca. 19 wt% of dolomite. By subtracting dolomite contribution to the weight loss due to carbonate, calcium carbonate (related to both crystalline phase and carbonatic cement matrix) is desumed to constitute ca. 18 wt% of the sludge.
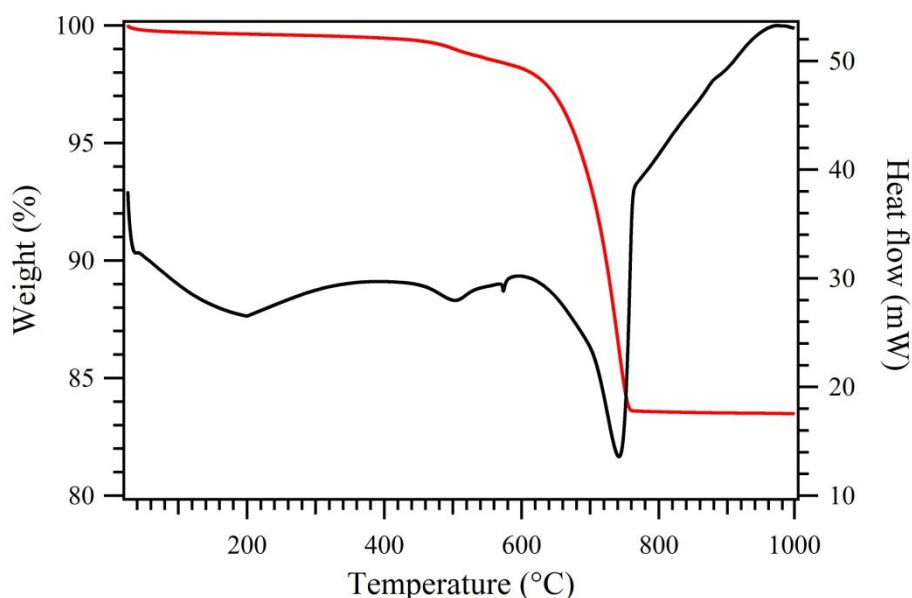
FIGURE 2.9. TG (red line) and DTA (black line) of Pietra Serena sewage sludge (sPS).

Figure 2.10 shows the XRPD patterns of the sPS before and after thermal treatment. As mentioned before crystalline phases detected in the original sPS sample are clinochlore, muscovite, quartz, albite, anorthite, calcite and dolomite. After heating, peaks related to clinochlore disappear as well as those related to calcite and dolomite, and carbonates decomposition was confirmed by the presence of reflections of lime (CaO) and periclase (MgO).

Selective chemical attack with HF was also used by using the same procedure described in § 2.1. It has been here applied only in order to evaluate the percentage of silica and alumina potentially reactive. Since calcium present in this material, reacts with HF producing calcium fluoride by-product this method does not permit to evaluate potentially reactive phase content. XRPD pattern of the solid residue (sPS_HF) is reported in Figure 2.10 and the results from ICP-AES are reported in Table 2.7.
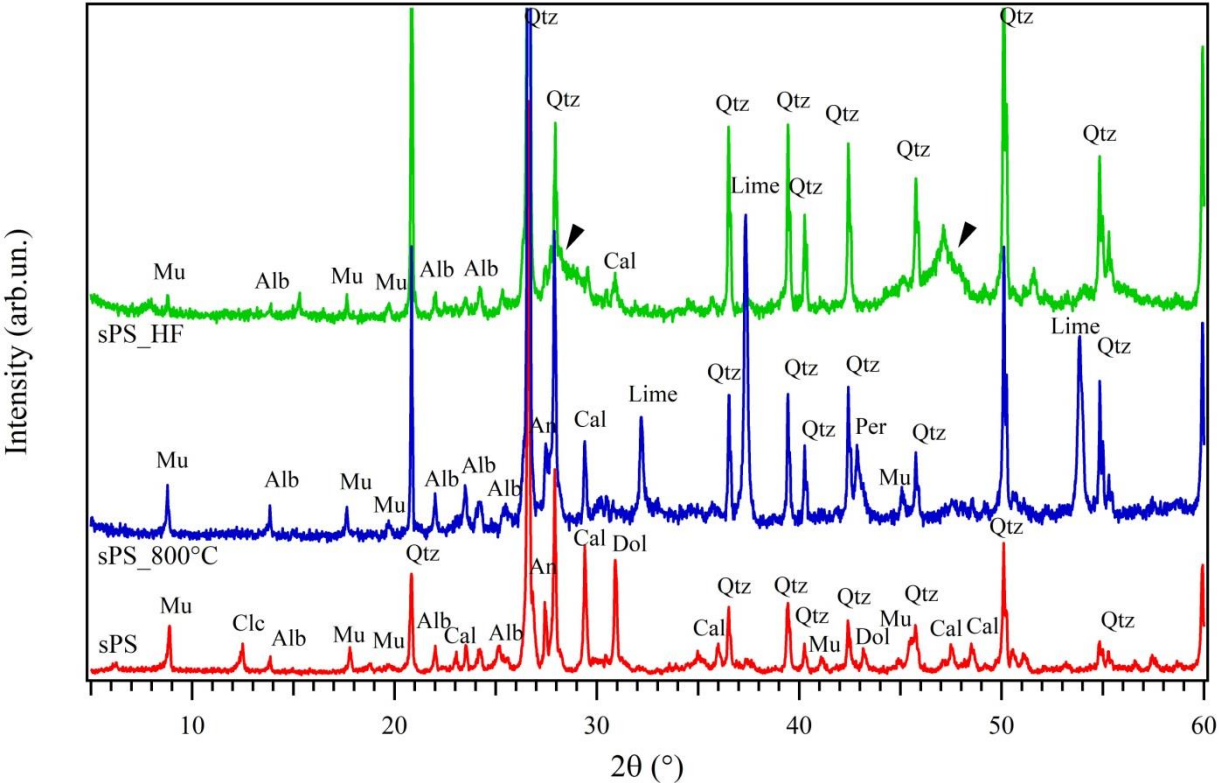
FIGURE 2.10. XRPD patterns of sPS sewage sludge before and after thermal treatment (red line and blue line respectively) and sPS after acid attack (green line).

From the XRPD pattern is possible to observe that the diffraction peaks of muscovite become less intense as well as that of anorthite. Peaks related to lime disappear and in the range between 28°-30° 2θ and 46°-49° 2θ, broad peaks reveal the formation of calcium fluoride compounds.

46

TABLE 2.7. Solubility of Si and Al after HF attack for sPS heated at 800° C

Sample	sPS		
SiO$_2$/Al$_2$O$_3$ reactive	4.48		
SiO$_2$/Al$_2$O$_3$ total (XRF)	5.25		
Soluble elements measure by ICP	ppm	Correspondents oxides (ppm)	Oxides wt % [a]
Si	64.59	138.17	13.76
Al	16.29	30.78	3.07
Fe	15.29	2.18	2.18
Ca	13.35	1.86	1.86
Mg	12.88	2.13	2.13
S	0.64	0.19	0.19
[a] Oxides percentage normalized to the initial weight of sample analyzed			

Figure 2.11 shows FT-IR spectra of sPS before and after thermal treatment. The presence of water is indicated by the humps at 1640 cm^{-1}, ascribable to H-O-H bending vibrations. The presence of carbonates is identified by the bands at around 1450 cm^{-1} (CO$_3^{2-}$ stretching
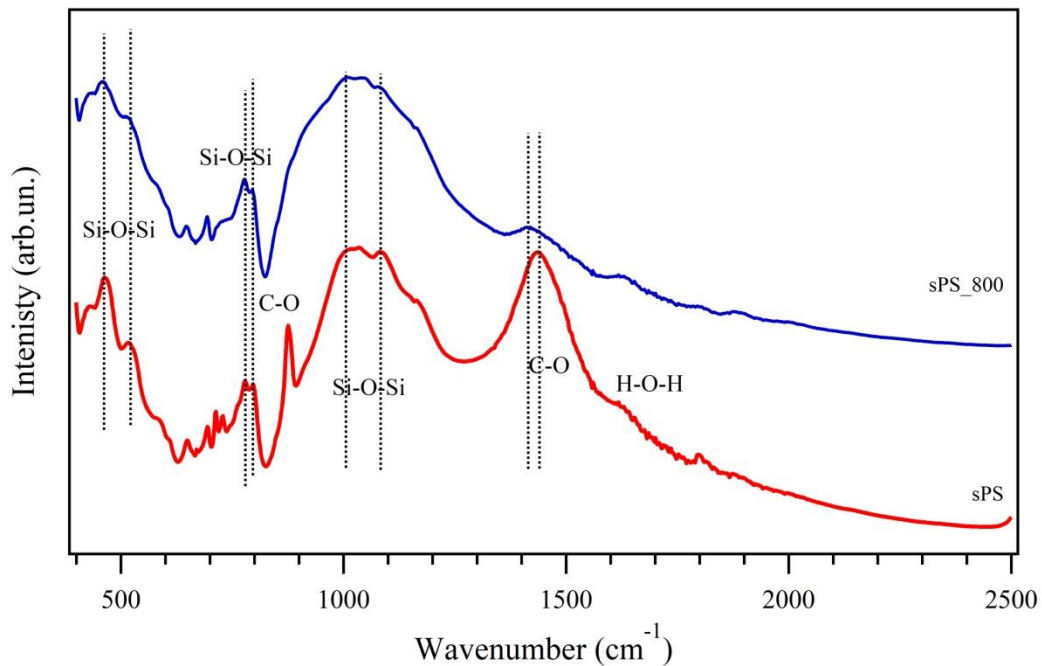
FIGURE 2.11. FT-IR spectra of sPS before and after thermal treatment (red line and blue line respectively).

vibrations) and the other C-O vibrations at 875 cm^{-1} and 710 cm^{-1} (Hughes. et al., 1995). It is evident how the spectrum of sPS_800°C is broader than that of sPS, thus suggesting a larger disorder in the former. In both spectra, peaks arising from the carbonate group (CO$_3^{2-}$) are at 870 cm^{-1}.

However, these peaks show slightly different features due the presence of different carbonate phases: calcite and dolomite. Peaks resulting from the CO_3^{2-} bending vibrations at 712 cm^{-1} and 727 cm^{-1} are present in the spectrum of sPS. It is worth underlining that these peaks are generally used to differentiate calcite from dolomite (Müller et al., 2014): the former is due to calcite and the latter to dolomite. The main bands related to Si-O symmetric stretching bond are centered at 1000 cm^{-1}, 1040 cm^{-1}, 1089 cm^{-1} and 1165 cm^{-1}, which are associated to quartz and silicate minerals, such as feldspars and micas. After thermal treatment, the spectrum in this region is broader than that of sPS, thus suggesting a larger disorder in the former. Features common to all spectra are the characteristic doublet at 780-790 cm^{-1} of quartz and peak at 450 cm^{-1} associated to Si-O-Si bending vibrations.

2.4 Alunite

Alunite ($KAl_3(SO_4)_2(OH)_6$) deriving from a vein of Piloni di Torniella mine was used in this study. Figure 2.12 shows XRPD patterns of the B1 alunite sample before (red line) and after thermal treatment (green line).
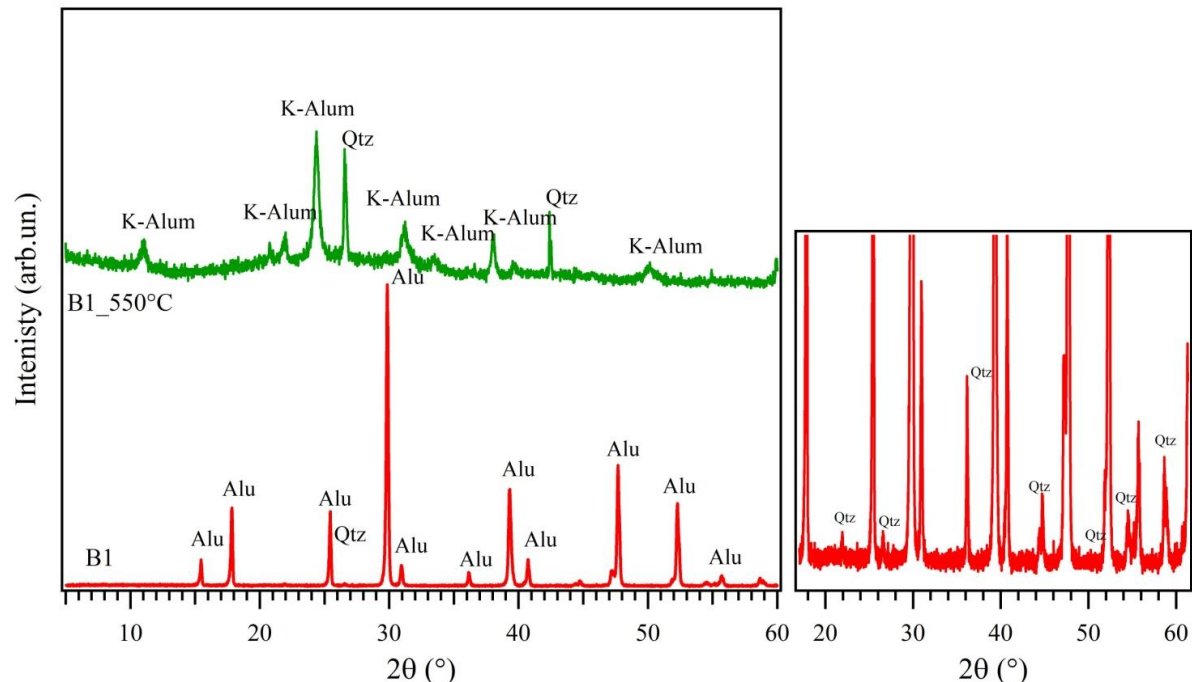
FIGURE 2.12. XRPD patterns of alunite before (red line) and after thermal treatment (green line).

Traces of quartz are also revealed but they are not visible, as the amount of quartz is relatively low. For this reason, an insertion on the right side of the figure shows the peaks related to quartz. After heating at 550°C, quartz peaks are retained and they are more visible. The characteristic peaks of alunite disappear and the lack of diffraction maxima is attributed to its dehydroxylation. Due to the thermal treatment, alunite transform into K-alum $(KAl_3(SO_4)_2)$ and amorphous alumina which is not detected by XRPD.

The processes involved in the thermal modification over the temperature 25°-1000°C is illustrated in Figure 2.13. The two endothermic peak at 429° C and 541° C on the DTG curve (red line) are attributed to dehydroxylation of alunite (see also Ece et al., 2007; Kristof et al., 2010), and its consequent transformation into anhydrous K-alum, Al_2O_3 and water, with a weight loss of 14.2 wt% on the TG curve (black line). The endothermic events at 621°C and 746° C with a weight loss of 21.23 wt% are associated with the loss of sulfate through a multistep process which produce desulfation of K-alum and consequent formation of amorphous Al_2O_3 and release of SO_3 (Ece et al., 2007; Kristof et al., 2010).
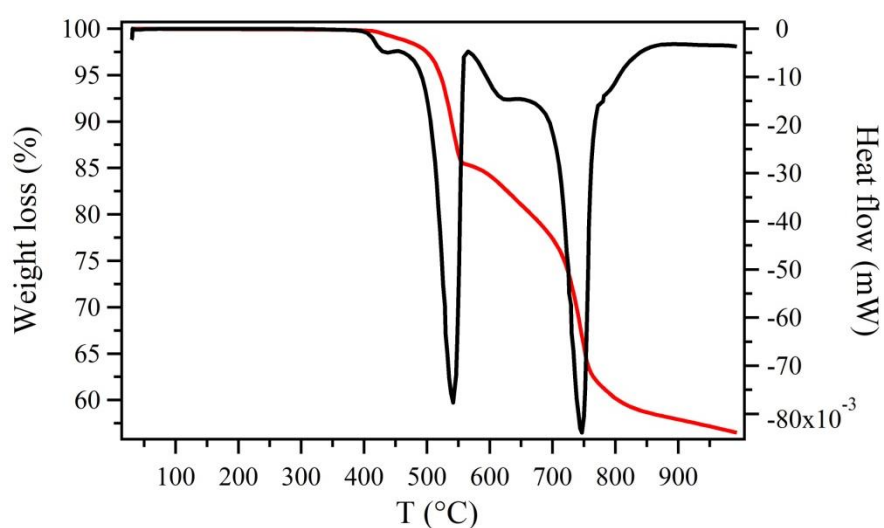
FIGURE 2.13. TG (red curve) and DTG (black curve) of alunite sample.

The FT-IR spectra of the alunite before and after thermal treatment are reported in Figure 2.14. Absorption band between 3483 cm^{-1} and 3500 cm^{-1} show the stretching modes of the Al-OH groups (Frost & Wain, 2007; Toumi & Tlili, 2008). The three bands at 1211 cm^{-1}, 1070 cm^{-1} and 1024 cm^{-1} are related to the SO_4^{2-} asymmetric stretching mode (Farmer, 1993;

Kloprogge & Frost, 1998; Bishop & Murrad, 2005, Frost & Wain, 2007). After thermal treatment the bands related to Al-OH modes disappears. The three asymmetric stretching bands became broader are shifted to higher frequencies, in particular at 1250 cm^{-1}, 1108 cm^{-1} and 1072 cm^{-1}.
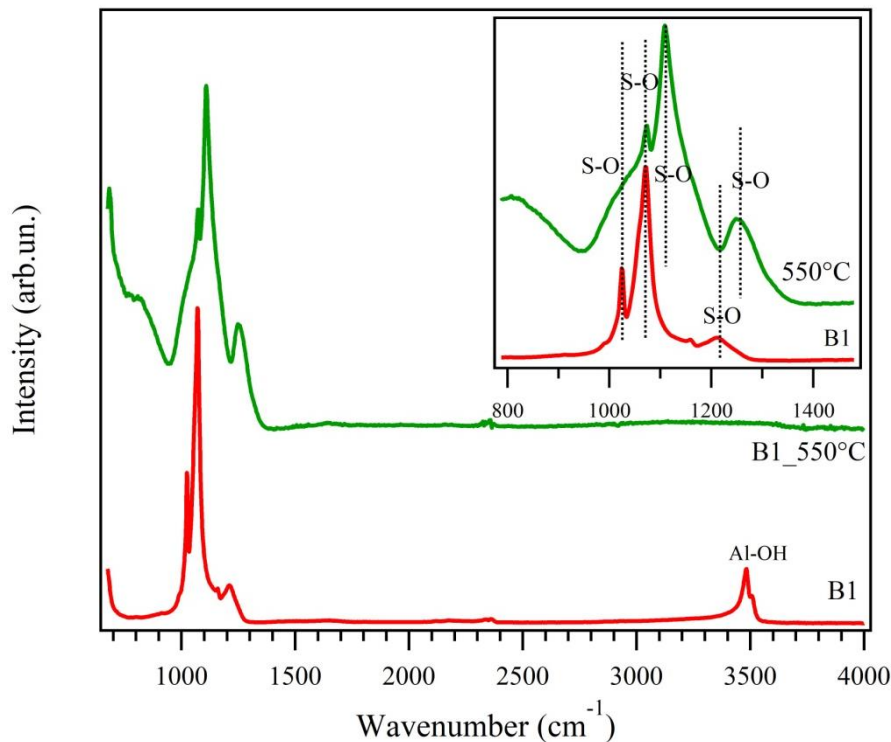
FIGURE 2.14. FT-IR spectra of alunite before (red line) and after thermal treatment (green line).

2.5 Other materials

Sodium silicate (density, 1.526 g/ml), was supplied by Ingessil S.r.l with the following composition: 14.37 wt% of Na_2O, 29.54 wt% of SiO_2 and 56 wt% of H_2O. Barium hydroxide octa-hydrate (Ba $(OH)_2 \cdot 8H_2O$, 97% purity), calcium carbonate ($CaCO_3$, 99% purity) and silica fume, (powder 0.2-0.3 μm avg. part. size) supplied by Sigma Aldrich in the preparation of the AAMs.

2.6 Characterization of starting materials

Loss on Ignition and X-ray Fluorescence Spectrometry

Loss on Ignition (L.o.I) and X-ray Fluorescence (XRF) analyses on L02-K kaolin have been carried out at Activation Laboratories Ldt. (Canada). Samples were preliminarily dried at 105°C, and the L.o.I, which includes H_2O^+, CO_2, S and other volatiles, was determined from the weight loss after roasting the sample at 1000° C for 2 hours. Fusion disks were then made by mixing a 0.75 g equivalent of the roasted sample with 9.75 g of a combination of lithium metaborate and lithium tetraborate with lithium bromide as a releasing agent. Samples were fused in Pt crucibles using an automated crucible fluxer and automatically poured into Pt molds for casting. Samples were analyzed on a Panalytical Axios Advanced wavelength dispersive XRF.

Sulfate content was determined by Combustion Infrared Detection method by using an Eltra CS-2000 analyzer.

X-ray Powder Diffraction

XRPD measurements were performed by using either a Panalytical X'Pert Pro X-ray diffractometer at University of Bari, Italy, collecting data in the range of 2-85° 2θ with a step width of 0.01° 2θ and time per step of 50 s, or a Philips PW 1808/10 X-ray diffractometer at University of Pavia, Italy, collecting data in the range of 2-65° 2θ with a step width of 0.01° 2θ and time per step of 0.5 s. In both cases, Cu-Kα radiation (λ = 1.5418 Å) was used. Phases identification was performed using X'Pert High Score software (Philips). Rietveld refinements of L02 samples have been conducted using GSAS software on XRPD patterns collected with the Panalytical X'Pert Pro X-ray.

Fourier Transform Infrared spectroscopy in Attenuated Total Reflectance (FTIR-ATR)

FTIR-ATR spectra were collected at room temperature in the range of wavenumbers between 670 and 4000 cm^{-1} with 4 cm^{-1} resolution by means of a ThermoScientific Nicolet iN10 MX micro-spectrometer. Spectra, recorded in ATR mode with a liquid nitrogen-cooled mercury cadmium telluride array detector, were calculated by Fourier transformation of 256 interferometer scans and total scanning time of 90 s. A germanium hemispherical internal reflection element (IRE) crystal with a diameter of 300 μm was used. The ATR accessory is mounted on the X-Y stage of the FTIR microscope, and the IRE crystal makes contact with the sample via a force level with pressure of 2 Pa. A 150×150 μm^2 aperture size was used. IR spectra were recorded on the surface of compressed powder pellets of the samples.

Thermal analysis

Thermogravimetric (TG) analyses were carried out using a TA Instruments AutoTGA 2950HR with V6.1A data acquisition software. A Pt crucible was filled with ca. 11 mg of powdered samples and heated at rate of 20°C/min under nitrogen flow, from room temperature (RT) up to 1000°C. Differential Thermal Analysis (DTA) was performed with a TA Instruments 2910 Modulated DSC V4.4E, equipped with a 1600°C DTA cell, on ca. 14 mg of sample. The sample was located in a Pt crucible and heated from 100°C up to 1200°C at rate of 20°C/min. Measurements were carried out in air with no gas flow, and Al_2O_3 was used as a reference material.

Acid attack with HF: clay reactivity

The fraction of reactive phase and reactive SiO_2/Al_2O_3 ratio of the starting materials were determined by means of selective chemical attack using a HF (1% V/V) solution. 1 g of each sample were mixed with 100 ml of a hydrofluoric acid solution (1% V/V) for 5 h under stirring. After the chemical attack, the solid residues and the solutions were separated by filtering using Albet®ash-less filter paper (% ash<0.01) for retention of particles under 2 μm (ref. DP5893125). The residues were washed with distilled water until neutral pH. After drying the filter papers contained, the residues were calcinated at 1000°C in a platinum crucible for 1 hour. The percentages of reactive phase contents were quantified by subtracting the final mass of the residue from the initial mass of the sample (except for sPS sample, because calcium fluoride precipitation did not permit to calculate the quantity of amorphous phases). The percentage of silica and alumina released during the selective chemical attack in the leachates was determined by ICP-AES.

ICP-AES analyses were conducted on a Varian 725-ES ICP atomic emission spectrometer (plasma power, 1.40 kW; plasma gas flow, 15.00 l/min; nebulizer gas flow, 0.85 l/min; read time, 5 s). The concentrations of soluble silicon and aluminum determined by the ICP-AES technique correspond to the average of three measurements for a given liquid sample.

References

Balan, E., Saitta, A. M., Mauri, F., & Calas, G., 2001. First-principles modeling of the infrared spectrum of kaolinite. American Mineralogist, 86(11-12), 1321-1330.

Bellotto, M., Gualtieri, A., Artioli, G., & Clark, S. M., 1995. Kinetic study of the kaolinite-mullite reaction sequence. Part I: Kaolinite dehydroxylation. Physics and chemistry of minerals, 22(4), 207-217.

Belviso, C., Cavalcante, F., Lettino, A., Fiore, S., 2013. A and X-type zeolites synthesised from kaolinite at low temperature. Applied Clay Science, 80, 162-168.

Belviso, C., Giannossa, L. C., Huertas, F. J., Lettino, A., Mangone, A., Fiore, S., 2015. Synthesis of zeolites at low temperatures in fly ash-kaolinite mixtures. Microporous and Mesoporous Materials, 212, 35-47.

Bergaya, F., Dion, P., Alcover, J.F., Clinard, C., Tchoubar, D., 1996. TEM study of kaolinite thermal decomposition by controlled rate thermal analysis. Journal of Materials Science, 31, 5069-5075.

Bertolani, M., & Loschi Ghittoni, A.G., 1989. Kaolin of Piloni di Torniella (Tuscany). L'Ind. Mineraria, 40 (2), 19-27.

Bich, C., Ambroise, J., & Péra, J., 2009. Influence of degree of dehydroxylation on the pozzolanic activity of metakaolin. Applied Clay Science, 44(3), 194-200.

Bish, D.L., 1993. Rietveld refinement of the kaolinite structure at 1.5 K. Clays and Clay Minerals, 41, 738-744.

Bishop, J.L., & Murad, E., 2005. The visible and infrared spectral properties of jarosite and alunite. American Mineralogist, 90(7), 1100-1107.

Caceres, P.G., Attiogbe, E.K., 1997. Thermal decomposition of dolomite and the extraction of its constituents. Minerals Engineering, 10(10), 1165-1176.

Castelein, O., Soulestin, B., Bonnet, J.P., Blanchart, P., 2001. The influence of heating rate on the thermal behaviour and mullite formation from a kaolin raw material. Ceramics International, 27, 517-522.

Chakraborty, A., 2003. New data on thermal effects of kaolinite in the high temperature region. Journal of Thermal Analysis and Calorimetry, 71(3), 799-808.

Clausi, M., Tarantino, S.C., Magnani, L.L., Riccardi, M.P., Tedeschi, C., Zema, M., 2016. Metakaolin as precursor of materials for applications in Cultural Heritage: Geopolymer-based mortars with ornamental stone aggregates. Applied Clay Science, 132, 589-599.

Dion, P., Alcover, J.F., Bergaya, F., Ortega, A., Llewellyn, P.L., Rouquerol, F., 1998. Kinetic study by controlled-trasformation rate thermal analysis of the dehydroxylation of kaolinite. Clay Minerals, 33, 269-276.

Dondi, M., 2000. Kaolinitic clays of volcanic origin: composition, technological properties and problems in ceramic applications. In Proceedings of the 1st Latin American Clay Conference, 2, 219-224.

Ece, Ö.I., & Schroeder, P.A., 2007. Clay mineralogy and chemistry of halloysite and alunite deposits in the Turplu area, Balikesir, Turkey. Clays and Clay Minerals, 55(1), 18-35.

Farmer, V.C., 1974. Infrared spectra of minerals. Mineralogical Society.

Fernández-Jiménez, A., & Palomo, A., 2003. Characterisation of fly ashes. Potential reactivity as alkaline cements. Fuel, 82(18), 2259-2265.

Frost, R.L., Kloprogge, J.T., Russell, S.C., Szetu, J.L., 1999. Vibrational spectroscopy and dehydroxylation of aluminum (oxo) hydroxides: gibbsite. Applied Spectroscopy, 53(4), 423-434.

Frost, R.L., Makó É., Kristóf, J., Horváth, E., Kloprogge, J.T., 2001. Mechanochemical treatment of kaolinite. Journal of Colloid and Interface Science, 239, 458-466.

Frost R.L., Wain, D.L., Wills, R.A., Musemeci, A., Martens W., 2006. A thermogravimetric study of the alunites of sodium, potassium and ammonium. Thermochimica Acta, 443, 56-61.

Frost, R.L., & Wain, D.L., 2007. A thermogravimetric and infrared emission spectroscopic study of alunite. Journal of Thermal Analysis and Calorimetry, 91(1), 267-274.

Frost, R. L., & Wain, D. L., 2008. Near-infrared spectroscopy of natural alunites. Spectrochimica Acta Part A: Molecular and Biomolecular Spectroscopy, 71(2), 490-495.

Gasparini, E., Tarantino, S.C., Ghigna, P., Riccardi, M.P., Cedillo-González, E.I., Siligardi, C.,Zema, M., 2013. Thermal dehydroxylation of kaolinite under isothermal conditions. Applied Clay Science, 80, 417-425.

Gasparini, E., Tarantino, S.C., Conti, M., Biesuz, R., Ghigna, P., Auricchio, F., Zema, M., 2015. Geopolymers from low-T activated kaolin: Implications for the use of alunite-bearing raw materials. Applied Clay Science, 114, 530-539.

Gorga, R., & Mottana, A., 1995. Caolinite e halloysite a Monte Altino di Roccastrada nelle rioliti ignimbritiche tardoplioceniche del centro estrusivo vulcanico di Sassoforte (Toscana, Italia). Rendiconti Lincei, 6(4), 269-283.

Gualtieri, A., & Bellotto, M., 1998. Modelling the structure of the metastable phases in the reactionsequence kaolinite-mullite by X-ray scattering experiments. Physics and Chemistry of Minerals, 25, 442-452.

Hughes, T.L., Methven, C.M., Jones, T.G., Pelham, S.E., Fletcher, P., Hall, C., 1995. Determining cement composition by Fourier transform infrared spectroscopy. Advanced Cement Based Materials, 2(3), 91-104.

Kavak, D., 2009. Removal of boron from aqueous solutions by batch adsorption on calcined alunite using experimental design. Journal of Hazardous Materials, 163(1), 308-314.

Kloprogge, J.T., & Frost, R.L., 1998. The dehydroxylation of basic aluminum sulfate: An infrared emission spectroscopic study. Thermochimica Acta, 320(1), 245-252.

Kristóf, J., Frost, R.L., Palmer, S.J., Horváth, E., Jakab, E., 2010. Thermoanalytical studies of natural potassium, sodium and ammonium alunites. Journal of Thermal Analysis and Calorimetry, 100(3), 961-966.

Krivenko, P.V., 1994. Alkaline cements. In Proceedings of the 1st. International Conference on Alkaline Cements and Concretes, Kiev, Ukraine, 1, 11-129. VIPOL Stock Company.

Küçük, F., & Yildiz, K., 2006. The decomposition kinetics of mechanically activated alunite ore in air atmosphere by thermogravimetry. Thermochimica acta, 448(2), 107-110.

Lambert, J. F., Millman, W. S., & Fripiat, J. J.,1989. Revisiting kaolinite dehydroxylation: A silicon-[29] and aluminum-[27] MAS NMR study. Journal of the American Chemical Society, 111(10), 3517-3522.

Ligas, P., Uras, I., Dondi, M., & Marsigli, M., 1997. Kaolinitic materials from Romana (north-west Sardinia, Italy) and their ceramic properties. Applied Clay Science, 12(1-2), 145-163.

Lombardi, G., & Mattias, P., 1987. The kaolin deposits of Italy. L'industria Mineraria, 6, 1-34.

Mazzuoli, R., 1967. Le vulcaniti di Roccastrada (Grosseto). Studio chimico-petrografico e geologico. Atti Società Toscana Scienze Naturali, 74, 315-73.

McIntosh, R.M., Sharp, J.H., Wilburn, F.W., 1990. The thermal decomposition of dolomite. Thermochimica Acta, 165(2), 281-296.

Meor-Yusoff, M.S., Masilana, M., Choo, T.F., 2007. Production of High Purity Alumina and Zeolite from Low-grade Kaolin. Journal of Advanced Materials and Research, 29, 187-190.

Mohammadi, M., & Salarirad, M.M., 2013. Dehydroxylation kinetics of alunite. Industrial & Engineering Chemistry Research, 52(22), 7333-7340.

Müller, C.M., Pejcic, B., Esteban, L., Delle Piane, C., Raven, M., Mizaikoff, B., 2014. Infrared attenuated total reflectance spectroscopy: an innovative strategy for analyzing mineral components in energy relevant systems. Scientific reports, 4.

Olszak-Humienik, M.; Jablonski, M., 2015. Thermal behavior of natural dolomite. Journal of Thermal Analysis and Calorimetry, 119(3), 2239-2248.

Osornio-Rubio, N.R., Torres-Ochoa, J.A., Palma-Tirado, M.L., Iménez-Islas, H.J., Rosas-Cedillo, R., Fierro-Gonzalez, J.C., Martínez-González, G.M., 2016. Study of the dehydroxylation of kaolinite and alunite from a Mexican clay with DRIFTS-MS. Clay Minerals, 51(1), 55-68.

Peccerillo, A., & Donati, S., 2003. The Tuscan Magmatic Province. Miocene to Recent plutonism and volcanism in the Tuscan Magmatic Province (central Italy), Periodico di Mineralogia, Special Issue, (72), 27-39.

Petit, S., Madejová, J., Decarreau, A., Martin, F., 1999. Characterization of octahedral substitutions in kaolinites using near infrared spectroscopy. Clays and Clay Minerals, 47, 103-108.

Provis, J. L., 2014. Geopolymers and other alkali activated materials: why, how, and what? Materials and Structures, 47(1-2), 11-25.

Ptáček, P., Kubátová, D., Havlica, J., Brandštetr, J., Šoukal, F., Opravil, T., 2010. The nonisothermal kinetic analysis of the thermal decomposition of kaolinite by thermogravimetric analysis. Powder Technology, 204, 222-227.

Ptáček, P., Šoukal, F., Opravil, T., Havlica, J., Brandštetr, J., 2011. The kinetic analysis of the thermal decomposition of kaolinite by DTG technique. Powder Technology, 208, 20-25.

Rios, C.A., Williams, C.D., Fullen, M.A., 2009. Nucleation and growth history of zeolite LTA synthesized from kaolinite by two different methods. Applied Clay Science, 42(3), 446-454.

Ruiz-Santaquiteria, C., Fernández-Jiménez, A., Skibsted, J., & Palomo, A., 2013. Clay reactivity: production of alkali activated cements. Applied clay science, 73, 11-16.

Russell, J. D., & Fraser, A. R., 1971. IR spectroscopic evidence for interaction between hydronium ions and lattice OH groups in montmorillonite. Clays and Clay Minerals, 19(1), 55-59.

Siddique, R., & Klaus, J., 2009. Influence of metakaolin on the properties of mortar and concrete: A review. Applied Clay Science, 43(3), 392-400.

Toumi M. & Tlili A., 2008. Rietveld refinement and vibrational spectroscopic study of alunite from el Gnater, central Tunisia. Russian Journal of Inorganic Chemistry, 53, 1845-1853.

Viti, C., Lupieri, M., Reginelli, M., 2007. Weathering sequence of rhyolitic minerals: the kaolin deposit of Torniella (Italy). Neues Jahrbuch für Mineralogie-Abhandlungen: Journal of Mineralogy and Geochemistry, 183(2), 203-213.

Vizcayno, C., Castelló, R., Ranz, I., Calvo, B., 2005. Some physico-chemical alterations caused by mechanochemical treatments in kaolinites of different structural order. Thermochimica Acta 428, 173-183.

Zema, M., Callegari, A.M., Tarantino, S.C., Gasparini, E., Ghigna, P., 2012. Thermal expansion of alunite up to dehydroxylation and collapse of the crystal structure. Mineralogical Magazine, 76 (3), 613-623.

Zemenová P., Kloužková A., Kohoutková M., Král, R., 2014. Investigation of the first and second dehydroxylation of kaolinite. Journal of Thermal Analysis and Calorimetry, 116, 633-639.

3 SYNTHESIS AND CHARACTERIZATION

In this section, the details of the processing conditions used for the preparation of alkaline activated materials are explained, together with a description of the experimental characterization of the reaction products.

3.1 L02-MK and Sl-MK with sodium silicate as activator

3.1.1 Pastes preparation

In order to investigate the effect of sulfate deriving from alunite in AAMs, binders prepared by using L02-MK have been compared to binders prepared by using mixtures of Sl-MK and alunite as starting materials. At this purpose, three sets of AAMs based on different metakaolin precursor and annealing temperature have been prepared. The three precursors are (all the details are reported in Table 3.1):

- L02-K annealed at 550°C for 3 hours (alunite 12.3 wt%).
- Sl-K kaolin and alunite (mixed in 90/10 weight proportion) annealed together at 550°C for 3 hours (hereafter-labeled Sl indicating metakaolin and A indicating alunite dehydroxylated).
- Sl-K kaolin annealed at 800°C for 2 hours and alunite annealed at 550°C for 3 hours (mixed in 80/20 weight proportion).

Synthesis parameters have been defined on the basis of the potential reactive SiO_2 and Al_2O_3 from available metakaolinite and alunite after each thermal treatment. Calculations have been made combining XRF results, Rietveld analysis and weight loss (%) from TG analyses for both clays and alunite on the bases of metakaolinite present after thermal treatment.

For Sl-K clay, stoichiometric calculations for the synthesis have been performed by considering that after thermal treatment at 550°C the metakaolinite amount is 43.5 wt.%, while, after thermal treatment at 800°C all kaolinite is transformed into metakaolinite. For L02-MK, all SiO_2 and Al_2O_3 amounts from kaolinite and alunite, as determined by Rietveld refinement, have been considered as reactive. The initial SiO_2/Al_2O_3 ratio for each set is resumed as follow:

- L02 (alunite 12.3 wt%) annealed at 550°C: $SiO_2/Al_2O_3 = 1.6$.
- Sl-K (90 wt%) and alunite (10 wt%) annealed together at 550°C: $SiO_2/Al_2O_3 = 1.5$.

- Sl-K (80 wt%) annealed at 800°C and alunite (20 wt%) annealed 550°C:

    $SiO_2/Al_2O_3 = 1.25$.

The initial SiO_2/Al_2O_3 molar ratios of the precursors has been modified by adding waterglass and eventually by adding silica fume in order to achieve two SiO_2/Al_2O_3 molar ratio (3.6 and 4.6) for each set, in separated experiments. Metakaolin based AAMs, with these silica content show good mechanical strength, good development of aluminosilicate gels with no formation of crystalline phases, as zeolites (Duxson et al., 2005; Fletcher et al., 2005; Komnitsas & Zaharaki, 2007).

$Al_2O_3/ (Na_2O + K_2O)$ molar ratio was maintained around 1 in order to avoid efflorescences. The ratio considers the alkalis from sodium silicate solution (waterglass). Liquid/solid ratio is variable from 0.35 to 0.70, and it has been chosen depending on the workability each mix; liquid value is referred to the water of the waterglass and the water eventually added to the mix. This ratio is strictly dependent on the specific surface area of the precursor employed, which is in turn, related to the particles granulometry, morphology and to the degree of crystallinity of the raw materials. Moreover the variability of this ratio is an important factor to take into account, for example an elevate L/S ratio could lead an increase of the porosity in the matrix and as consequence a decrease in mechanical strength (Older & Robler, 1985).

Finally, in order immobilize sulfate deriving from alunite in AAMs, two samples were prepared by using $(Ba(OH)_2 \cdot 8H_2O)$ $(BaO/SO_4 = 1:1)$ and calcium oxide $(CaO/SO_4 = 1:1)$ respectively. Ba reacts with Na_2SO_4 giving the precipitation of insoluble barium sulfate; Ca could react with SO_4^{2-} and Al^{3+} to form ettringite or other sulfo-aluminate compounds.

Pastes were prepared by mechanically mixing the precursor powder (thermally treated) with sodium silicate for 5 minutes, then poured into cylindrical molds, having size 2cm in diameter and 4 cm in height, and cured at 50° C for 20 hours in sealed vessels to ensure 99% relative humidity (R.H.).

TABLE 3.1. Details of pastes preparation with sodium silicate as activating solution.

Sample	Clay/Alunite proportion in 100g (wt %)	L/S (ratio)	*SiO_2/Al_2O_3	*SiO_2/Na_2O	*Al_2O_3/Na_2O	*SO_4/CaO	*SO_4/SiO_2	*SO_4/Al_2O_3
Sl$_{550}$_s46	100	0.33	4.6	4.6	1.0	-	-	-
Sl$_{550}$A10_s36	91/9	0.35	3.6	4.0	1.1	32.0	0.05	0.18
Sl$_{550}$A10_s46	91/9	0.41	4.6	5.0	1.1	32.0	0.04	0.18
Sl$_{800}$A20_s36	82/18	0.48	3.6	3.6	1.0	65.0	0.09	0.31
Sl$_{800}$A20_s46	82/18	0.50	4.6	4.7	1.1	65.0	0.10	0.5
L02_s36	80/20	0.44	3.6	2.3	1.3	26.3	0.07	0.25
L02_s46	80/20	0.74	4.6	7.7	1.7	26.3	0.05	0.25
L02_Ca_s36	80/20	0.50	3.6	4.2	1.2	0.50	0.07	0.25
L02_Ba_s36	80/20	0.39	3.6	4.2	1.2	26.3	0.07	0.25

*Oxides ratios are expressed in molar ratio

Sl = Sl-K kaolin; L02 = L02-K kaolin; A = alunite initial wt%; s36 and s46 = SiO_2/Al_2O_3 molar ratio.

3.1.2 Samples characterization

The reaction products formed were studied using XRPD, FTIR-ATR, leaching tests, and FE-SEM. XRPD and FTIR-ATR analysis procedure have been already described in § 2.6.

Sulfate solubility

Leaching tests were performed according to UNI-EN 1245 standard: "Compliance test for leaching of granular waste materials and sludge; Part 1: One stage batch test at a liquid to solid ratio of 2 l/kg for materials with high solid content and with particle size below 4 mm (without or with size reduction). 1g geopolymer was weighted into 50 mL PP centrifuge tubes, mixed with 20 mL of pure water and shaken on a rotating plate (150 rpm) at room temperature for 24 h to ensure equilibration. Sulfates equilibrium concentrations were measured on the centrifuged (4500 rpm, 15 min) and filtered (0.45 μm nylon membrane) samples by ion chromatography with a DX 500 Ion Chromatograph (Dionex, Milan, Italy) equipped with a GP40 gradient pump, CD20 conductivity detector and anion self-regenerating suppressor (ASRS 400, 4 mm). The samples were properly diluted with ultrapure water, then 70 μL of each sample were injected into a 250×4 mm IonPac AS23 coupled with an AG23 50×4 mm guard-column at a flow rate of 1.0 mL min^{-1}. The eluent was 8×10^{-4} M NaHCO$_3$, 4.5×10^{-3} M Na$_2$CO$_3$. The results for the analyzed sample are reported in Table 3.2.

TABLE 3.2. Results of sulfate solubility after leaching test and percentage of retention in the solid sample

Sample	SO$_4^{2-}$ calculated in 1g of the initial mix (g)	SO$_4^{2-}$ measured by ICP-OES (mg)	SO$_4^{2-}$ retained after water leaching (wt%)
Sl$_{550}$A10_s36	0.028	26.7 (1)	3.0 (1)
Sl$_{550}$A10_s46	0.026	17.8 (1)	28.5 (1)
Sl$_{800}$A20_s36	0.064	45.7 (1)	15.5 (1)
Sl$_{800}$A20_s46	0.057	35.4 (1)	27.0 (1)
L02_s36	0.042	27.9 (1)	21.0 (1)
L02_s46	0.039	8.8 (1)	36.0 (1)
L02_Ca_s36	0.042	22.3 (1)	44.2 (1)
L02_Ba_s36	0.037	6.12 (1)	80.4 (1)

Field Emission Scanning Electron Microscopy

Carbon coated and chromium coated samples in powder were investigated with a Field Emission Scanning Electron Microscope (FESEM), TESCAN Mira 3 XMU-series equipped with EDAX energy dispersive spectrometer (EDS) Analysis of morphological features were performed from the micro scale to the nano scale. Secondary electron (SE) and In Beam images were collected at a working distance of 15.8 mm and 5 mm respectively, with an acceleration voltage of 20 kV.

3.2 L02-MK and sPS with sodium hydroxide as activator

3.2.1 Pastes preparation

L02-K kaolin and Pietra Serena sewage sledge were annealed at 550°C for 3 hours and at 800°C for 2 hours respectively and then mixed in different weight proportions and added to sodium hydroxide solutions at different molarities (8M, 6M and 4M), as reported in Table 3.3. Sodium hydroxide solutions were obtained by dissolving NaOH pellets (supplied by Sigma-Aldrich Co.; purity of 99 wt %) in deionizer water. The slurries were mixed for 3 minutes by using a mechanical mixer before being poured in $1 \times 1 \times 6$ cm^3 prismatic steel molds and compacted by mechanical vibrations for 60s to remove the entrained air.

Liquid/solid ratio for each formulation was chosen in order to guarantee the minimum workability of the slurry and to allow its pouring in the molds. Specimens were cured at 85° C for 20 hours in sealed vessels to ensure 100% R.H. conditions. At the end of the curing, specimens were unmolded and stored at room temperature until the end of curing time. Some experiments were also conducted curing the sample directly at 25°C in a room with 99%R.H. condition.

Information about the molar ratio, the starting materials proportions and the curing conditions of each mixture are reported in Table3.3.

Table 3.3. Scheme of AAMs binders preparation with L02-K and sPS precursors and sodium hydroxide as activating solutions.

Samples	sPS in the initial solid mix (wt%)	CaO calculated in the mix (wt.%)[a]	Curing temperature (°C)	Molarity of NaOH solution	L/S (ratio)	$*SiO_2/Al_2O_3$	$*CaO/SiO_2$	$*SiO_2/Na_2O$	$*Al_2O_3/Na_2O$	$*SO_4/CaO$	$*SO_4/SiO_2$
L02-100-8M_1D_85C	0	-	85°	8	0.38	1.8	-	3.4	1.9	-	0.11-
L02-90-sPS-8M_1D_85C	10	2.0	85°	8	0.43	1.9	0.7	2.8	1.5	1.15	0.11
L02-80-sPS-8M_1D_85C	20	3.9	85°	8	0.43	2.0	0.6	2.8	1.4	0.51	0.10
L02-80-sPS-6M_1D_85C	20	3.9	85°	6	0.44	2.0	0.6	2.7	1.3	0.51	0.10
L02-80-sPS-4M_1D_85C	20	3.9	85°	4	0.43	2.0	0.6	4.9	2.4	0.51	0.10
L02-50-sPS-8M_1D_85C	50	9.8	85°	8	0.50	2.5	0.5	2.0	0.8	0.13	0.07
L02-50-sPS-8M_1D_25C	50	9.8	25°	8	0.50	2.5	0.5	2.0	0.8	0.13	0.07
L02-50-sPS-6M_1D_85C	50	9.8	85°	6	0.48	2.5	0.5	2.7	1.0	0.13	0.07
L02-50-sPS-6M_1D_25C	50	9.8	25°	6	0.48	2.5	0.5	2.7	1.0	0.13	0.07
L02-50-sPS-4M_1D_85C	50	9.8	85°	4	0.49	2.5	0.5	4.4	1.6	0.13	0.07
L02-50-sPS-4M_1D_25C	50	9.8	25°	4	0.49	2.5	0.5	4.4	1.6	0.13	0.07

[a] CaO wt % is referred to the sPS wt % addition in the mix, assuming that all the Ca from carbonates is available as CaO

[b] Oxides ratio are referred to molar ratio in each mix, calculated taking into account the reactive moles of SiO_2 and Al_2O_3 after selective chemical attack.

3.2.2 Samples characterization

Reaction products have been characterized by mechanical tests, XRPD and FT-IR analysis, leaching tests, SEM-EDS and Nuclear Magnetic Resonance (MAS-NMR) analysis. The techniques employed are described hereafter.

Mechanical tests

Flexural and compressive strengths of the resulting materials were measured after one day of curing using an IBERTEST AUTOTEST-200/10 SW test frame. Flexural strengths were calculated as the average value of six measurements, while the average compressive strengths values were measured on twelve specimens.

X-ray Powder Diffraction

XRPD patterns were recorded in a Bragg-Brentano (reflection) X'Pert, a MDP PRO (PANalytical) diffractometer using Cu Kα1 radiation (λ = 1.5409 Å), [Ge (111) primary monochromator]. Data were collected in the range 2-65° 2θ with an angular step of 0.01° 2θ and time per step of 5s.

FT-IR analysis

FTIR spectra were obtained by analyzing, at room temperature, pellets containing 1.0 mg of crushed sample and 300 mg of KBr by a Thermo Scientific NICOLET 6700 spectrometer. The range of wavelength collected was between 400 and 4000 cm^{-1} with 4 cm^{-1} of resolution. Spectra were calculated by Fourier transformation of 64 interferometer scans and total scanning time of 23s.

SEM-EDS analysis

SEM JEOL JSM 5400, equipped with an OXFORD LINK-ISIS-EDX energy dispersive X-ray spectrometer, was used to investigate the microstructure of samples. Analyses were performed, in vacuum mode, on fracture surfaces of the specimens covered by carbon coating. Images were collected using secondary electron (SE) at a working distance of 15 mm with an acceleration voltage of 20 kV. EDS analyses (on spots) were done with

accelerating voltage of 20 kV, working distance of 15 mm and beam current of 20 µA and acquiring for 30s per spot analysis. Chemical compositions were determined considering 100 wt % oxide content on an H_2O- and CO_2-free basis.

Leaching tests

Leaching tests were performed according to UNI-EN 1245 standard, as mentioned in the § 3.1.2, "*sample characterization*". Sulfate quantification of the leachates were performed by Ion Chromatography (IC). The results are reported in the following Table.

TABLE 3.4. Solubility measurements of sulfate ion after leaching tests.

Samples	SO_4^{2-} calculated in 1 g of the initial solid mix (g)	SO_4^{2-} measured in the liquid (ppm)	SO_4^{2-} in the liquid (g)	SO_4^{2-} retained in the mix after leaching (wt %)
L02-100-8M_1D	0.043	1972.55	0.039	7.82
L02-90-sPS-8M_1D	0.039	880.77	0.018	54.27
L02-50-sPS-6M_1D_85C	0.021	502.67	0.010	53.02
L02-50-sPS-8M_1D_25C	0.021	543.99	0.011	49.16
L02-50-sPS-8M_1D_85C	0.021	334.30	0.007	68.76

MAS-NMR analysis

The NMR spectra were recorded on a Bruker Avance-400 spectrometer (^{27}Al: 104.3 MHz; spinning rate, 10 kHz; 200 acquisitions; reference, $Al(H_2O)_6^{3+}$; ^{29}Si: 79.5 MHz; spinning rate, 10 kHz; 1000 acquisitions; reference, TMS).

3.3 Alkali fusion of L02-K, Sl-K and sPS

3.3.1 Synthesis procedure

Syntheses of zeolites have been started from sulfate-bearing clay (L02-K) as well as from synthetic mixtures of alunite and high-grade kaolin (Sl-K) in different proportions. Products have been compared to those obtained by using the high-quality kaolin without alunite. Finally, a mixture (50/50 wieght proportion) of L02-K and Pietra Serena sewage sludge (previously heated at 800°C, sPS_800) have been also prepared. Zeolites were synthesized using molten salt procedure which convert aluminosilicates as fly ash or metakaolin into zeolites (Park et al., 2000; Andac et al., 2005; Yusoff et al., 2007; Ríos et al., 2009; Belviso et al., 2013; Belviso et al., 2015). Syntheses procedures have been conducted by melting kaolin

and kaolin-silica mixtures with NaOH (1:1.2 weight ratio). Fumed SiO_2 has been added to modify the SiO_2/Al_2O_3. The mixtures have been heated at 550°C for 2 hours in a Pt crucible. The alkaline reagent acts as a fondant agent during heating (Ríos et al., 2009). The resultant solid mixture was cooled and grounded with a mortar and pestle for a few minutes. Afterward, the powder was mixed with distilled water in different S/L ratios (see Table 3.5), and stirred for 12 hours at room temperature. At the end, the suspensions were incubated in vessels at 50° C for 96, 360 and 720 hours in separated experiments. At the end of the incubation period, all products were filtered by using a Buchner funnel, rinsed with distilled water to remove the excess alkali and the solid residues was dried in an oven at 80° C for 12 hours.

TABLE 3.5. Scheme of synthesis conditions for Sl-K and L02-K series and resulting products.

Sample	Clay/Alunite proportion (wt %)[a]	SiO_2/Al_2O_3 molar ratio	Solid/Liquid proportion
Slm_s36d4	100/0	3.6	1g/5ml
Slm_s46d4	100/0	4.6	1g/5ml
Slm_NaOHd4	100/0	2.0	1g/5ml
Slm_s36d30	100/0	3.6	1g/33ml
SlA10m_s36d4	91.5/8.5	3.6	1g/33ml
SlA10m_s36d30	91.5/8.5	3.6	1g/33ml
SlA10m_s36d15_HT	91.5/8.5	3.6	1g/50ml
SlA20m_s36d4	82/18	3.6	1g/5ml
SlA20m_s46d4	82/18	4.6	1g/5ml
L02m_NaOHd7	80/20	1.6	1g/5ml
L02m_s36d4	80/20	3.6	1g/5ml
L02m_s36d30	80/20	3.6	1g/5ml
L02m_s46d4	80/20	4.6	1g/5ml
L02m_s46d30	80/20	4.6	1g/5ml
L02m_sPS$_{800}$NaOHd4	80/20[a]	2.8	1g/5ml

[a] This ratio is referred to the clay/alunite. The ratio L02-K and sPS_ 800 is 50/50 wt%
SiO_2/Al_2O_3 ratio is referred to mixtures kaolin-fumed silica. No silica has been added to Slm_NaOHd4 and L02m_sPs$_{800}$NaOHd4.

3.3.2 Samples characterization

TG-DTA analyses for the L02-K and Sl-K and alunite mixture have been conducted during the heating process in alkaline medium. After incubation, samples have been characterized by XRPD and SEM-EDS analysis. The methods descriptions for TG-DTA and XRPD analysis are reported hereafter. FTIR-ATR analysis, leaching tests, SEM-EDS analyses were also carried out and the details of these methods are described in § 3.1.2.

Thermal analysis

Thermo gravimetric analysis (TG) and differential thermal analysis (DTA) of the mixtures of both L02-K and Sl-K kaolin mixed with the sodium hydroxide were performed using a TA Instrument LINESIS STA PT1000 with a weight resolution up to 0.5 μg. The sample was located in a Pt crucible and heated from 100°C up to 1200° C at rate of 20° C/min.

X-ray Powder Diffraction

XRPD measurements were performed by using a Panalitical X'Pert Pro X-ray diffractometer for quantitative analysis. Data were collected in the range of 2-85 °2θ with a step width of 0.01° 2θ and time per step of 50 s.

SEM-EDS analysis

SEM JEOL JSM 5400, equipped with an OXFORD LINK-ISIS-EDX energy dispersive X-ray spectrometer, was used to investigate the microstructure of samples. Analyses were performed, in vacuum mode, on fracture surfaces of the specimens covered by carbon coating. Images were collected using secondary electron (SE) at a working distance of 15 mm with an acceleration voltage of 20 kV. EDS analyses (on spots) were done with accelerating voltage of 20 kV, working distance of 15 mm and beam current of 20 μA and acquiring for 30s per spot analysis. Chemical compositions were determined considering 100 wt % oxide content on an H_2O- and CO_2-free basis.

References

Andaç, Ö., Tatlıer, M., Sirkecioğlu, A., Ece, I., & Erdem-Şenatalar, A., 2005. Effects of ultrasound on zeolite A synthesis. Microporous and Mesoporous Materials, 79(1), 225-233.

Belviso, C., Cavalcante, F., Lettino, A., & Fiore, S., 2013. A and X-type zeolites synthesised from kaolinite at low temperature. Applied Clay Science, 80, 162-168.

Belviso, C., Giannossa, L. C., Huertas, F. J., Lettino, A., Mangone, A., & Fiore, S., 2015. Synthesis of zeolites at low temperatures in fly ash-kaolinite mixtures. Microporous and Mesoporous Materials, 212, 35-47.

Duxson, P., Lukey, G.C., Separovic, F., Van Deventer, J.S.J., 2005. Effect of alkali cations onaluminumincorporation in geopolymeric gels. Industrial & Engineering Chemistry Research, 44(4), 832-839.

Fernández-Jiménez, A., De La Torre, A.G., Palomo, A., López-Olmo, G., Alonso, M.M., Aranda, M.A.G., 2006. Quantitative determination of phases in the alkaline activation of fly ash. Part II: Degree of reaction. Fuel, 85(14), 1960-1969.

Fletcher, R.A., MacKenzie, K.J., Nicholson, C.L., Shimada, S., 2005. The composition range of aluminosilicate geopolymers. Journal of the European Ceramic Society, 25(9), 1471-1477.

Komnitsas, K., & Zaharaki, D., 2007. Geopolymerisation: A review and prospects for the minerals industry. Minerals Engineering, 20(14), 1261-1277.

Older, I., & Rößler, M., 1985. Investigations on the relationship between porosity, structure and strength of hydrated Portland cement pastes: II. Effects of pore structure and degree of hydration. Cements and Concrete Research, 15(4), 401-410.

Park, M., Choi, C.L., Lim, W.T., Kim, M.C., Choi, J., Heo, N.H., 2000. Molten-salt method for the synthesis of zeolitic materials I. Zeolite formation in alkaline molten-salt system. Microporous and Mesoporous Materials 37, 81-89.

Rios, C. A., Williams, C. D., & Fullen, M. A., 2009. Nucleation and growth history of zeolite LTA synthesized from kaolinite by two different methods. Applied Clay Science, 42(3), 446-454.

Santaquiteria-Ruiz, C., Fernández-Jiménez, A., Skibsted, J., & Palomo, A., 2013. Clay reactivity: production of alkali activated cements. Applied Clay Science, 73, 11-16.

Yusoff-Meor, M. S., Masilana, M., & Choo, T. F., 2007. Production of High Purity Alumina and Zeolite from Low-grade Kaolin. J. Adv. Mater. Res, 29-30.

RESULTS AND DISCUSSION

4 ALKALI ACTIVATION OF SULFATE-BEARING CLAY

In this section, the feasibility to produce AAMs from low-T activated sulfate-bearing clay has been assessed. The results discussed here are focused on the investigation of the effects of SO_4^{2-} on the nature and chemical composition of the resulting products. As mentioned in § 1.7, some studies have been conducted on the effect of the sulfate in alkali activation system (e.g. Lee and van Deventer, 2003; Criado et al., 2010; Desbats-Le Chequer & Frizon, 2011; Komnitsas et al., 2013). Actually, sulfate has been studied in fly ash systems, as possible alkali activation catalyst in zeolites formation or retarding agent in the condensation reaction of the silicon and aluminum species (Criado et al., 2010). The presence of sulfate ions in the solution and in pores may repel the negative charge on the aluminosilicates and may lead to similar condition to those prevailing in binders based on low Portland cement and high fly ash contents (Brough et al., 2001; Palomo et al., 2007). On the other hand, studies on the effects of addition of small amount of certain oxyanions (e.g., nitrate, sulfate, phosphate, etc.) have shown that these anions promote the synthesis of mesoporous materials. They can shorten crystallization time and depending on the alkali ion used in the activation solution, the anionic species considered can also enhance the nucleation of certain zeolites, making these materials a promising resource for waste encapsulation matrices (Laha & Kumar, 2002; Le Chequer & Frizon, 2011).

This work is an experimental investigation of the possibility of sulfate retention by the AAMs, and of the effect of this anion in the alkali activation process, in terms of phases composition and microstructure of the resulting AAMs.

Sodium silicate (waterglass) has been used for the alkaline activation of sulfate bearing clay. In parallel, alkali activation was carried out on synthetic mixtures of alunite and high-grade kaolin for comparison. Details of synthesis parameters are reported in § 3.1.

All samples have been analyzed by XRPD, SEM-EDS, FT-IR, and leaching tests have been carried out in order to quantify the soluble sulfate phases in AAMs.

Experiments for the stabilization of sulfate have been also conducted by adding $Ba(OH)_2$ or CaO. Ba(OH) is used for stabilizing sulfate rich aqueous level waste with blast furnace slag (Mobasher et al., 2014). CaO is added to reproduce calcium-aluminate or sulfo-aluminate cement-based materials, which can sometimes accommodate much higher sulfate contents without undergoing degradation process. Table 4.1 shows a list of the analyzed samples,

respective starting materials proportion, FT-IR main peaks positions before and after water leaching and the new phases detected after alkali reaction.

TABLE 4.1. Results for L02-K and Sl-K based AAMs with sodium silicate

Samples	Clay/ Alunite ratio (wt%)in 100 g	Si-O-T vibration from FT-IR, before water leaching (cm^{-1})	Si-O-T vibration from FT-IR, after water leaching (cm^{-1})	New phase found by XRPD analysis
Sl_{550}_s46	100	1014	-	No new phase-
Sl_{550}A10_s36	91.5:8.5	1014	998	Thenardite
Sl_{550}A10_s46	91.5:8.5	1020	1037	Thenardite
Sl_{800}A20_s36	82:18	1029	1031	Thenardite
Sl_{800}A20_s46	82:18	1041	1037	Thenardite
L02_s36	80:20	1006	1018	Thenardite
L02_s46	80:20	1018	1018	Thenardite
L02_Ca_s36	80:20	-	-	Thenardite
L02_Ba_s36	80:20	-	-	Barium-potassium-sulfate

Sl = Sl-K kaolin; L02 = L02-K kaolin; A = alunite initial wt%; s36 and s46 = SiO_2/Al_2O_3 molar ratio.

4.1 Phase composition

XRPD patterns of L02-MK and Sl-MK based AAMs are reported in Figure 4.1 and Figure 4.2, respectively.
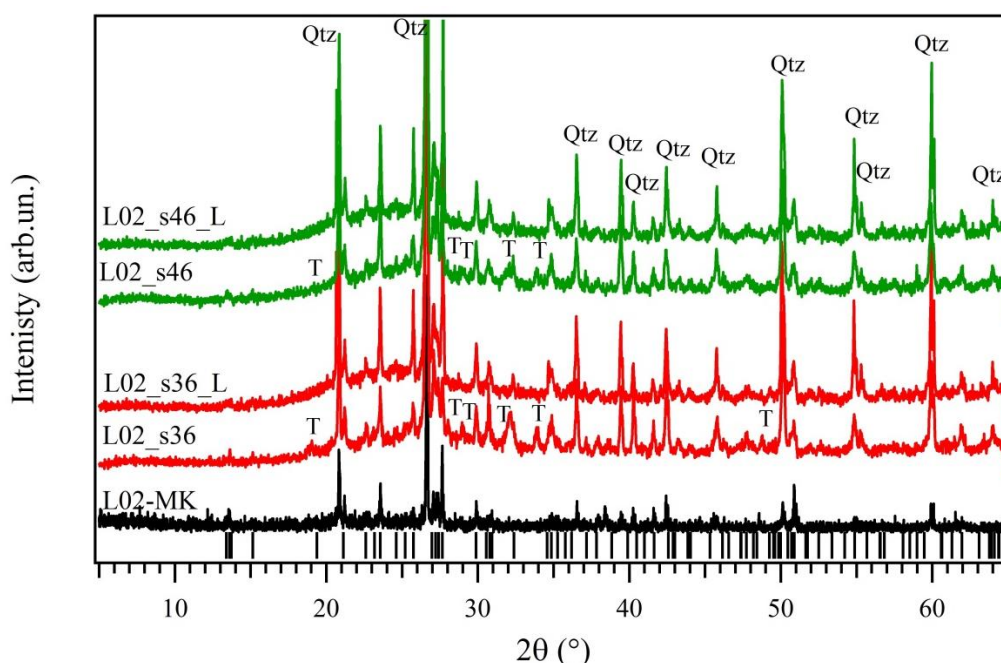
FIGURE 4.1. XRPD patterns of L02-MK based binders. Black: L02-MK; red: samples with SiO_2/Al_2O_3 = 3.6; green: samples with SiO_2/Al_2O_3 = 4.6; L= after leaching; vertical black lines indicate feldspars peak positions. T = thenardite (Na_2SO_4); Qtz = quartz.

The XRPD patterns of the corresponding precursor for each set of binders have been reported for comparison. All diffraction patterns display peaks due to crystalline phases deriving from the precursors, like quartz for Sl-MK-based AAMs and quartz and feldspars for L02-MK-based AAMs, which do not take part in the reaction. It is worthy to note that traces of kaolinite are still recognizable when Sl-K is heated at 550°C (Figure 4.2 a, violet pattern).
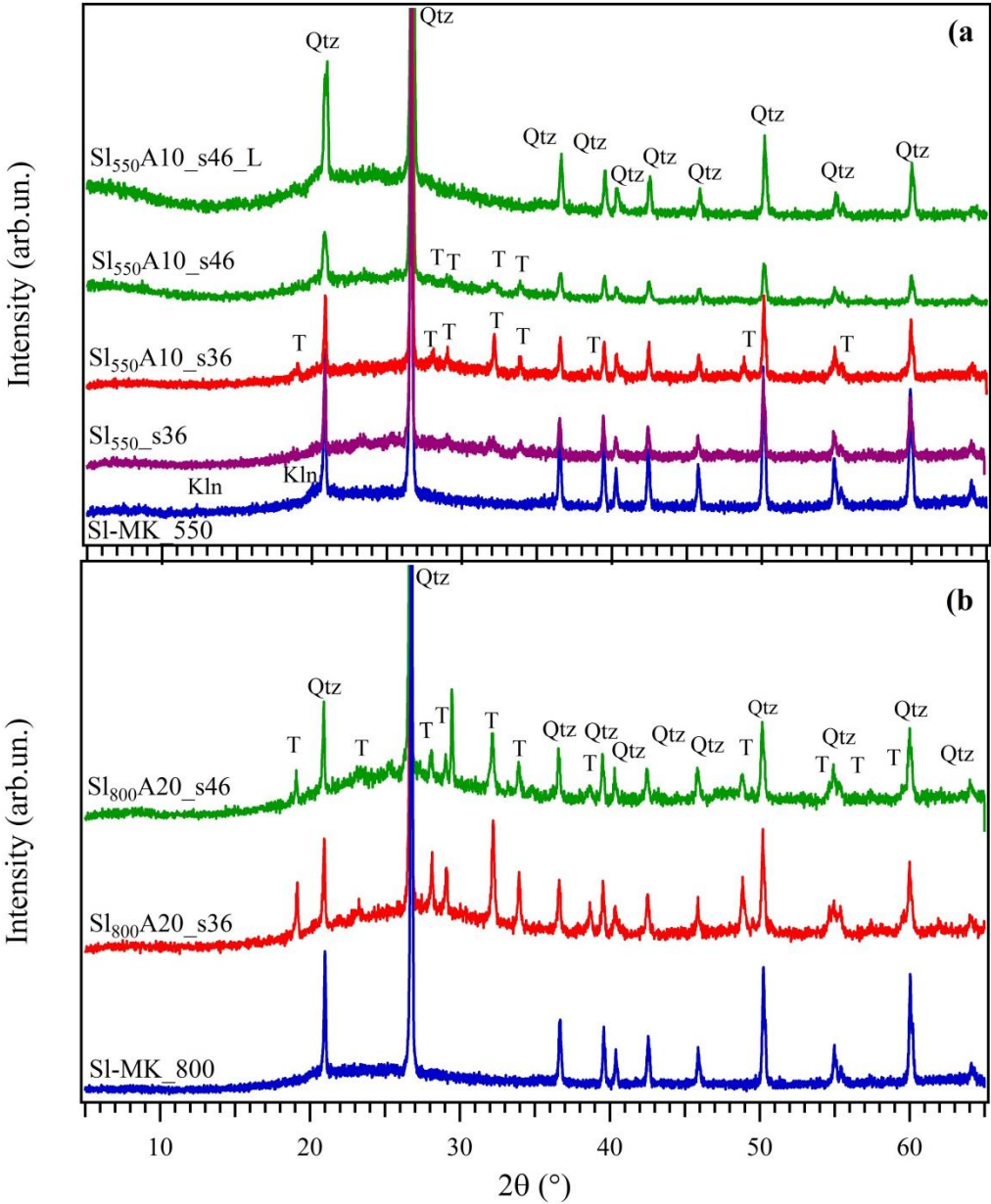
FIGURE 4.2. a) XRPD patterns of Sl-MK-based binders with kaolin heated at 550°C; b) Sl-MK-based binders with kaolin heated at 800°C. Reference metakaolins are reported for comparison in each graph. Red patterns = samples with $SiO_2/Al_2O_3 = 3.6$; green patterns = samples with $SiO_2/Al_2O_3 = 4.6$; L= after leaching; T = thenardite; Qtz = quartz.

This kaolin needs temperatures higher than 550° C to transform completely into metakaolin, as explained in § 2.2.

XRPD patterns of AAMs obtained from L02-MK (Figure 4.1) and Sl-MK with alunite addition, (Figure 4.2) show similar features. A "hump" centered in the range between 21° and 30° 2θ is visible in all samples. This signal, which indicates the formation of an amorphous aluminosilicate, the aluminosilicate gel, is considered the distinguishing feature of the diffraction pattern of AAMs. The position of this hump is independent on the aluminosilicate source and activating solution, as well as on the curing conditions as also reported in many example in literature (e.g. Barbosa & McKenzie, 2003; Rowles and O'Connor, 2003; Fletcher et al., 2005; Pereira et al., 2007; Dimas et al., 2009; Gasparini et al., 2015).

It is possible to observe that no peaks attributable to zeolites have been found in the patterns. In fact, at the SiO_2/Al_2O_3 ratio used for the synthesis, the gel is stable with no tendency -or very low tendency- towards amorphous/crystalline transformation (e.g. De Silva & Sagoe-Crenstil, 2008). The only crystalline by-product formed is thenardite (Na_2SO_4, PDF: 070-1541). Thenardite can precipitate directly from solution due to water evaporation after curing (Navarro et al., 2000). This phase is present in all samples containing sulfate. Thenardite is soluble in water and peaks referable to it are not observed in the XRPD patterns of samples after leaching.

4.2 Textural and microstructural properties

To point out the differences in the microstructure and chemical composition of these AAMs, SEM-EDS analyses at different length scales have been carried out for samples with and without alunite in the starting mixture.

Figure 4.3 shows the SE micrographs of the fracture surface of the L02_s36 (Figure 4.3 a, c and e) and of L02_s46 (Figure 4.3 b, d and f) respectively. At 5 Kx (Figure 4.3 a and b), the textures appear homogeneous for both samples, confirming the amorphous nature of the reaction product. At 10 Kx (Figure 4.3 b and c) a few voids and the platy-shape morphology typical of the meta-kaolin based AAMs are recognizable. At this length scale, some differences in morphology between the two samples are observed. At lower silica content (SiO_2/Al_2O_3 = 3.6), the amorphous particles that form the gel appear rounded or sub rounded. At higher silica content (SiO_2/Al_2O_3 = 4.6) instead, the matrix morphology appears more

compact although articulated and an indented surface could be recognized, as shown in Figure 4.3c and d, respectively.
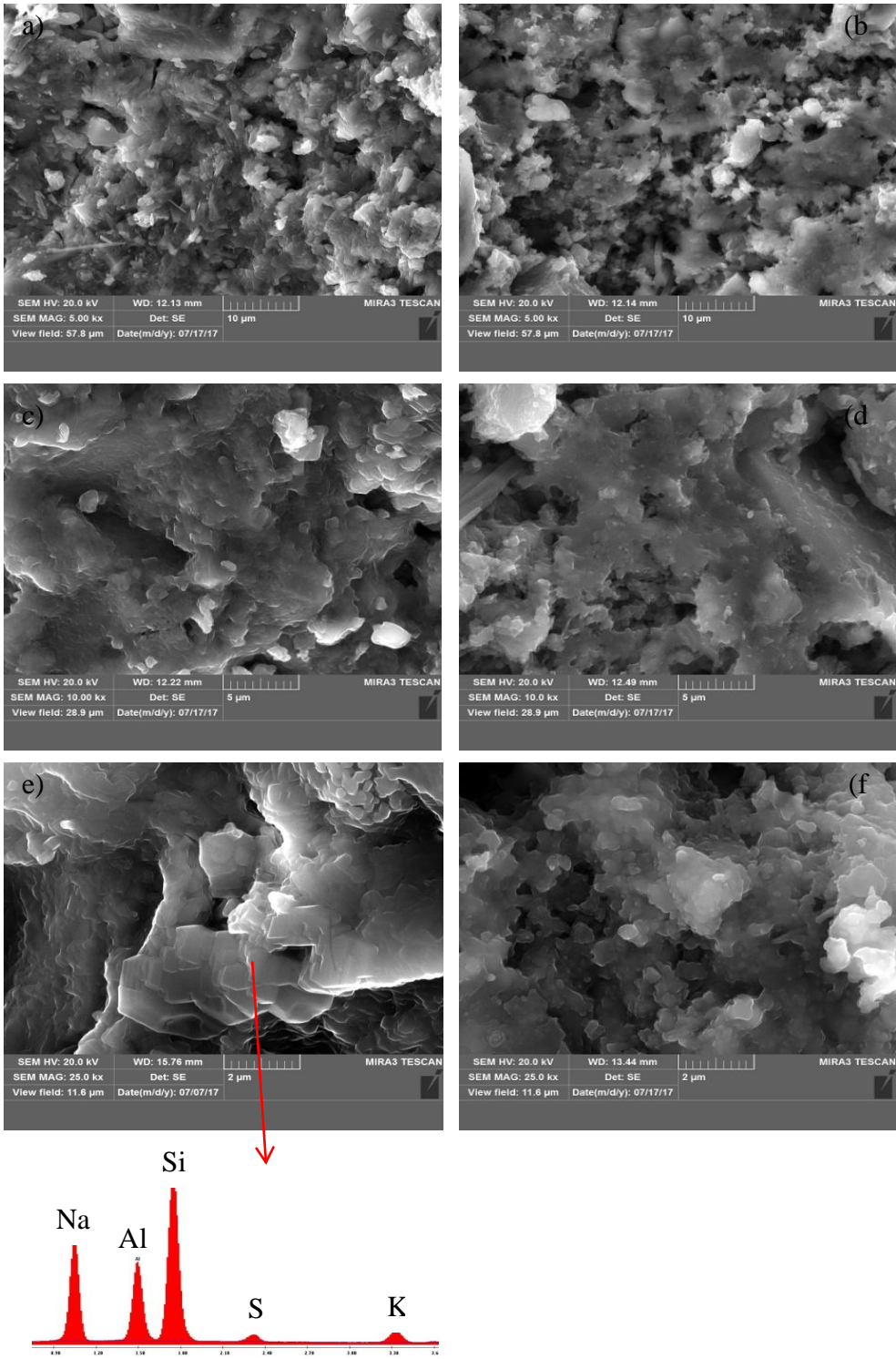
FIGURE 4.3. SE-Micrographs of L02_s36 (a, c and e) and L02_s46 (b, d and f) samples at different length scales.

At 25 Kx, L02_s36 sample shows some incipient crystalline growths embedded in the amorphous matrix. On the basis of EDS analyses and morphology, these crystals could be attributed to framework silicates, like zeolites or feldspathoids, while at this enlargement, L02_s46 shows the distinctive granular aspect of a N-A-S-H gel and no crystals are detected. The increase of soluble silicon in the activating solution improves the stability of the materials and does not promote crystalline phases formation (Duxon et al., 2007).

Comparing samples containing alunite ($Sl_{550}A10\_s46$) with those without alunite (Sl_{550}_s46) obtained from the high-grade kaolin, it is possible to observe that there are no significant differences in their microstructures detectable at lower magnification, as shown in the inset of Figures 4.4 a and b, respectively. At this scale, both matrices appear compact with a dense texture. At 20 Kx, particles arranged to form aggregates with the typical platy-shape morphology of the products of alkali activation of metakaolin are observed in both samples. Some residual particles of metakaolin precursor, which are not completely dissolved, are still visible in the sample Sl_{550}_s46 (Figure 4.4 b), in agreement with the partial dehydroxylation of Sl-K at this temperature and consequent partial conversion into metakaolinite.

However, at this length scale, the sample containing alunite (Figure 4.4 a) appears less interconnected and more granular than the sample without alunite (Figure 4.4 b), and the texture of the matrix appears more homogeneous and more compact in absence of sulfate. These morphological differences might be related to the presence of sulfate and consequently, to the gel process formation.
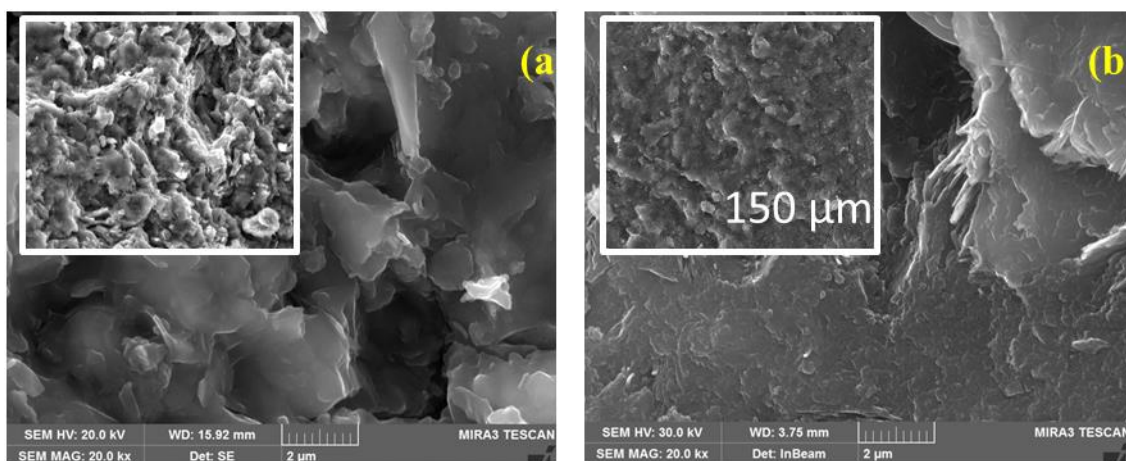
FIGURE 4.4. SE-Micrographs of $Sl_{550}A10\_s46$ (a) and Sl_{550}_s46 (b) samples at different length scales.

In order to investigate the effect of the soluble silica in the mixtures containing sulfate, SEM analyses have been carried out on $Sl_{550}A10\_s36$ and $Sl_{550}A10\_s46$ samples (Figure 4.5). At low enlargement (5.0 Kx), the analysis of the microstructure for both samples confirms the development of the alkali activated gel. By comparing these textures with those of L02-_s36 (Figure 4.3 a) and L02_s46 (Figure 4.3 b), they seem to have less compact microstructures.
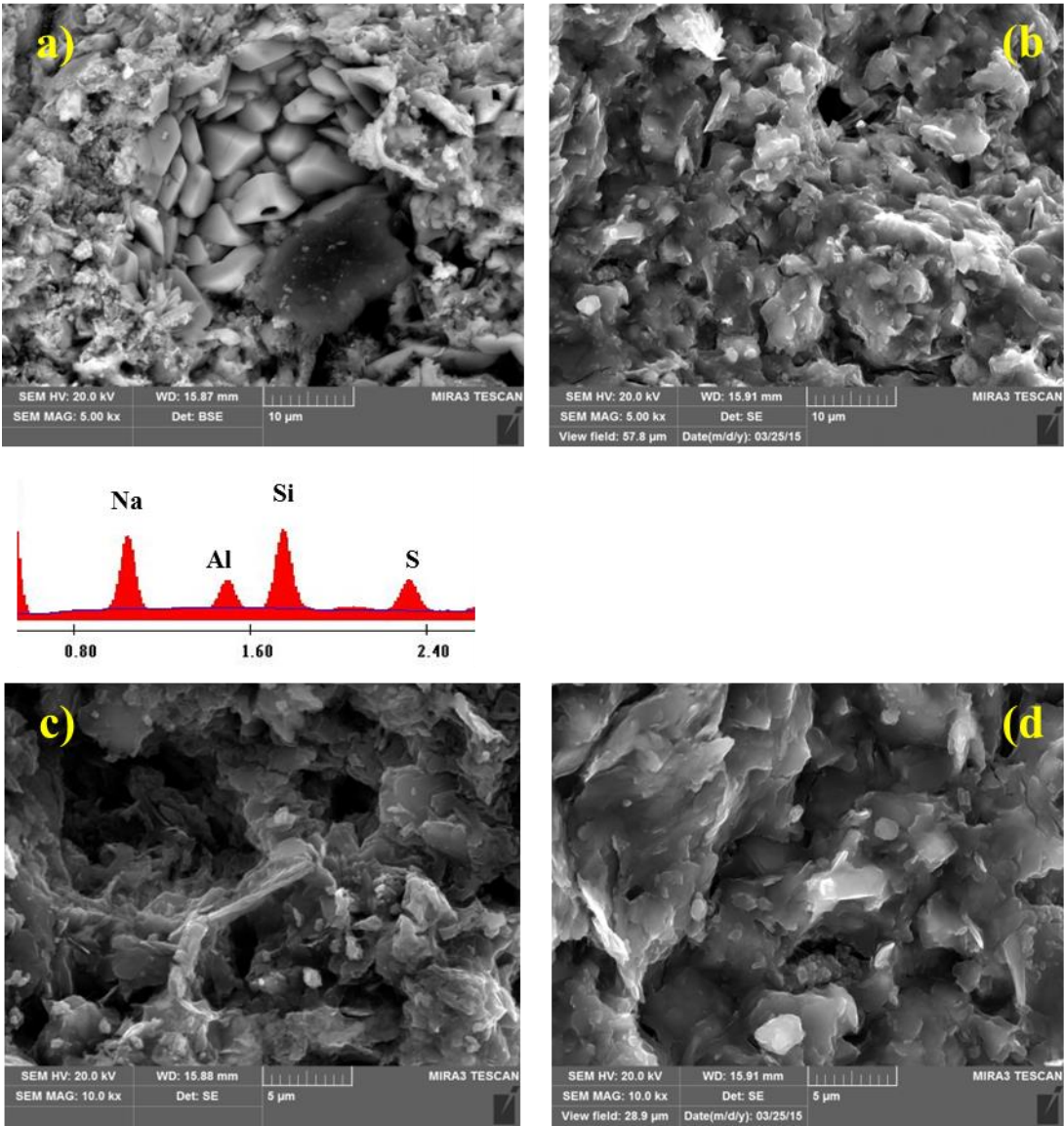
FIGURE 4.5. SE-Micrographs of fracture surfaces of $Sl_{550}A10\_s36$ (a, c) and $Sl_{550}A10\_s46$ (b, d) samples at different length scales.

The presence of grains and particles scattered in all the matrix of the pastes makes the microstructure less homogeneous. A common morphological feature is the metakaolin tendency to arrange itself into parallel planes and both samples exhibit some unreacted

particles. Morphological differences related to SiO_2/Al_2O_3 different molar ratios can be observed comparing $Sl_{550}A10\_s36$ (Figure 4.5 a and c) and $Sl_{550}A10\_s46$ (Figure 4.5 b and d), respectively. The distinctive textural features are mostly related to two factors: the different degrees of development and homogeneity of the AAMs matrix and the amount of precipitates and neo-formed crystalline phases, which can also produce by-products. At 5.0 Kx, the sample with SiO_2/Al_2O_3 ratio = 3.6 exhibits a less compact texture, comprising dense particulates, which appears more fragmented with respect to that of the sample with SiO_2/Al_2O_3 ratio = 4.6 (Figure 4.5 a and b).

Defects in the gel network are also represented by the presence of small crystals, as tetragonal prisms, which have been found in a void, as shown in Figure 4.5 a. These crystals are composed by Na, Al, Si and S, as detected from the EDS spectra (Figure 4.5 a), and from their shape and composition, they could be intended as zeolites. At higher magnification, the matrix displays an evident porosity and the grains appear less interconnected than the sample with higher silica content (Figure 4.5 c and d). No crystalline phases have been detected in the latter sample and the matrix connection of the gel network appears more developed, as shown in Figure 4.5 b.

Theoretically, Si-O-Si linkage are stronger than Si-O-Al bond, meaning that the compactness of the binder should increase with Si/Al ratio since the density of Si-O-Si increase with Si-O-Si ratio (De Jong and Brown, 1980).

Indeed, a lower silica content in the mixture suggests a tendency of these alkaline systems to favor the transformation of zeolitic precursor into crystalline aluminosilicate at incipient state of crystallization, as revealed in Figure 4.5 a. Besides the differences related to the silica content, it is also possible to observe that all samples already described which contain sulfate show a gel that appears less reacted than that of the sample in absence of sulfate (Sl_{550}_s46).

4.3 Sulfate quantification in AAMs

The efficiency of AAMs matrix to hold sulfate and the actual concentration of sulfate ions have been evaluated after leaching on the extracted liquid (data are reported in Table 3.2 § 3.1.2) and on the solid residues by BSE-EDS analyses. Overall, the sulfate retention is below 50 wt%. However, even if a soluble sulfate phase (thenardite) is formed in all samples, as confirmed by XRPD, not all the sulfate is leached out.
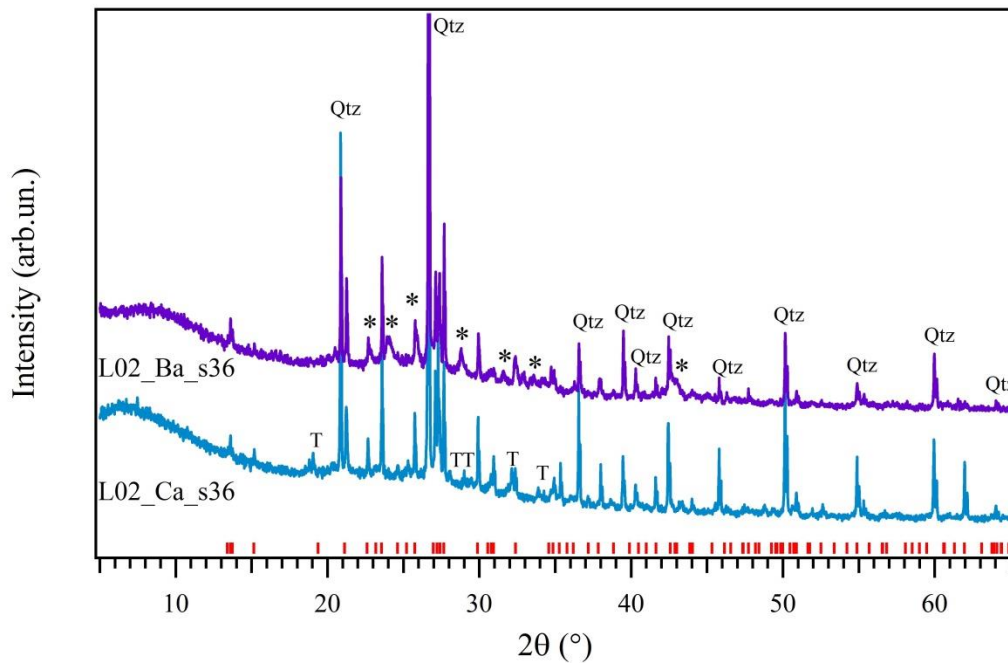
FIGURE 4.6. XRPD of L02-MK-based AAMs prepared adding CaO and Ba(OH)$_2$·8H$_2$O) to the mixture with SiO$_2$/Al$_2$O$_3$ = 3.6. Red lines represent feldspars form the original precursor. T = thenardite; Qtz = quartz; * = barium sulfate (BaSO$_4$)

This means that there is a capability of these binders to retain and immobilize part of the sulfate inside the matrix. It has been seen that when CaO is added to the L02_s36 (CaO/SO$_4$ = 1:1), sulfate retention increases from 31.0 wt % to 44.5 wt %, meaning that calcium is able to hold sulfate, likely by forming calcium sulfate compounds, which however, are not detected by XRPD, as reported in Figure 4.6. This evidence suggests that an external additional source of calcium has a positive effect on the sulfate retention in this matrix and the supplied CaO could be achieved by the addition of a lime source as the clinker in the hybrid cements. Adding Ba(OH)$_2$·8H$_2$O to the L02_s36 (BaO/SO$_4$ = 1:1), the sulfate retention is 80 wt %, as expected, due to formation of barium sulfate phase, as shown in Figure 4.6.

4.4 Analysis of residues after leaching test

Backscattered electron images of L02_s36 and L02_s46 samples have been carried out on powder pellets, after water leaching, and are reported in Figure 4.7.
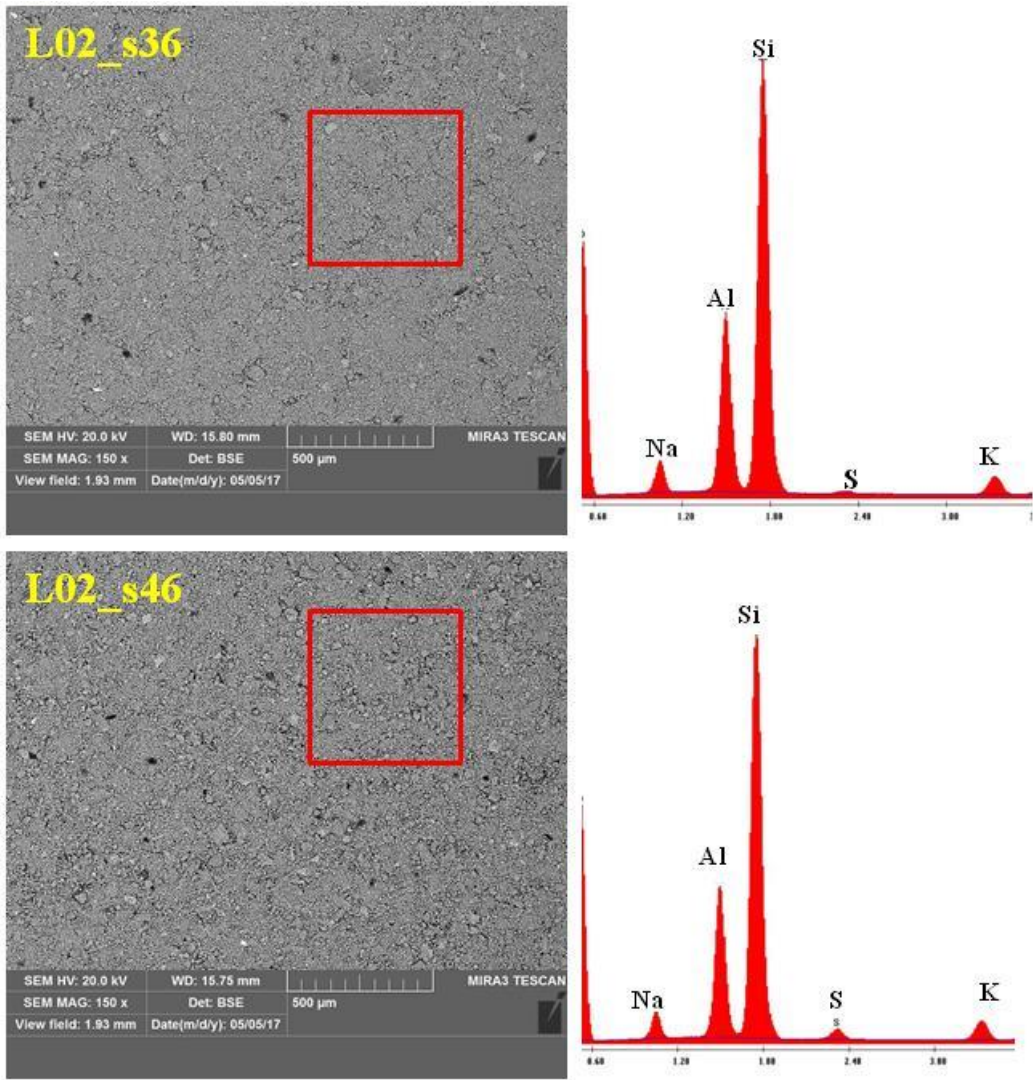
FIGURE 4.7. BSE images and EDS analyses of L02_s36 and L02_s46 samples after leaching.

At 150x, the microstructures appear composed by a light matrix and several darker grains scattered in the matrix. These dark portions are recognizable also in the surface fracture not only when the samples are prepared as pellets. EDS analyses reported in Figure 4.7 are referred to an area of 500 μm in size. Both samples result composed by Si, Al, and Na corresponding to the aluminosilicate N-A-S-H gel composition, with an amount of K and S. S content appears higher in the L02_s46 matrix with respect to L02_s36 matrix. SE and BSE images of the dark particles scattered on the matrices of the samples have been reported in Figure 4.8.
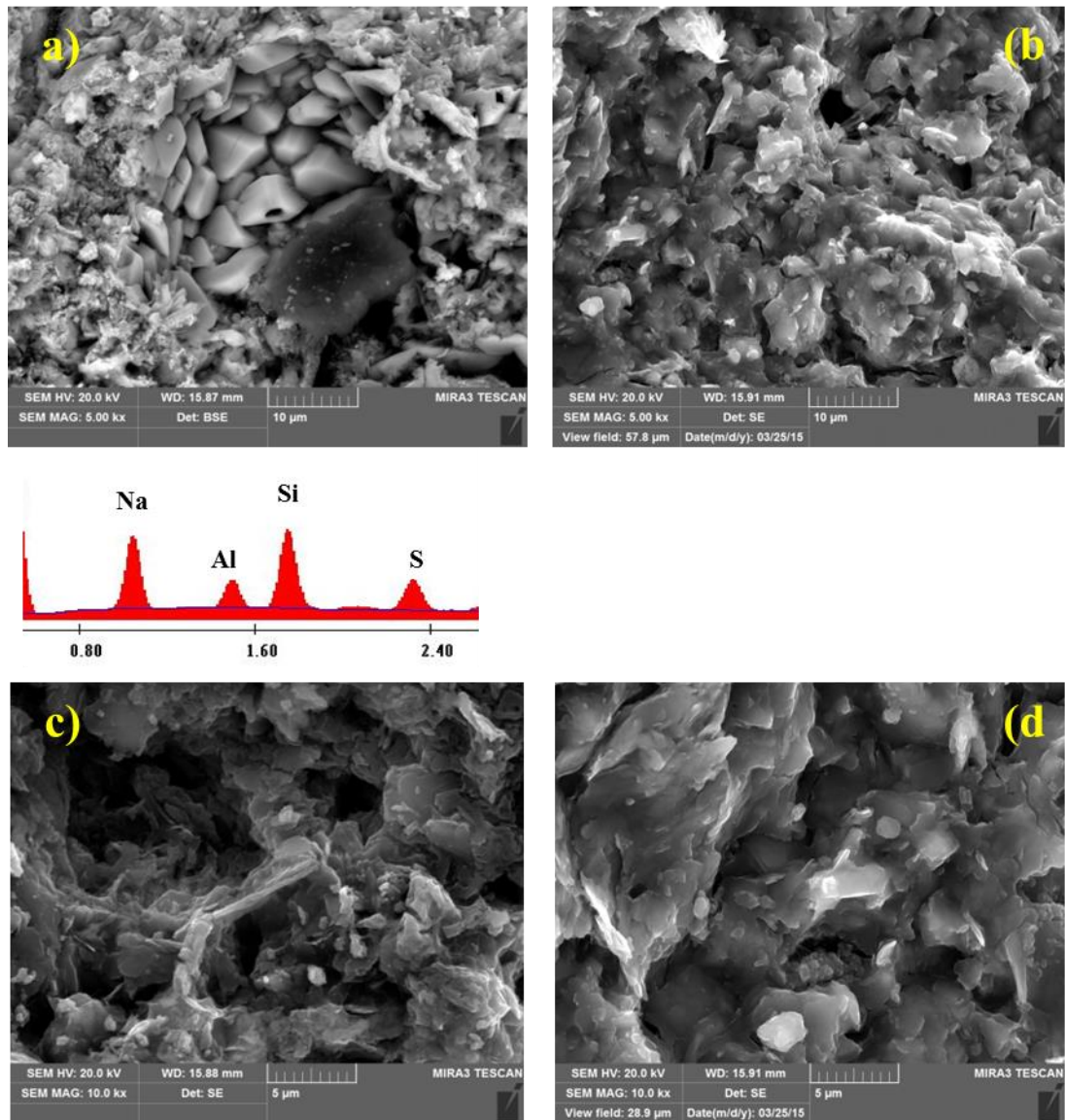
FIGURE 4.8. BSE and SE micrographs and EDS analyses of dark particles after water leaching: (a, b) L02_s36 sample; (c, d) L02_s46 sample.

From a morphological point of view, it is possible to notice that these dark portions appear more dense and seems as loosely structured precipitated which are in continuity with the surrounding matrix, as showed by morphological image carried out in secondary electron modes (Figure 4.8 b and d). However, BSE images reveal some differences in chemical composition with respect to the matrix. EDS analyses carried out on an area of 5 μm around those particles show that they are composed of Na, Al, Si, K and S (Figure 4.8). Nevertheless, the Al/Na ratio is lower with respect to that of the matrices, while the S content, for both samples, appears higher in these portions than in the corresponding matrices. These findings

81

might suggest that they are localized portions of the gel, likely as zeolitic precursors, which are able to hold the sulfate.

4.5 FT-ATR analysis

Figure 4.9 shows the infrared spectra of the starting materials after thermal treatment and of the reaction products of alkaline activation before and after water leaching. Samples prepared without alunite are also reported for comparison.

Quartz is recognizable in all samples by the presence of double peaks at 750-775 cm^{-1} and 694 cm^{-1} that are related to the Si-O-Si symmetric stretching vibration (Farmer, 1974; Lee and van Deventer, 2003). All spectra show the Si-O-T stretching vibration band in the range 1000-1050 cm^{-1} (position that varies depending on the SiO_2/Al_2O_3 molar ratio and precursor used), which is attributed to sodium aluminosilicate gel formed as a result of the alkaline activation (e.g. Alonso & Palomo, 2001; Lee and van Deventer, 2003; Lee and van Deventer, 2004; Khan et al., 2015). In L02-MK and Sl-MK spectra, this band related to TO_4 tetrahedra is at higher frequencies than those of alkaline activated samples. The shift of this band to lower wavenumbers indicates that some changes occurred in the length of Si-O-T bonds, due to the extent of aluminum incorporation or due to an increase in the concentration of non-bridging oxygen atoms (Palomo & Glasser, 1992; Alonso & Palomo, 2001; Rees et al., 2007). Samples containing alunite show a shoulder around 1100 cm^{-1} and 1200 cm^{-1}, which represent the strongest stretching vibration of SO_4^{2-} (Farmer, 1974; Bishop and Murrad, 2005; Gasparini et al., 2015). Thenardite is evident in L02$_{550}$_s36 (dotted red line) for the presence of the peak at 1101 cm^{-1} related to vibration modes of the S-O bonds. From a visual point of view, this band is still evident after water leaching in all samples containing sulfate.

Bands related to CO_3^{2-} stretching vibrations are at 1400 cm^{-1}. The formation of these bands could be attributed to sodium carbonates (Farmer, 1974; Fernández-Jiménez and Palomo, 2009). These are formed because of carbonation in air of the excess of Na^+ cations that are free to move inside the pore network and consequently to the water evaporation are brought to the surface of the sample. They disappear after water leaching.
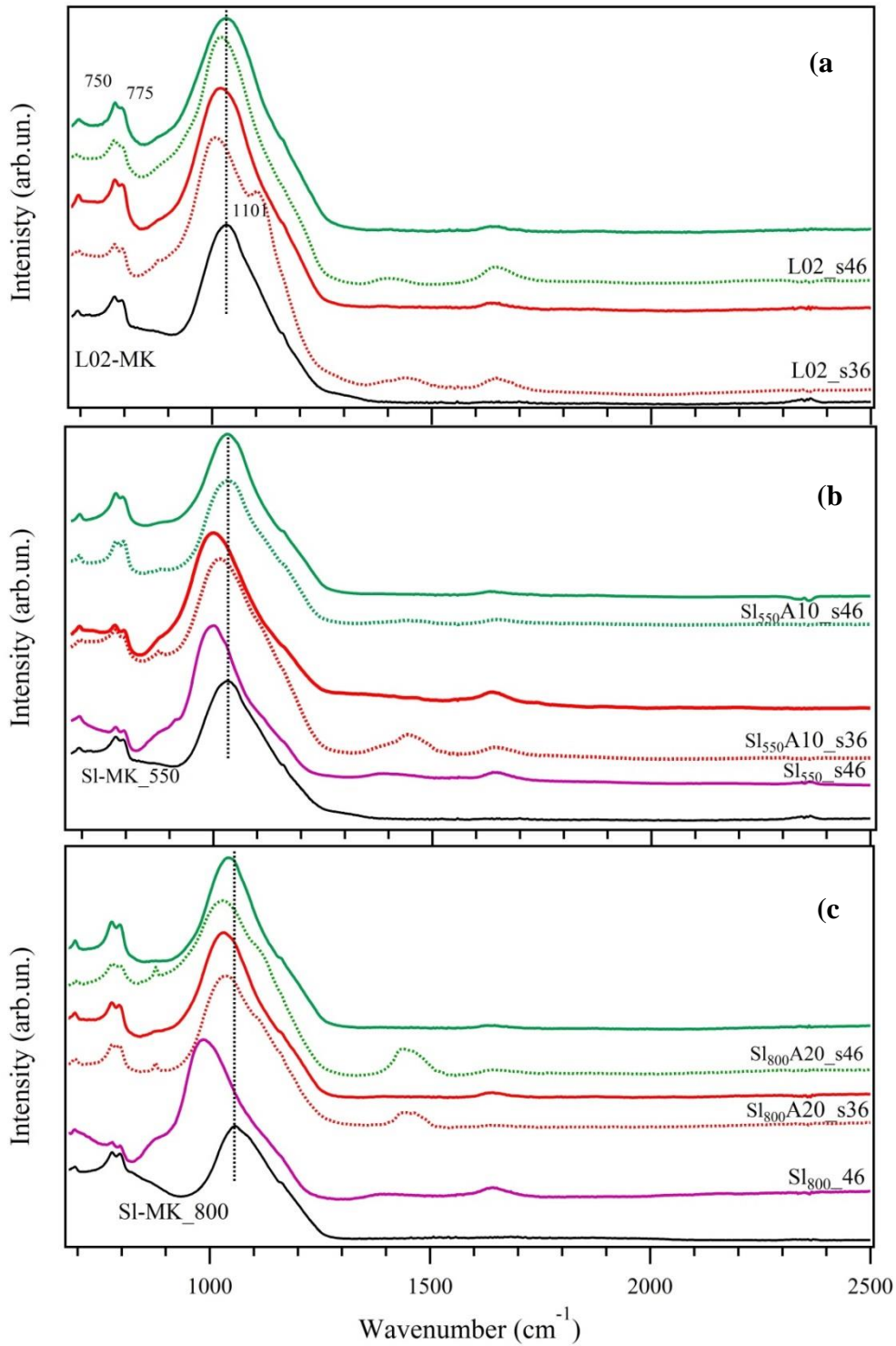
FIGURE 4.9. FT-IR spectra: a) L02-MK series; b) Sl$_{550}$-series c) Sl$_{800}$-series. Dotted lines represent spectra before leaching test; bold lines represent spectra after leaching test. Black lines represent the spectra of the heated precursors for each series. Violet line represents the correspondent binder without alunite.

A more detailed study of the region between 800 cm^{-1} and 1300 cm^{-1} was conducted on the samples that retain more sulfate after water leaching. In order to examine in depth the effect related to the presence of the sulfate in these materials, the corresponding binder without alunite has been analyzed for comparison. Identification of the phases forming this band involved their deconvolution, as reported in Figure 4.10. The fit has been carried out using Multipeak Fitting package of Igor Pro 6.37. It converged with nearly flat residuals.

The band related to the original sulfate-bearing L02-MK kaolinitic clay was found to include four signals (Figure 4.10 a), which comprise: metakaolinite (represented by blue line), feldspars, quartz and sulfate (red lines). A further broad peak centered at lower wavenumber has been also included in all fits to take into account the tails of the fitted region at low wavenumbers.

Alkaline activated samples (Figure 4.10 b and c) show a decrease in intensity of the peaks related to metakaolinite (blue line) and the occurrence of a peak attributed to the aluminosilicate gel (green line), which is formed at its expense, for both SiO_2/Al_2O_3 molar ratios. Deconvoluted spectrum for Sl-MK is composed by an intense peak related to meatkaolinite (blue line) and quartz are (red line) as expected (Figure 4.10 d). After alkaline activation (Figure 4.10 e), it is possible to observe that the intensity of the peak related to metakolinite clearly decrease and a broad intense peak of the aluminosilicate gel (green line) is formed. These evidences clearly mean that almost all the metakaolinite has reacted. However, when sulfate is added to Sl-MK, the peaks related to the gel appears lower than the peak related to metakaolinite with respect to the sample without sulfate, as reported in Figure 4.10 f and g. This finding is evident for both SiO_2/Al_2O_3 molar ratios and it might suggest that the degree of reaction is lower in presence of sulfate and larger amount of meatakolinite remained unreacted.

FIGURE 4.10. Deconvoluted spectra for the T-O bond asymmetric stretching bond in sulfate bearing AAMs. a) L02-MK; b) L02_s36; c) L02_s46; d) Sl-MK; e) Sl$_{550}$_s46; f) Sl$_{550}$A10_s46; g) Sl$_{800}$A10_s46. Blue line attributed to metakaolinite; green line attributed to alluminosilicate gel.
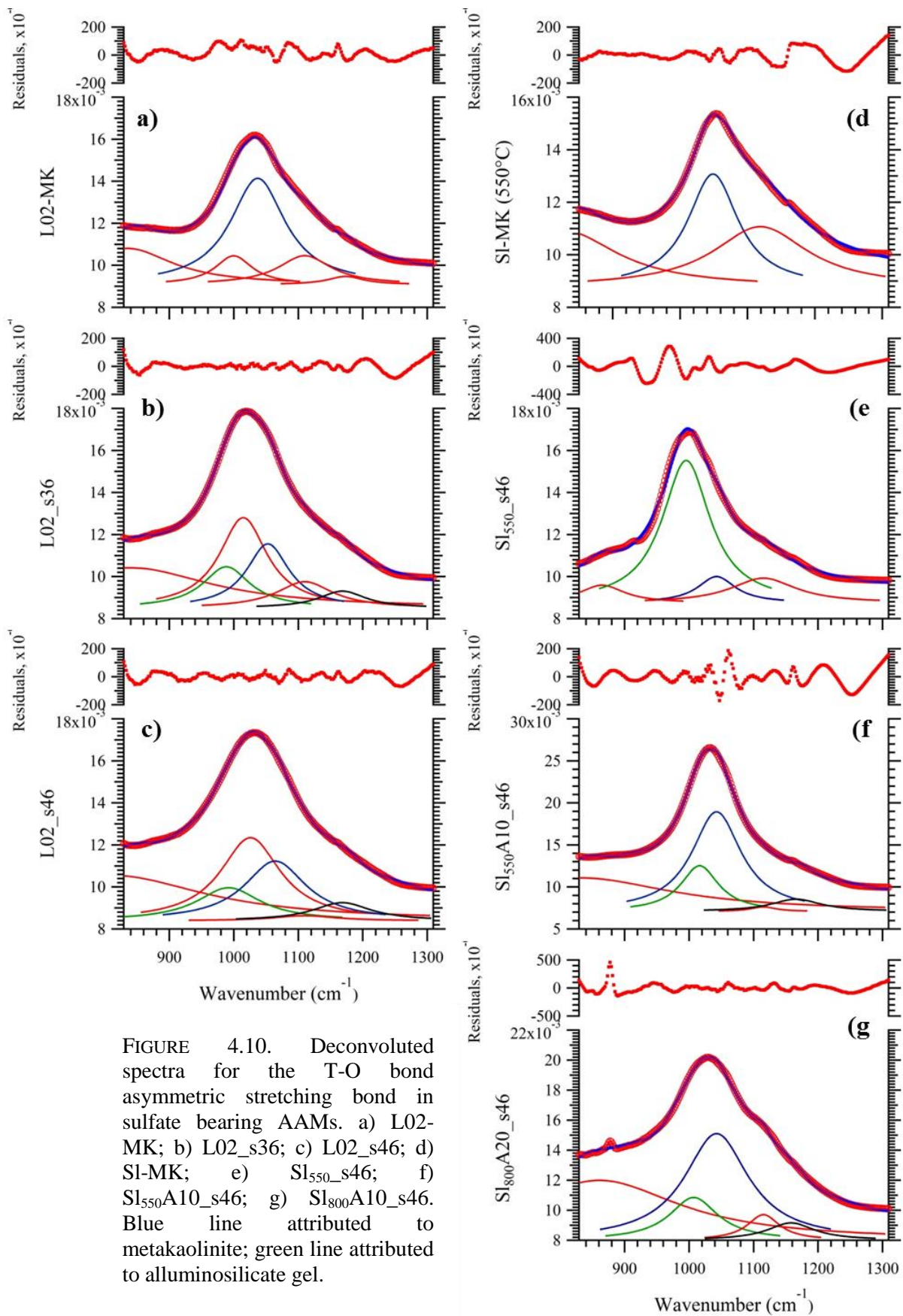
4.6 Conclusions

The products of alkali activation of the AAMs based on L02-MK and Sl-MK (with and without alunite addition) include mainly an amorphous N-A-S-H gel and no new crystalline phases apart for thenardite have been detected by the XRPD analyses. The latter is soluble in water and disappeared after leaching tests. However, it seems that not all the sulfate is leached out after tests and sulfate solubility results a bit higher in the sample with lower SiO_2/Al_2O_3. Morphological analyses outline that, regardless the soluble silica content, an amorphous gel is formed from all mixtures. However, signs of incipient gel crystallization can be noted in sulfate containing samples with SiO_2/Al_2O_3 ratio is 3.6, hence when less soluble silica is available to the process. By comparing the samples containing sulfate to those without sulfate, it is possible to notice that the gel formation seems to be affected by its occurrence, even if the amorphous gel is formed in all cases. Sulfate in alkaline system is said to retard or interrupt gel formation and accelerate zeolites formation; sulfate ions in solution may repel the negative charge of the aluminosilicate thus hindering the condensation reaction and lowering the degree of metakaolin dissolution (Criado et al., 2010). Differently from what observed in literature in the present study the gel appears to be well formed, and no crystalline zeolite phases have been found by XRPD.

Leaching tests and chemical analyses performed on leached solution as well as on the resulting leached materials have demonstrated that not all sulfate is combined with sodium to form thenardite but some amount is still present in the samples. The data are confirmed also by chemical, microstructural and semi-quantitative EDS analyses. Infrared spectra of sulfate-bearing AAMs after water leaching are dominated by the vibration of Si-O-T bonds related to the formation of amorphous N-A-S-H gel and by the S-O bonds of the sulfate anion, which however seems not to form new compounds. Chemical microanalyses have revealed that the presence of sulfur-rich particles containing Si and Al, likely amorphous or nano-sized zeolites phases, might be the responsible structures able to take the sulfate in the gel. However, since lower leachability have been found in the samples with higher silica content and lower capability to form zeolitic phases, the uptake of sulfate ions by the gel itself cannot be excluded. The data obtained until now suggest that the at this SiO_2/Al_2O_3 molar ratio, the properties of the amorphous AAMs gel are obtained in presence of sulfate ion, and more compactness of the gel microstructure however could be adjusted adding soluble silica into the mix, as well as the sulfate retention capability. The ability to retain sulfate by the gel or by

nano-zeolite-like structures eventually formed makes these binders a promising materials in the exploitation of their matrix as ion encapsulation/immobilization matrix. Optimization of the synthesis parameters, like for example adding calcium oxide or varying the soluble silica content in order to change the stability between amorphous-crystalline, could provide a way to improve the sulfate retention and achieve its complete immobilization. The possibility to vary the synthesis parameters based on the mix formulation makes these materials highly versatile and promising as waste encapsulating materials.

References

Alonso, S., & Palomo, A., 2001. Alkaline activation of metakaolin and calcium hydroxide mixture: influence of temperature, activator concentration and solid ratio. Materials Letters, 47(1), 55-62.

Barbosa, V.F.F., MacKenzie, K.J.D., 2003. Thermal behaviour of inorganic geopolymers and composites derived from sodium polysialate. Materials Research Bulletin, 38(2), 319-331.

Bich, C., Ambroise, J., Péra, J., 2009. Influence of degree of dehydroxylation on the pozzolanic activity of metakaolin. Applied Clay Science, 44, 194-200.

Bishop, J.L., & Murad, E., 2005. The visible and infrared spectral properties of jarosite and alunite. American Mineralogist, 90(7), 1100-1107.

Bistrow, C.M., 1987. World kaolin: genesis, exploitation and application Industrial minerals, 238, 45-59.

Brough, A. R., Katz, A., Sun, G. K., Struble, L. J., Kirkpatrick, R. J., & Young, J. F., 2001. Adiabatically cured, alkali-activated cement-based wasteforms containing high levels of fly ash: Formation of zeolites and Al-substituted CSH. Cement and Concrete Research, 31(10), 1437-1447.

Burciaga-Diaz, O., Escalante-Garcia, J.I., Gorokhovsky, A., 2012. Geopolymers based on a coarse low- purity kaolin mineral: Mechanical strength as a function of the chemical composition and temperature. Cement and Concrete Composites, 34(1), 18-24.

Christidis, G.E., Scott, P.W., Marcopoulos, T., 1995. Origin of the Bentonite Deposits of Eastern Milos, Aegean, Greece: Geological, Mineralogical and Geochemical Evidence. Clays and Clay Minerals, 43(1), 63-77.

Clausi, M., Tarantino, S.C., Magnani, L.L., Riccardi, M.P., Tedeschi, C., Zema, M., 2016. Metakaolin as a precursor of materials for application in Cultural Heritage. Applied Clay Science, 132, 589-599.

Criado, M., Palomo, A., Fernández-Jiménez, A., 2005. Alkali activation of fly ashes. Part 1: effect of curing conditions on the carbonation of the reaction products. Fuel, 84, 2048–2054.

Criado, M., Jiménez, A. F., & Palomo, A., 2010. Effect of sodium sulfate on the alkali activation of fly ash. Cement and Concrete Composites, 32(8), 589-594.

De Jong, B.H.W.S.; Brown G.E., 1980. Polymerization of silicate and aluminate tetrahedra in glasses, melts, and aqueous solutions-I. Electronic structure of $H_6Si_2O_7$, $H_6AlSiO_7^{1-}$, and $H_6Al_2O_7^{2-}$. Geochimica et Cosmochimica Acta, 44, 491-511.

De Silva, P., & Sagoe-Crenstil, K., 2008. Medium-term phase stability of Na_2O-Al_2O_3-SiO_2-H_2O geopolymer systems. Cement and Concrete Research, 38(6), 870-876.

Desbats-Le Chequer, C., & Frizon, F., 2011. Impact of sulfate and nitrate incorporation on potassium-and sodium-based geopolymers: geopolymerization and materials properties. Journal of Material Science, 46(17), 5657-5664.

Dimas, D. D., Giannopoulou, I. P., & Panias, D., 2009. Utilization of alumina red mud for synthesis of inorganic polymeric materials. Mineral processing & Extractive metallurgy review, 30(3), 211-239.

Dondi, M., 2000. Kaolinitic clays of volcanic origin: composition, technology properties and problems in ceramic applications. Proceeding of the 1st Latin American Clay Conference, Funchal, 2, 219-224.

Duxson, P., Provis, J.L., Lukey, G.C., Mallicoat, S.W., Kriven,W.M., Van Deventer, J.S.J., 2005. Understanding the relationship between geopolymer composition, microstructure and mechanical properties. Colloids and Surfaces A: Physicochemical and Engineering Aspects, 269(1), 47-58.

Duxson, P., Fernández-Jiménez, A., Provis, J.L., Lukey, G.C., Palomo, A., van Deventer, J.S.J., 2006. Geopolymer technology: the current state of the art. Journal of Material Science, 42, 2917-2933.

Duxson, P., Provis, J.L., Lukey, G.C., van Deventer, J.S.J., 2007a. The role of inorganic polymer technology in the development of 'green concrete'. Cement and Concrete Research, 37, 1590-1597.

Duxon, P., Mallicoat, S.W., Lukey, G.C., Kriven, W.M., van Deventer J.S.J., 2007b. The effect of alkali and Si/Al ratio on the development of mechanical properties of metakaolin-based geopolymers. Colloid and Surface, 292, 8-20.

Ece, I.Ö., & Schroeder, P.A., 2007. Clay mineralogy and chemistry of halloysite and alunite deposits in the Turplu area, Balikesir, Tuekey. Clays and Clay Minerals, 55, 18-35.

Evans, I.S., 1970. Salt crystallization and rock weathering: a review, Rev. Geomorphol. Dyn. 19, 153-177.

Farmer, V.C., 1974. The Infrared Spectra of Minerals. Mineralogical Society, London.

Fernández-Jiménez, A., & Palomo, A., 2009. Nanostructure/microstructure of fly ash geopolymers (pp. 89-117). CRC Press/Taylor and Francis: Boca Raton, FL, USA.

Fletcher, R.A., MacKenzie, K.J.D., Nicholson, C.L., Shimada, S., 2005. The composition range of aluminosilicate geopolymers. Journal of the European Ceramic Society, 25(9), 1471-1477.

Gasparini, E., Tarantino, S.C., Ghigna, P., Riccardi, M.P., Cedillo-González, E.I., Siligardi, C., Zema, M., 2013. Thermal dehydroxylation of kaolinite under isothermal conditions. Applied Clay Science, 80-81, 417-425.

Gasparini, E., Tarantino, S.C., Conti, M., Biesuz, R., Ghigna, P., Auricchio, F., Riccardi, M.P., Zema, M., 2015. Geopolymers from low-T activated kaolin: implications for the use of alunite-bearing raw materials. Applied Clay Science, 114, 530-539.

Giannopoulou, I., & Panias, D., 2008. Structure, design and applications of geopolymeric materials. National Technical University of Athens, School of Mining and Metallurgical Engineering, Athens, Greece.

Goudie, A.S., 1977. Sodium sulfate weathering and the disintegration of the Mohenjo-Daro, Pakistan, Earth Surface Processes and Landforms, 2(1), 75-86.

Hajimohammadi, A., Provis, J.L., van Deventer, J.S.J., 2010. Effect of alumina release rate on the mechanism of geopolymer gel formation. Chemistry of Materials, 22(18), 5199-5208.

Harben, P.W., & Bates, R.L., 1990. Industrial minerals geology and world deposits. Metal Bulletin, London.

Heller-Kallai, L., & Lapides, I., 2007. Reactions of kaolinites and metakaolinites with NaOHcomparison of different samples (Part 1). Applied Clay Science, 35(1), 99-107.

Johnson, E.B.G., & Arshad, S.E., 2014. Hydrothermally synthesized zeolites based on kaolinite: a review. Applied Clay Science, 97, 215-221.

Kani, E.N., Allahverdi, A., Provis J.L., 2012. Efflorescence control in geopolymer binders based on natural pozzolan. Cement and Concrete Composite, 34, 25-33.

Khan, M. I., Azizli, K., Sufian, S., Man, Z., 2015. Sodium silicate-free geopolymers as coating materials: Effects of Na/Al and water/solid ratios on adhesion strength. Ceramics International, 41(2), 2794-2805.

Komnitsas, K., Zaharaki, D., 2007. Geopolymerization: a review and prospects for the minerals industry. Minerals engineering, 20(14), 1261-1277.

Krivenko, P.V., Kovalchuk, G.Y., 2007. Directed synthesis of alkaline aluminosilicateminerals in a geocement matrix. Journal of Material Science, 42, 2944-2952.

Küçük, F., & Yildiz, K., 2006. The decomposition kinetics of mechanically activated alunite ore in air atmosphere by thermogravimetry. Thermochimal Acta, 448, 107-110.

Kuzvart, M., 1984: Industrial minerals and rocks. Elsevier, Amsterdam, 454 pp. Annex 3

Laha, S. C., & Kumar, R., 2002. Promoter-induced synthesis of MCM-41 type mesoporous materials including Ti-and V-MCM-41 and their catalytic properties in oxidation reactions. Microporous and Mesoporous Materials, 53(1), 163-177.

Lee, W.K.W., & van Deventer, J.S.J., 2003. Use of infrared spectroscopy to study geopolymerization of heterogeneous amorphous aluminosilicates. Langmuir, 19, 8726-8734.

Lee, W.K.W., & van Deventer, J.S.J., 2004. The interface between natural siliceous aggregates and geopolymers. Cement and Concrete Research, 34, 195-206.

Marschner, H., 1978. Application of salt crystallization test to impregnated stone, in: UNESCO/RILEM International Symposium on Deterioration and Protection of Stone Monuments Reilure, Paris, 3.4, 1-15.

Mobasher, N., Bernal, S.A., Hussain, O.H., Apperley, D.C., Kinoshita, H., Provis, J.L., 2014. Characterisation of $Ba(OH)_2$-Na_2SO_4- blast furnace slag cement-like composites for the immobilisation of sulfate bearing nuclear wastes. Cement and Concrete Research, 66, 64-74.

Murray, H.H., & Keller, W.D., 1993. Kaolins, kaolins and kaolins. In *Kaolin Genesis and Utilization*, H.H. Murray, W. Bundy, and C. Harvey, eds., The Clay Mineral Society, Boulder, Colorado, 1-24.

Navarro-Rodriguez, C., Doehnea, E., Sebastian, E., 2000. How does sodium sulfate crystallize? Implications for the decay and testing of building materials. Cement and Concrete Research, 30, 1527-1534.

Oh, J.E., Clark, S.M., Monteiro, P.J., 2011. Determination of the bulk modulus of hydroxycancrinite, a possible zeolitic precursor in geopolymers, by high-pressure synchrotron X-ray diffraction. Cement and Concrete Composites, 33(10), 1014-1019.

Palomo, A., & Glasser, F. P., 1992. Chemically-bonded cementitious materials based on metakaolin. British ceramic. Transactions and journal, 91(4), 107-112.

Palomo, A., Fernández-Jiménez, A., Kovalchuk, G., Ordoñez, L. M., & Naranjo, M. C., 2007. OPC-fly ash cementitious systems: study of gel binders produced during alkaline hydration. Journal of Materials Science, 42(9), 2958-2966.

Palomo, A., Krivenko, P., Garcia-Lodeiro, I., Kavalerova, E., Maltseva, O., Fernández-Jiménez, A., 2014. A review on alkaline activation: new analytical perspectives. Materiales de Construcción, 64(315), 022.

Pereira, P. F., Caiut, J. M., Ribeiro, S. J., Messaddeq, Y., Ciuffi, K. J., Rocha, L. A., ... & Nassar, E. J., 2007. Microwave synthesis of YAG: Eu by sol–gel methodology. Journal of Luminescence, 126(2), 378-382.

Provis, J.L., 2013. Geopolymers and other alkali activated materials: why, how, and what? Materials and Structures, 47(1-2), 11-25.

Provis, J.L., & Bernal, S.A., 2014. Geopolymers and related alkali-activated materials. Annual Review of Materials Research, 44, 299-327.

Provis, J.L., Lukey, G.C., and van Deventer, J.S.J., 2005. Do geopolymers actually contain nanocrystalline zeolites? A reexamination of existing results. Chemistry of Materials, 17(12), 3075-3085.

Rashad, A.M., 2013. Alkali-activatedmetakaolin: a short guide for civil engineer - an overview. Construction and Building Materials, 41, 751-765.

Rees, C.A., Provis, J.L., Lukey, G.C., van Deventer, J.S.J., 2007. In situ ATR-FTIR study of the early stages of fly ash geopolymer gel formation. Langmuir, 23, 9076-9082.

Rowles, M., & O'connor, B., 2003. Chemical optimisation of the compressive strength of aluminosilicate geopolymers synthesised by sodium silicate activation of metakaolinite. Journal of Materials Chemistry, 13(5), 1161-1165.

Ruiz-Santaquiteria, C., Fernández-Jiménez, A., Skibsted, J., Palomo, A., 2013. Clay reactivity: production of alkali activated cements. Applied Clay Science, 73, 11-16.

Siddique, R., & Klaus, J., 2009. Influence of metakaolin on the properties of mortar and concrete: A review. Applied Clay Science, 43(3), 392-400.

Sitarz, M., Mozgawa, W., Handke, M., 1997. Vibrational spectra of complex ring silicate anions-method of recognition. Journal of molecular structure, 404(1-2), 193-197.

Sitarz, M., Handke, M., Mozgawa, W., Galuskin, E., & Galuskina, I., 2000. The non-ring cations influence on silicooxygen ring vibrations. Journal of Molecular Structure, 555(1), 357-362.

Van Jaarsveld, J.G.S., Van Deventer, J.S.J., Lorenzen, L., 1997. The potential use of geopolymeric materials to immobilise toxic metals: Part I. Theory and applications. Minerals Engineering, 10(7), 659-669.

Van Jaarsveld, J.G.S., Van Deventer, J.S.J., Lukey, G.C., 2003. The characterization of source materials in fly ash-based geopolymers. Materials Letters, 57(7), 1272-1280.

Winkler, E.M., &Wilhelm, E.J., 1970. Salt burst by hydration pressures in architectural stone in urban atmosphere. Geological Society of America Bulletin, 81(2), 567-572.

Yan, H., Xue-min, C., Mao, J., Le-ping, L., Xing-dong, L., Jin-yu, C., 2012. The hydrothermaltransformation of solid geopolymers into zeolites. Microporous and Mesoporous Materials, 161, 187-192.

Youssef, H., Ibrahim, D., Komarneni, S., 2008. Microwave-assisted versus conventional synthesis of zeolite A from metakaolinite. Microporous and Mesoporous Materials, 115, 527-534.

Zema, M., Callegari A.M., Tarantino, S.C., Gasparini, E., Ghigna, P., 2012. Thermal expansion of alunite up to dehydroxylation and collapse of the crystal structure. Applied Clay Science, 80-81, 417-425.

Winkler, E.M., &Wilhelm, E.J., 1970. Salt burst by hydration pressures in architectural stone in urban atmosphere. Geological Society of America Bulletin, 81(2), 567-572.

Yan, H., Xue-min, C., Mao, J., Le-ping, L., Xing-dong, L., Jin-yu, C., 2012. The hydrothermaltransformation of solid geopolymers into zeolites. Microporous and Mesoporous Materials, 161, 187-192.

Youssef, H., Ibrahim, D., Komarneni, S., 2008. Microwave-assisted versus conventional synthesis of zeolite A from metakaolinite. Microporous and Mesoporous Materials, 115, 527-534.

Zema, M., Callegari A.M., Tarantino, S.C., Gasparini, E., Ghigna, P., 2012. Thermal expansion of alunite up to dehydroxylation and collapse of the crystal structure. Applied Clay Science, 80-81, 417-425.

5 ALKALI ACTIVATION OF MIXTURES OF SULFATE-BEARING CLAY AND SANDSTONE SEWAGE SLUDGE

In this chapter, the sewage sludge derived by the cultivation of an ornamental stone, now simply dismissed, has been used as precursor in the AAMs preparation.

The aim of this study is to explore the features of an aluminosilicate multi-component system in the presence of NaOH alkaline as activator, along with the reaction products formed in the system. In particular, in this section, the effects of: i) addition of Pietra Serena sandstone sewage sludge (10%, 20% or 50% weight proportion, to sulfate-bearing clay; ii) molarity of the activating solution (4, 6 or 8M NaOH solution); and iii) curing temperature (85°C or 25°C) have been evaluated. The presence of CaO produced after dehydroxylation of sPS can modify the mechanical properties of the binder and the type and composition of the reaction products, leading to the development of hybrid alkaline cements (Garcia Lodeiro et al., 2013a). Moreover, CaO can react with sulfate to form calcium sulfo-aluminate hydrate phases, similar to those observed in the OPC system as ettringite (AFt compound) or monosulfate (AFm compound), etc. Hence, CaO presence in the reacting system could offer further paths to increase the sulfate uptake and storage in the solid products.

All the details of the preparation of the AAMs are reported in Table 3.3, § 3.2.1. The hardened products obtained from the different syntheses have been characterized from mechanical, physical-chemical and microstructural viewpoints. The results are summarized in Table 5.1.

From mechanical tests, it has been observed that pastes prepared by activating L02-MK with 8M NaOH and those prepared by mixing sPS_800 (10 wt%) with L02-MK at 8M NaOH do not develop mechanical strength after curing at 25°C (99% R.H.), even after 28 days of setting time. Whereas, when sPS_800 is at 50 wt% in the mix, the effect of curing at room temperature is significant after 20 hours and 7 and 28 days of setting (date related to samples cured at 7 and 28 days are not reported hereafter). On the other hand, it has been observed that when pastes are cured at 85°C, they harden after 20 hours only. For this reason, the results discussed in this chapter regard all the AAMs binders after 20 hours of curing. The work has been organized in three parts:

- in the first part, the effects of mixing sPS_800 (10, 20 or 50 weight proportion) to L02-MK in the alkali activation have been evaluated in terms of mechanical properties

and reaction products. The alkalinity of the solution has been chosen in order to promote N-A-S-H gel formation;

- in the second part, the effects of the molarity of the activating solution (4, 6 or 8M NaOH solution) have been evaluated;

- in the third part, the effects of sPS_800 in L02-MK with different molarities of alkaline activator and curing temperature (85°C or 25°C) have been evaluated.

TABLE 5.1. Scheme of results fior L02_sPS AAMs activated with NaOH solution, at different molarities and curing temperature.

Samples		Compressive strength (MPa)	Flexural strength (MPa)	New phases found by XRPD analysis
L02-100-8M_1D_85C	A	4.4 (1)	0.95 (5)	Gibbsite, thenardite
L02-90-sPS-8M_1D_85C	A	11.8 (9)	2.6 (4)	CAN, YUG
L02-80-sPS-8M_1D_85C	A,B	10.6 (9)	3.0 (5)	CAN
L02-80-sPS-6M_1D_85C	B	8.7 (5)	1.9 (1)	U-phase, CAN
L02-80-sPS-4M_1D_85C	B	4.5 (2)	1.5 (2)	Ettringite
L02-50-sPS-8M_1D_85C	A,C	10.3 (2)	3.0 (1)	U-phase, CAN, SOD, killalaite
L02-50-sPS-8M_1D_25C	C	0.9 (1)	0.12 (1)	CAN
L02-50-sPS-6M_1D_85C	C	8.6 (6)	1.5 (1)	U-phase, CAN
L02-50-sPS-6M_1D_25C	C	1.6 (4)	0.56 (3)	-
L02-50-sPS-4M_1D_85C	C	4.0 (3)	0.93 (8)	Zeo-P, Ettringite, CSH
L02-50-sPS-4M_1D_25C	C	1.16 (3)	0.38 (7)	Zeo A

A - Samples selected for determining the effects of mixing sPS_800 (10wt%, 20wt% or 50wt%) to L02-MK
B - Samples selected for determining the effects of the molarity of the activating solution (4, 6 or 8M NaOH solution)
C - Samples selected for determining the effects of molarities of alkaline activator and curing temperature (85 ºC or 25 ºC)

5.1 Study of the effect of Pietra Serena sewage sludge content

In this section, pastes made by mixing L02-MK and sPS_800 in different weight proportions (100/0, 90/10, 80/20 and 50/50) have been prepared. The molarity of sodium hydroxide solution has been fixed at 8M and the pastes have been cured at 85°C at 99% R.H for 20 hours.

Mechanical strength results

The mean values of three tests for flexural strength and six tests for compressive strength are reported in Table 5.1 and plotted in Figure 5.1.
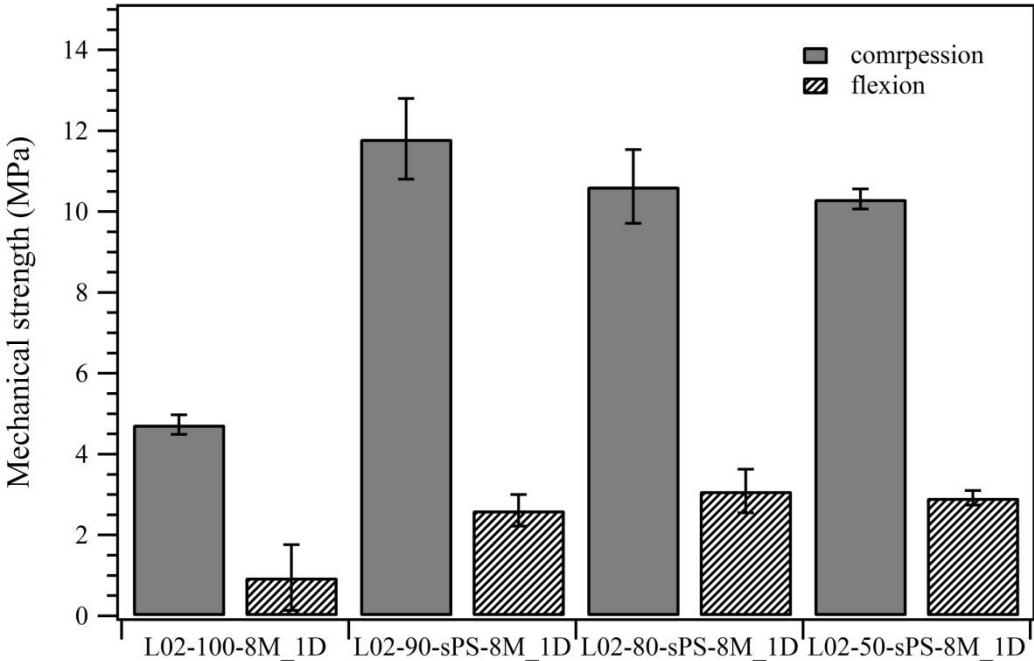
FIGURE 5.1. Compressive strength (filled bars) and flexural strength (pattern bars) in MPa for L02-MK and sPS_800 mixtures activated with 8M NaOH, after curing for 20 hours at 85°C.

Overall, the measured compressive strength values vary from a minimum of 4.7 (1) MPa to a maximum of 12.8 (1) MPa, and the flexural strength varies from 0.1 (8) to 3.0 (5) MPa. The lowest average values of strength are obtained for the sample prepared mixing only L02-MK and NaOH solution, L02-100-8M_1D. When 10 wt% of sPS_800 is added to L02-MK, the

value of compressive strength is 12.0 (1) MPa and flexural strength is 2.6 (3) MPa. This value is three times higher than that achieved for L02-100-8M_1D. At 20 wt% of sPS_800 addition to L02-MK, the average value of compressive strength is 10.6 (9) MPa and flexural strength is 3.0 (5) MPa, whereas, at 50 wt% of sPS_800, L02-50-sPS-8M_1D sample shows average values of compressive and flexural strengths of 10.3 (2) MPa and 3.0 (2) MPa, respectively. From these results, it is possible to observe that when L02-MK is activated only with NaOH, the values of mechanical strength are low. This could be attributed to a not complete reaction of metakaolin with the activating solution or to the presence of crystalline by-products in the hardened product, which could affect the mechanical properties.

After the addition of just 10 wt% of sPS_800 to the L02-MK, mechanical properties considerably increase. As reported in literature, addition of small amounts of Ca in low calcium systems could result in a remarkable improvement in strength (Dombrowski et al., 2007). As mentioned before, when sPS is heated at 800° C, calcium from the original dolomite and calcite is present mainly in the form of highly reactive CaO oxide that with hydration behaves as in cements, enhancing the mechanical performance of the final material (Yip et al., 2005; Yip et al., 2008). However, a further increase of sPS_800 content in the mix does not correspond to an increase of the average values of mechanical strength. In fact, L02-80-sPS-8M_1D and L02-50-sPS-8M_1D show similar values of mechanical strength. This fact might be related to the fast hardening of the slurry when more sPS_800 is mixed to L02-MK. The formation of a solid external crust makes difficult to put pastes into the molds, this affecting the strength values. This condition is more evident when 50 wt% of sPS_800 is added to the mixture as in the case of L02-50-sPS-8M_1D. A possible explanation could be given by the hydration of CaO, which is a well-known exothermic reaction. In fact, during mechanical mixing with the activating solution, slurries suddenly tend to harden when a temperature of around 50°C is reached.

XRPD

XRPD patterns of the sample prepared with only L02-MK and NaOH is reported in Figure 5.2. As a reference, the XRPD pattern of the L02-MK is also reported. As mentioned in § 2.1, after thermal treatments, only quartz and feldspars deriving from the original raw material are identified in the anhydrous materials. After activation, the binder shows a more or less marked halo between 20° and 35° 2θ, which is typical of the amorphous gel precipitation

(Palomo et al., 1999; Shi et al 2006; Garcia- Lodeiro et al., 2013a). Crystalline phases detected as reaction products in this sample are thenardite, Na_2SO_4, and gibbsite, $Al(OH)_3$. After curing, unmolded samples have been stored in chamber at 25°C and 99% R.H), before being broken. Crystals of thenardite have been also macroscopically detected as efflorescence on the surface of the sample just after some hours (Figure 5.3 a). After being removed from the surface, the crystals have been analyzed by XRPD and the result is reported in the graph of Figure 5.2 c.
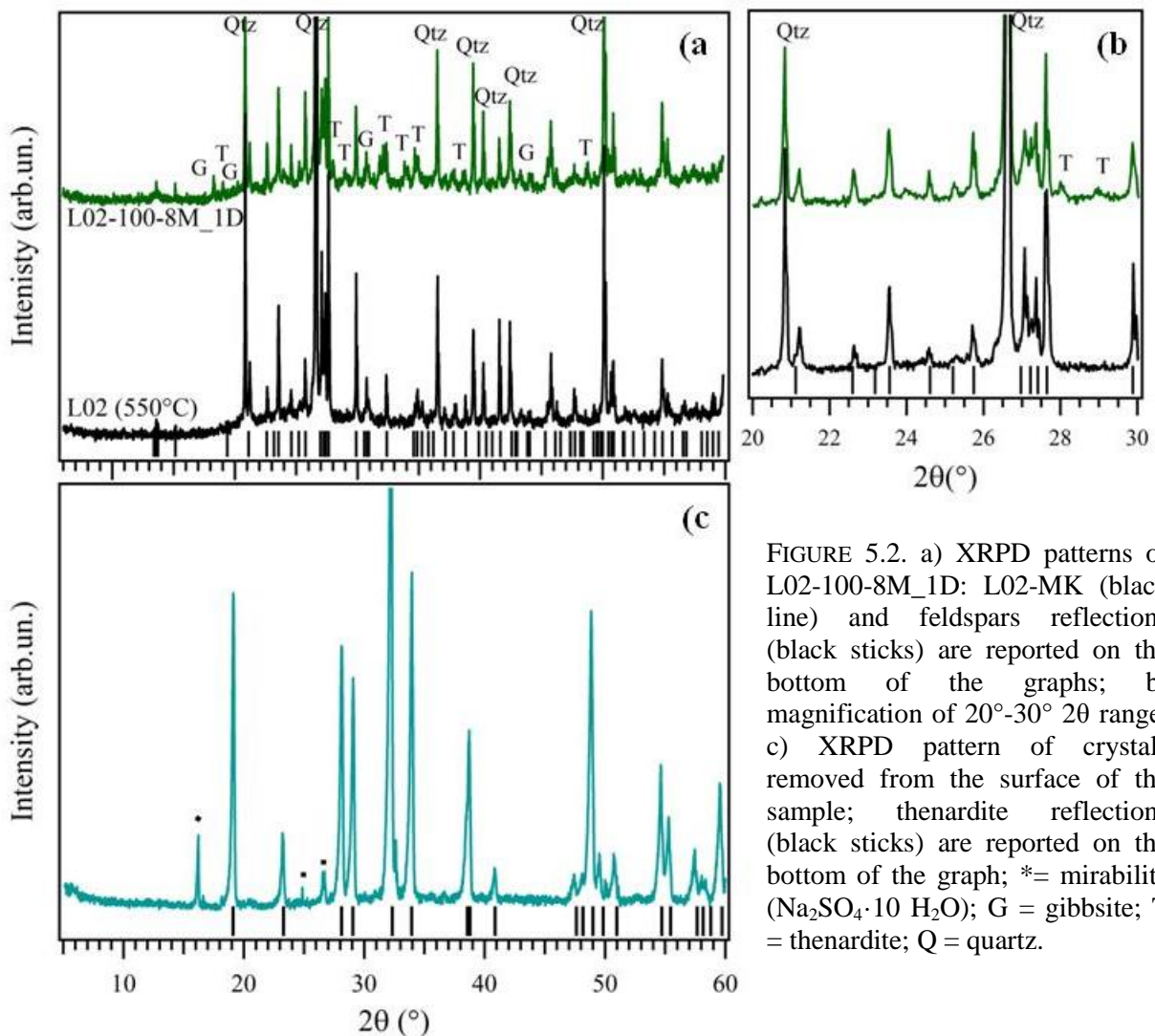
FIGURE 5.2. a) XRPD patterns of L02-100-8M_1D: L02-MK (black line) and feldspars reflections (black sticks) are reported on the bottom of the graphs; b) magnification of 20°-30° 2θ range; c) XRPD pattern of crystals removed from the surface of the sample; thenardite reflections (black sticks) are reported on the bottom of the graph; *= mirabilite ($Na_2SO_4 \cdot 10\ H_2O$); G = gibbsite; T = thenardite; Q = quartz.

The main reflections are referred to thenardite (PDF: 070-1541), even if some peaks could be attributed to an hydrated phase related to this mineral likely mirabilite (peaks around 16°, 18° and 23° 2θ), or some other polymorphs of thenardite, which commonly occurs during its

hydration as intermediate phase. Thenardite could precipitate directly from solution and it may be related to the evaporation rate of the sample after curing (Navarro et al., 2000).

FIGURE 5.3. L02-100-8M_1D binder (a) and L02-90-sPS-8M_1D binder (b) after curing at 85°C for 20h. After curing the sample have been stored in a chamber at 25°C and at 99% R.H.

The other reaction product detected by XRPD is gibbsite (PDF: 070-2038). The presence of this phase may suggest that the aluminum available from the starting materials is not entirely involved in the gel formation and part of it precipitates as crystals.

Figure 5.4 shows the comparison among the samples made using L02-MK and sPS_800 in different proportions. For comparison, the XRPD pattern of the anhydrous mixture of L02-MK and sPS_800 before the alkaline activation is reported. The phases detected are quartz, feldspars, plagioclase and, in minor amounts, lime derived from the decarbonation of calcite and dolomite. After alkaline activation, also in this mixtures, all samples show a signal related to the amorphous feature of aluminosilicate gel (e.g. Barbosa et al., 2000; Barbosa & McKenzie, 2003; Rowles & O'Connor, 2003; Fletcher et al., 2005; Dimas et al., 2009) recognizable by the hump between 25°-35° 2θ (Figure 5.4 a and b). CAN-type zeolites, in particular reflections correspondent to a sulfate-bearing cancrinite, named vishevite (PDF: 046-1333) are revealed in all samples containing sPS_800 showing the phase reflection at the position of 13.5°, 21.0°, 24.0° 2θ. Peaks related to a calcium aluminosilicate hydrate compound, identified as YUG-type zeolite (PDF: 039-1372) have been also detected. In the L02-50-sPS-8M_1D together to CAN-type zeolites, peaks related to SOD-type zeolites (in particular correspondent to a sulfate-bearing sodalite, PDF: 073-1734) has been identified. In this pattern U-phase (sodium calcium sulfo-aluminate, PDF: 044-0272) has been found. This phase belongs to AFm compound (hydrated calcium aluminates, commonly formed in cements systems), whit the difference that it contains sodium between the layers. Several peaks not well matched, related to a poorly crystalline calcium silicate hydrate phase (C-S-H)

as killalaite (PDF: 029-0332), are identified. C-S-H phases are not detected in the binder made with 10 wt% and 20 wt% of sPS_800. Generally, poorly crystalline C-S-H phases together with AFm compounds are recognized in cement-based systems composed of high aluminates cement or Portland cement and in the presence of sulfate and alumina (e.g. Li et al., 1996). In fact, it is well known that the main components of cements are poorly crystalline calcium-silicate-hydrate (C-S-H) gel and crystalline phases of portlandite, ettringite, and Al_2O_3-Fe_2O_3- (AFm) phases (such as monosulfate and monocarboaluminate) could be formed (Moon et al., 2015).

Generally, it is possible to observe that a small amount of sPS_800 in the mixture can control the efflorescence. Crystalline zeolites phase as CAN-type, in particular a sulfate-bearing cancrinite, are formed in all sample regardless the sPS content. When 50 wt% of sPS_800 is added to the mix beside to zeolites, calcium sulfo-aluminate product as U-Phase and poorly crystalline C-S-H phases are formed. According to literature, in traditional concrete it has been found that U-Phase is formed when the alkaline concentration is high (>4 M) (Li et al., 1996). The latter could have important influences, both favorable and unfavorable on the properties, performance and durability of the binders, producing expansion phenomena.
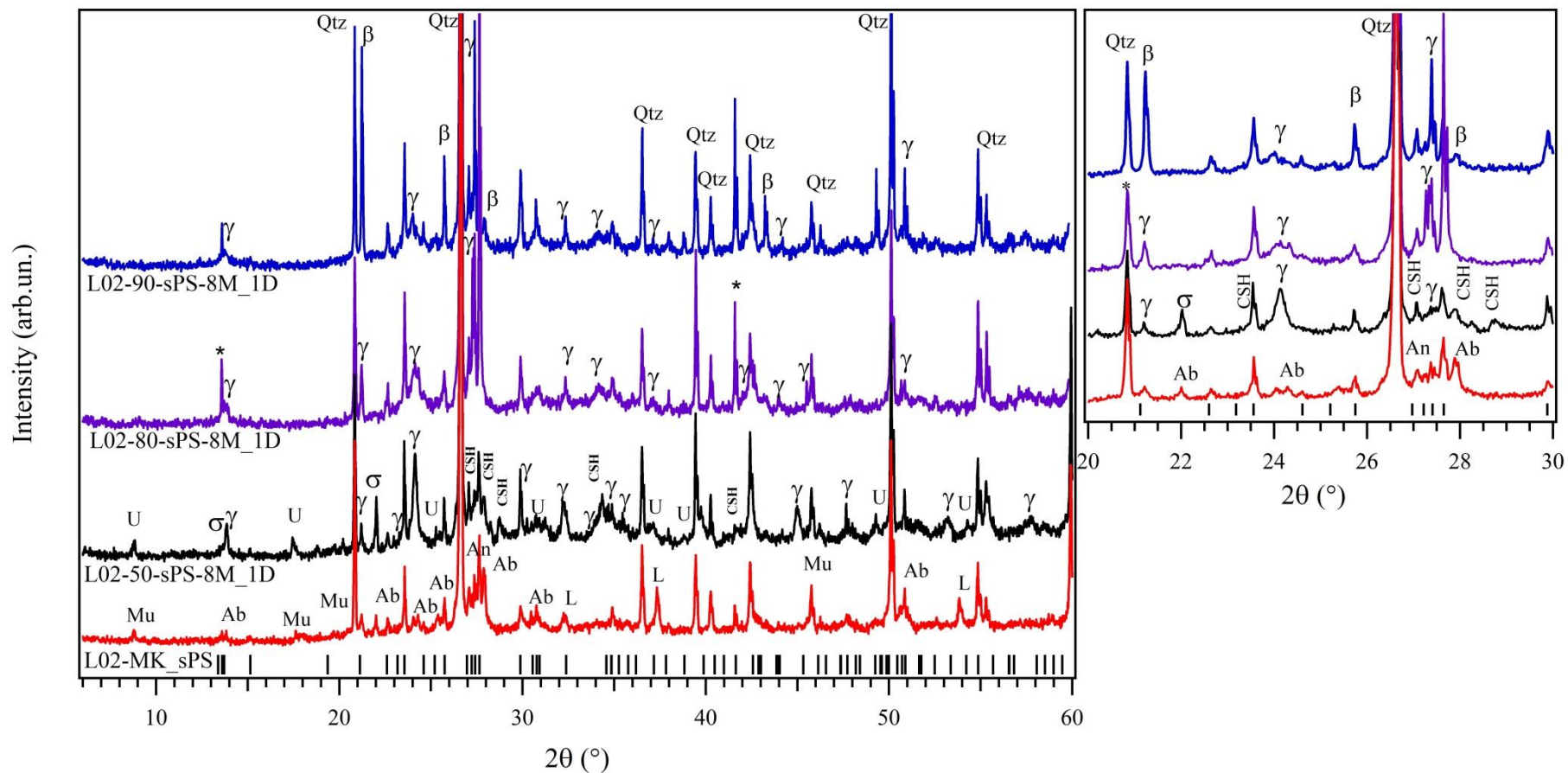
FIGURE 5.4. XRPD patterns of the samples L02-90-sPS-8M_1D, L02-80-sPS-8M_1D and L02-50-sPS-8M_1D; On the bottom for comparison, XRPD pattern of the L02_sPS mix after thermal treatment (red line). Black sticks represent the feldspars reflections. A magnification of 20°-30° 2θ range is reported on the right box. U = U-Phase $(NaCa_4Al_2O_6(SO_4)_{1.5}\cdot15H_2O)$; γ,* = CAN-type zeolites; CSH = killalaite; σ = SOD-typezeolites; β = YUG-type zeolite; Q = quartz; Mu = muscovite, Ab = albite; L = lime.

SEM-EDS

The cross sections of the AAMs products have been analyzed by SEM-EDS to ascertain the type of gel or gels formed in the different systems, with and without calcium. The micrograph of the L02-100-8M_1D, L02-90-sPS-8M_1D and L02-50-sPS-8M_1D are shown in Figure 5.5, Figure 5.6 and Figure 5.7 respectively.
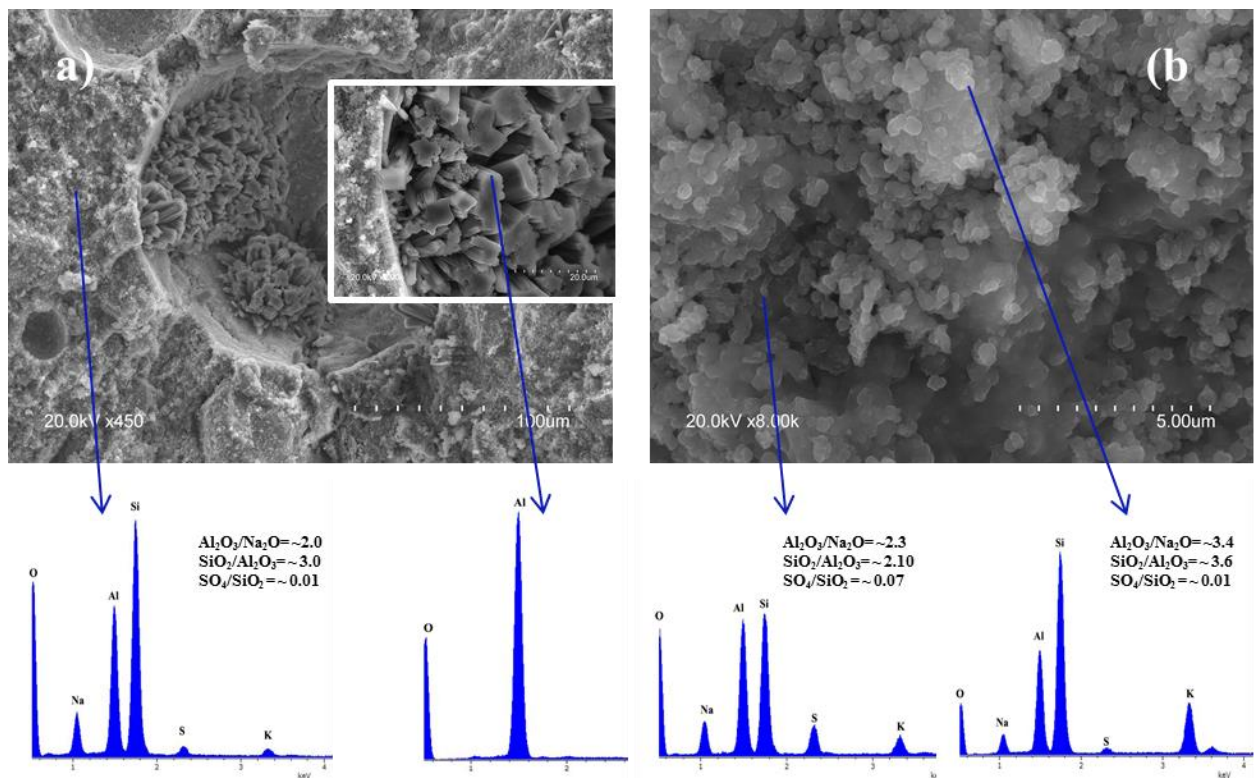
FIGURE 5.5. SE-Micrographs and EDS analyses of L02-100-8M_1D, after curing at 85°C for 20 hours.

At low magnifications (450x), Figure5.5a, the presence of heterogeneous porosity is evident. The micrograph shows spherical voids of 100 μm in size probably due to air bubbles trapped in the matrix during the synthesis. However, these pores result filled by several crystals, which are attributed to gibbsite (confirmed also by XRPD analysis) and they results spread overall the surface of the sample. In general, gibbsite crystals show a very large dispersion in growth morphology and crystal size when they grow from synthetic caustic soda solutions (Sweegers et al., 2001). A particular of the gibbsite crystals is reported at higher magnification in the insertion in Figure5.5a. However, the presence of crystals inside the voids should not influence the mechanical strength sity. Figure 5.5b shows a micrograph at

8.00 Kx of magnification, which revealed the matrix of the L02-100-8M_1D sample. This displays amorphous features, with the distinctive granular aspect of an N-A-S-H gel. Ultra-fine particles seem to be confined into isolated elements and partially bonded together. These morphological features of the gel have been found in zeolites systems at very early stages of crystallization (Chandrasekhar & Pramada, 2008) and could confirm the nature of N-A-S-H as amorphous precursor of zeolites.

From semi-quantitative EDS analyses of more than 50 points analysis, the matrix shows an average SiO_2/Al_2O_3 ratio of 3 (see Table 5.2), which appears higher with respect to the initial calculated SiO_2/Al_2O_3 molar ratio of 1.8 (see Table 3.3, § 3.2.1). This could be explained by the presence of gibbsite representing an index of a not complete reaction of the aluminum in the gel process, meaning that the gel is depleted in Al and is enriched in Si content. Micrographs of L02-90-sPS-8M_1D sample, at different length scales are reported in Figure 5.6. At 3.5 Kx the Figure 5.6a displays clearly the differences in microstructure of this sample with respect to L02-100-8M_1D sample. At this length scale, the amorphous features of the gel are confirmed. It is evident how the matrix shows a tendency to organize itself into parallel layers, a morphological feature related to metakaolin. Small agglomerates with a not well-defined morphology and with composition resembling that of thenardite are detected in the matrix, as reported in the insertion on the right side of the micrograph. At higher magnification, Figure 5.6b, it can be possible to notice that the gel is characterized by an inhomogeneous microstructure; some interconnected acicular crystals interrupt the continuity of the matrix. Their identification by EDS analysis results difficult because the small particles dimension. However, from EDS analyses reported below the micrograph, is possible to notice that the matrix and the crystals are very different in composition, except for the alumina content which is lower ($Al_2O_3/Na_2O = \sim 0.3$) with respect to the matrix ($Al_2O_3/Na_2O = \sim 0.6$) meaning that these crystals could be zeolites. At higher magnification (12 Kx), Figure 5.6c, and two types of morphologically distinguishable gels are recognizable: one more granular with concatenated spherical particles interconnected to create small clusters of aluminosilicate gel (left side of the micrograph), and another in which the arrangement in parallel planes is revealed. From EDS analysis, the SiO_2/Al_2O_3 molar ratio is the same in both side of the matrix.
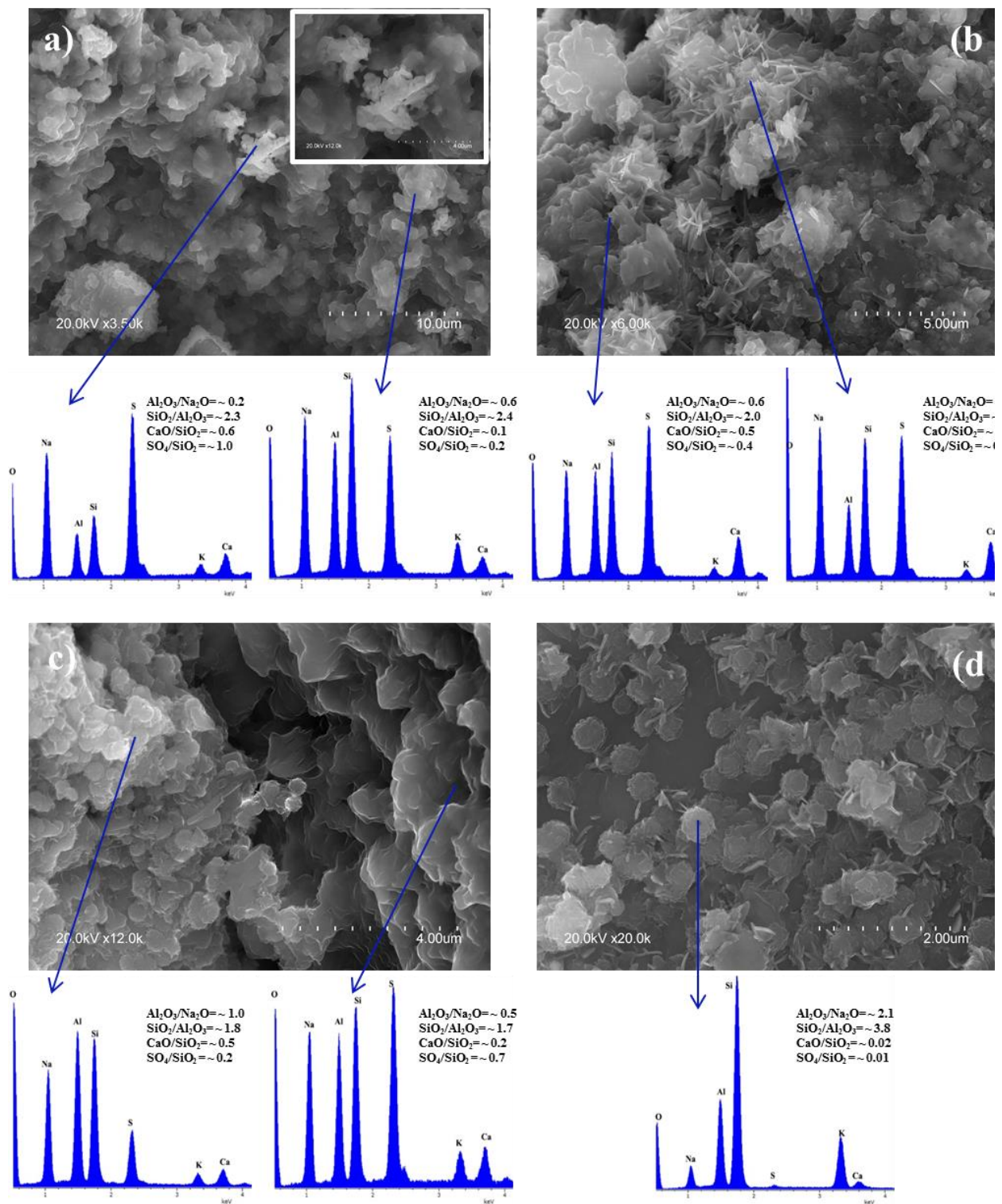
FIGURE 5.6. SE-Micrographs and EDS analyses of L02-90-sPS-8M_1D, after curing at 85°C for 20 hours

The left side seem to have more alumina, more calcium oxide and less sulfate content with respect to the right side. The average SiO_2/Al_2O_3 molar ratio of the matrix (calculate up to 50 points analyses) is overall around 3 while the theoretical average SiO_2/Al_2O_3 molar ratio calculated on the basis of reactive silica and alumina content in the original precursors, is around 2, meaning that this gel could be enriched in silica. Finally, at magnification of 20.0 Kx (Figure5.6d) in some portion of the sample, nanocrystals with spherical morphology and SiO_2/Al_2O_3 molar ratio resembling sodalites at the beginning of their formation have been detected. Their SiO_2/Al_2O_3 molar ratio is 3.8 and results higher with respect to the other part of the matrix, and calcium and sulfate are absent.

Figure 5.7 shows a series of micrographs relative to L02-50-sPS-8M_1D sample. At this enlargement (5.0 Kx) the analysis of the microstructure confirms the development of the amorphous gel, which is however, characterized by an inhomogeneous microstructure as confirmed by the subsequent images at higher magnification (Figure 5.7 b, c, and d). The contribution of CaO hydration is evidenced by the occurrence of some elongated particles not interconnected and distributed on the surface (Figure 5.7a). Figure 5.7c (at magnification of 12.0 Kx) shows a gel structure with needle-shaped elements, more or less 1 μm in size interconnected to several spherical particles that give rise to a quite porous microstructure. The spherical particles contain higher calcium oxide content (CaO/SiO_2 molar ratio of 3.0-4.0) and lower sulfate amount, as shown from EDS analysis reported in the graph below. Finally, at 20.0 Kx some spherical and tabular nanocrystals are also detected. Table 5.2 shows the oxides molar ratios of the analyzed samples. The EDS analyses shows no important differences in composition between the oxides molar ratio, and the sulfate results distributed in the whole matrix. At higher magnification (10.0 Kx), (Figure 5.7b) the gel structure appears made up by acicular fibers and several crystalline phases as small hexagonal prisms, which could resemble zeolites. Morphology of these crystals and the presence of calcium could suggest that they might be cancrinite zeolites (Barnes et al., 1999).

TABLE 5.2. Oxides molar ratio calculated by the average of EDS-analysis

Average molar ratio by EDS	Na_2O/Al_2O_3	Al_2O_3/Na_2O	SiO_2/Na_2O	SiO_2/Al_2O_3	CaO/SiO_2	SO_4^{2-}/SiO_2	SO_4^{2-}/Al_2O_3	SO_4^{2-}/Na_2O
L02-100-8M _1D	0.23	4.42	5.98	1.35	0.01	0.02	0.03	0.12
L02-90-sPS-8M_1D	1.56	0.64	1.84	2.86	0.16	0.23	0.66	0.42
L02-50-sPS-8M_1D	1.15	0.87	2.69	3.09	0.73	0.04	0.11	0.10
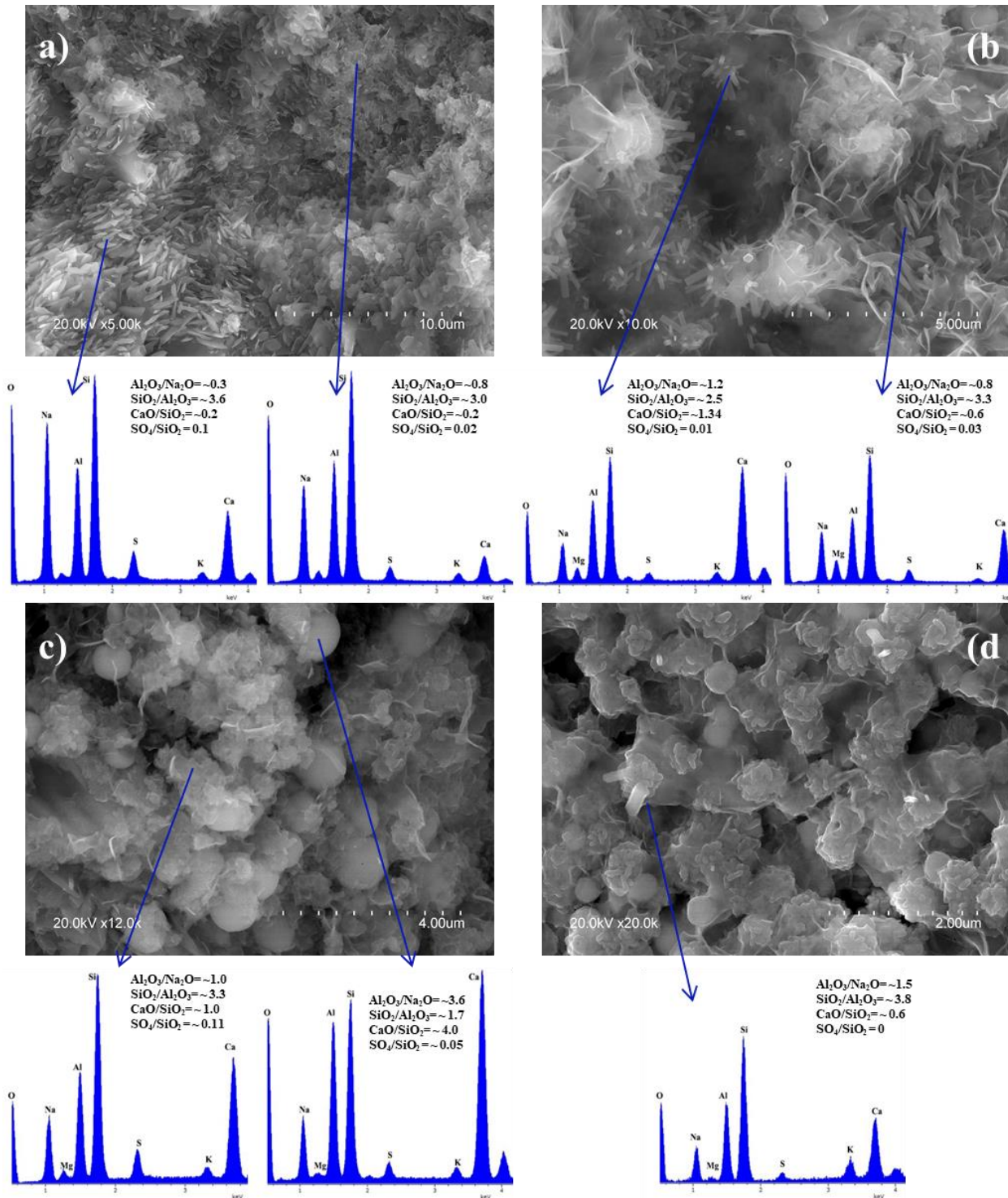
FIGURE 5.7. SE-Micrographs and EDS analyses of L02-50-sPS-8M_1D.

The acicular particles are distinctive of the early crystallization stages of calcium silicate hydrated compounds (C-S-H) (Taylor, 1986; Hranice, 2002) and a similar microstructure and composition are found in literature using sandstone sediments (Dong et al., 2014; Li et al., 2014). More exhaustive (over 30) EDS analyses have been conducted to determine the composition of the gel phases. Only for two samples, the Al_2O_3/SiO_2 and CaO/SiO_2 ratios have been plotted in Figure 5.8. The composition ranges which, according to the literature (Garcia-Lodeiro et al 2011; Pardal et al., 2009) characterize the main types of gels, (C-S-H, C-(A)-S- H, C-A-S-H, N-A-S-H and (N,C)-A-S-H), are also marked on the figure. As the graph in Figure 5.8a shows, L02-90-sPS-8M_1D sample exhibits a number of compositional clusters. While most of the points are positioned in the N-A-S-H and N-C-A-S-H gel ranges, a certain (much smaller) number of points are located in the C-A-S-H gel zone. The situation is different when more sPS is added to L02- MK, as reported for L02-50-sPS-8M_1D sample (Figure 5.8 b). Here, the points are clustered primarily in the ranges characteristic of high aluminum (N,C)-AS-H and C-A-S-H gels. A smaller cluster, have been also observed to lie within the C-(A)-S-H gel (hydration product) range. The findings confirmed that in this type of multi-component systems the main reaction product was a mix of gels: C-(A)-S-H (due to the presence of Ca from sPS_800) and C-A-S-H as well as (N,C)-A-S-H (from the activation of alkaline aluminosilicates). The precipitates were not pure gels, but rather products containing other post-dissolution ionic species. For example in the N-AS-H-like gel, much of the original sodium was replaced by calcium as result of well-known ionic exchange mechanisms (Garcia- Lodeiro at al., 2010; Garcia- Lodeiro et al., 2011) The resulting product is an intermediate C-A-S-H gel. Furthermore, the co-existence of C-A-S-H and N-(C)-A-S-H gels and the prevalence of one over the other depend on the calcium content and the alkalinity of the system (Yip et al., 2005; Yip et al., 2008).
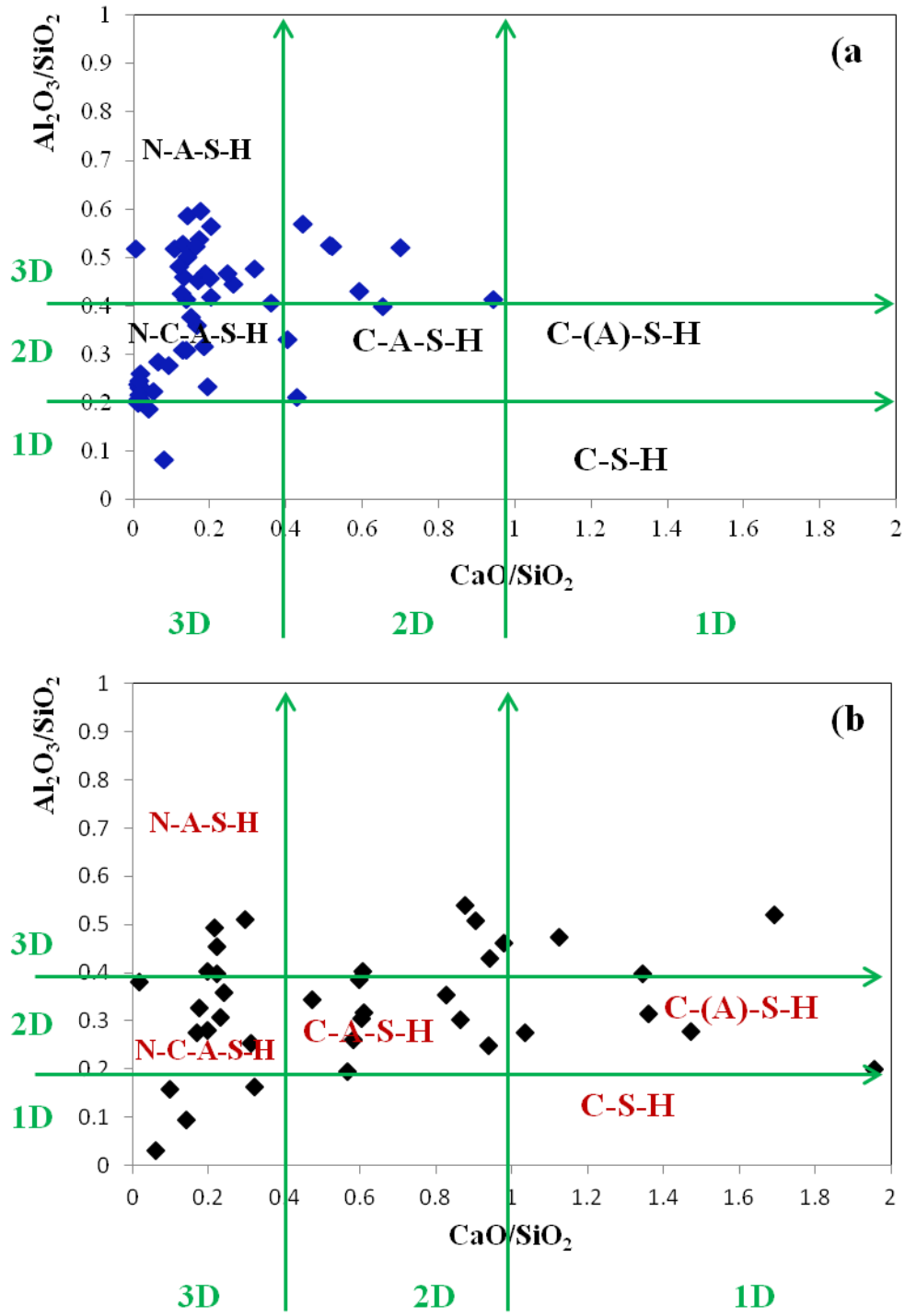
FIGURE 5.8. Al$_2$O$_3$/SiO$_2$ vs. CaO/SiO$_2$ ratios for gels precipitating in hybrid cements (based on EDS findings), a) L02-90-sPS-8M_1D; b) L02-50-sP-8M_1D

^{27}Al AND ^{29}Si MAS NMR

In order to evaluate the structure at short-range length scale of the various gels formed for the alkali-activated binders, MAS-NMR spectroscopy was used for examining the local environment of ^{29}Si and ^{27}Al(see Figures 5.9, 5.10).
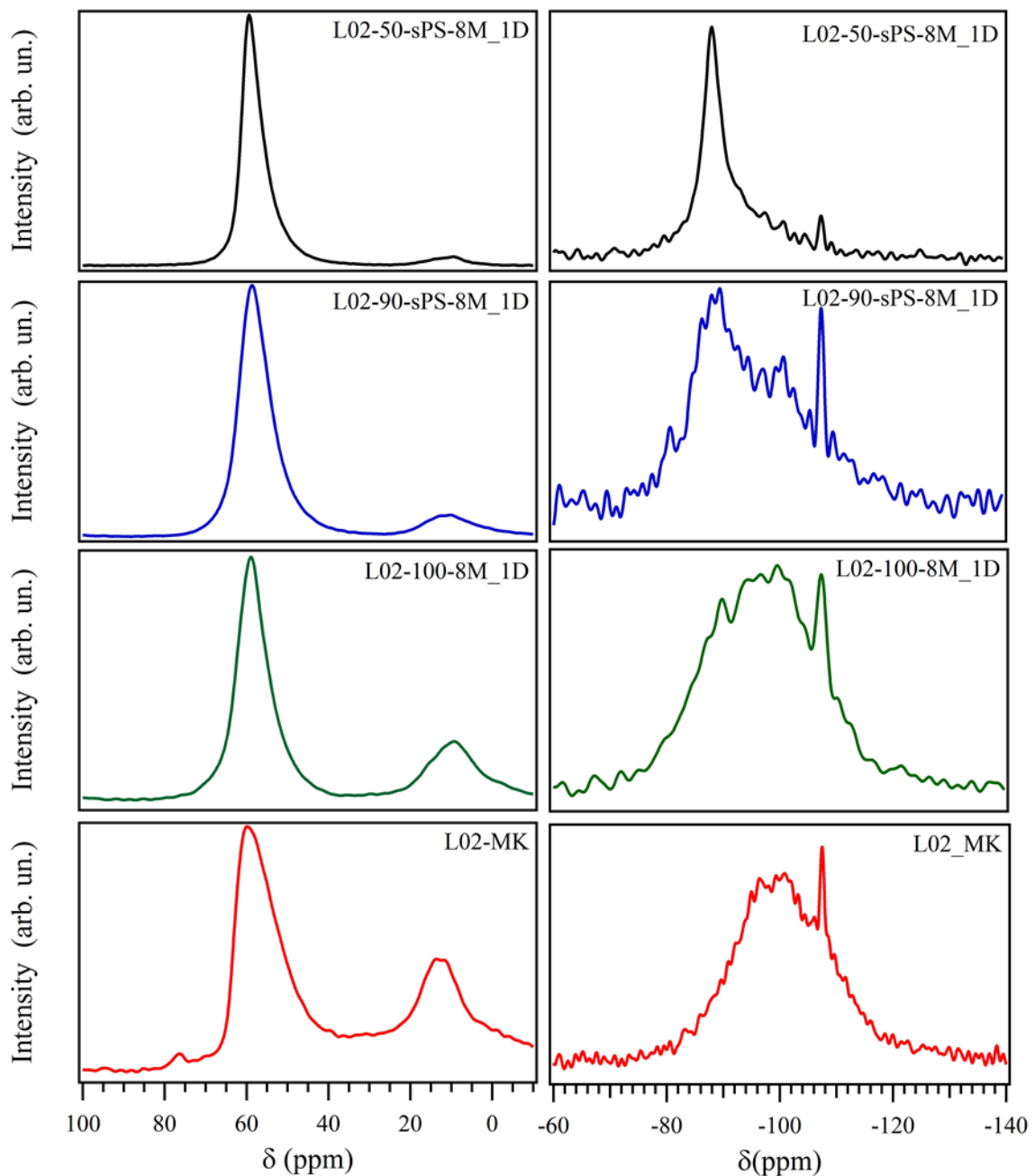
FIGURE 5.9. ^{27}Al and ^{29}Si MAS-NMR spectra of: L02-100-8M_1D; L02-90-sPS_8M_1D; L02-50-sPS-8M_1D and L02-MK..

The ^{27}Al MAS-NMR spectra (Figure 5.9 a), for the L02-MK before activation reveals the presence of Al in tetrahedral (δ = 70–50 ppm), at little fivefold (δ = 30–40 ppm) and octahedral (δ = -20-0ppm) coordination. This signal reflects the amorphous nature of the starting metakaolin in which tetrahedrally coordinated Al species are the dominating components; whereas the fractions of the other different coordination states are lower (Engelhardt & Michel 1987; Rocha & Klinowski 1990; Buchwald & Kaps 2007). The relative intensity of octahedral aluminum can be associated to the presence of Al_2O_3 from the dehydroxilation of alunite (Nielsen et al., 2007).

The Al(4Si) sites in alkali activated pastes exhibit ^{27}Al chemical shifts in the range 50-65 ppm. This range suggests that AlO_4 tetrahedra are present and likely surrounded by three or four silicon atoms. The symmetry of this signal and the fact that it is narrower than in the resonances of the starting materials, suggests its possible association with tetrahedral aluminum, Al(IV). This resonance at 58.8 ppm, probably due to an overlay of tetrahedral Al within the framework of the zeotypes, with octahedral Al present in the N-A-S-H, (N,C)-A-S-H and C-A-S-H type cementing gels described in the literature (Engelhardt & Michel, 1987, Garcia-Lodeiro et al., 2015). Furthermore, penta-coordinated aluminum is not detected in any of the alkali-activated samples. This observation strongly indicates that almost all of the Al(V) species in the starting materials have been dissolved during the alkaline activation process. However, a little signal of Al (VI) is observed. In L02-MK-100-8M-1D sample, the signal appears at 9.8 ppm and can be associated to a crystalline Gibbsite (Isobe et al., 2003), also detected by XRPD. However in the sample with calcium from sPS (samples L02-MK-90-sPs-8M-1D and L02-MK-50-sPs-8M-1D), the signal has low intensity and appears near to 10.6 ppm associated to the formation of AFm phases as U-Phase.

The ^{29}Si MAS NMR spectra of L02-MK shows a broad and poorly defined signal, reflecting the structural disorder and heterogeneous distribution of the silicon atoms in the dehydroxylated clay. The sharp peak at -107 ppm is associated to the presence of quartz (Engelhardt, & Michel, 1987; MacKenzie, & Smith, 2002) in the original material, and this peak not change in the alkali activated samples. A significant change is observed in the appearance of the resonances for the blends after alkali activation, an indication that chemical and structural transformations take place in the process. The presence of calcium in the mixtures gives rise to sharper signals, which shift towards less negative values, this suggests the formation of less polymerized gels (N-A-S-H, (N,C)-A-S-H and C-A-S-H), (Garcia-Lodeiro et al., 2015). Although, the partly overlapping signals reveal the existence of a

number of distinct features, they cannot be readily interpreted due to the overlap with resonances attributed to silicon sites in the unreacted materials, the cementitious gel/gels, and the zeolites formed during alkali activation.

In order to facilitate the interpretation from ^{29}Si MAS NMR, the experimental spectra have been deconvoluted (Table 5.3 and Figure 5.10). Thus, the spectra are deconvoluted using, when is possible the same number of peaks. The assignment of the peak is not easy especially in the samples with the highest content of calcium. For example, the signal at -89 ppm that in the sample L02-100-8M_1D can be associated with Q^4(4Al) units from the N-A-S-H gel-like structures and/or zeolites, in the L02-90-sPS_8M_1D, and in the L02-50-sPS-8M_1D samples may also be due to the presence of Q^3(3Al) units. In original sample, seven signals are detected. L02-MK can be interpreted in terms of resonances associated to highly (Q^4 (mAl)) units which can be assigned to Q^4 (mAl) structural units of the quartz deriving from the original precursor (Engelhardt, & Michel, 1987; MacKenzie, & Smith, 2002), to the sanidine (Anbalagan et al., 2009).and to metakaolinite (Garcia-Lodeiro et al., 2015). In the sample L02-100-8M_1D eight signals are detected, some of which are new signal that appear at approximately −89.0, −93, −96, −99 and −103 ppm (see Figure 5.10 and Tables 5.4). According to earlier ^{29}Si NMR studies of aluminosilicate frameworks (Engelhardt, & Michel, 1987; MacKenzie, & Smith, 2002), these can be assigned to Q^4(4Al), Q^4(3Al), Q^4(2Al), Q^4(1Al) and Q^4(0Al) respectively from the formation of N-A-S-H. Signal at -86.6 ppm can be associated to unit Q4(4Al) in sodalite-type zeolites structures. Obviously, the relative intensities assigned to each Q4 (mAl) structural unit in the reaction products are not precisely accurate since unreacted materials also contributes to these values.

In the sample L02-90-sPS-8M_1D a different shape in the spectrum profile is observed, and an intense peak at -89.1 ppm could be attributed to Q^4 (mAl) typical of N-A-S-H gel. Peaks at -85.9 and -97.0 ppm could be related to Q^3(mAl) for C-A-S-H gel but also Q^4(mAl) units in N-A-S-H gel. According to literature, sodalite has a chemical shift of approximately -85 ppm and cancrinite to -87.3 ppm, due to different Si/Al ratio. The contribution of theses zeolitic phase to the signal at -85 and -89 could be also considered. Sodalite type phases have not been observed by XRPD in this sample, however the presence of small amounts (below XRPD detection limit) of this zeolite cannot be excluded, as in zeolite synthesis it has already been observed that SOD-type zeolite transform into CAN-type one (Reyes et al., 2013).
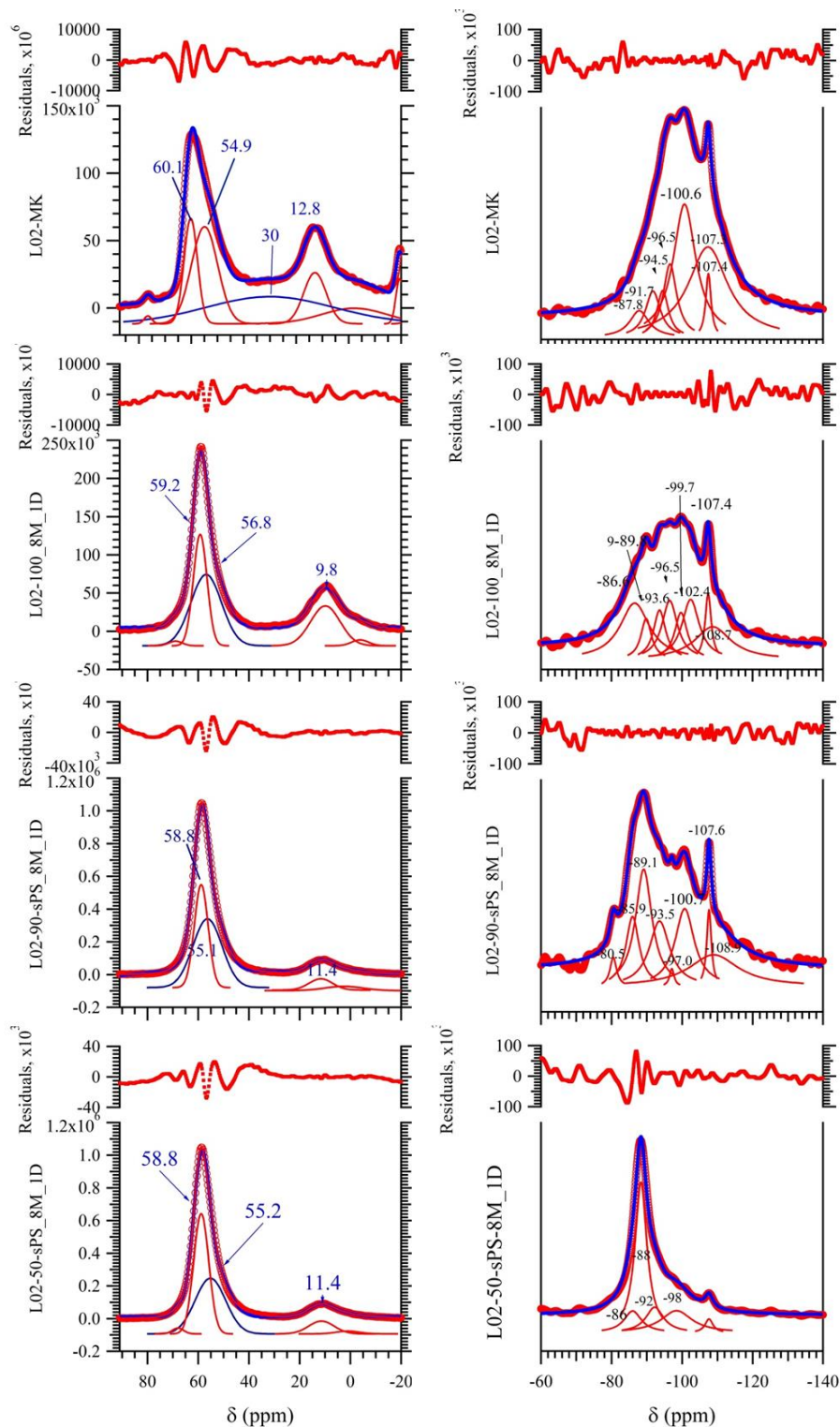
FIGURE 5.10. ^{27}Al and ^{29}Si MAS NMR spectra deconvolution of L02-100-8M_1D; L02-90-sPS-8M_1D; L02-50-sPS-8M_1D and L02-MK. Blue line = simulated spectrum using a number of Gaussian signal.

In the sample L02-50-sPS-8M_1D resonances from $Q^4(mAl)$ and $Q^3(mAl)$ silicate sites may overlap; therefore the correct assignment isdifficult, (see tentative assignment in Table 5.3).

In any case the silicon concentration in the framework is not sufficiently high to observe resolved resonances for -99 and -97 ppm Q^4(1Al) and Q^4 (2Al). The intense signal at -88.1 can be associated to the formation of larger amount of C-A-S-H gel but more likely to the presence of cancrinite.

TABLE 5.3. ^{29}Si NMR Chemical shift (δ) values (ppm) on ^{29}Si spectra shifts to Q^n (nAl) environments.

		Q^1, Q^2	Q^4 (4Al) Q^3 (3Al) Q^2 (0Al)	Q^4 (4Al) Q^3 (2Al)	Q^3 (1Al)	Q^4 (3Al) Q^3 (0Al)	Q^4 (2Al)	Q^4 (1Al)	Q^4 (0Al)	Q^4 (0Al)	Q^{4a}
L02-MK	position (ppm)	-	-87.8(3)	-	-92.0(3)	-94.5(2)	-96.5(3)		-100.6(1)	-107.3(2)	-107.4(0)
	Area (%)		0.56		7.50	5.80	10.76		32.96	38.76	3.63
L02-100-8M_1D	position (ppm)	-	-86.6(1)	-89.8	-	-93.7(1)	-96.5(1)	-99.7(1)	-102.4(2)	-107.4(0)	-108.7(5)
	Area (%)		28.94	7.46		10.43	15.89	10.27	18.05	6.90	2.06
L02-90-sPS-8M_1D	position (ppm)	-80.5(1)	-85.96(3)	-89.1(3)		-93.6(2)	-97.1(3)		-100.7(1)	-108.9	-107.6(2)
	Area (%)	<1%	12.22	25.36		17.64	<1%		19.68	20.68	4.64
L02-50-sPS-8M_1D	position (ppm)	-79.7(3)	-86	-88.2(2)		-93.0(3)	-97.5(1)		-100.5(2)		-107.616
	Area (%)	<1%	<1%	65.89		22.53	<1%		11.57		<1%

[a] Signal associated with quartz (δ = -107 to -108 ppm) and fully polymerized amorphous silica (Engelhardt & Michel, 1987; McKenzie & Smith, 2002)

LEACHING TEST

Data from leaching test hereafter discussed are reported in Table 3.4, § 3.2.2. The results have shown that the quantity of sulfate anion (expressed in wt%) measured in solution, for the sample without sPS_800, is 92%wt meaning that all SO_4^{2-} present in the initial mixture reacts to sodium and precipitates as thenardite when the excess of water evaporates. Addition of sPS_800 in the mix causes a positive effect in sulfate retention by the solid AAMs. In fact, adding just 10 wt % of sPS_800, the sulfate retention is of 54 wt% while adding 50 wt % of sPS_800, the sulfate retention shows a value of 69 wt %. It is no easy to understand where sulfate could be retained. It could be trapped into zeolites structures, as in the case of L02-90-sPS-8M_1D in which CAN-type zeolites have been found (as confirmed also by XRPD). However, as shown by SEM-EDS analysis some sodium sulfate it has been also identified in the sample, meaning that 10 wt % of calcium is not enough to avoid the formation soluble sodium sulfate. In the L02-50-sPS_8M sample, the retention of sulfate is higher and in this case together with CAN-type zeolites, calcium sulfo-aluminate hydrates compound are detected. These compounds could be the vehicles able to reducing sensibly the sulfate leaching due to the reaction between SO_4^{2-} and CaO in this system. However, it cannot be excluded also that the sulfate is retained by the amorphous gel.

FT-IR

Figure 5.11 shows the spectra from L02-MK binder and L02-sPS mixed binders, before (dashed curves) and after water leaching (bold curves). For comparison, spectra of anhydrous L02-MK and sPS_800 in FT-ATR are reported in the insertion. Features common to all spectra are the hump at 1640 cm^{-1}, ascribable to H-O-H bending vibration and the bands relater to crystalline phases as quartz and feldspars, from the original raw materials, which do not take part to the reaction. The presence of quartz in the original raw materials, give rise to a series of bands at 1080 cm^{-1}, 796- 779 cm^{-1} (double band), 697 cm^{-1} and 460 cm^{-1}. Also feldspars show a broad bands in the region between 1000 cm^{-1} and 1100 cm^{-1}, and to lower frequencies at 727 cm^{-1}, 638 cm^{-1}, 580 cm^{-1}, 540 cm^{-1} (Harris et al., 1989; Criado et al., 2010; Xu et al., 2003). All these phases are formed by tetrahedral of Si and Al with different structural arrangements, causing an overlapping of the different vibration modes.
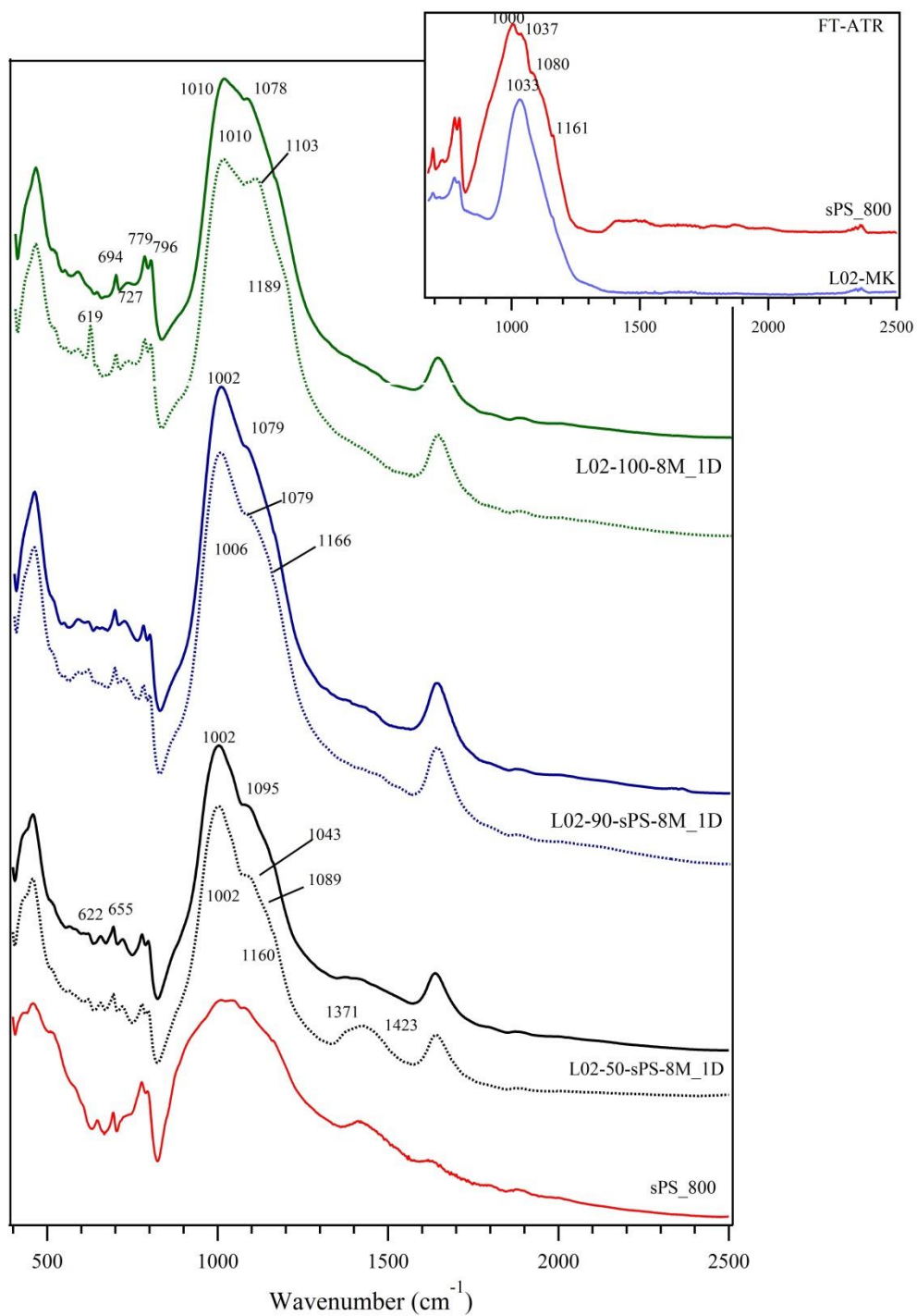
FIGURE 5.11. FT-IR spectra of L02-100-8M, L02-90-sPS-8M_1D and L02-50-sPS-8M_1D; dotted lines represent spectra before leaching tests, bold lines represent the spectra after leaching test

.

All samples show the main peak centered at 1010-1000 cm^{-1} that is normally related to the asymmetric stretch of the Si-O-T bonds, where T is Al or Si in tetrahedral coordination.

The shift of these peaks from higher wavenumber in the L02-MK (at 1037 cm^{-1}) to lower wave number in the AAMs (1000 cm^{-1}) has been established as the evidence of the sign of the aluminosilicate phase and indicates the formation of the aluminosilicate amorphous gel (Lee &van Deventer, 2003; Fernández-Jiménez & Palomo, 2005).

All samples show another evident peak in the in the range between 1079 and 1095 cm^{-1}, that is attributed to the aluminosilicate phase as quartz and feldspars. Regarding the sulfate vibration modes, the fundamental diagnostic absorption band positions related to the SO_4^{2-} are theoretically at 1030 cm^{-1} and 1170-1086 cm^{-1} for the symmetric and asymmetric stretching modes respectively, while the most important deformation related to symmetric and asymmetric bending vibration are at 475 cm^{-1} and 632-605 cm^{-1} respectively (Ross, 1974). In the L02-100-8M_1D spectrum, thenardite is revealed by one peak at 619 cm^{-1} that disappears after water leaching and another peak at 1103 cm^{-1} related to vibration modes of the S-O bonds, which is shifted towards slightly lower frequencies (at 1078 cm^{-1}) after leaching, and finally, a shoulder at 1189 cm^{-1}. The latter, may be attributed to sodium sulfate polymorphs (e.g. mirabilite), and it disappears after leaching, indicating the dissolution of this phase in water (Farmer, 1974; Ross, 1974; Navarro et al., 2000; Lane 2007; Criado et al, 2010). Peaks from gibbsite (detected also by XRPD) are not visible as they are in the range of 1010-1020 cm^{-1} (Kloprogge et al., 2002; Balan et al., 2006) therefore within the main Si-O-T wavenumber region.

The spectrum of L02-90-sPS-8M_1D shows two main peaks at 1006-1002 cm^{-1} and 1080 cm^{-1}, representative of the amorphous aluminosilicate gel structure and the aluminosilicate phase present from raw materials. The overall region appears sharper with respect to the sample without sPS_800, suggesting more ordered structure of the gel. The occurrence of the hump at 1166 cm^{-1} is related to SO_4^{2-} asymmetric stretching vibration, which is evident also after water leaching. This band has lower amplitude after leaching, however its presence suggests that sulfate is still inside the sample, although no new crystalline phase has been detected by XRPD. Different is the situation when more sPS_800 is added to the L02-MK, as shown by L02-50-sPS-8M_1D sample. The bands between 1000 cm^{-1} and 1160 cm^{-1} became sharper with respect to those showed for the sample L02-90-sPS-8M_1D and three main bands are revealed at 1043 cm^{-1}, 1090 cm^{-1} and 1160 cm^{-1}. The presence of the small band at 1043 cm^{-1} has been attributed to quartz and silicate minerals from the sPS_800, which could

117

contribute to increase of the amount of unreacted material. The peak at 1095 cm^{-1} is shifted to lower frequencies, at 1089 cm^{-1} after water leaching. In addition, here, the hump at 1160 cm^{-1} attributed to SO_4^{2-} asymmetric stretching vibration remains unchanged, confirming that most of the sulfate present form alunite is still in the matrix of the sample.

Only for L02-50-sPS-8M_1D, two peaks at 622 cm^{-1} and 655 cm^{-1} have been detected and they can be attributed to cancrinite like minerals.

Generally, the IR spectra of these samples confirmed the formation of alkaline aluminosilicate gel, as the main T-O stretching band is shifted toward lower frequencies with respect to the same peak in metakaolin. When L02-MK is activated in absence of sPS_800, the band related to the SO_4^{2-} vibration are mainly attributed to soluble sodium sulfate phases, which disappear after washing this sample. The hump associated to SO_4^2 vibration in the sample with 10 wt% of sPS_800 is visible after water leaching even if it appears sensibly reduced due to the loss of a percentage of soluble sodium sulfate that might be formed and leached out. Finally, when 50 wt% of sPS_800 is added to the mix, the T-O region became sharper and the hump related to SO_4^2 vibration does not change after water leaching, meaning that the solubility percentage of sulfate is reduced.

5.2 Study of the effect of the molarity of NaOH activator

In this section mixtures of L02-MK and sPS_800 (80/20 wt%) have been activated by using NaOH solution at 4M, 6M, and 8M. Pastes have been cured for 20h at 85°C at 99% R.H. conditions.

Mechanical strength

The mean values of three tests for flexural strength and six tests for compressive strength are reported in Table 5.1 and plotted in Figure 5.12. As shown from the graph the results highlight a positive trend related to the increase of molarity of the activating solution. Sample activated with 4M NaOH solution shows the lowest value of compressive and flexural strength with 4.5 (2) and 1.5 (2) MPa respectively.
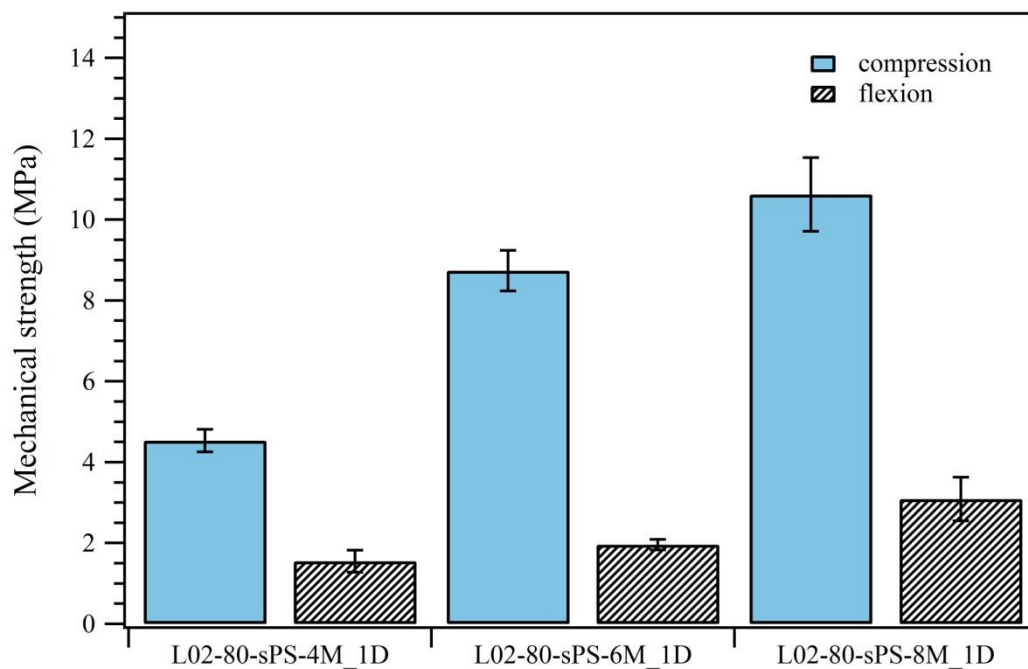
FIGURE 5.12. Compressive strength (filled bars) and flexural strength (line bars) of the L02-80-sPS binders, activated with 8M, 6M and 4M NaOH solutions, after curing at 85°C and 20 hours
.

L02-80-sPS-6M_1D sample shows a value of compressive strength of 8.7 (5) MPa and flexural strength of 1.9 (1) MPa. Thus, when the alkalinity of the NaOH solution rises to 6M the mechanical strength shows values two times higher. Finally, the sample activated with 8M

NaOH solution, shows average value of compressive and flexural strength of 10.6 (9) MPa and 3.0 (5) MPa respectively.

As reported in literature, generally the optimal alkalinity of the NaOH solution for metakaolin and fly ash system is estimated at 8M (Duxson et al., 2005b, Fernández-Jiménez & Palomo, 2005). In lower calcium system, lower alkalinity of the activating solution may adversely affects the mechanical properties of the cements obtained, because the ionic strength generated in the binder-activating solution system is not high enough to satisfactorily hydrolyze the silicon and aluminum present in the starting materials. This fact could lead to an increase of the unreacted materials and indeed, the reaction degree of the reaction of metakaolin with NaOH solution increases with the alkali concentration.

XRPD

Phases analysis of these AAMs is reported in Figure 5.13. Quartz and feldspars, deriving from the original raw materials, are present in all samples. All patterns display a halo around 20°-35° 2θ which is indicative of the occurrence of the amorphous phase. Observing all three patterns, this halo appears slightly less pronounced in L02-80-sPS-4M_1D sample, meaning that the amount of amorphous phase formed could be lower with respect to the other samples. The main crystalline product at 4M sample is ettringite ($Ca_6Al_2(SO_4)3(OH)_{12}·26H_2O$, PDF: 041-1451), which is stable at these alkaline concentrantion, as reported by Li et al.(1996). Reflections related to calcium-silicate-hydrate compound (PDF: 043-1488) have also been identified.

The XRPD pattern of L02-80-sPS-6M_1D sample, shows similarly to the other samples an halo related to the amorphous phase, U-phase (sodium calcium sulfo-aluminate phase, PDF: 044-0272) has been identified together with CAN-type zeolites, in particular a sulfate-bearing cancrinite, named vishevite (PDF: 043-1333). Some reflections at 21° and 28° 2θ are related to a sulfate of calcium and sodium, named wattevillite (PDF: 041-1360). Finally, at 8M NaOH, the L02-80-sPS-8M_1D sample reveals peaks which are indicative of CAN type zeolite (PDF: 043-1333), as only crystalline product in this sample. According to literature, U-Phase is stable at 6M in cement based-system composed by high aluminate cement or in presence of high proportion of Na_2SO_4 (Li et al., 1996). As well as ettringite, also U-Phase crystals could have an opposite influence on mechanical strength depending on if they are formed during the plastic state of binder or after concrete has set (Katsioti et al., 2009).

However, their presence after one day might indicate that they are formed in the first stage of the hydration process of these binders, which is comparable with the same process, which occurs in OPC cementitious systems (e.g. Gougar et al., 1996). Moreover, in literature many examples (e.g., Shi, 1999; Kovalchuk et al., 2007; Najafi & Allahverdi, 2009; Criado et al., 2010) of alkali activation of fly ash as well as metakaolin at higher molarity confirm the occurrence of zeolites as secondary reaction products.
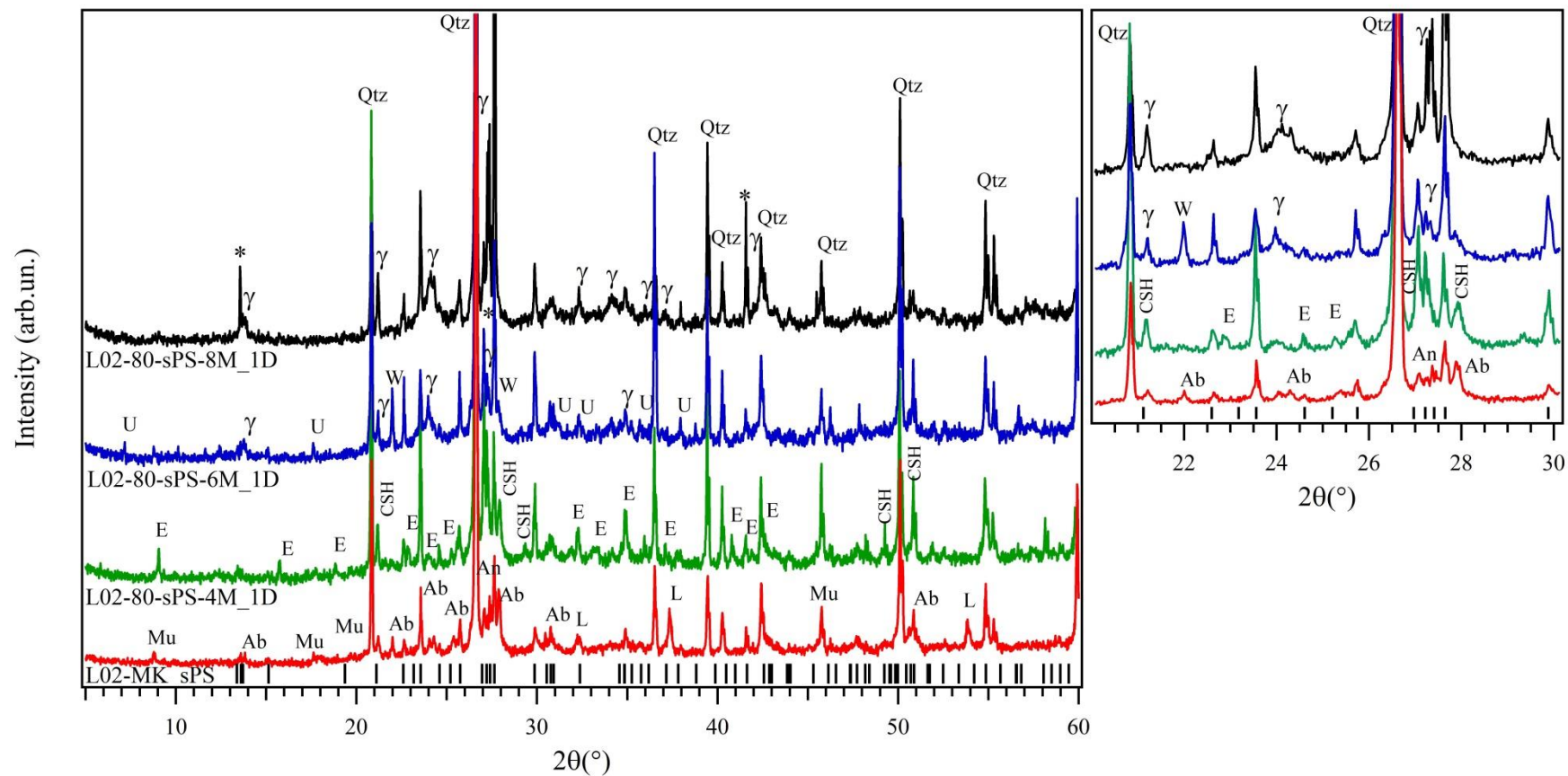
FIGURE 5.13. XRPD patterns of the AAMs prepared mixing L02-MK and sPS_800 (80/20 wt% proportion) activated with NaOH solution (4M, 6M or 8M) and cured at 85°C for 20 hours. On the bottom for comparison, XRPD pattern of the L02_sPS mix after thermal treatment (red line). Black sticks represent the feldspars reflections. A magnification of 20°-30° 2θ range is reported on the right box. U = U- phase ($NaCa_4Al_2O_6 (SO_4)_{1.5} \cdot 15H_2O$); γ, * = CAN-type zeolites; E = $Ca_6Al_2(SO_4)_3(OH)_{12} \cdot 26H_2O$); CSH = calcium silicate hydrate; W = wattevilleite; Q = quartz; Mu = muscovite, Ab = albite; L = lime.

SEM-EDS

Figure 5.14 shows shows a micrographs of L02-80-sPS-4M_1D sample. At 600x it is possible to observe a heterogenous matrix composed mainly by needle-like morphology crystals.
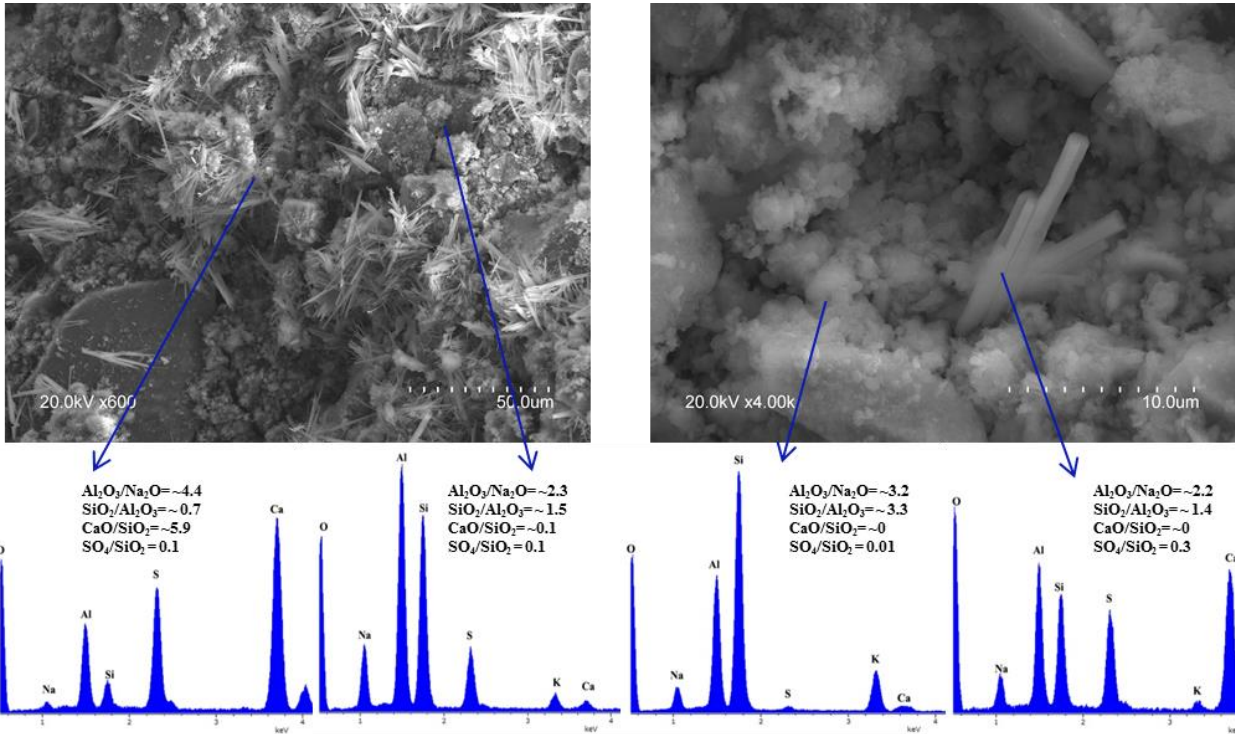
FIGURE 5.14. SE-Micrograph and EDS analyses of L02-80-sPS_8M_1D sample.

These have been recognized as ettringite crystals (as revealed also by XRPD analysis) and they are spread overall the surface of the sample. The shape and the position of these crystals suggest that ettringite is uniformly dispersed throughout cement paste at a submicroscopic level (less than a micrometer in cross-section) likely, as products precipitated from the solution at the end of the reaction process. The formation of ettringite in the fresh, plastic concrete is the mechanism that controls stiffening. Traces of feldspars and quartz are evident as well as some angular and sub angular fragment of unreacted particles (Figure 5.14a). EDS analyses of two points of this sample show that the crystals have a composition which could be attributed to ettringite confermed by the absence of sodium oxide. The other point of the sample which seem to be amorphous, shows a different chemical composition whit higher value of Na_2O and SiO_2, as reported in the graphs below the micrograph. At higher magnification, (4.0 Kx) (Figure 5.14b), the matrix is composed by granular particles, which

are not interconnected, and in some points it is possible to find crystals as those shown in the micrograph. According to the values reported from mechanical strength at 4M, the development of the ettringite in this sample as well as the low alkalinity of the activating solution affect badly the mechanical properties.

5.3 Study of the effect of curing temperature

In this section L02-MK and sPS_800 at fixed proportion, (50/50 wt %) have been prepared by using NaOH solution at 4M, 6M, and 8M. Pastes have been cured at 85°C and 25°C at 99% R.H. conditions.

Mechanical strength

Average values of compressive and flexural strength are reported in Table 5.1, and plotted in Figure 5.15 for samples cured at 25° C, and in Figure 5.16, for samples cured at 85° C.
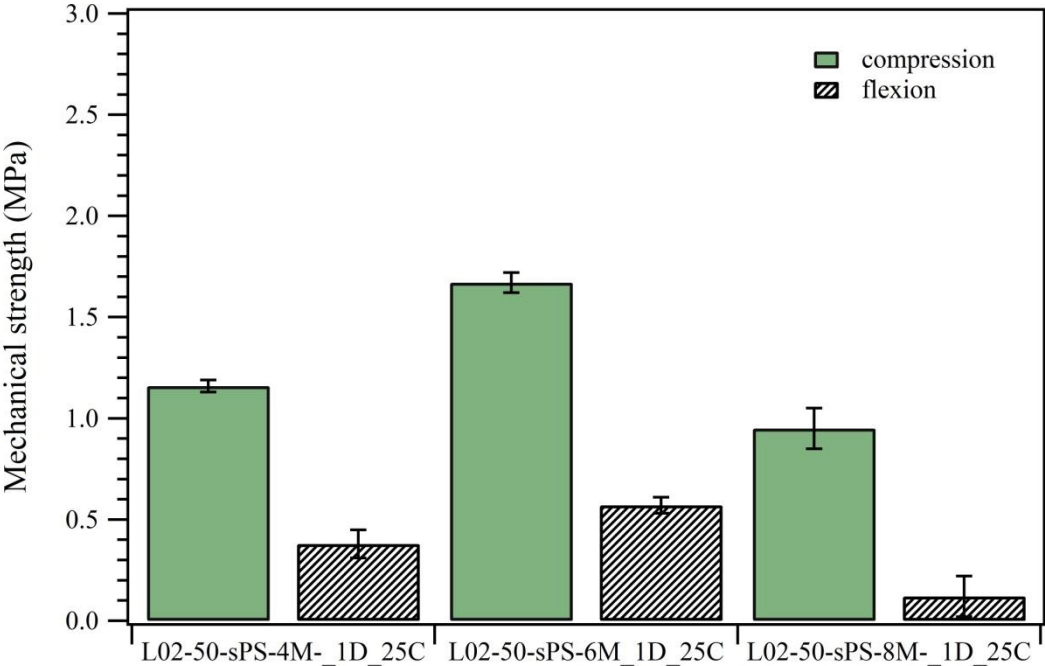
FIGURE 5.15. Compressive strength (filled bars) and flexural strength (line bars) of L02-50-sPS binders, activated with 4M, 6M and 8M NaOH solutions after curing at 25°C for 20 h.

The samples cured at 25°C exhibit lower values of mechanical strength, with values of compressive strength that not exceeded 2 MPa. At this curing condition, after one day, the pastes not harden and do not develop mechanical strenght.

Different is the situation for samples cured at 85°C. As reported in Figure 5.16, it is possible to note a positive trend in which the increase of molarity of activating solution improves the mechanical strength. The mechanical strength increases linearly with increasing the molarity of the activating solution with an average rate of 1.5.
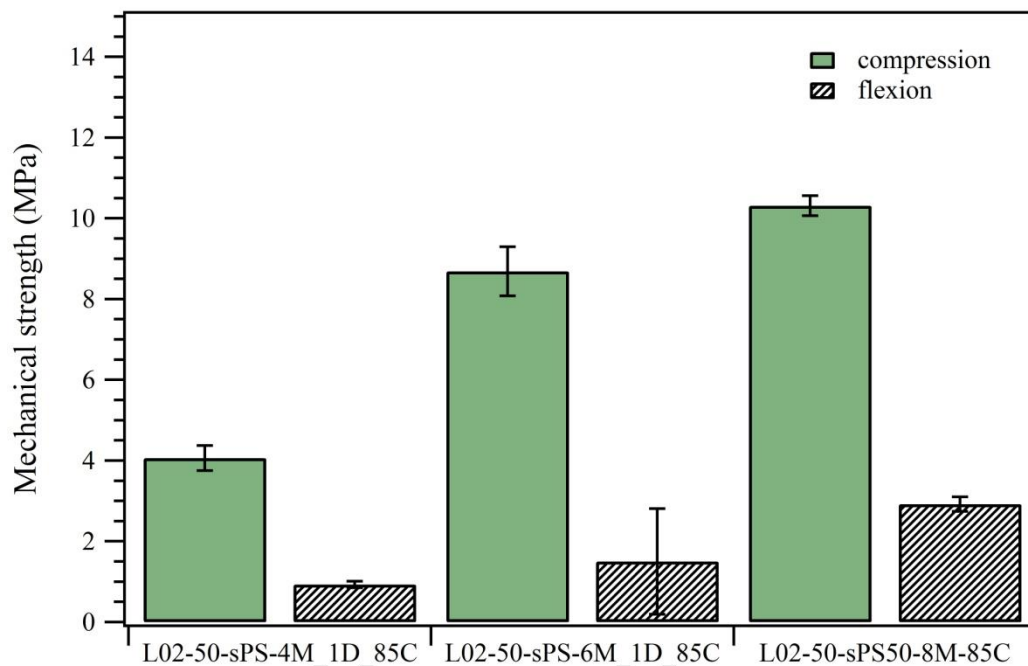
FIGURE 5.16. Compressive strength (filled bars) and flexural strength (line bars) of L02-50-sPS binders, activated with 4M, 6M and 8M NaOH solutions after curing at 85°C for 20 h.

From the results, it is possible to observe that, regardless the amount of sPS_800 and the effect of molarity, the temperature is a prevalent factor in hardening of the pastes for these mixtures. In fact, at 25°C the sample does not develop a mechanical strength and the reason could be related to the fact that the dissolution and subsequently condensation of reactive phases occur slowly. In contrast, high temperature promotes the advancement of the reaction process, a relatively rapid paste densification and increase of compressive strength.

XRPD

Figure 5.17 and Figure 5.18 show XRPD patterns of the AAMs after 20 hours of curing at 25°C and 85°C respectively. Quartz and feldspars from the original raw materials are present in all samples. In Figure 5.17, patterns show a halo around 20°-35° 2θ which represents the amorphous phase, typical of the gel formation. L02-50-sPS-4M_1D_25C pattern reveals the presence of crystalline phase identified as A-zeolite (PDF: 039-0222). Few reflections of calcium carbonate, in particular one of its polymorphs, vaterite (PDF: 005-0586), is also identified. Although, calcite is the most stable polymorph under Earth's surface conditions, $CaCO_3$ precipitate as vaterite in the presence of SO_4^{2-} (Fernández-Diaz et al., 2010). In the sample made using solution 6M NaOH, no new crystalline products are revealed from XRPD. Finally, L02-50-sPS-8M_25C_1D sample, prepared using 8M NaOH solution, shows some peaks related to CAN-type zeolites (particularly hydroxicancrinite, PDF:046-1457). Figure 5.18 shows the XRPD patterns of binders cured at 85°C. The halo related to the alkaline gel formation is also evident at around 20°-35° 2θ. In the XRPD pattern of the sample prepared by using 4M NaOH, it is possible to observe reflections related to ettringite (PDF: 072-0646) and calcium silicate hydrate compounds (PDF: 043-1488). Traces of P zeolite have also been detected (PDF: 080-0700). Increasing alkalinity of NaOH solution to 6M, (L02-50-sPS-6M_85C_1D sample), U-phase (PDF: 044-0272) have been found. Some traces of a poorly crystalline calcium silicate hydrate phase (PDF: 003-0594) have been also identified. L02-50-sPS-8M sample reveals the presence of U-phase (PDF: 044-0272) as well, together with poorly crystalline calcium silicate hydrate phase, identified as killalaite (PDF 038-0514). Moreover, CAN-type zeolite, vishnevite (PDF: 046-1333), have been also detected in this sample.

At this curing temperature, as already discussed in previous section, the formation of different calcium sufoaluminate compound depends on the alkalinity of the solution. Ettringite is stable at 4M NaOH while at higher NaOH concentration U-Phase is formed.

.
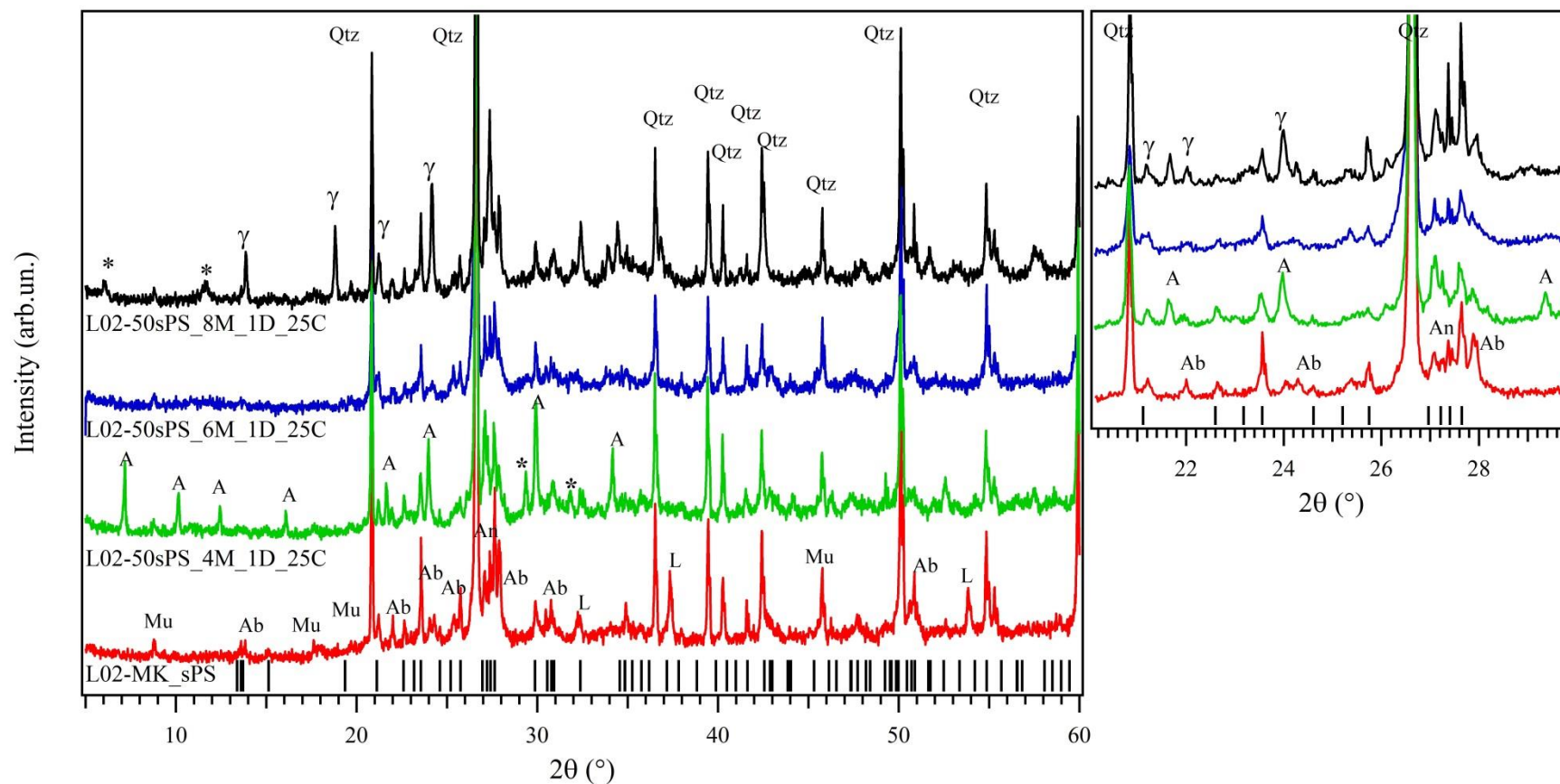
FIGURE 5.17. XRPD patterns of the AAMs prepared mixing L02-MK and sPS (50/50 wt% proportion) activated with NaOH solutions (4M, 6M and 8M) and cured at 25°C for 20h. On the bottom for comparison, XRPD pattern of the L02_sPS mix after thermal treatment (red line) is reported. Black sticks represent the feldspars reflections. A magnification of 20°-30° 2θ range is reported on the right box. A = A zeolites; γ = CAN-type zeolites; Q = quartz; Mu = muscovite, Ab = albite; L = lime; * = unmatched peaks.

FIGURE 5.18 XRPD patterns of the AAMs prepared mixing L02-MK and sPS (50/50 wt%) activated with NaOH solution (4M, 6M and 8M) and cured at 85°C for 20 h. For comparison, on the bottom an XRPD pattern of the L02_sPS mix after thermal treatments (red line) is reported. The black sticks represent the feldspars reflections. A magnification of 20°-30° 2θ range is reported on the right box. U = U-phase ($NaCa_4Al_2O_6(SO_4)_{1.5} \cdot 15H_2O$); γ = CAN-type zeolite; σ = SOD-type zeolites; E = $Ca_6Al_2(SO_4)_3(OH)_{12} \cdot 26H_2O$); P = P-zeolites; Q = quartz; Mu = muscovite, Ab = albite; L =lime.

SEM-EDS

To point out the differences in the compressive strength with the effect of curing temperature of the AAMs based on L02_sPS mixture of fixed composition, only the sample activated with 6M molar solution have been chosen for SEM-EDS analyses. L02-50-sPS6M_25C_1D and L02-50-sPS6M_85C_1D micrographs have been reported in Figure 5.19 and in Figure 5.20. Figure 5.19 shows, L02-50-sPS6M_25C_1D at 1.8 Kx and 2.0 Kx. At these magnifications, the matrix appears heterogeneous. The heterogeneity is related to the presence of grains scattered in the matrix as rectangular-elliptical plate (size around 30 µm, as reported in Figure 5.19a), which are surrounded by small rounded particles. From EDS analyses it is possible to note that there are differences in compositions between the plates and the surrounded area as shown from the EDS spectrum (Figure 5.19a). Higher values of Al_2O_3 and CaO with respect to the matrix could suggest that this could be attributed to the U-Phase. This phase or other AFm compounds have not been detected by XRPD, but is it possible that they amorphous and so they are not morphologically distinguishable from the surrounded matrix. Figure 5.19b shows some angular and sub-angular grains of quartz and others relicts belonging to the starting materials. Figure 5.19c and d show images at higher magnification, at 6Kx and at 8Kx respectively. From the images, it is possible to observe metakaolin plates, which are not completely dissolved during the alkaline activation process, arranged in parallel planes. Overall, the formation of the gel seems be low. In Figure 5.19c, some aggregates display a defined morphology resembling crystals at the beginning of their formation. From EDS analysis it is difficult to identify the actual phase, even if by considering the high content of silica and alumina one may speculate that they might be zeolites. Some points more rich in sulfate and sodium oxide likely related to the sodium sulfate compound formation have been detected. It might be possible to assume that sodium sulfate is formed at the beginning of the alkaline reaction and then when the gel starts to form, it reacts with the silicon and calcium forming sulfate-calcium-silicate compounds. The SEM images and EDS analyses suggest that the digestion of solid precursor is not complete.
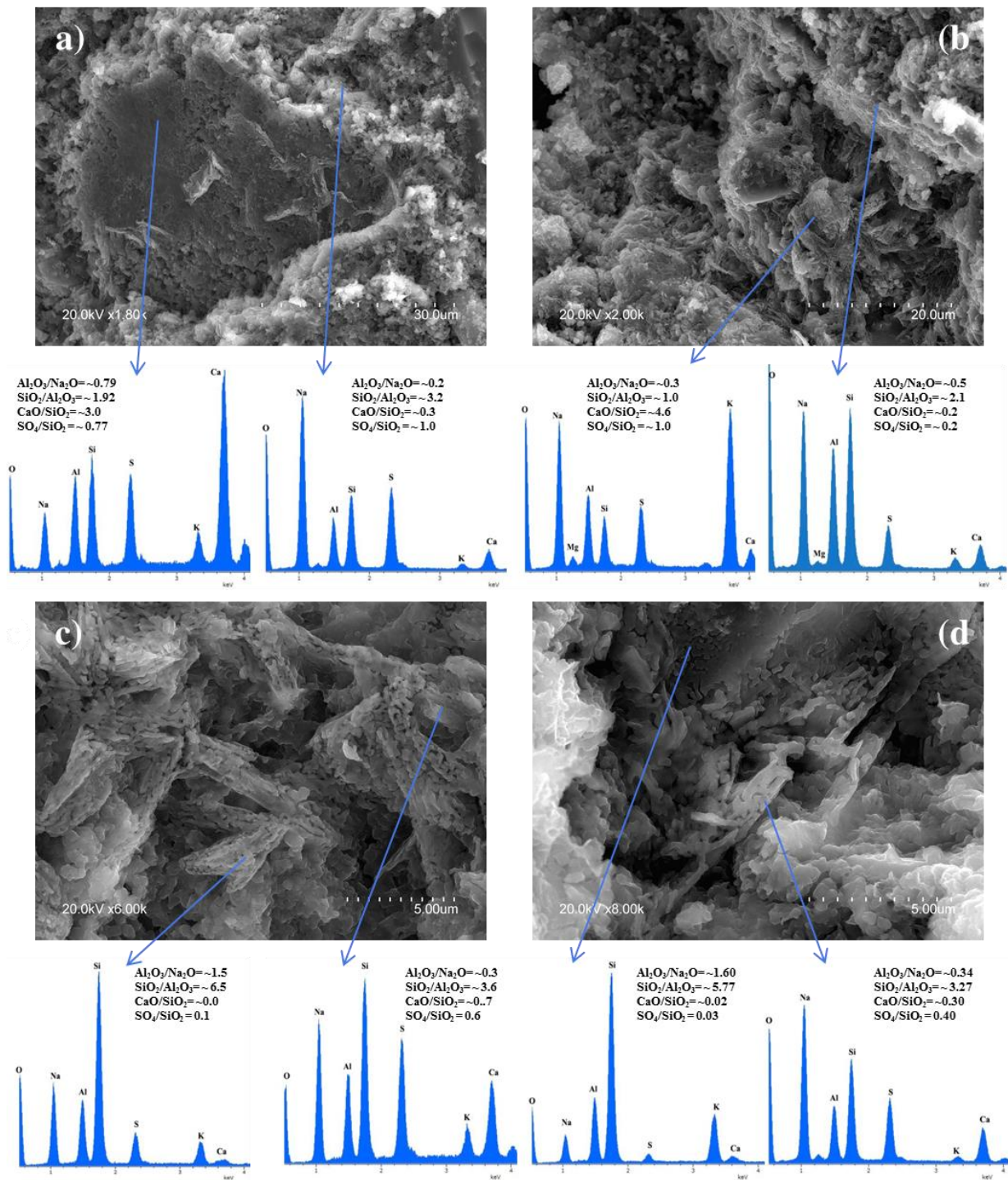
FIGURE 5.19. SE-Micrographs and EDS analyses of L02-50-sPS-6M_25C_1D sample after curing at 25°C for 20 h.

Figure 5.20 shows the SEM-EDS analysis for L02-50-sPS-6M_85C_1D sample. The gel structure appears inhomogeneous, as for sample L02-50-sPS-8M_85C_1D. Clusters of acicular fibers interconnected with several rounded particles are also evident.
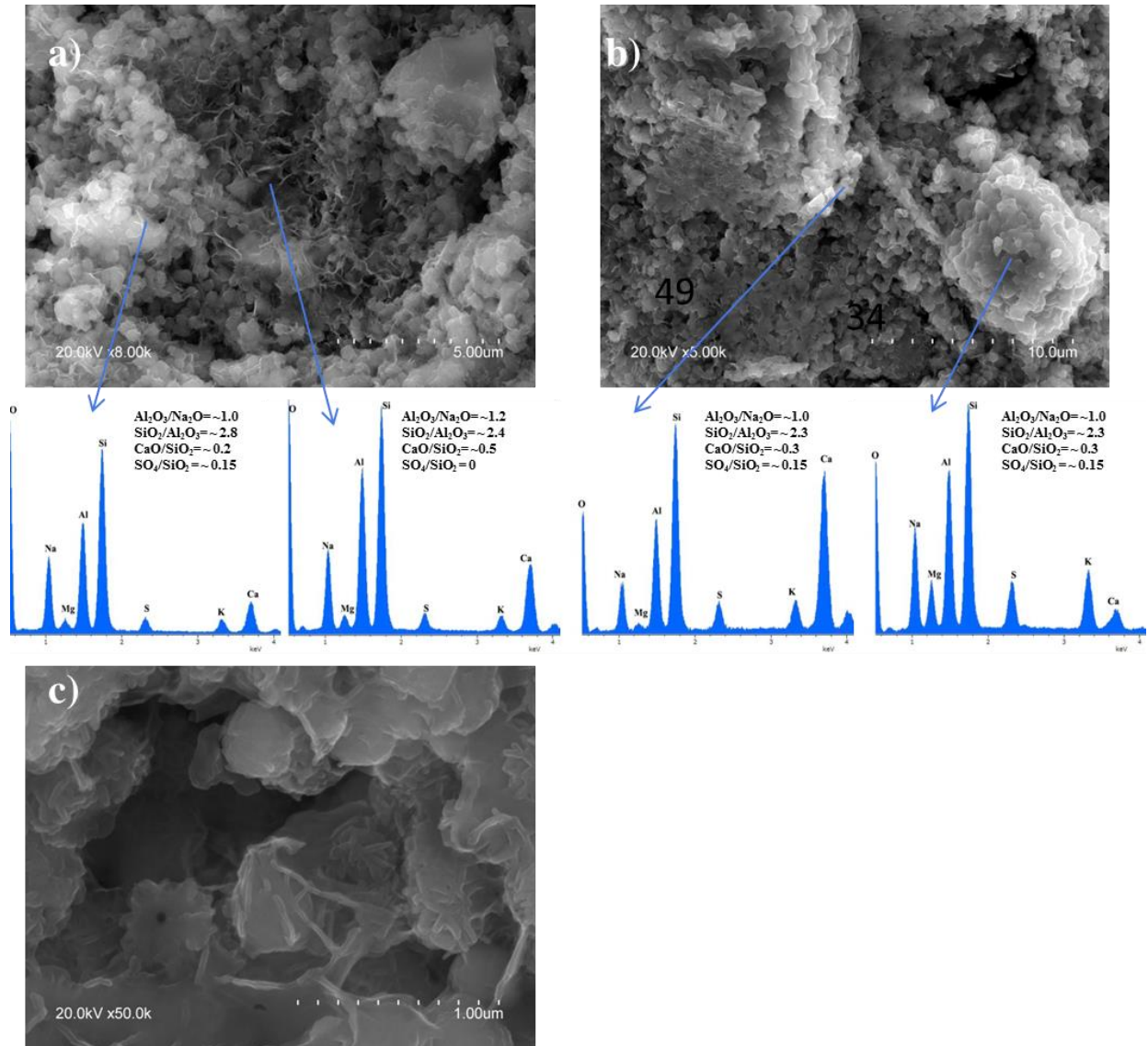
FIGURE 5.20. SE-Micrographs and EDS analyses of L02-50-sPS-6M_85C_1D after curing at 85°C for 20 h.

In this sample, it is possible to distinguish two types of gels as shown in Figure 5.20a. The typical acicular shape morphology of the C-A-S-H gel is recognizable together with the granular morphology typical of N-A-S-H gel. More exhaustive (over 30) EDS analyses conducted to determine the composition of the gel phases yielded the Al_2O_3/SiO_2 and CaO/SiO_2 ratios, are plotted in Figure 5.21a, and b. The composition ranges which, characterize the main types of cementations gels (C-S-H, C-(A)-S-H, C-A-S-H, N-A-S-H and (N,C)-A-S-H) according to literature (Garcia-Lodeiro et al 2011; Pardal et al., 2009),
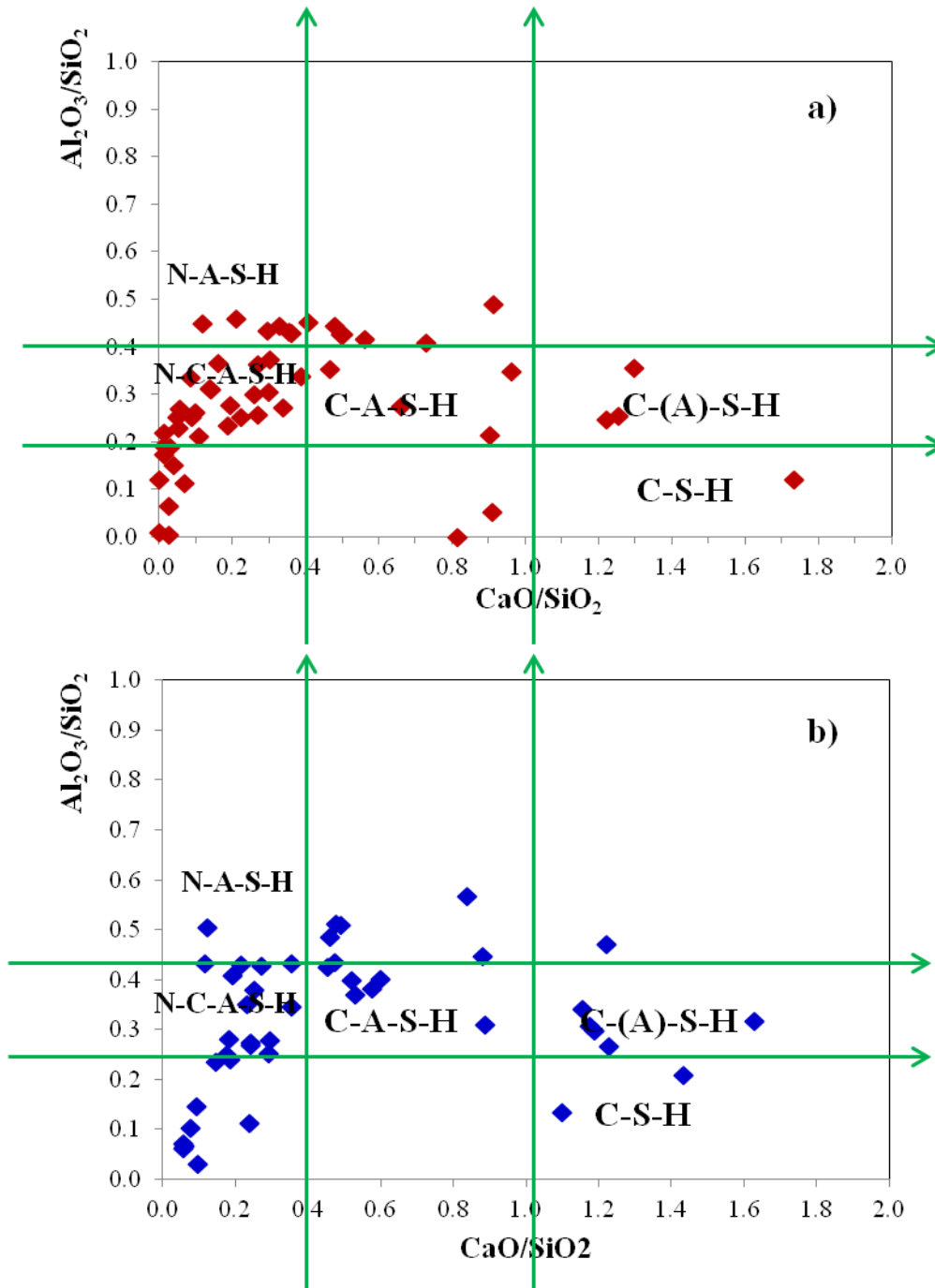
FIGURE 5.21. Al$_2$O$_3$/SiO$_2$ vs. CaO/SiO$_2$ ratios for gels precipitating in hybrid cements (based on EDS findings) L02-50-sPS-6M_25C, b) L02-50-sPS-6M_85C.

are marked on the figure. From the graphs, it s possible to observe that there are no differences in the type of gel in relation to the curing temperature. In both cases, most of the points are located in the (N,C)-A-S-H zone although, for the sample cured at 85°C there are a smaller clusters which lie within the C-A-S-H and C-(A)-S-H areas.

The finding confirms that in this type of multi-components system and at these alkaline conditions, the main reaction products are two types of gels.

Leaching tests

Leaching tests have been conducted on the samples activated at 6M and cured at 85°C and on the samples activate at 8M cured at 85°C and 25°C. As reported in Table 3.4, § 3.2.2, the results are very satisfactory in terms of sulfate retention. Sample activated at 6M and cured at 85°C reveals sulfate retention of 53wt%, while the samples activated at 8M and cured at 25°C show a value of 50wt % whereas the sample cured at 85°C of 70 wt %. The latter shows the best value in term of sulfate retention. The results highlights how U-Phase, formed at 6M and 8M, and CAN zeolites can hold sulfate in their structure. At 25° C only A-zeolites and traces of X-zeolites have been detected. The fact that sulfate is not completely leached out in the sample cured at 25°C could support the hypothesis that sulfate might be retained sulfo-aluminate compounds as revealed by SEM-EDS analyses in which some plates rich in sulfur and calcium have been attributed to amorphous sodium calcium sulfo-aluminate compound as U-Phase.

FT-IR

Figure 5.22a shows FT-IR spectra of s L02-50-sPS-8M sample after curing at 25°C and 85°C while Figure 5.22b shows the FT-IR spectra of L02-50-sPS-6M sample after curing at 85°C. Both the figures include the spectra before and after water leaching. A spectrum of sPS_800 was reported in each graph, for comparison. The presence of water is indicated in all spectra by the humps at 1640 cm^{-1}, ascribable to H-O-H bending vibrations. Features common to all spectra are the peaks at 450 cm^{-1}, associated to Si-O-Si bending vibrations; the distinctive doublet at 780-790 cm^{-1} and the peak at 1080-1090 cm^{-1}of quartz. Also feldspars show a broad bands in the region between 1000 and 1100 cm^{-1}, at lower frequencies at 727, 638, 580, 540 cm^{-1} (Harris et al., 1989; Criado et al., 2010; Xu et al., 2003). As mentioned before, SO_4^{2-} vibration modes are generally at 1030 cm^{-1} and at 1170-1086 cm^{-1} for the symmetric and asymmetric stretching modes respectively, while the most important deformation related to symmetric and asymmetric bending vibration are at 475 and 632-605 cm^{-1} respectively (Ross, 1974).

133
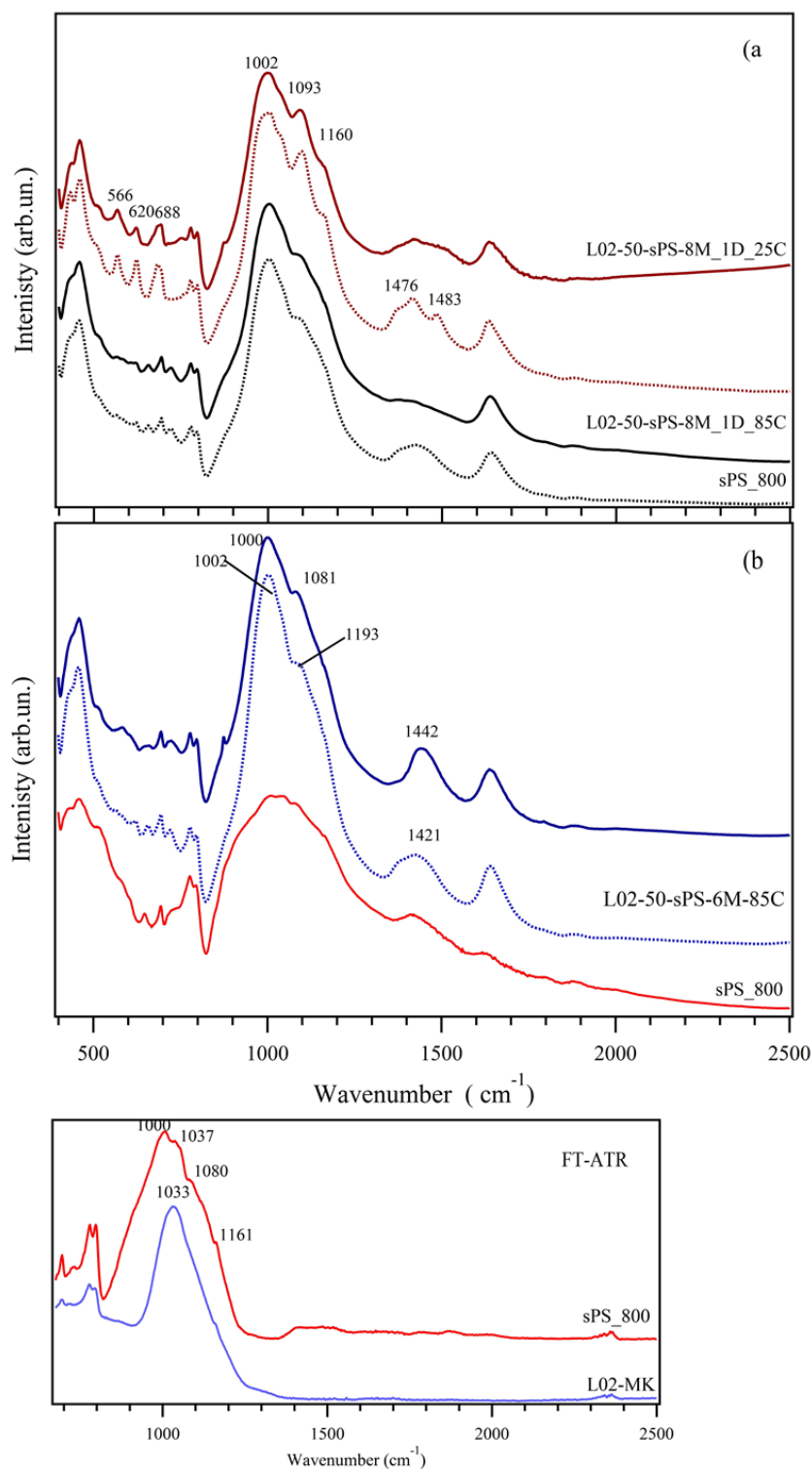
FIGURE 5.22 a) FT-IR spectra of samples L02-50-sPS-8M_1D_85C and L02-50-sPS-8M _1D_25C; b) FT-IR spectra of L02-50-sPS-6M_1D_85C. Dotted and bold line represent sample before and after leaching tests, respectively. Spectrum of sPS_800 (red line) after thermal treatment is reported for comparison. The box below represents the spectra of L02-MK and sPS_800 collected by FT-ATR.

According to literature the occurrence of the main band at 1000-1002 cm^{-1} is indicative of the formation of the amorphous gel (Lee & Van Deventer, 2003; Fernandez & Palomo, 2005).

The shift of this band toward lower frequencies with respect to L02-MK indicates in fact a different coordinated environment of TO group in aluminosilicate gels. This band is centered also at 1002 cm^{-1} in the sample cured at 25°C, meaning that metakaolin has partially dissolved and the Si-O-T groups are formed likely as aluminosilicate gel. Spectra show that the various concentrations of NaOH do not affect the position of the main band corresponding to Si–O-T stretching vibrations. In the region between 500 to 800 cm^{-1} only L02-50-sPS-8M_25C sample, before and after leaching tests three well defined peaks at 566, 620 and 688 cm^{-1} that may be attribute of CAN-type zeolites evidenced by XRPD.

5.4 Conclusions

In this part of the work, the alkali activation of a blended system composed by a sulfate-bearing clay and a sandstone sewage sludge has been assessed. NaOH has been used as activator. Parameters as molarity of activating solution and curing temperature have been also evaluated.

The results obtained have demonstrated that, overall, the addition of sPS_800 to L02-MK affects positively the mechanical properties and sulfate retention.

When sulfate-bearing clay (L02-MK) is activated with sodium hydroxide at 8M, mechanical strength values are the lowest of the series after curing the pastes at 85°C, while after curing at 25°C, the slurry do not harden. The formation of efflorescence, thenardite (Na_2SO_4), as confirmed by XRPD analysis, is also macroscopically evident in this sample. Its occurrence means that part of the sodium has been subtracted to the system to form thenardite, thus hindering the gel formation. Crystals of gibbsite have been also identified by XRPD and SEM-EDS analysis. Their occurrence might be related to an excess of reactive aluminum content which in turn may be detrimental, as reported by (De Silva & Sagoe-Crenstil, 2008). An overly high aluminum concentration accelerates aluminates and silicates condensation rate considerably, shortens setting time, raises the crystallinity of the reaction products (more zeolites and less gel), and lowers the final strength. However, beside gibbsite and thenardite, no zeolites have been detected after one day.

When alkaline activation of L02-MK is carried out in the presence of sPS_800 (10%-20%-50% weight proportion), mechanical strength values considerably increase and no efflorescences have been formed as revealed by XRPD and FT-IR results. The formation of an amorphous aluminosilicate with cementitious properties is the main reaction product.

Effects of the CaO content, deriving from sPS_800, in the mixtures lead to the formation of hydrated calcium silicate of C-(A)-S-H gel type together with N-A-S-H gel, which are clearly visible by SEM-EDS analyses. Literature studies have shown that the co-precipitation of these two gels in hybrid cements is possible (Alonso & Palomo, 2001; Yip et al., 2005; Palomo et al., 2007). Although, recent research has revealed that, the two products do not develop singly as two separate gels, but that they interacts undergoing structural and compositional change in the process (García-Lodeiro et al., 2011).

Leaching tests have demonstrated that, when L02-MK is activated only with NaOH, sulfate is not retained in the sample. While a little amount of sPS_800 content (i.e., 10 wt% of sPS which, corresponds to 2 wt % of CaO in the mix) is able to reduce sensibly the sulfate solubility (over 50%), and as sPS_800 content increase, the sulfate retention reaches values of 70%. These effects could be ascribed to the formation of some crystalline products, CAN-type zeolites, or sulfo-aluminate compounds as Ettringite or U-Phase, as observed by XRPD analysis. However, it cannot be excluded that sulfate might be uptake also by the gel.

CAN-type zeolites have been found in all sample with sPS_800 activated at 8M and cured at 85°C. Samples which contain 50 wt % of sPS_800 show the presence of Ettringite and U-Phase. Both have been found after curing at 85°C, however their occurrence is depending on the alkalinity of the solution. Ettringitie is formed at 4 M, while U-Phase is formed at 6M and 8M.

Experiments made maintaining fixed the calcium content in the system and varying the alkalinity of the solution have shown affect sensibly the mechanical properties of these binders. As well-known from literature, generally NaOH 8M provides a better dissolution of metakaolin and the releasement of siliceous and aluminum species in the hydrolysis process involved in AAMs formation. In this blended system, a reduction of the alkalinity of NaOH solution produces a decrease of the mechanical properties but promotes the formation of AFt (as ettringite) and AFm (as U-phase, a sodium-substituted AFm) which are calcium sulfo-aluminate compounds commonly found in concrete (Damidot & Glasser., 1993). Ettringite is the most insoluble phase in the CaO-SiO_2-$CaSO_4$-H_2O system. However, it well-know that the stability of the AFm phase increases as temperature and/or pH of the system rises. Monosulfate becomes increasingly stable at the expense of ettringite as temperature and/or pH increase (Damidot & Glasser., 1993).

Low alkalinity of the activating solution is enough to trap the sulfate by the formation of sulfo-aluminate compounds but affects sensibly mechanical strength.

Finally, when more calcium is added to the mixtures (corresponding at 9.8 wt% of lime in the system, see Table 3.3), varying molarities and curing conditions, the results have demonstrated that mechanical strength is strictly related to the curing temperature. Even if calcium could accelerate the setting, samples cured at 25°C for one day do not develop strength. With increasing temperature, at 85°C, it has been seen that CaO, certainly accelerates setting and strength development with respect to the samples cured at 25°C. The latter have demonstrated that, despite they do not harden after one day of curing, show a values of sulfate retention of 50%. This value is perfectly comparable to those showed for the sample activated at 8M with 10 wt% of sPS_800 and at 6M with 50wt% of sPS_800 both cured at 85°C.

References

Alonso, S., & Palomo, A., 2001. Alkaline activation of metakaolin and calcium hydroxide mixtures: influence of temperature, activator concentration and solids ratio. Materials Letters, 47(1), 55-62.

Anbalagan, G., Sankari, G., Ponnusamy, S., & Gunasekaran, S., 2009. Investigation of silicate mineral sanidine by vibrational and NMR spectroscopic methods. Spectrochimica Acta Part A: Molecular and Biomolecular Spectroscopy, 74(2), 404-409.

Balan, E., Lazzeri, M., Morin, G., & Mauri, F., 2006. First-principles study of the OH-stretching modes of gibbsite. American Mineralogist, 91(1), 115-119.

Barbosa, V.F., MacKenzie, K.J., Thaumaturgo, C., 2000. Synthesis and characterisation of materials based on inorganic polymers of alumina and silica: Sodium polysialate polymers. International Journal of Inorganic Materials, 2, 309-317.

Barbosa, V.F., MacKenzie, K.J., 2003. Synthesis and thermal behaviour of potassium sialate geopolymers. Materials Letters, 57, 1477-1482.

Barnes, M.C., Addai-Mensah, J., Gerson, A.R., 1999. The mechanism of the sodalite-to-cancrinite phase transformation in synthetic spent Bayer liquor. Microporous and Mesoporous Materials, 31(3), 287-302.

Buchwald, A., Hilbig, H., & Kaps, C., 2007. Alkali-activated metakaolin-slag blends—performance and structure in dependence of their composition. Journal of materials science, 42(9), 3024-3032.

Chandrasekhar, S., & Pramada, P. N., 2008. Microwave assisted synthesis of zeolite A from metakaolin. Microporous and Mesoporous Materials, 108(1-3), 152-161.

Criado, M., Jiménez, A. F., & Palomo, A., 2010. Effect of sodium sulfate on the alkali activation of fly ash. Cement and Concrete Composites, 32(8), 589-594.

Damidot, D., & Glasser, F.P., 1993. Thermodynamic investigation of the CaO- Al_2O_3- $CaSO_4$- H_2O system at 25° C and the influence of Na_2O. Cement and Concrete Research, 23(1), 221-238.

Dimas, D. D., Giannopoulou, I. P., & Panias, D., 2009. Utilization of alumina red mud for synthesis of inorganic polymeric materials. Mineral processing & Extractive metallurgy review, 30(3), 211-239.

Dombrowski, K., Buchwald, A., & Weil, M., 2007. The influence of calcium content on the structure and thermal performance of fly ash based geopolymers. Journal of Materials Science, 42(9), 3033-3043.

Dong, Y., Yan, Y., Zhang, S., & Li, J., 2014. Wood/polymer nanocomposites prepared by impregnation with furfuryl alcohol and nano-SiO_2. BioResources, 9(4), 6028-6040.

Duxson, P., Provis, J.L., Lukey, G.C., Mallicoat, S.W., Kriven, W.M., van Deventer, J.S.J., 2005b. Understanding the relationship between geopolymer composition, microstructure and mechanical properties. Colloids and Surfaces A: Physicochemical and Engineering Aspects, 269, 47-58.

Engelhardt, G., & Michel, D., 1987. High-resolution solid-state NMR of silicates and zeolites.

Farmer, V.C., 1974. Infrared spectra of minerals. Mineralogical Society.

Fernández-Jiménez, A., & Palomo, A., 2005. Mid-infrared spectroscopic studies of alkali-activated fly ash structure. Microporous and Mesoporous Materials, 86(1), 207-214.

Fernández-Díaz, L., Fernández-González, Á., & Prieto, M., 2010. The role of sulfate groups in controlling $CaCO_3$ polymorphism. Geochimica et Cosmochimica Acta, 74(21), 6064-6076.

Fletcher, R.A., MacKenzie, K.J.D., Nicholson, C.L., Shimada, S., 2005. The composition range of aluminosilicate geopolymers. Journal of the European Ceramic Society, 25(9), 1471-1477.

García-Lodeiro, I., Fernández-Jiménez, A., Palomo, A., Macphee, D.E., 2010. Effect of calcium additions on N-A-S-H cementitious gels. Journal of the American Ceramic Society, 93(7), 1934-1940.

Garcia-Lodeiro, I., Palomo, A., Fernández-Jiménez, A., & Macphee, D.E., 2011. Compatibility studies between NASH and CASH gels. Study in the ternary diagram Na_2O-CaO-Al_2O_3-SiO_2-H_2O. Cement and Concrete Research, 41(9), 923-931.

Garcia-Lodeiro, I., Fernández-Jiménez, A., & Palomo, A., 2013a. Variation in hybrid cements over time. Alkaline activation of fly ash–portland cement blends. Cement and Concrete Research, 52, 112-122.

García-Lodeiro, I., Fernández-Jiménez, A., Palomo, A., 2013b. Eco-efficient concrete: 17. Alkali-activated based concrete. Elsevier Inc. Chapters.

Garcia-Lodeiro, I., Palomo, A., & Fernández-Jiménez, A., 2015. An overview of the chemistry of alkali-activated cement-based binders. In Handbook of alkali-activated cements, mortars and concretes (pp. 19-47).

Gougar, M. L. D., Scheetz, B. E., & Roy, D. M., 1996. Ettringite and C-S-H Portland cement phases for waste ion immobilization: A review. Waste management, 16(4), 295-303.

Harris, M. J., Salje, E. K., Guttler, B. K., & Carpenter, M. A., 1989. Structural states of natural potassium feldspar: An infrared spectroscopic study. Physics and Chemistry of Minerals, 16(7), 649-658.

Hranice, C., 2002. The effect of water ratio on microstructre and composition of the hydration products of Portland cement pastes. Ceramics - Silikáty, 46(4), 152-158.

Isobe, T., Watanabe, T., De La Caillerie, J. D. E., Legrand, A. P., & Massiot, D., 2003. Solid-state 1H and ^{27}Al NMR studies of amorphous aluminum hydroxides. Journal of colloid and interface science, 261(2), 320-324.

Katsioti, M., Tsakiridis, P. E., Giannatos, P., Tsibouki, Z., & Marinos, J., 2009. Characterization of various cement grinding aids and their impact on grindability and cement performance. Construction and Building Materials, 23(5), 1954-1959.

Kloprogge, J.T., Ruan, H.D., Frost, R.L., 2002. Thermal decomposition of bauxite minerals: infrared emission spectroscopy of gibbsite, boehmite and diaspore. Journal of Materials Science 37, 1121-1129.

Kovalchuk, G., Fernández-Jiménez, A., & Palomo, A., 2007. Alkali-activated fly ash: effect of thermal curing conditions on mechanical and microstructural development–Part II. Fuel, 86(3), 315-322.

Lane, M.D., 2007. Mid-infrared emission spectroscopy of sulfate and sulfate-bearing minerals. American Mineralogist, 92, 1-18.

Lee, W.K.W., & Van Deventer, J.S.J., 2003. Use of infrared spectroscopy to study geopolymerization of heterogeneous amorphous aluminosilicates. Langmuir, 19(21), 8726-8734.

Li, G., Le Bescop, P., & Moranville, M., 1996. The U phase formation in cement-based systems containing high amounts of Na2SO4. Cement and Concrete Research, 26(1), 27-33.

Li, C., Zhang, T., & Wang, L., 2014. Mechanical properties and microstructure of alkali activated Pisha sandstone geopolymer composites. Construction and Building Materials, 68, 233-239.

MacKenzie, K.J., & Smith, M.E., 2002. Multinuclear solid-state nuclear magnetic resonance of inorganic materials (Vol. 6). Elsevier.

Moon, J., Yoon, S., Monteiro, P.J., 2015. Mechanical properties of jennite: A theoretical and experimental study. Cement and Concrete Research, 71, 106-114.

Najafi Kani, E., & Allahverdi, A., 2009. Application of FTIR technique in characterizing molecular structure of natural pozzolan-based geopolymer cement. Iranian Journal of Materials Science and Engineering, 6(2), 1-10.

Navarro-Rodriguez, C., Doehnea, E., Sebastian, E., 2000. How does sodium sulfate crystallize? Implications for the decay and testing of building materials. Cement and Concrete Research, 30, 1527-1534.

Nielsen, U., Majzlan, J., Phillips, B., Ziliox, M., & Grey, C.P., 2007. Characterization of defects and the local structure in natural and synthetic alunite (K, Na, H_3O) Al_3 $(SO_4)_2$ $(OH)_6$ by multi-nuclear solid-state NMR spectroscopy. American Mineralogist, 92(4), 587-597.

Palomo, A., Grutzeck, M.W., Blanco, M. T., 1999. Alkali-activated fly ashes: a cement for the future. Cement and cConcrete Research, 29(8), 1323-1329.

Palomo, A., Fernández-Jiménez, A., Kovalchuk, G., Ordoñez, L.M., Naranjo, M.C., 2007. OPC-fly ash cementitious systems: study of gel binders produced during alkaline hydration. Journal of Materials Science, 42(9), 2958-2966.

Pardal, X., Pochard, I., Nonat, A., 2009. Experimental study of Si-Al substitution in calcium-silicate-hydrate (CSH) prepared under equilibrium conditions. Cement and Concrete Research, 39(8), 637-643.

Reyes, C. A. R., Williams, C., & Alarcón, O. M. C., 2013. Nucleation and growth process of sodalite and cancrinite from kaolinite-rich clay under low-temperature hydrothermal conditions. Materials Research, 16(2), 424-438.

Rocha, J., & Klinowski, J., 1990. 29 Si and 27 Al magic-angle-spinning NMR studies of the thermal transformation of kaolinite. Physics and Chemistry of Minerals, 17(2), 179-186.

Ross, S.D., 1974. Sulfates and other oxy-anions of Group VI. In V.C. Farmer, Ed., The Infrared Spectra of Minerals, 423-444.

Rowles, M., & O'connor, B., 2003. Chemical optimisation of the compressive strength of aluminosilicate geopolymers synthesised by sodium silicate activation of metakaolinite. Journal of Materials Chemistry, 13(5), 1161-1165.

Shi, C., & Day, R. L., 1999. Early strength development and hydration of alkali-activated blast furnace slag/fly ash blends. Advances in Cement Research, 11(4), 189-196.

Shi, C., Roy, D., Krivenko, P., 2006. Alkali-activated cements and concretes. CRC press.

Sweegers, C., De Coninck, H. C., Meekes, H., Van Enckevort, W.J.P., Hiralal, I.D.K., Rijkeboer, A., 2001. Morphology, evolution and other characteristics of gibbsite crystals grown from pure and impure aqueous sodium aluminate solutions. Journal of Crystal Growth, 233(3), 567-582.

Taylor, H. F., 1986. Proposed structure for calcium silicate hydrate gel. Journal of the American Ceramic Society, 69(6), 464-467.

Yip, C.K., Lukey, G.C., Van Deventer, J.S.J., 2005. The coexistence of geopolymeric gel and calcium silicate hydrate at the early stage of alkaline activation. Cement and Concrete Research, 35(9), 1688-1697.

Yip, C.K., Lukey, G.C., Provis, J.L., van Deventer, J.S., 2008. Effect of calcium silicate sources on geopolymerisation. Cement and Concrete Research, 38(4), 554-564.

Xu, H., & van Deventer, J.S., 2003. The effect of alkali metals on the formation of geopolymeric gels from alkali-feldspars. Colloids and Surfaces A: Physicochemical and Engineering Aspects, 216(1), 27-44.

6 SYNTHESIS OF ZEOLITES VIA MOLTEN SALT METHOD

Zeolites are generally synthesized by chemical processes, which yield uniform and purer phases as compared to the natural zeo-types in terms of structures, sizes of pores and cages in their frameworks. Fly ash and kaolin, being rich in minerals containing silica and alumina, can be used for the synthesis of zeolites. The type of zeolites formed is dependent on temperature, pressure, concentration of the reactant solution, pH, process of activation and ageing period, SiO_2 and Al_2O_3 contents of the raw materials (Barrer, 1981). As mentioned in §1.8, zeolites formation can be obtained following the same route as used for alkaline activation of metakaolin or fly ash.

In this part of the work, zeolites syntheses have been carried out starting from the same raw materials used for AAMs synthesis, in order to investigate if sulfate-bearing zeolites phases could be similarly formed as in AAMs binders. The idea was based on the existing knowledge related to the effect of the presence of small amount of sulfate anion, which could act as possible activation catalyst in this system on the nucleation and crystallization of certain zeolites. As mentioned in § 1.8 (and reference therein), many studies have demonstrated that some oxyanions could lead to the nucleation of certain zeolite types. Hackbarth et al. (1999) have shown that nucleation of the cancrinite structure is promoted by the presence of anions such as NO^{3-}, $S_2O_3^{2-}$ and SO_3^{2-}, which act as structure-driving agents. Most of the zeolites encountered in this alkaline activated system (sulfate-bearing clay and Pietra Serena sewage sludge, § 5.1, 5.2, 5.3.) when NaOH is the activator, have been mainly identified as CAN-type zeolites, in particular (SO_4^{2-})-bearing cancrinite, synthetic analogue of the mineral vishnevite.

Zeolites materials have been prepared using the well-known molten-salt method. Syntheses have been started from sulfate-bearing clay (L02-K) as well as from synthetic mixtures of alunite and high-grade kaolin (Sl-K) in different proportions. Products have been compared to those obtained by using the high-quality kaolin without alunite. A mixture composed by L02-K and Pietra Serena sewage sludge (sPS_800) has been also prepared. All the details of the preparation of the syntheses and references are reported in § 3.3.3.

Table 6.1 summarizes the results obtained using different raw materials and synthesis parameters, for both Sl-K, with and without alunite mixtures, L02-K mixtures and L02 and sPS_800 mixtures.

TABLE 6.1 Scheme of synthesis conditions for Sl-K and L02-K series and resulting products.

Sample	Clay/Alunite proportion (wt %) in 1g	SiO_2/Al_2O_3 molar ratio	S/L proportion	XRD phases
Slm_s36d4	100/0	3.6	1g/5ml	Y, A
Slm_s46d4	100/0	4.6	1g/5ml	Traces of Y
Slm_NaOHd4	100/0	2.0[b]	1g/5ml	Y, A, P
Slm_s36d30	100/0	3.6	1g/33ml	Y, A
SlA10m_s36d4	91.5/8.5	3.6	1g/33ml	Y, CAN
SlA10m_s36d30	91.5/8.5	3.6	1g/33ml	Y, CAN
SlA10m_s36d15_HT*	91.5/8.5	3.6	1g/50ml	CAN
SlA20m_s36d4	82/18	3.6	1g/5ml	CAN, SOD
SlA20m_s46d4	82/18	4.6	1g/5ml	CAN
L02m_NaOHd7	80/20	1.6	1g/5ml	CAN
L02m_s36d4	80/20	3.6	1g/5ml	CAN
L02m_s36d30	80/20	3.6	1g/5ml	CAN
L02m_s46d4	80/20	4.6	1g/5ml	CAN
L02m_s46d30	80/20	4.6	1g/5ml	CAN
L02m_sPS$_{800}$NaOHd4[a]	80/20	2.8[b]	1g/5ml	CAN

*Sample with label HT = mechanical and thermal stirring (50°C), before incubation in water

[a] The ratio referred to clay/Pietra Serena sewage sludge is 50/50 wt%

[b] SiO_2/Al_2O_3 ratio is referred to the ratio without addition of silica fume

Sl, L02 = kaolins used; A = alunite wt %; s36 and s46 = silica fume addition; d4 = 720 hours; d7 = 168 hours; d30 = 720 hours of incubation.

6.1 Phase composition

XRPD patterns of the solid products obtained by alkali fusion at 550°C for 2 hours of L02-K and mixture of Sl-K and Alunite 10 wt% prior to incubation are presented in Figure 6.1. They show the presence of feldspar and quartz deriving from the original raw materials and new peaks related to the formation of sodium silicate (PDF: 072-0079) and sodium carbonate (PDF: 077-2082).
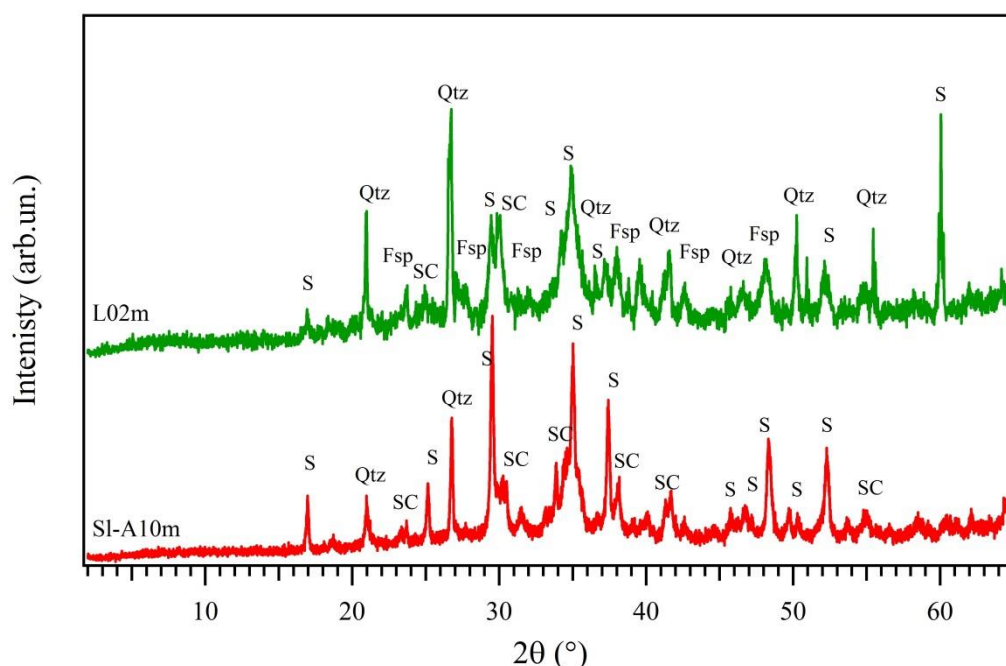
FIGURE 6.1. XRPD patterns of the solid products obtained by alkali fusion at 550°C of L02-K (green) and mixture of Sl-K and Alunite 10 wt% (red). Qtz = quartz; Fsp = feldpsars; S = sodium silicate; SC = sodium carbonate.

Figure 6.2 shows DTA curves of mixtures of Sl-K and L02-K with NaOH and silica fume. Two endothermic peaks are visible below 550°C, likely related to melting of kaolin and alunite.
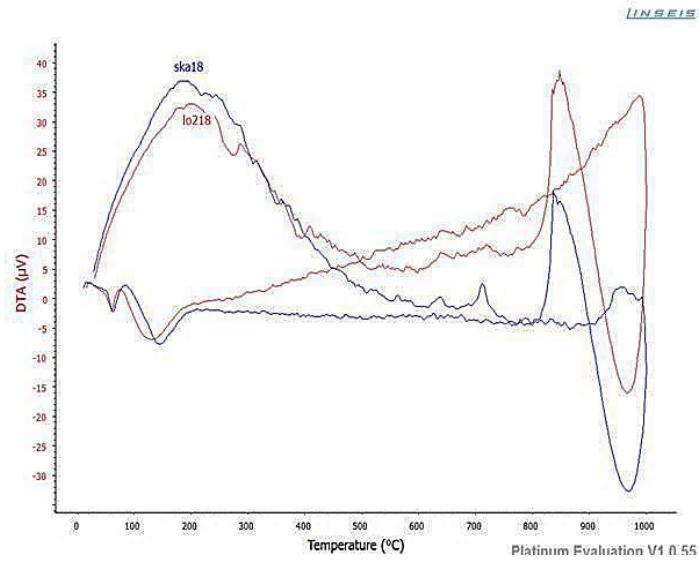
FIGURE 6.2. DTA analysis of mixture of Sl-K and L02-K with NaOH and fumed silica.

XRPD patterns of the samples synthesized by using only the Sl-K kaolin, after 4 days of incubation, are reported in Figure 6.3. All patterns show the presence of quartz, which remains from the original raw material. Y-type zeolites (PDF: 076-064) and A-type zeolite (PDF: 039-0223) are formed in the presence of NaOH without SiO_2 addition for the sample Slm_NaOHd4 and in the sample with SiO_2/Al_2O_3 molar ratio 3.6 (Slm_s36d4). Only quartz and trace of zeolites Y (PDF: 076-064) are detected in the sample with higher silica content
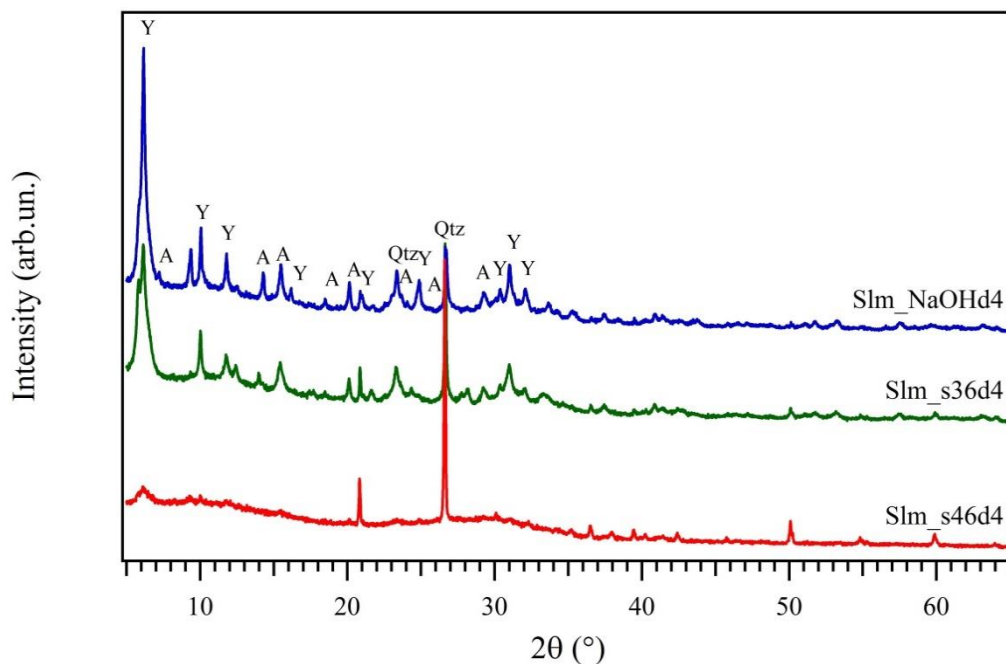
FIGURE 6.3. XRPD patterns of Slm_s46d4, Slm_s36d4 and Slm_NaOHd4 samples after 4 days of incubation at 50°C. Qtz = quartz; Y = Y-type zeolite; A = A-type zeolites.   145

(Figure 6.3, red pattern, $SiO_2/Al_2O_3 = 4.6$). It is well known from literature that kaolinite (Si/Al ~1) is ideally suitable for the synthesis of A-type zeolites, which has similar Si/Al ratio, while Y-type zeolite is formed at higher silica content (Barnes et al., 1999; Chandrasekhar et al., 2004; Belviso et al., 2013). Moreover, some authors have reported that firing temperature of the kaolinitic precursors could influence the formation of zeolite X or Y (Howell & Acara, 1964; Howell et al., 1965). When alunite is added to the Sl-K clay, CAN-type zeolite is the main reaction product as reported in Figure 6.4. In particular, a sulfate-bearing cancrinite, which is the synthetic analogue of the mineral vishnevite (PDF: 000-04320) has been identified. Some traces referred to zeolite Y (PDF: 076-064) have been found also in the sample with 20 wt% alunite after 96 h of incubation (Figure 6.4, green pattern). However, these samples have been incubated with more water than the other samples (see Table 6.1). Quartz and feldspar from the original raw materials are always detected. All samples shown a hump in the region between 22° and 32° 2θ, meaning than an amount of amorphous phase is present after 96 h and also after prolonged time of incubation.
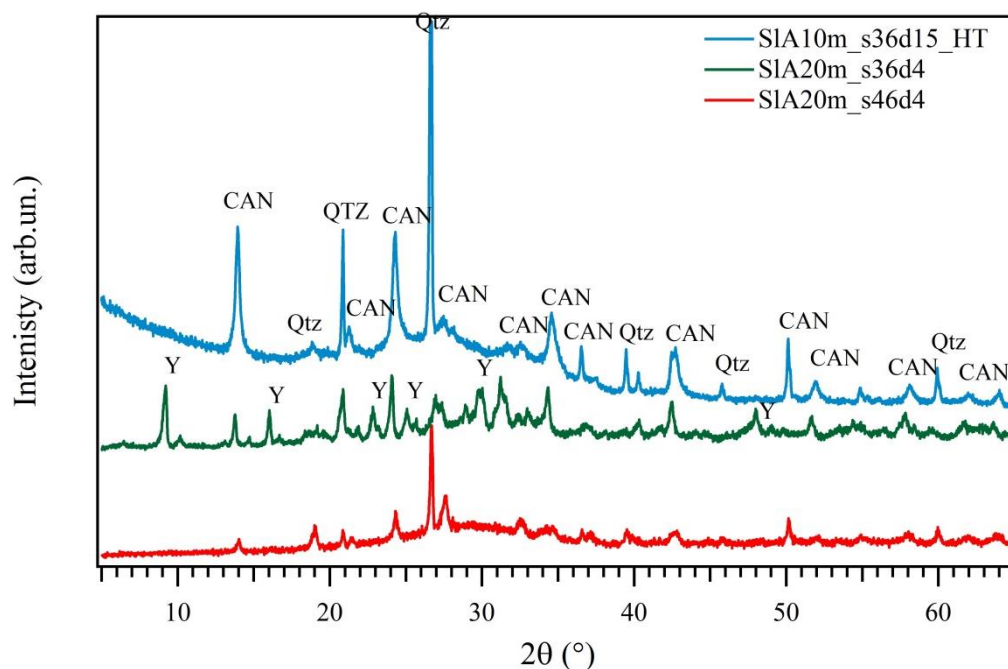
FIGURE 6.4. XRPD patterns of SlA20m_s46d4, SlA20m_s36d4, SlA10m_s36d15 samples after incubation at 50°C. Qtz = quartz; Y = Y-type zeolite; CAN = CAN-type zeolite.

Figure 6.5 shows the XRPD patterns of the samples synthesized starting from the sulfate-bearing clay (L02-K) after 720 h of incubation. Results after 96 h of incubation, here not

reported, are the same but with less intense reflections, certainly due to the shorter incubation time.

Figure 6.5 shows well-crystalline patterns with strong reflections for all the reaction products. CAN-type zeolite is the main reaction product. As already observed for the other samples synthethised from alunite containing mixtures, CAN-type zeolites have been identified as sulfate-bearing cancrinite (PDF: 000-4320). Quartz and feldspars, deriving from the original precursor, are detected as already observed for the other samples.
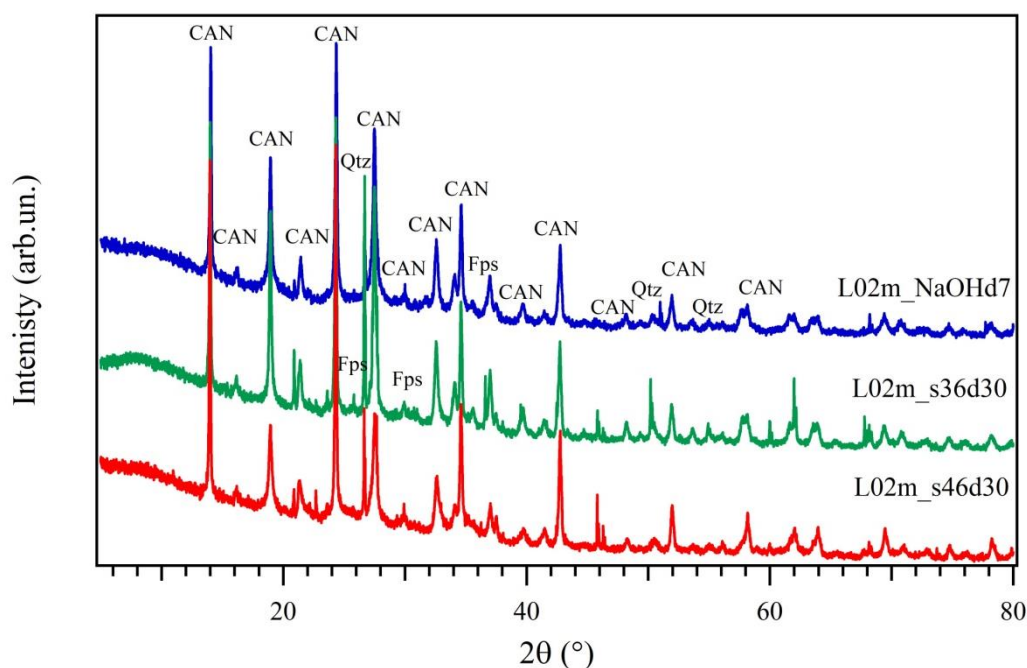
FIGURE 6.5. XRPD patterns of L02m_s46d30, L02m_s36d30 and L02m_NaOHd7 samples after incubation at 50°C. Qtz = quartz; Fps = feldpsars; CAN = CAN-type zeolite.

Figure 6.6 shows XRPD patterns of zeolitization of a mixture of L02-K and sPS_800 after 96 h, and compared with that obtained from L02-K only, and after 168 h of incubation. It is possible to observe that CAN-type zeolites are the main reaction products already after 96 h. The results obtained from a qualitative phase analyses have shown that CAN-type zeolite occurs in all products from alunite-containing mixtures. After alkaline treatment, the high-grade clay shows the occurrence of Y and A zeolites in both samples without silica fume addition and with SiO_2/Al_2O_3 3.6. In the system with higher silica content ($SiO_2/Al_2O_3 = 4.6$), formation of crystalline phases is hindered.
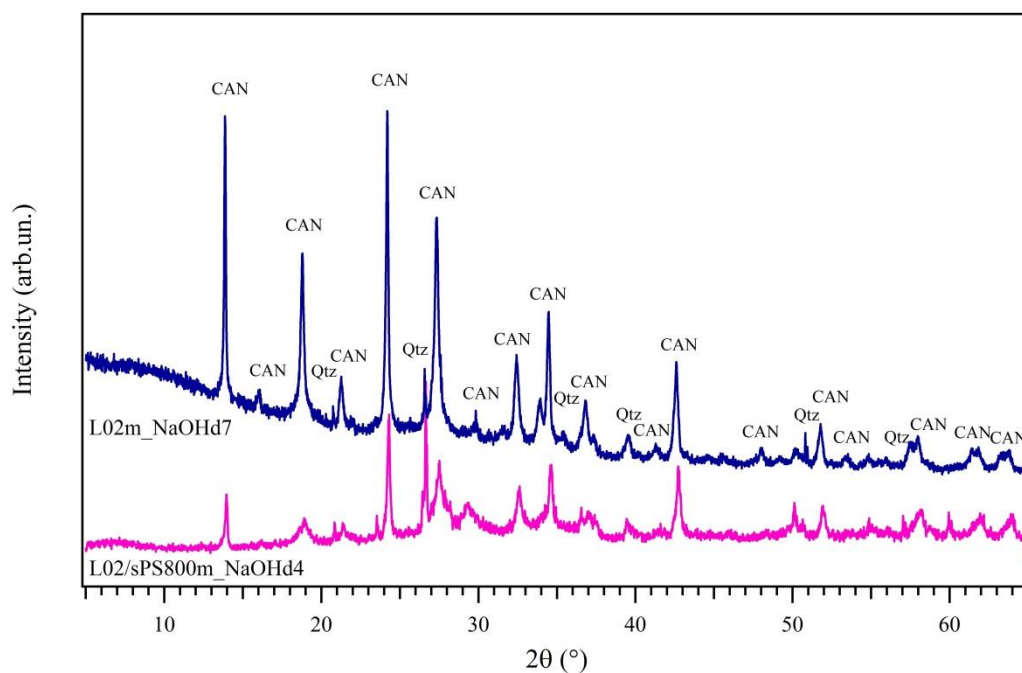
FIGURE 6.6. XRPD patterns of L02m_NaOHd7, L02/sPS800m_NaOHd4 samples after incubation at 50°C. Qtz = quartz; CAN = CAN-type zeolite.

This could be in agreement with the fact that in systems with high silica content and mild temperature conditions, AAMs are stable with no tendency, or very low tendency, towards the amorphous-crystalline trasformation (De Silva & Sagoe-Crenstil, 2008). When sulfate is added to the high-grade kaolin, after 4 days of incubation, CAN-type zeolites are formed, and in this case, differences related to the silica fume addition are significant. Samples with SiO_2/Al_2O_3 lower than 3.6 show crystals of CAN-type zeolites and traces of Y zeolites have been found in the sample with $SiO_2/Al_2O_3 = 3.6$. Raising the SiO_2/Al_2O_3, only a few traces of CAN could be identified and the amorphous region between 20-35° 2θ is evident. On the contrary, activation by molten salt methods of L02-K clay seems not to be affected by the silica content and CAN-type zeolites formation occurs for the whole three batches. Even though a quantitative analysis has not been carried out at this stage, from a visual point of view, it is evident that L02-K shows a higher tendency to form CAN-type zeolite than Sl-K clay, as highlighted by the strong reflections of the corresponding peaks and less pronounced amorphous halo in the region of 20-35° 2θ.

CAN building units contain the extraframework cations (Na, Ca), anions and anionic groups (mainly CO_3^{2-} plus minor SO_4^{2-}) so the large channels are filled by carbonate groups in ideal cancrinite and by sulfate groups in ideal vishnevite (e.g., Bonaccorsi & Merlino 2005). There

is a complete solid solution between cancrinite and vishnevite, with intermediate terms named sulfatic cancrinite or carbonatic vishnevite (Hassan & Grundy 1984).

6.2 Textural and microstructural properties

Figure 6.7 shows a micrograph of sample Slm_s36d30 after 720 hours of incubation time. At this length scale (30 Kx), sodalite crystals (not detected by XRPD analysis) have been observed as "ball shape" morphology together with octahedral morphology, typical of zeolite Y. However, this sample has been incubated with a higher S/L ratio than that used for the other samples, so that the mixture is more diluted. SEM observations confirmed that the product of Sl-K clays mixture show the same zeolitic phases even though different dilutions and incubation times have been used.
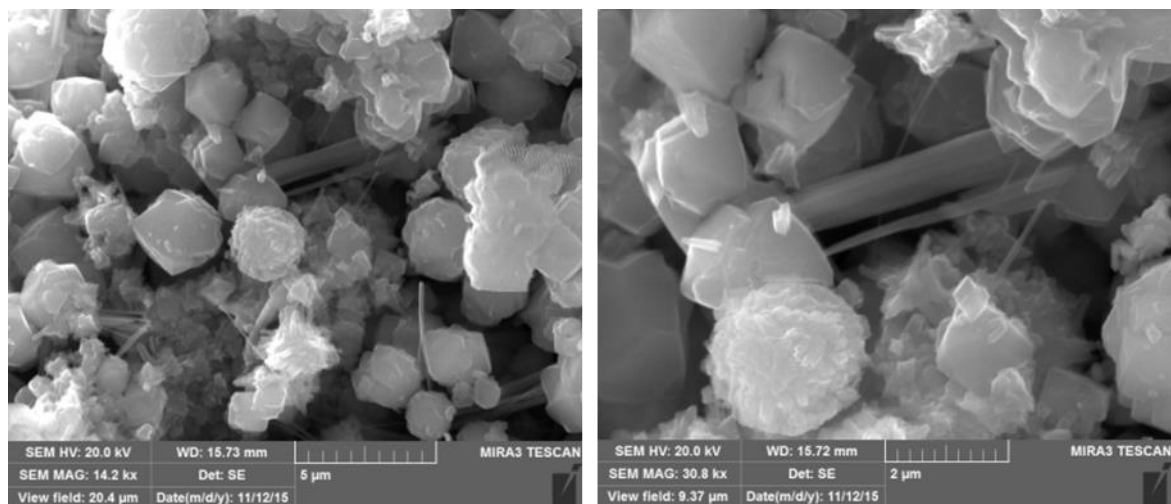
FIGURE 6.7. SE-Micrograph of the Slm_s36d4 sample at different length scales after 720 hours of incubation.

SEM images of the Slm_NaOHd4 sample after 96 h of incubation and S/L ratio of 1g/5ml shows, similarly to the previous sample, some cubic zeolites with the "cotton ball"-like morphology. These are not detected by XRPD analyses and could be attributed to SOD-type zeolites. However, the crystals size is less than 1 μm.

Figure 6.8 shows L02m_s36d4 sample after 96 h of incubation, wherein only "ball-shape" morphology of nano-sized crystals are evident. At this scale, the crystals do not show developed morphology, and because of their small size, they cannot be identified by this technique.
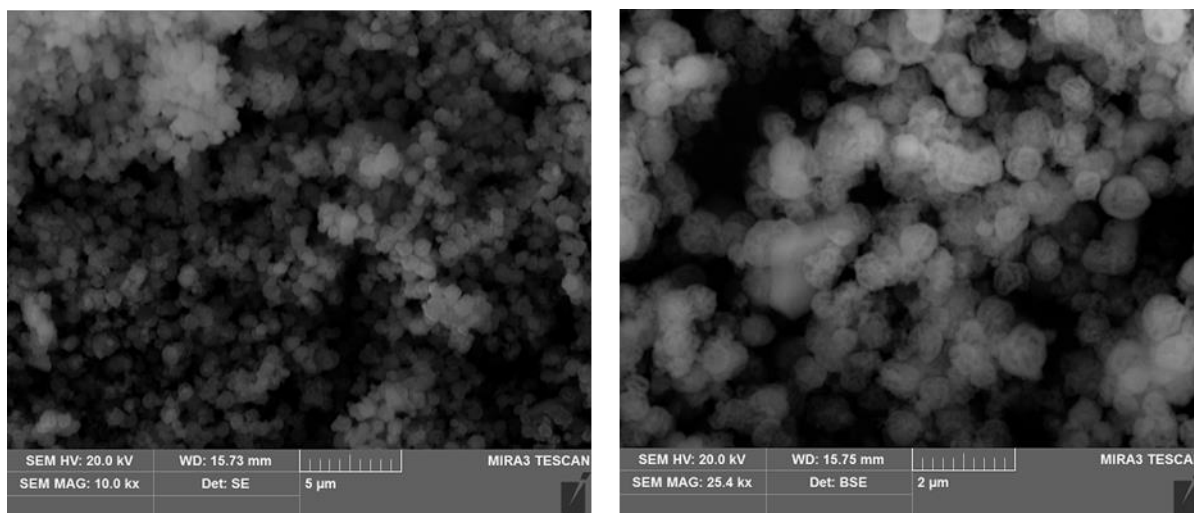
FIGURE 6.8 Micrograph of the L02m_s36 sample at different length scales after 720 hours of incubation.

6.3 Conclusions

These experimental investigations show that syntheses of sulfate-bearing cancrinite could be achieved by using molten salt method and low temperature of incubation.

No sulfate salts have been observed and the absence of SO_4^{2-} in the supernatant liquid after incubation, confirmed by ICP-OES, indicates that sulfate is all contained in the zeolites. SlmA10_s36d15, after 360 hours of incubation, shows 87 wt% of sulfate retention, while L02m_s36d4 and L02m_s36d30 show sulfate retention of 64 wt% and 98.5 wt%, respectively.

From XRPD analysis, already after 96 hours of incubation, reflections of CAN-type zeolites are observed in all samples containing sulfate. SEM-EDS reveals small clusters with morphology resembling sodalite typical "ball-shape" morphology, however sodalite have was not detected by XRPD. According to literature (Barnes et al., 1999), a phase transformation among sodalite-cancrinite, which involves solution-mediated mechanisms with sodalite dissolution, and subsequent cancrinite precipitation (which is more stable with respect to sodalite) could be possible in this system.

The presence of sulfate anion in this system seems to drive the nucleation and precipitation of CAN-type zeolites, likely acting as a 'structure director' during crystallization as already observed for other anions such as nitrate, thiosulphate or sulfite.

References

Barnes, M. C., Addai-Mensah, J., & Gerson, A. R., 1999. The mechanism of the sodalite-to-cancrinite phase transformation in synthetic spent Bayer liquor. Microporous and Mesoporous Materials, 31(3), 287-302.

Barrer, R. M., 1981. Zeolites and their synthesis. Zeolites, 1(3), 130-140.

Belviso, C., Cavalcante, F., Lettino, A., & Fiore, S., 2013. A and X-type zeolites synthesized from kaolinite at low temperature. Applied Clay Science, 80, 162-168.

Bonaccorsi, E., & Merlino, S., 2005. Modular microporous minerals: cancrinite-davyne group and CSH phases. Reviews in Mineralogy and Geochemistry, 57(1), 241-290.

Chandrasekhar, S., & Pramada, P. N., 2004. Kaolin-based zeolite Y, a precursor for cordierite ceramics. Applied Clay Science, 27(3), 187-198.

De Silva, P., & Sagoe-Crenstil, K., 2008. Medium-term phase stability of Na_2O-Al_2O_3-SiO_2-H_2O geopolymer systems. Cement and Concrete Research, 38(6), 870-876.

Hackbarth K., Gesing T.M., Fechtelkord M., Stief F. & Buhl J.-C. 1999. Synthesis and crystal structure of carbonate cancrinite $Na_8[AlSiO_4]_6CO_3(H_2O)_{3.4}$, grown under low-temperature hydrothermal conditions. Micropor. Mesopor. Mater., 30, 347-358.

Hassan, I., & Grundy, H. D., 1984. The character of the cancrinite-vishnevite solid-solution series. The Canadian Mineralogist, 22(2), 333-340.

Howell, P.H., Acara, N.A., 1964. US Patent No. 3,119, 660.

Howell, P.H., Acara, N.A. Jr., Towne, M.K., 1965. Br. Pat. No. 980, 891.

CONCLUSIONS

This Ph.D. study has assessed the possibility to valorize through the alkali activation process two different Italian raw materials: a sulfate-bearing kaolinitic clay and Pietra Serena sewage sludge for the synthesis of AAMs. The former is currently unused resource and the latter simply discarded in landfills. Considered the need to have a long-term, secure supply of the materials for the cement production, different raw materials need to be evaluated. In particular, the systematic recovery of residual sludge from mining and stones cultivation needs to be recognized as a way of implementing environmental safeguard and conservation of non-renewable resources. The results are promising, as both resources demonstrated to be reactive in the alkali activation process giving an aluminosilicate gel binder as main product.

Throughout this work, it has become clear that, in alkaline cement design, both raw material and activator must be selected carefully. However, a deep knowledge of the starting materials allows the use of any silico-aluminous material of natural or industrial origin in the process of alkaline activation. A thorough analysis of the chemical composition and physical-chemical properties of the raw materials is necessary in order to assess cement system performance. This knowledge would allow selecting the synthetic parameters or the most appropriate dosage for the desired application.

Beside the first more applicative objective, a second, fundamental objective of this thesis has underpinned the study of the effect of the sulfate deriving from L02-K clay in the alkali activation process. The study has been carried out either in presence of sodium silicate or sodium hydroxide as activators.

In the system $Na_2O–Al_2O_3–SiO_2–H_2O(–SO_4)$, achieved by activating sulfate-bearing kaolinitic clay with sodium silicate, the amorphous N-A-S-H gel is the main reaction product in presence or in absence of sulfate ions. The morphology of the gel seems to be affected by the sulfate presence, but its effect is weakened by soluble silica. Signs of incipient crystallization of the gel have been observed in the AAMs with lower silica content in the reacting system (SiO_2/Al_2O_3 ratio = 3.6, which is however high and unfavorable to zeolites crystallization). In all samples containing sulfate, no new crystalline phases have been found apart from thenardite, which forms as by-product after setting time. It is leached in water, but part of sulfate remains in the samples. These findings indicate that sulfate may be trapped in amorphous insoluble phases, likely the aluminosilicate gel itself or nanozeolites. The amount of unsoluble sulfate is higher in samples with the highest SiO_2/Al_2O_3 ratio. A further and detailed study of the amorphous reaction products is needed in order to verify sulfate uptake in the N-A-S-H gel and/or zeolites.

The system Na_2O–CaO–Al_2O_3–SiO_2–H_2O–SO_4 has been achieved by blending sulfate-bearing kaolinitic clay and residual sludge of Pietra Serena cultivation. The use of heat-treated sludge, sPS_800, add reactive CaO to the investigated system. NaOH solutions of different molarities have been used as activators. These blends require hydrating and curing conditions used for alkaline cements rather that those used for OPC. Such conditions allow the dissolution of metakaolinite. The behavior of sPS_800 is similar to pozzolanic cement, in which the calcium oxide produced by decarbonation is hydrated and reacts with the silica present in the material to generate a C-S-H gel, which can contribute to enhance the mechanical performances of the final material. Best values of compressive strength after one day of curing at 85°C have been obtained for the sample with 2 wt% CaO in the mix, with values that are three times higher than the those of L02-MK activated with NaOH. In the mixtures with sPS_800, interaction between the different precursors occurs, giving rise to a mixture of N,(C)-A-S-H / C-(A)-S-H gels, similar to those produced in so-called mixed alkali cements or *hybrid cements*. In this system, calcium sulfo-aluminate compounds such as U-phase or ettringite are formed. The actual formation of one or the other depends on the alkalinity of the activation solution. Sulfate-bearing cancrinite has been found in all samples prepared at 8M and cured at 85°C. Formation of cancrinite and ettringite is considered desirable, as both structures can trap sulfate, in fact they can be used for nuclear waste encapsulation via cementation. Ettringite is also desired in systems like calcium sulfo-aluminate cements to produce special binders such as shrinkage-resistant and self-stressing cements.

The crystalline products of the reaction of the two kaolinitic clays with alkali have been evaluated. Zeolitation of Sl-K was carried out under molten condition in the absence or presence of sulfate by adding thenardite to the mixture. In the former case, it gave A and Y zeolite, as expected. On the other hand, when sulfate is contained in the reacting mixtures sulfate bearing cancrinites are the main reaction products.

Therefore, it can be concluded that sulfate ion could drive the nucleation and precipitation of CAN-type zeolites, likely acting as a 'structure director' during crystallization. From these findings, one may speculate that sulfate may have the same effect also in alkali activation process and that the local structure of the N-A-S-H gel may resemble that of cancrinite. A possible continuation of this work could focus on the experimental verification of this hypothesis.

Acknowledgments